# Thermal and Spectral Effects in Intracavity Raman Lasers

Gerald Michael Bonner

University of
Strathclyde
Glasgow

MACQUARIE
UNIVERSITY
SYDNEY ~ AUSTRALIA

A thesis presented in fulfilment of the requirements for the degree of Doctor of Philosophy.

Department of Physics, University of Strathclyde
Department of Physics and Astronomy, Macquarie University

2013

## Declaration of Authenticity and Author's Rights

This thesis is the result of a joint enrolment PhD project between the University of Strathclyde in the UK and Macquarie University in Australia, and it has been prepared to meet the submission requirements of both universities.

This thesis is the result of the author's original research. It has been composed by the author and has not been previously submitted for examination which has led to the award of a degree.

The copyright of this thesis belongs to the author under the terms of the United Kingdom Copyright Acts as qualified by University of Strathclyde Regulation 3.50. Due acknowledgement must always be made of the use of any material contained in, or derived from, this thesis.

Signed:

Date:

# Contents

# Acknowledgements

Thanks are due to many people who have supported me throughout this slightly crazy venture of doing a PhD at two universities on opposite sides of the world. First and foremost to my supervisors, Dr Alan Kemp and Dr Helen Pask. Thank you both for giving me this opportunity and for your guidance and support. You were always ready to help and I have learned much from you that I will value for years to come.

Thanks also to the many researchers at both universities who have helped me in various ways, Dr Walter Lubeigt for teaching me the basics of laser construction, Drs Vasili Savitski, John-Mark Hopkins, David Burns, Patsy Millar, Alex MacLean, Rich Mildren, Aaron McKay, and Andrew Lee for readily sharing their know-how, tips, tricks and stashes of good equipment with me, and to Dr David Spence, for spending much time explaining the theory behind Raman lasers to me, and especially for his guidance on Chapter 5.

Thanks are also due to several collaborators – Prof. Takashige Omatsu of Chiba University, with whom I worked on the thermal lens measurements reported in Chapter 3, the groups of Prof. Jiyang Wang and Prof. Huaijin Zhang of Shandong University, who grew the $BaWO_4$ crystal used in many of my experiments, and Dr Ian Friel and his colleagues at Element Six Ltd, who supplied the diamond samples tested in Chapter 2.

I'm also very grateful for the support of fellow PhD students in both research groups: Rolf, Peter, Sean, Elisabeth, Ewan, Daniel, Jipeng, Lily, Jonas, Chris – thank you for being such excellent team mates. Thanks also to fellow students and office mates in both departments – Loyd, Fiona, Sharon, Caroline, Daniele, Johannes, Ondra, Alex, Jocelyn, Yuan, Robert and Jana (there *is* a PHD Comic for everything!).

Thanks are also due to the technical and administrative staff at both universities – Paul Hynd, Walther Adendorrf, Ewan Mulhern, Lynda McLaughlin, Sharon Kelly, Lisa Flanagan, Grace Tedman, Carol McNaught, Laura Yang and Lisa Chanell.

Thank you to my friends here in Glasgow who have always supported me and to the many new friends who welcomed me so warmly to Sydney – David, Martin, Jeeson, Brendan, Michael, Beth, Elyse, Jeremy, Chris, Martin, Robert, Nick, Angelo, Justin, Emily, Annemarie, Stephen, William and too many others to list here. Thank you all.

Finally, I must express my deepest gratitude to my parents and my sister, Lucy. Thank you for all your love and support.

# Abstract

Stimulated Raman scattering is a convenient way to extend the spectral coverage of well-established solid-state laser sources. In an intracavity Raman laser, a Raman crystal is placed inside the cavity of the fundamental laser, and the output frequency is red-shifted by an amount corresponding to a vibrational energy level of the Raman crystal. Despite the physical simplicity of these lasers, the interactions between the various optical fields are complex, and must be understood in order to realise efficient, high power operation. This thesis presents a detailed investigation of thermal and spectral effects in CW intracavity Raman lasers.

A disk geometry was used to reduce the thermal lens in the laser gain crystal, thereby permitting more flexible cavity design. This facilitated experiments to probe and control the thermal and spectral effects.

Diamond was assessed as a potential Raman crystal with weak thermal lensing. The optical losses in several crystals were measured and while some low loss material was identified, the supply of such material is not yet reliable.

The thermal lens in a common Raman crystal, $BaWO_4$, was measured and found to be negative and astigmatic. Using a coupled cavity configuration, experiments were performed to disentangle the effects of the thermal lenses in the laser gain and Raman crystals. This information was used to refine the cavity design and improve the performance of the laser in a more systematic way than would otherwise have been possible. It was shown that Raman lasers using laser gain disks can provide comparable performance to rod-based systems.

The first ever detailed investigation into spectral broadening in CW crystalline intracavity Raman lasers was undertaken using a combination of theory and experiment. The use of etalons to limit the broadening was investigated and it was found that these could improve the spectral brightness of the laser.

# Chapter 1

# Introduction

The laser was once described as a “solution looking for a problem”, but in the five decades since Maiman’s first demonstration [1], lasers have become ubiquitous, finding application in tasks ranging from eye surgery to cutting steel. Bulk solid state lasers, based around doped dielectric crystals or glasses, can be compact devices, providing high quality output beams. However, such devices can only operate at wavelengths corresponding to transitions between energy levels of species that have suitable properties for laser action. If solid state lasers could be operated at new wavelengths without sacrificing other aspects of their performance, yet more applications would be opened up. Extending the spectral coverage of solid state lasers is therefore a major topic of research. Such efforts include searching for laser materials that will provide gain directly at new wavelengths, while other approaches are based around nonlinear frequency conversion techniques.

This thesis presents work on one such technology - intracavity Raman lasers, which change the wavelength of the output from a conventional laser gain material via stimulated Raman scattering. The goal of this work was to investigate and mitigate/manage the thermal and spectral problems which arise in such systems.

In this chapter, the physics of stimulated Raman scattering will be described and the construction of Raman lasers will be discussed with an emphasis on continuous wave intracavity Raman lasers, which are the focus of this thesis. The performance of such devices will be reviewed. The key challenges in building and operating intracavity Raman lasers will then be described. A major theme of the work presented in this thesis is the use of a disk geometry for the laser gain crystal in Raman lasers, and therefore disk laser technology will also be reviewed. Finally, an outline of this thesis will be given.

## 1.1 Stimulated Raman scattering

Raman scattering is a well known phenomenon whereby light scatters inelastically from a material, exchanging energy with the vibrational energy levels of the material.

Spontaneous Raman scattering was first observed by CV Raman in 1928 [2] and since then Raman spectroscopy has been an extremely useful tool for probing the vibrational energy level structure of many materials. Spontaneous Raman scattering is a weak process – in condensed matter typically only 1 part in $10^6$ of the incident radiation will be scattered [3]. However, when the intensity of the pump light is sufficiently high the process becomes much more efficient, as the large numbers of pump and scattered [Stokes] photons stimulate more scattering events. Stimulated Raman scattering (SRS) was one of the first nonlinear optical processes discovered after the invention of the laser – in 1962 the process was first observed in a nitro-benzene cell that was being used to Q-switch a ruby laser [4] and it was subsequently seen in other organic liquids also [5]. Soon afterwards the effect was also observed in solids, such as diamond and calcite [6], and gases, such as hydrogen and methane [7].

Raman scattering is shown schematically in Figure 1.1. A pump or fundamental photon interacts with a material, generating a Stokes photon and a phonon in the material's vibrational energy levels. The frequency of the Stokes photon, $\omega_{\mathrm{S}}$, is red-shifted relative to that of the fundamental photon, $\omega_{\mathrm{F}}$, such that energy is conserved:

$$\omega_{\mathrm{S}} = \omega_{\mathrm{F}} - \omega_{\mathrm{R}} \tag{1.1}$$

where $\omega_{\mathrm{R}}$ is the frequency of the material vibration. If the upper vibrational energy level is already populated, then the reverse process can happen, whereby the material vibration returns to its ground state and the fundamental photon is blue-shifted, generating an anti-Stokes photon. However, in thermal equilibrium the population of the upper vibrational energy level is generally negligible [8].

The field driving the SRS process is referred to as either the pump field or the fundamental field. The former term is more appropriate for single pass Raman generators and external cavity Raman lasers, while the latter is used when dealing with intracavity Raman lasers (the different configurations of Raman lasers will be described in Section 1.2.1). Since the work presented in this thesis deals with intracavity Raman lasers, the following terminology will be used: the diode laser light used to pump the

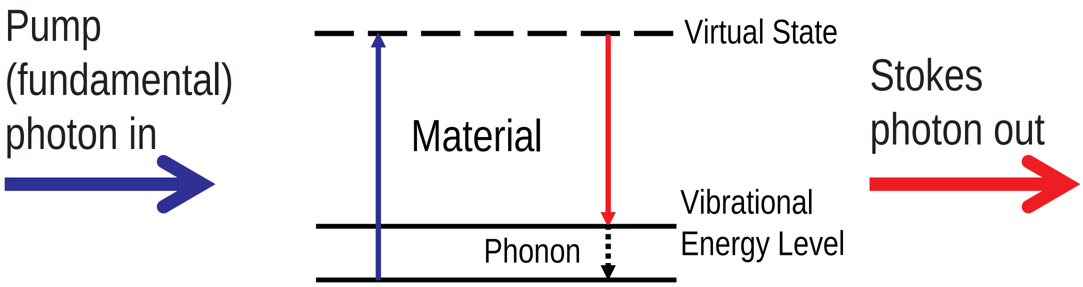

**Figure 1.1:** Schematic of the Raman scattering process. This phenomenon occurs spontaneously at low intensities but at high intensities the process becomes stimulated leading to efficient transfer of energy from the pump field to the Stokes field.

laser gain material will be referred to as the pump field, the light emitted by the laser gain material will be referred to as the fundamental field, and the Raman-shifted light will be referred to as the Stokes field. It should be noted that there is no harmonic relationship between the "fundamental" field and the Stokes field; the term "fundamental" is used simply to avoid confusion with the diode laser pump source.

As mentioned above, at high intensities Raman scattering becomes a stimulated process leading to much more efficient transfer of energy from the fundamental field to the Stokes field. Stimulated Raman scattering (SRS) is a third-order nonlinear effect but unlike many other nonlinear frequency conversion techniques, such as second harmonic generation, it is not necessary to phase match SRS – the process is "automatically phase-matched" since the phonon field always adopts the correct phase such that the Stokes field is coherently driven. This makes Raman lasers more compact and robust than, for example, optical parametric oscillators, which require careful control of the phases of the intracavity fields.

SRS can also cascade to higher orders, in other words the 1st Stokes field, if it reaches sufficiently high intensities, can itself drive the SRS process and be Raman-shifted by the same Raman transition to the 2nd Stokes frequency and so on [9]. This extends the accessible range of wavelengths and also opens up the possibility of multiple wavelength lasers, which will be discussed later.

A brief review of the standard theory of SRS will now be given [3, 8–10]. SRS depends upon the imaginary part of $\chi^{(3)}$, the third order nonlinear susceptibility, which is proportional to the square of the normal mode derivative of the molecular polarisability tensor, ${}^{\partial\alpha}/_{\partial q}$. Penzkofer *et al* [10] apply a quantum treatment to derive the rate of change of the occupation number of a single Stokes mode, $n(k_\mathrm{S})$;

$$\frac{\mathrm{d}n(k_\mathrm{S})}{\mathrm{d}t} = N\left(\frac{\partial\alpha}{\partial q}\right)^2 \frac{4\pi^3\omega_\mathrm{S}}{\mu_\mathrm{F}\mu_\mathrm{S}^2 m\omega_\mathrm{R}c}\big(1+n(k_\mathrm{S})\big)\, I_\mathrm{F}\,\rho\left(\omega_\mathrm{S}-\omega_\mathrm{F}+\omega_\mathrm{R}\right) \tag{1.2}$$

where $N$ is the number density of Raman-active molecules, $\mu_\mathrm{F}$ and $\mu_\mathrm{S}$ are the refractive indices of the Raman medium at the fundamental and Stokes frequencies respectively, $m$ is the reduced mass for the oscillating molecule, $c$ is the speed of light and $I_\mathrm{F}$ is the intensity of the fundamental laser light. Assuming a spectrally narrow fundamental field and a homogeneously broadened Raman transition [10], the spectral distribution of the interaction is given by

$$\rho\left(\omega_\mathrm{S}-\omega_\mathrm{F}+\omega_\mathrm{R}\right) = \frac{1}{\pi}\frac{\Delta\omega_\mathrm{R}/2}{\left(\omega_\mathrm{S}-\omega_\mathrm{F}+\omega_\mathrm{R}\right)^2+\left(\Delta\omega_\mathrm{R}/2\right)^2} \tag{1.3}$$

where $\Delta\omega_\mathrm{R}$ is the full width at half maximum (FWHM) of the Raman peak, which is related to $T_2$, the dephasing time over which the phonon field loses coherence: $\Delta\omega_\mathrm{R}/2 = 1/T_2$ [10].

When $n(k_\mathrm{S})$ is very low, spontaneous Raman scattering occurs (indicated by the 1 in the brackets in Equation 1.2). However, when $n(k_\mathrm{S}) \gg 1$,the number of Stokes photons increases exponentially. Transforming to spatial coordinates via $\mathrm{d}/\mathrm{d}t \rightarrow (\mathrm{d}/\mathrm{d}z)(c/\mu_\mathrm{S})$, it is found that

$$n_\mathrm{S} \propto \exp\left(g_\mathrm{R} I_\mathrm{F} z\right) \tag{1.4}$$

where the Raman gain coefficient is [10]

$$g_\mathrm{R}(\omega_\mathrm{S}) = N\left(\frac{\partial\alpha}{\partial q}\right)^2 \frac{4\pi^2\omega_\mathrm{S}}{\mu_\mathrm{F}\mu_\mathrm{S}c^2 m\omega_\mathrm{R}} \frac{\Delta\omega_\mathrm{R}/2}{\left(\omega_\mathrm{S}-\omega_\mathrm{F}+\omega_\mathrm{R}\right)^2 + \left(\Delta\omega_\mathrm{R}/2\right)^2}. \tag{1.5}$$

At the centre of the Raman peak, the gain is

$$g_\mathrm{R} = N\frac{4\pi^2\omega_\mathrm{S}}{\mu_\mathrm{F}\mu_\mathrm{S}c^2 m\omega_\mathrm{R}\left(\Delta\omega_\mathrm{R}/2\right)}\left(\frac{\partial\alpha}{\partial q}\right)^2 = \frac{8\pi^2 N}{\hbar n_\mathrm{S}^2\omega_\mathrm{S}^3\left(\Delta\omega_\mathrm{R}/2\right)}\left(\frac{\partial\sigma}{\partial\Omega}\right) \tag{1.6}$$

where the integrated Raman scattering cross-section is [9, 10]

$$\left(\frac{\partial\sigma}{\partial\Omega}\right) = \frac{\omega_\mathrm{S}^4\mu_\mathrm{S}}{c^4\mu_\mathrm{F}}\frac{\hbar}{2m\omega_\mathrm{R}}\left(\frac{\partial\alpha}{\partial q}\right)^2. \tag{1.7}$$

It can be seen from Equation 1.6 that the Raman gain is proportional to the Stokes frequency, and therefore is higher for shorter fundamental wavelengths. The gain is also higher for higher values of $\partial\alpha/\partial q$ and narrower Raman transitions (smaller $\Delta\omega_\mathrm{R}$). It should be noted that the above expressions apply to the steady state regime, in which the duration of the fundamental pulse is long compared to the phonon dephasing time $T_2$ [8], which is $\sim 10\,\mathrm{ps}$ for many common Raman crystals [9]. In the transient regime the Raman gain is generally lower than in the steady state regime, and it does not depend on the Raman linewidth [8]. This thesis is concerned with continuous wave (CW) Raman lasers and therefore the steady state regime is the most relevant.

Since the intensity of the Stokes field is proportional to the number of Stokes photons, it follows from Equation 1.4 that

$$I_\mathrm{S}(z) = I_\mathrm{S}(0)\exp\left(g_\mathrm{R} I_\mathrm{F} z\right). \tag{1.8}$$

Therefore, the Stokes field experiences exponential gain when passing through the Raman medium in the presence of an intense fundamental field. Equation 1.8 has a similar form to the equation for the amplification of a beam of light by stimulated emission in a pumped laser gain material:

$$I_\mathrm{F}(z) = I_\mathrm{F}(0)\exp\left(\sigma N^* z\right) \tag{1.9}$$

where $\sigma$ is the stimulated emission cross-section and $N^*$ is the population inversion density [11]. The similarity between these two equations reveals the potential to make a Raman laser by placing the Raman gain material in a resonant cavity, analogous to a conventional laser based around stimulated emission. However, it should be noted that there is no population inversion involved in SRS – the Stokes field only experiences gain when the fundamental field is present as well. This means that there is effectively no energy storage in Raman lasers, and so Raman lasers cannot be Q-switched, although they can be, and often are, pumped with Q-switched fundamental sources. Various configurations of Raman lasers will be described in the next section.

## 1.2 Raman lasers

Many of the properties of the Raman effect described above make it an attractive way to alter the frequency of laser sources. SRS offers greater choice of output wavelength compared to frequency-doubling or frequency-tripling [3], which are by definition limited to harmonics of the fundamental laser source. In contrast, SRS offers small shifts of wavelength, which can be cascaded to higher order if necessary, and there is some degree of choice in the size of the shift, which depends on the Raman material chosen. Of course, Raman lasers are only tunable to the extent that the initial laser source is tunable (SRS itself is not tunable) and so they do not offer the very high wavelength flexibility of optical parametric oscillators (OPOs) [3]. On the other hand, they are simpler and more robust than OPOs since the automatic phase-matching of SRS removes the need for phase-matching technology. Raman lasers are also very compatible with well-established solid state laser technology [8], and can be constructed in a number of ways, which will now be examined.

### 1.2.1 Configurations for Raman lasers

A variety of possible configurations for Raman lasers are shown in Figure 1.2. In a Raman generator the pump (fundamental) pulses make a single, or sometimes double, pass through the Raman medium and spontaneously scattered Stokes light is amplified. Strictly speaking a Raman generator is not actually a Raman laser since there is no cavity around the Raman medium for the Stokes field. Therefore, Raman generators do not have a threshold as such, but there is a critical intensity above which the conversion efficiency rises rapidly [8]. This critical intensity is typically of the order of $100\,\mathrm{MW\,cm^{-2}}$, and Raman generators are typically pumped with picosecond fundamental laser sources [9]. Such high intensities can be close to, or above, the damage thresholds of some Raman crystals, and additional non-linear effects such as self-focussing can exacerbate these problems [8]. Higher order SRS is also often observed in Raman generators, as energy cascades from the 1st to the 2nd Stokes wavelength and so on, and the configuration does not provide any way to easily suppress the generation of unwanted higher Stokes orders [8]. Sometimes, a single mirror is added to double pass the fundamental and Stokes pulses to increase the gain.

External cavity Raman lasers are constructed by placing a cavity for the Stokes field

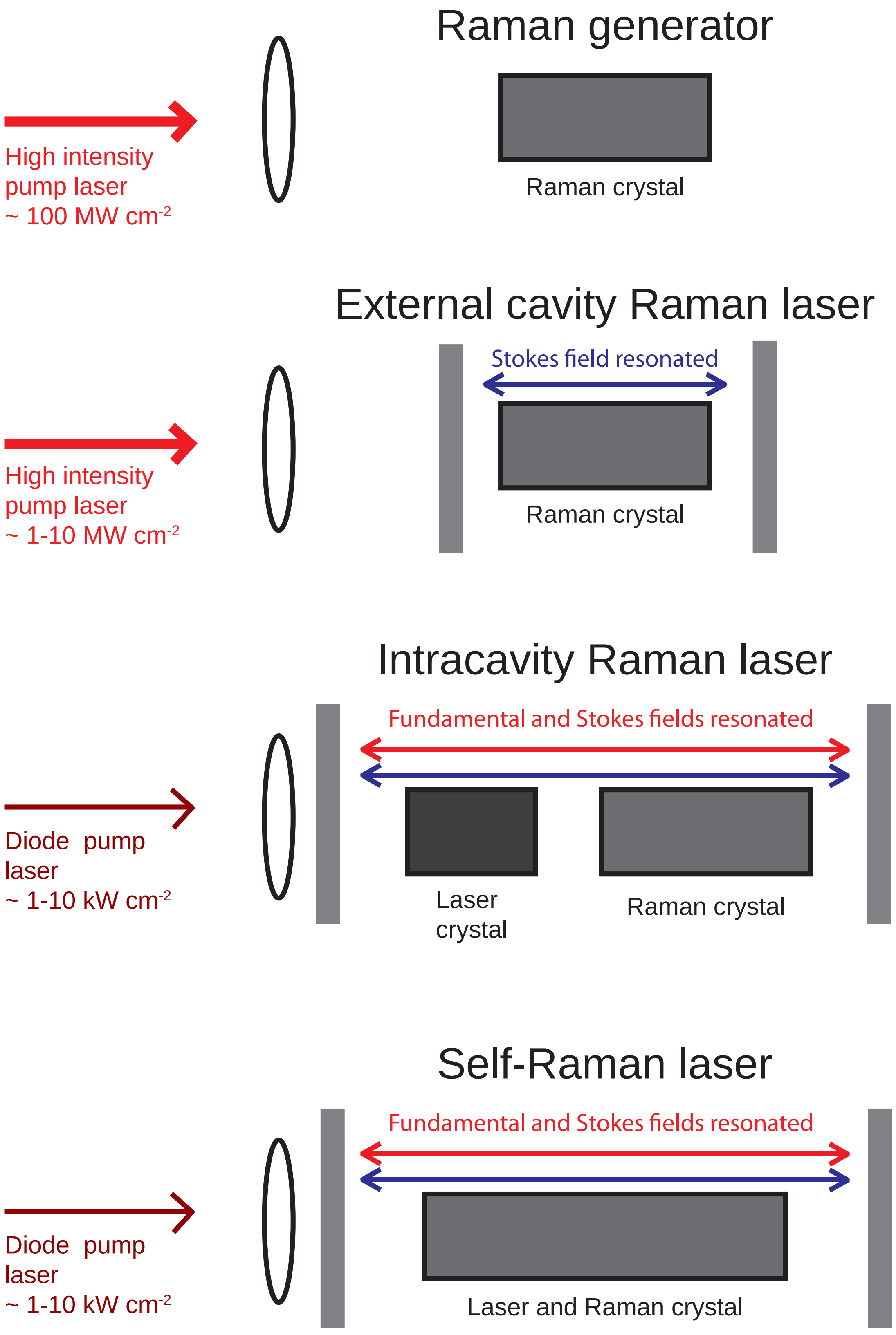

**Figure 1.2:** Raman laser configurations. Orders of magnitude are given for the threshold intensities for oscillation of the Stokes field (or efficient conversion in the case of the Raman generator).

around the Raman medium. The enhanced intracavity intensity of the Stokes field significantly reduces the pump (fundamental) intensities required for efficient conversion. The Stokes field will oscillate in the cavity when the threshold condition is satisfied [8]:

$$R_1 R_2 \exp\left(2 g_\mathrm{R} I_\mathrm{F} l_\mathrm{R}\right) \geq 1 \tag{1.10}$$

where $l_\mathrm{R}$ is the length of the Raman medium and $R_1$ and $R_2$ are the mirror reflectivities. The cavity losses at the Stokes wavelength have been assumed to be dominated by the mirror transmission, which is reasonable since external cavity Raman lasers operate with output couplings of up to 50 % [9]. Typically pump (fundamental) intensities of the order of $1\,\mathrm{MW\,cm^{-2}}$ to $10\,\mathrm{MW\,cm^{-2}}$ are required to reach threshold in external cavity Raman lasers [8].

The Stokes cavity brings other benefits, as well as reducing the threshold. Appropriate choice of mirror coatings makes it possible to select the desired Stokes order by making both mirrors highly reflecting for all Stokes orders below the desired one, and only output coupling the desired wavelength [9]. Significant output coupling of the desired Stokes order then suppresses the generation of higher orders. The external cavity also provides some control of the transverse spatial mode of the Stokes field, leading to improved output beam quality [8].

In an intracavity Raman laser, the Raman medium is placed inside the laser cavity of the fundamental source itself. The cavity is resonant for both the fundamental and Stokes wavelengths. The very high intracavity fundamental intensity leads to a low threshold, such that the Raman threshold can be reached when the laser gain crystal is pumped with diode laser intensities of the order of $10\,\mathrm{kW\,cm^{-2}}$ or less. Placing the Raman crystal in the same cavity as the laser gain crystal makes it possible to build compact systems and, in principle, these are simple devices which can be based on mature diode-pumped solid state laser technology, especially Nd-based sources. The only major adaptation required to the components used for a diode-pumped Nd laser, apart from the addition of the Raman crystal itself, is extending the high reflectivity range of the mirrors to include the Stokes wavelength, and likewise extending the low reflectivity range of the anti-reflection coatings on the crystal surfaces. Intracavity optical elements can be inserted for a variety of purposes, for example acousto-optical Q-switches to make the fundamental laser (and hence the Raman laser) operate in a pulsed mode. A self-Raman laser is particularly compact, as in such a system the same crystal is used as both the laser gain medium and the Raman medium, with the dopant ions providing laser gain and the host lattice providing Raman gain, for example Nd:$\mathrm{GdVO_4}$.

In practice, the behaviour of intracavity Raman lasers is complicated, due to the interactions between the fundamental and Stokes fields and the population inversion, and due to the thermal lenses which arise in the cavity. The SRS process provides a nonlinear output coupling to the fundamental field, and this in turn feeds back into the efficiency of the stimulated emission process. Raman beam cleanup [12] results in the Stokes field generally having higher beam quality than the fundamental field, the beam quality of which is often actually degraded by the SRS process. Temporal effects also occur – for example the variation of the relaxation oscillation frequency with pump power is different below and above the Raman threshold [13]. The nonlinear coupling of the fundamental field to the Stokes field can also lead to spectral broadening, an effect which will be studied in much more detail later in this thesis. The thermal behaviour of intracavity Raman lasers is also complex because two thermal lenses arise in the cavity, one in the laser gain medium and one in the Raman medium, and these behave differently. Thermal effects will also be investigated in detail later in this thesis.

The low thresholds of intracavity Raman lasers make this configuration particularly suitable for CW operation, and most CW crystalline Raman lasers are intracavity devices. These systems are the focus of the work presented in this thesis.

### 1.2.2 Overview of Raman lasers

Raman lasers can be constructed using various materials including dielectric crystals [9], glass fibres (for example [14]) and gases (for example [15]). Crystalline Raman lasers can be particularly compact and robust, and are the topic of this thesis.

Crystalline Raman lasers can operate in a variety of regimes. Extensive work has been done on Q-switched sources in all three of the configurations described above. Many such devices are reviewed in articles by Piper and Pask [9] and Černý *et al* [16]. Note that in these systems it is the fundamental laser source that is Q-switched - as noted above the SRS process itself cannot be Q-switched since there is no energy storage. The highest average power obtained from such systems to date is 24.5 W at 1193 nm in 29 ns pulses at 40 kHz from an external cavity diamond Raman laser [17]. However, this was an unusual system not only because it used diamond as a Raman material but also because the fundamental source was a cryogenically-cooled Yb:YAG laser. A noteworthy result from a simpler, more conventional, system was the 10.5 W at 1180 nm that Chen *et al* obtained from a Q-switched, intracavity Nd:YAG/$SrWO_4$ Raman laser [18].

Ultrafast Raman lasers have also been demonstrated, taking the form of synchronously pumped external cavity systems. Devices operating in the visible (573 nm) [19] and the ultraviolet (275.7 nm) [20] have been demonstrated, pumped with the second harmonic of a modelocked Nd:YAG laser and the fourth harmonic of a modelocked Nd:$YVO_4$ laser respectively. In both cases diamond was used as the Raman crystal. A similar system based on $KGd(WO_4)_2$ has also been demonstrated operating at the 1st and 2nd Stokes wavelengths (559 nm and 589 nm) [21].

Until 2004, crystalline intracavity Raman laser work concentrated on pulsed devices, since the high peak power available in Q-switched pulses makes it easier to reach Raman threshold. However, over the last decade there has been considerable interest in CW systems. The work in this thesis deals entirely with CW intracavity Raman lasers and so these devices will now be reviewed in more detail.

## 1.3 CW crystalline Raman lasers

### 1.3.1 Reaching threshold in CW regime

The high intensities required for efficient Raman conversion make it challenging to reach the Raman threshold in the CW regime. As noted above, Raman generators and external cavity Raman lasers are usually pumped with pulsed fundamental sources, the high peak powers of which lead to efficient Raman laser operation at moderate average powers. However, there have been several demonstrations of CW external cavity Raman lasers based on crystals. The first CW crystalline Raman laser was an external cavity $Ba(NO_3)_2$ system pumped with CW powers of up to 5.5 W at 514 nm from an Ar-ion laser [22]. A maximum output power of 164 mW was obtained, with threshold $< 2.5$ W [22]. The cavity mirrors had reflectivities of 0.16 % and 0.36 % at the Stokes wavelength. The same group later demonstrated a 2nd Stokes external cavity Raman laser based around the same fundamental source and the same Raman crystal [23], giving a maximum output power of 21.7 mW at the 2nd Stokes wavelength of 576.7 nm. The threshold was 3.4 W for the 1st Stokes field and 3.67 W for the 2nd Stokes field [23]. Much more recently, a CW external cavity Raman laser has been demonstrated using diamond as the Raman crystal [24]. The excellent thermal properties of diamond made it practical to focus the 1064 nm pump (fundamental) light from a $Nd{:}YVO_4$ laser to a 30 µm radius spot in the diamond, leading to an intensity of $0.8\,\mathrm{MW\,cm^{-2}}$ at the threshold pump power of 11.3 W. An output power of 10.2 W at 1240 nm was obtained for a pump power of 31 W at 1064 nm [24]. More recently, the same group reported 15 W output power from an external cavity diamond Raman laser pumped with 42 W from a single longitudinal mode Yb-based fibre laser [25].

However, the majority of CW crystalline Raman lasers are intracavity systems. The cavity is resonant for both the fundamental and the Stokes fields, and all the mirrors are highly reflecting for the fundamental wavelength, resulting in very high intracavity intensities. This makes it possible to reach the Raman threshold by pumping the laser gain crystal with only a few watts of diode laser pump light. The output coupling for the Stokes field is generally low, often in the region of 0.5 %, so the intracavity Stokes intensity is also high.

### 1.3.2 Behaviour of CW intracavity Raman lasers

The behaviour of CW intracavity Raman lasers is complex, as energy flows between the population inversion in the laser gain material and the fundamental and Stokes fields. A useful model of these devices has been developed by Spence *et al* [26] that illustrates the trends underlying this behaviour and highlights the key parameters which influence the performance of these lasers. The key results of this model will be summarised here. The model assumes top hat transverse profiles for the various fields, and that the mode radii do not vary within the laser and Raman crystals (though they can be different in the two crystals). The fundamental and Stokes modes are assumed to be perfectly matched throughout the cavity. The model also assumes that all the gain and loss processes are spread throughout the cavity and occur simultaneously, which is valid for small single-pass gains and losses. These assumptions result in rate equations for the population inversion, fundamental and Stokes intracavity powers [26]:

$$\frac{\mathrm{d}N^*}{\mathrm{d}t} = \frac{P_\mathrm{P}\lambda_\mathrm{P}}{hcA_\mathrm{L}l_\mathrm{L}} - \frac{2\lambda_\mathrm{F}\sigma_\mathrm{L}N^*P_\mathrm{F}}{hcA_\mathrm{L}} - \frac{N^*}{\tau_\mathrm{L}} \tag{1.11a}$$

$$\frac{\mathrm{d}P_\mathrm{F}}{\mathrm{d}t} = \frac{c\sigma_\mathrm{L}N^*P_\mathrm{F}l_\mathrm{L}}{l} - \frac{2cP_\mathrm{F}P_\mathrm{S}g_\mathrm{R}l_\mathrm{R}}{lA_\mathrm{R}\lambda_\mathrm{F}/\lambda_\mathrm{S}} - \frac{cP_\mathrm{F}\left(T_\mathrm{F}+L_\mathrm{F}\right)}{2l} \tag{1.11b}$$

$$\frac{\mathrm{d}P_\mathrm{S}}{\mathrm{d}t} = \frac{2cP_\mathrm{F}P_\mathrm{S}g_\mathrm{R}l_\mathrm{R}}{lA_\mathrm{R}} - \frac{cP_\mathrm{S}\left(T_\mathrm{S}+L_\mathrm{S}\right)}{2l} \tag{1.11c}$$

$$l = \left[l_\mathrm{C} + l_\mathrm{L}\left(n_\mathrm{L}-1\right) + l_\mathrm{R}\left(n_\mathrm{R}-1\right)\right] \tag{1.11d}$$

where $N^*$ is the laser crystal population inversion density, $P_\mathrm{F}$, $P_\mathrm{S}$ are fundamental and Stokes intracavity powers, respectively, $T_\mathrm{F}$, $L_\mathrm{F}$ and $T_\mathrm{S}$, $L_\mathrm{S}$ are the output coupling transmissions and round-trip losses for the fundamental and Stokes fields, respectively. In the laser and Raman crystals: $A_\mathrm{L}$, $A_\mathrm{R}$ are the spot areas (with corresponding spot radii $r_\mathrm{L}$, $r_\mathrm{R}$), $l_\mathrm{L}$, $l_\mathrm{R}$ are the crystal lengths, and $n_\mathrm{L}$, $n_\mathrm{R}$ are the crystal refractive indices (assumed equal at all wavelengths). $l_\mathrm{C}$ is the cavity length, $l$ is the optical cavity length, $\sigma_\mathrm{L}$, $\tau_\mathrm{L}$ are the laser crystal emission cross section and upper level lifetime, $g_\mathrm{R}$ is the stimulated Raman gain coefficient, $P_\mathrm{P}$ is the incident diode pump power, $\lambda_\mathrm{P}$ , $\lambda_\mathrm{F}$ , $\lambda_\mathrm{S}$ are the wavelengths of the pump, fundamental and Stokes fields, respectively [26].

The rate equation for the population inversion (Equation 1.11a) has a growth term related to the pump power, a loss term due to stimulated emission and a loss term due to spontaneous emission and non-radiative decay as in a conventional laser. Meanwhile, the rate equation for the fundamental power (Equation 1.11b) has a growth term related to stimulated emission, a loss term related to the SRS conversion and a loss term related to other losses in the cavity (including mirror transmission). Finally the Stokes power (Equation 1.11c) grows due to the SRS conversion but experiences losses due to parasitic losses and transmission through the cavity mirrors.

From these equations, Spence derives expressions for the diode pump power required to reach the Raman threshold:

$$P_\mathrm{th} = \frac{A_\mathrm{R}}{g_\mathrm{R}l_\mathrm{R}}\frac{\lambda_\mathrm{F}}{\lambda_\mathrm{P}}\frac{\left(T_\mathrm{S}+L_\mathrm{S}\right)\left(T_\mathrm{F}+L_\mathrm{F}\right)}{4} \tag{1.12}$$

and the ratio of the output Stokes power to the diode pump power, when $P_\mathrm{P} > P_\mathrm{th}$:

$$\frac{P_\mathrm{S}^\mathrm{OUT}}{P_\mathrm{P}} = \frac{T_\mathrm{S}}{(T_\mathrm{S}+L_\mathrm{S})}\frac{\lambda_\mathrm{P}}{\lambda_\mathrm{S}} - \frac{T_\mathrm{S}\,(T_\mathrm{F}+L_\mathrm{F})}{4}\frac{\lambda_\mathrm{F}}{\lambda_\mathrm{S}}\frac{A_\mathrm{R}}{P_\mathrm{P}g_\mathrm{R}l_\mathrm{R}} \tag{1.13}$$

assuming that the intracavity intensity of the fundamental field at the Raman threshold (and above) is much greater than the saturation intensity of the laser transition, such that spontaneous emission from the laser crystal can be ignored [26].

Equations 1.12 and 1.13, highlight the importance of minimising the losses at both wavelengths. In Equation 1.13, the first term represents the efficiency with which Stokes photons are coupled out of the cavity and also incorporates the maximum possible efficiency set by the quantum defect between the pump and Stokes wavelengths, while second term determines how close the laser comes to this theoretical maximum efficiency, taking account of how efficiently energy is coupled from the fundamental field to the Stokes field. The ratio $(P_\mathrm{P}g_\mathrm{R}l_\mathrm{R})\,/A_\mathrm{R}$ is a dimensionless parameter which can be referred to as a Raman coupling parameter [26].

### 1.3.3 Review of CW intracavity Raman lasers

CW intracavity Raman lasers based on crystalline gain media were first demonstrated in 2005, both in a self-Raman configuration, using Nd:KGW to provide both laser and Raman gain [27], and with separate crystals, Nd:YAG and KGW, acting as the laser gain and Raman media respectively [28]. Since then, such devices have been demonstrated using a wide variety of Raman crystals, while Nd-doped crystals remain the most widely used fundamental sources thanks to the maturity of the associated crystal growth, mirror coating and diode pump laser technologies. Many conventional Raman crystals have Stokes shifts around $700\,\mathrm{cm}^{-1}$ to $1000\,\mathrm{cm}^{-1}$, such that a fundamental field at 1064 nm is shifted to 1150 nm to 1180 nm [29]. As mentioned above, the cascading nature of the SRS process makes it possible to shift the wavelength further, for example by resonating the fundamental, 1st and 2nd Stokes fields and only coupling out a small fraction of the 2nd Stokes radiation [30]. Intracavity frequency doubling of the 1st Stokes field provides access to the yellow/orange part of the spectrum [31] while sum frequency generation using the fundamental and 1st Stokes fields produces a different wavelength in that spectral region [32].

The output wavelength and maximum output power of most crystalline CW intracavity Raman lasers are plotted in Figure 1.3. It can be seen that numerous systems have been demonstrated operating in the near infrared and the visible, generally providing a few watts of output power. Several systems of particular interest are highlighted with numbers in the figure, and these will now be described in more detail.

(1) The highest reported output powers from CW intracavity Raman lasers were reported by Savitski *et al* in 2012 [33]. A side-pumped Nd:YLF rod was used and two different Raman lasers were constructed around this fundamental gain crystal, one

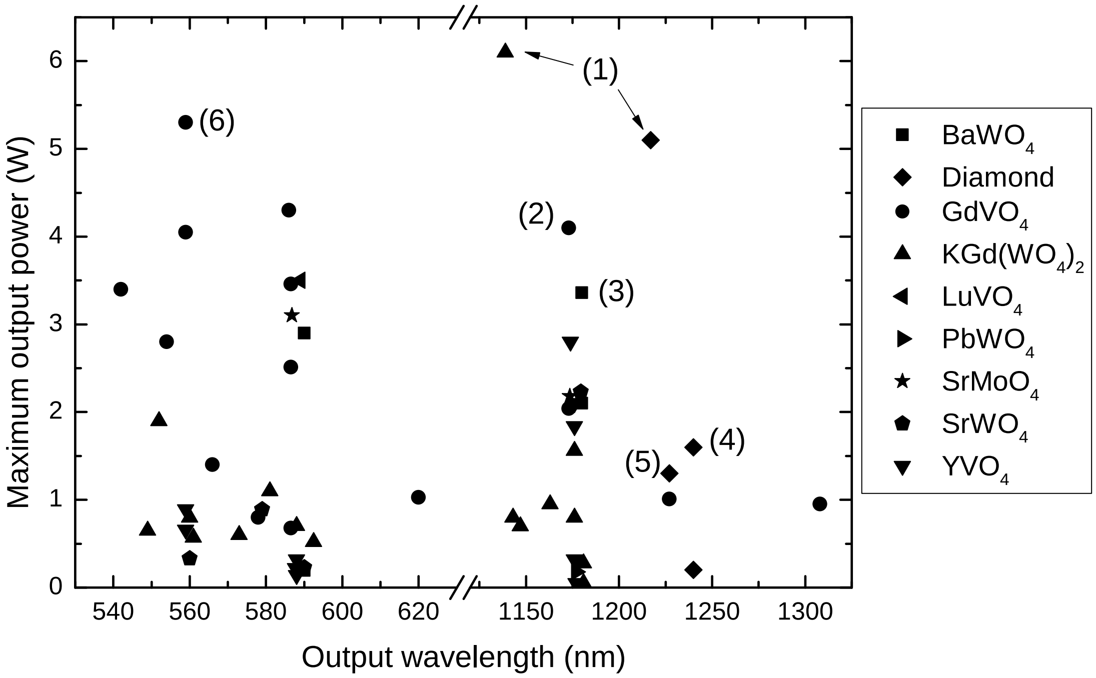

**Figure 1.3:** Summary of CW intracavity Raman laser performance [27, 28, 30–63]. Symbols denote the Raman crystal used – in some cases this is also the host for the laser ions (ie in self-Raman lasers). The numbered systems are described in more detail in the main text.

using diamond as the Raman material and one using $KGd(WO_4)_2$. The Nd:YLF laser operated on the 1047 nm transition. The diamond system produced 5.1 W of output power at the 1st Stokes wavelength of 1217 nm for 153 W of incident diode laser pump power. (The Nd:YLF rod was part of a commercial side-pumped gain unit, and the incident powers were quoted based on the manufacturer's calibration [33].) The $KGd(WO_4)_2$ system produced 6.1 W of output power at the 1st Stokes wavelength of 1139 nm for 150 W of incident diode pump power. In both cases the output beam quality was significantly better than that of the 1047 nm output when the Nd:YLF was operated as a conventional laser, with the improvement in beam quality being greatest when diamond was used as the Raman crystal [33].

(2) Most intracavity Raman lasers are based on end-pumped laser gain crystals rather than side-pumped crystals, and the highest output power to date from an end-pumped system was demonstrated by Lin *et al* who used a double-end-pumping scheme to efficiently pump a Nd:$GdVO_4$ self-Raman laser [34]. An output power of 4.1 W was achieved for 36 W incident pump power, most of which was thought to be absorbed [34], leading to a diode-Stokes conversion efficiency of 11.2 %. The Raman threshold was 1.6 W incident diode pump power at 880 nm. The authors noted that the double-end-pumping scheme led to improved mode overlap and temperature distribution in the crystal [34].

(3) In 2009, Fan et al [35] reported the highest output to date from a single-end-

pumped, 1st Stokes CW Raman laser operating in the near infrared. They obtained 3.36 W at 1180 nm from a Nd:$YVO_4$/$BaWO_4$ laser, pumped with an 808 nm diode laser. The diode-to-Stokes optical conversion efficiency was 13.2 %. This system is of particular interest because Nd:$YVO_4$ and $BaWO_4$ are heavily used in the work presented in this thesis.

(4) Another system of relevance to the present work is the Nd:$YVO_4$/diamond system reported by Lubeigt *et al* in 2011 [36]. A Nd:$YVO_4$ disk bonded to a diamond heat-spreader was used as the fundamental laser gain crystal and a separate diamond rod was used as the Raman crystal. 1.6 W at the 1st Stokes wavelength of 1240 nm was obtained for an absorbed diode laser pump power of 15 W at 808 nm, a conversion efficiency of $\sim 11\,\%$. Very similar Nd:$YVO_4$ disk lasers are used extensively in this thesis.

(5) As noted above, most CW intracavity Raman lasers to date have used Nd-doped crystals as laser gain media. However, there have been several systems built using semiconductor disk lasers (SDLs, also known as vertical external-cavity surface-emitting lasers) [37, 51, 59]. SDLs combine the wavelength-flexibility of semiconductor lasers with the high beam quality and flexible design of free-space laser cavities. Using diamond as the Raman crystal, Parrotta *et al* obtained 1.3 W at the 1st Stokes wavelength of 1227 nm for an absorbed pump power of 9 W. The tunability of the SDL fundamental laser meant that the output Stokes wavelength could be tuned over a range of 1217 nm to 1244 nm [37].

(6) The highest power obtained to date from any CW Raman laser with intracavity sum frequency generation was reported by Lee *et al* [32]. Sum frequency mixing of the fundamental and 1st Stokes fields in a Nd:$GdVO_4$ self-Raman laser produced 5.3 W at 559 nm, corresponding to a diode-visible optical conversion efficiency of 21 %. The Nd:$GdVO_4$ crystal was pumped with an 880 nm diode laser in order to reduce thermal loading in the crystal, and an intracavity mirror was used to prevent backwards propagating visible radiation from being lost via absorption in the Nd:$GdVO_4$.

The summary above has used maximum output power as a performance metric, but for some applications that require only low power levels it may be more desirable to have a low Raman threshold, and high conversion efficiency at modest pump powers. Lisinetskii *et al* [52] demonstrated a Nd:$KGd(WO_4)_2$/$KGd(WO_4)_2$ Raman laser based on a composite crystal (that is, a $KGd(WO_4)_2$ rod of which only a small length was doped with $Nd^{3+}$ ions), which had a Raman threshold of 230 mW diode laser pump power. A maximum output power of 277 mW was obtained at the 1st Stokes wavelength of 1181 nm for an absorbed diode laser pump power of 2 W, corresponding to a diode-Stokes conversion efficiency of 13.9 % [52], which compares favourably to the 14.4 % conversion efficiency obtained at 9 W absorbed pump power from the SDL/diamond

Raman laser in [37] and to the 13.2 % conversion efficiency obtained by Fan *et al* when pumping their Nd:$YVO_4$/$BaWO_4$ laser with 25.5 W incident pump power [35].

High diode-visible conversion efficiencies are also often obtained when using a $\chi^{(2)}$ material to generate either the second harmonic (SHG) of the Stokes wavelength, or the sum frequency (SFG) of the fundamental and Stokes wavelengths. As noted above, Lee *et al* generated 5.3 W at 559 nm for an incident diode pump power of 25 W, corresponding to a diode-visible optical conversion efficiency of 21 %, via SFG of the fundamental and Stokes fields in a Nd:$GdVO_4$ self-Raman laser [32]. The Raman threshold was 2.2 W of incident power at 880 nm. Li *et al* obtained a comparable diode-visible conversion efficiency of 17 % from a miniature Nd:$YVO_4$ self-Raman laser [53] operating at an incident pump power of just 3.8 W, producing 660 mW at 559 nm.

It was noted above that SRS is a cascading process, so that the 1st Stokes field can, when sufficiently intense, drive further SRS leading to the generation of the 2nd Stokes wavelength. Lee *et al* generated 950 mW at the 2nd Stokes wavelength of 1308 nm from a Nd:$GdVO_4$ self-Raman laser, with a conversion efficiency of 6.8 % from the diode laser pump power [30].

The combination of $\chi^{(2)}$ frequency conversion with SRS enables the construction of multi-wavelength lasers. By changing the temperature or the angle of the $\chi^{(2)}$ crystal, the phase-matching condition can be satisfied for SHG of the fundamental field, SFG of the fundamental and Stokes fields, or SHG of the Stokes field [47]. If the 2nd Stokes field is also generated, then further wavelengths become accessible [30]. Care must be taken to balance the strength of the coupling of the various nonlinear processes in these flexible devices [53, 64, 65].

## 1.4 Key challenges in Raman laser design and operation

To build an efficient Raman laser, it is necessary to simultaneously optimise the flow of energy from the pump beam to the fundamental field, via the population inversion, and the conversion from the fundamental field to the Stokes field [26]. If a $\chi^{(2)}$ frequency conversion stage is included then the nonlinear coupling of the SHG or SFG process must also be optimised [26, 47, 53, 65]. It is necessary to optimise the mode sizes in each of the crystals - it is desirable to have a small spot in the Raman crystal to increase the Raman coupling parameter, thereby reducing the Raman threshold and increasing the conversion efficiency [26]. The mode size in the laser gain crystal should be chosen to optimise the extraction of energy from the population inversion and the fundamental beam quality as far as possible.

It is not only the absolute mode size that matters – the spatial overlap between the fundamental and Stokes fields in the Raman crystal is also important. The model developed by Spence *et al* [26], outlined in Section 1.3.2 above, assumed perfect overlap between the fields throughout the crystal but in reality this may not be the case and imperfect overlap between the fundamental and Stokes modes in the Raman crystal reduces the effective Raman gain [13]. The lengths of the various crystals must also be chosen to optimise the coupling parameters for the various processes [26, 54]. With longer crystals, it becomes difficult to maintain small mode sizes throughout the entire crystal and so it is necessary to compromise between crystal length and average mode size in the crystal (Spence's model assumed a constant mode size in each crystal, although it was varied from one crystal to another [26]).

It is clear therefore that careful cavity design is required to engineer appropriate mode sizes in crystals of suitable length in order to build an efficient intracavity Raman laser. However, there are other issues which constrain the cavity design. Strong thermal lenses develop in Raman lasers [41], and these make it difficult to build long, multi-mirror cavities in which appropriate mode sizes can be obtained. In fact, the majority of CW intracavity Raman lasers are based on short, linear cavities (see for example [35, 41, 47]). Small mode sizes, meanwhile, can exacerbate the thermal problems [66, 67]. Of course, short, linear cavities have the advantage of being simple, compact systems but this must be balanced against the design constraints they impose. Another factor that must be taken into account is the round-trip optical loss in the cavity. As noted in Section 1.3.2, CW intracavity Raman lasers are extremely sensitive to losses at both the fundamental and the Stokes wavelengths. The benefits gained from adding another mirror or some other component must therefore be balanced against the losses introduced by such an element, while bulk losses in crystals may limit the optimal crystal length [53]. Relatively complex, multi-layer coatings are required to minimise losses at mirror and crystal surfaces across a broad range of wavelengths, and these coatings are sometimes susceptible to optical damage, which can also place a lower limit on useful spot sizes at various points in the cavity. Finally, complex spectral competition effects have been observed in intracavity Raman lasers [41, 44, 45, 52–54] and therefore the optimal coupling parameters for each process in the cavity may be different from those predicted by a model such as that in [26].

These three issues that present particular challenges for CW intracavity Raman laser design (optical losses, thermal effects and spectral effects) will now be discussed in more detail. Each of these are investigated in the work presented later in this thesis, with a particular emphasis on thermal and spectral effects.

### 1.4.1 Optical losses

CW intracavity Raman lasers are very sensitive to losses at either the fundamental or the Stokes wavelength. Losses at both wavelengths affect both the threshold and slope efficiency of the Raman laser [26], as can be seen from Equations 1.12 and 1.13. It is necessary to maintain high intracavity intensities at both the fundamental and Stokes wavelengths and therefore the cavity mirrors are all highly reflecting at the fundamental wavelength, and only a very small fraction of the Stokes field (generally less than 1 %) is coupled out to form the output beam. Therefore, even small parasitic losses can be significant relative to the coupling of energy from the fundamental field to the Stokes field and relative to the output coupling of the Stokes field.

Minimising optical losses in the cavity is therefore essential in order to build an efficient Raman laser. Self-Raman lasers have an advantage in this regard as the number of surfaces is minimised when the same crystal provides both laser and Raman gain [52]; however, self-Raman lasers present greater thermal problems and offer limited choice of output wavelength.

High quality coatings on mirrors and crystal surfaces are vital, while the work of Li *et al* has shown that bulk crystal losses can be significant also, even in well-established crystals such as LBO [53]. In cases where bulk losses are important, the increase in gain (or nonlinear coupling in the case of frequency doubling crystals like LBO) with length must be balanced against the increasing losses [53]. The availability of low loss crystals is crucial for the successful introduction of novel materials as intracavity components in Raman lasers, as recent work with diamond shows [36, 55]. An investigation into losses in synthetic diamond will be presented in Chapter 2 of this thesis.

### 1.4.2 Thermal effects

Thermal problems [67] are often the limiting factor in solid-state lasers. Some energy is inevitably converted to heat in the laser amplification process, and the poor thermal behaviour of crystals, especially in rod geometries, gives rise to various detrimental effects ranging from crystal fracture to thermal lensing, which can affect the stability of the cavity, the efficiency and the output beam quality [68]. Thermal problems can be particularly acute in intracavity Raman lasers because two thermal lenses develop in the cavity: one in the conventional laser gain crystal and a second one in the Raman crystal due to the inelastic nature of SRS. These lenses behave differently – the former scales with pump power [67] but the latter scales with the Stokes power [8]. Since the Stokes power can itself be affected by the strength of the thermal lenses, the thermal behaviour of these systems is complex. Thermal problems can be more severe in self-Raman lasers, since the entire heat load from both the laser gain and SRS processes is deposited in a single crystal [41].

A detailed discussion of the origin and effects of thermal lenses in laser and Raman crystals will be presented in Chapters 3 and 4. For now, a brief review of CW intracavity Raman lasers that displayed thermal problems will be given. The Nd:GdVO$_4$ frequency-doubled self-Raman laser reported by Dekker *et al* in [41] was limited by thermal problems. The output power at 586 nm was 678 mW in the CW regime, but when the pump beam was chopped at a 50 % duty-cycle, the instantaneous output power rose to 1.88 W. The authors estimated that the thermal lens had a focal length of approximately 20 mm, and noted that the known heat loads could not fully account for such a strong thermal lens [41]. They postulated that there was some unknown additional heat load, possibly associated with the blue fluorescence observed in many

Raman lasers when SRS is occurring [28, 41, 43]. A Nd:$GdVO_4$/$KGd(WO_4)_2$ Raman laser reported by the same authors also showed improved performance when operating in the quasi-continuous wave (QCW) regime [42].

Lee *et al* also estimated a thermal lens focal length of 20 mm from observations of the onset of cavity instability in a frequency-doubled Nd:$YVO_4$ self-Raman laser [31]. A number of Raman lasers have been constructed using diode pump lasers at 880 nm rather than 808 nm in order to reduce the heat load in the Nd-doped laser gain crystals (for example [32, 57]) and direct measurements of the thermal lens in a Nd:$GdVO_4$ self-Raman laser under 808 nm and 880 nm pumping have shown that this leads to a significant reduction in the thermal lens strength [69]. Other means to reduce the strength of the thermal lens in the laser gain crystal have included the use of Nd:YLF [46], the material properties of which lead to partial cancellation between positive and negative contributions to the thermal lens and hence a relatively weak lens overall, and the use of a disk geometry [36].

In this thesis, experimental and numerical approaches to determining the strength of the thermal lenses in intracavity Raman lasers and to improving cavity design to cope with these lenses will be presented.

### 1.4.3 Spectral effects

Spectral problems are also sometimes encountered in Raman lasers. These can take at least three forms. Firstly, as discussed above, SRS is a cascading process and if the 1st Stokes field becomes intense enough it can drive the generation of the 2nd Stokes wavelength and so on. If a single Stokes order is desired for the output of the laser, then a sufficiently high output coupling for the desired wavelength combined with low mirror reflectivities for longer wavelengths will suppress the generation of higher order Stokes fields. However, if the goal is to build a multi-wavelength laser, which can be switched between Stokes orders (and the second harmonics or sum frequencies thereof) then it is necessary to resonate all desired Stokes fields in the cavity and competition with higher Stokes orders can become problematic. For example, in [47], intracavity SHG/SFG in a Nd:$GdVO_4$ self-Raman laser was used to selectively generate 532 nm (the second harmonic of the fundamental field), 559 nm (the sum frequency of the fundamental and 1st Stokes fields) and 586 nm (the second harmonic of the 1st Stokes field). In this case the generating of 532 nm was impeded by unwanted conversion of the fundamental field to the 1st Stokes wavelength. Similar problems would arise if one wanted to generate the second harmonic of the 1st Stokes field in a laser cavity that was also resonant for the 2nd Stokes wavelength. Recently, Lee *et al* proposed using a second SFG crystal to suppress unwanted Stokes modes in these multi-wavelength devices [64].

In many ways it is unsurprising that spectral problems arise in these multi-wavelength Raman lasers, since in such systems the cavity must be resonant for many wavelengths. However, spectral problems can also arise in simpler devices. Secondary, weaker, Raman transitions in the Raman crystal can lead to the generation of unwanted wavelengths, limiting the efficiency of conversion to the desired wavelength. In theory the first Raman line to reach threshold will clamp the intracavity intensity of the fundamental field at its [Raman] threshold value, and thereby prevent any weaker Raman lines from ever reaching threshold, but in practice this does not always occur [54]. For example, Lee *et al* observed competition between the main $925\,\mathrm{cm}^{-1}$ Raman shift and a weaker shift at $332\,\mathrm{cm}^{-1}$ when operating the laser polarised parallel to the c-axis of the $BaWO_4$ crystal [49]. Rotating the crystal by 90° eliminated this problem because the $332\,\mathrm{cm}^{-1}$ shift is significantly weaker when the fundamental field is polarised parallel to the a-axis. In Raman lasers using separate laser and Raman gain crystals, the laser gain crystal may still be Raman-active (eg $Nd{:}YVO_4$ or $Nd{:}GdVO_4$), and in such cases competition can occur between SRS in the Raman crystal and undesired SRS in the laser gain crystal [54]. In such cases it is necessary to ensure that the crystal lengths and mode areas in each crystal are such that the desired SRS process is considerably stronger than the undesired shift, taking account of the different Raman gain coefficients for the two crystals [53].

The generation of undesired Stokes wavelengths is not the only spectral problem that can arise in intracavity Raman lasers – the behaviour of the fundamental field can also be problematic. Since the Raman crystal is placed in the same cavity as the fundamental laser gain crystal, the SRS process acts as a nonlinear output coupling for the fundamental field, which then tries to "avoid" the frequency-dependent loss presented to it by the SRS process, leading to spectral broadening of the fundamental field. This has been observed in a variety of intracavity Raman lasers [35, 41, 42, 44, 45, 52], and can be a significant effect. For example, Fan *et al* [35] observed spectral broadening in a $Nd{:}YVO_4/BaWO_4$ laser, in which the fundamental peak broadened from 0.2 nm wide at the Raman threshold to 1.05 nm wide at maximum pump power, whilst the Stokes peak broadened from 0.15 nm to 0.5 nm. In another case, Lisinetskii *et al* [52] observed that the fundamental field in their $Nd{:}KGd(WO_4)_2/KGd(WO_4)_2$ laser broadening from $5\,\mathrm{cm}^{-1}$ to $24\,\mathrm{cm}^{-1}$ (0.6 nm to 2.7 nm). Sometimes a separate transition in the fundamental gain medium can also reach threshold due to the loss presented to the main transition by the SRS process. For example, Dekker *et al* observed oscillation of the orthogonally polarised 1066 nm line in their frequency-doubled $Nd{:}GdVO_4$ self-Raman laser in addition to the main line at 1063 nm [41].

This broadening of the fundamental spectrum is problematic, firstly if a narrowband Stokes output is desired but even more generally because a broad fundamental spectrum leads to a reduction in the effective Raman gain [70]. A detailed investigation into the mechanism and effects of spectral broadening and into methods of spectral control in intracavity Raman lasers will be presented in Chapter 5 of this thesis.

## 1.5 Use of a disk geometry for the laser gain crystal

As discussed in Section 1.4, thermal lenses arise in both crystals in an intracavity Raman laser and often limit the performance of the laser and constrain the design of the cavity. In this work, a disk geometry was used to reduce the strength of the thermal lens in the laser gain crystal, which made it possible to build longer, more complex cavities and permitted much more flexibility in cavity design. This facilitated direct measurements of the strength of the thermal lens in the Raman crystal by making it easier to access the Raman crystal with a probe beam, independently of the laser gain crystal. Furthermore, by using a coupled cavity configuration it was possible to partially separate the fundamental and Stokes cavities and thereby carry out experiments to partially disentangle the effects of the two thermal lenses. When investigating spectral effects, the coupled cavity configuration was also useful since it made it possible to put etalons in the fundamental cavity only, without directly affecting the Stokes field. It can be seen therefore that using a disk geometry for the laser gain crystal has enabled much of the work presented in this thesis on more specific aspects of intracavity Raman laser behaviour, and therefore a brief overview of disk lasers will now be given.

### 1.5.1 Thin disk lasers

A more detailed discussion of thermal effects in solid state lasers will be given in Chapter 3, but one key point is that transverse temperature gradients (that is, transverse to the direction of propagation of the cavity field) make a significant contribution to the strength of the thermal lens in the crystal. Axial temperature gradients are less problematic. Thin disk lasers [71] are designed to have primarily axial heat flow and consist of a thin slice of gain crystal, with a mirror coated directly onto the rear surface of the crystal. The disk is mounted on a heat sink, as shown in Figure 1.4 and the pump laser is focussed to a spot radius that is larger than the disk is thick (a typical thin disk laser might use a laser gain disk 100 µm to 200 µm thick and a pump spot radius of 1 mm to 2 mm [72]). This leads to predominately axial heat flow in the disk and a minimal transverse temperature gradient, minimising the thermal lens. Thin disk lasers are scalable – if the pump spot radius and pump power are simultaneously increased such that the pump power density remains constant, then a thin disk laser can be scaled to higher powers without an increase in the strength of the thermal lens [71], to first order at least. CW output powers of up to 5.3 kW from a single disk have been demonstrated [72].

One disadvantage of thin disk lasers is that they require complex pump optics. Only a small fraction of the pump light is absorbed on one pass[1] through a disk 100 µm to 200 µm thick and therefore the unabsorbed pump radiation must be collected and redirected back through the disk, often multiple times - up to 16 passes have been

---

[1] A pass is defined here as the trip through the disk and back out the front after reflection off the rear surface.

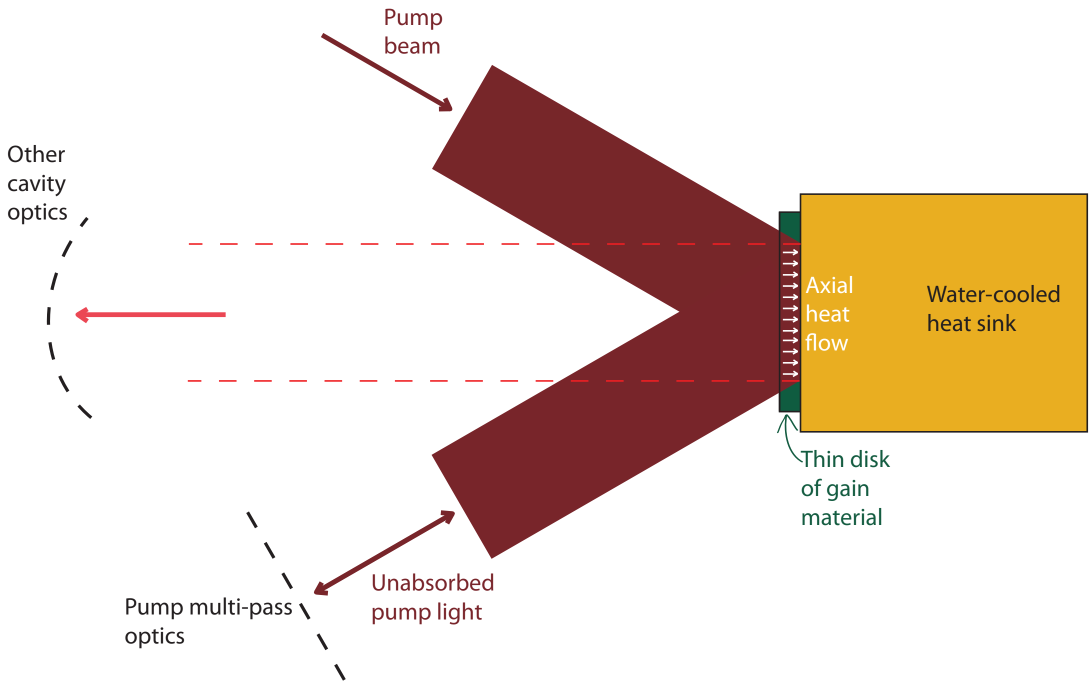

**Figure 1.4:** Schematic of thin disk laser concept.

used [72]. This generally involves a large parabolic mirror and carefully aligned folding mirrors, increasing the complexity and reducing the robustness of the laser.

### 1.5.2 Use of thick disks with diamond heatspreaders

A second approach is to use a slightly thicker disk (typically 250 µm to 500 µm) bonded to a diamond heatspreader [73]. The diamond heatspreader facilitates heat extraction through the front face of the disk as well as the rear, effectively doubling the cooling area and halving the distance the heat must flow to reach the sink. This reduces both the temperature rises and the stresses in the disk [74]. While such systems have not to date been true thin disks from a thermal management perspective (since the pump spot radius is similar to or slightly smaller than the disk thickness), the diamond heatspreader promotes disk-like behaviour.

These disk lasers represent a compromise between favourable thermal behaviour and the simplicity of the pump optics and geometry. The stronger the pump absorption, the less of a compromise has to be made, and therefore materials with strong absorption peaks such as Nd:$YVO_4$ and Nd:$GdVO_4$ have been investigated for use in such lasers [75, 76], despite their lower thermal conductivity compared to a material like Nd:YAG [67, 77, 78]. A disk laser of this type, based on Nd:$YVO_4$, has been demonstrated giving 25.7 W output at 1064 nm, with $\sim 55\,\%$ slope efficiency with respect to absorbed pump power, $\sim 35\,\%$ with respect to incident pump power for one pass of the disk [76].

Disk lasers of similar design, using Nd:$YVO_4$ disks and diamond heatspreaders, are used extensively in the work presented in this thesis.

## 1.6 Thesis outline

In Chapter 2, measurements of the optical losses in synthetic diamond will be presented. These experiments were carried out at the beginning of the PhD project with a view to using diamond as a Raman crystal in order to take advantage of its remarkable thermal properties; however, while the potential of diamond in this regard was demonstrated, access to suitably high quality diamond is still unreliable and the author did not have access to sufficiently low loss diamond to build viable diamond Raman lasers. Therefore, in the subsequent chapters the work presented was carried out using more conventional Raman crystals.

In Chapter 3, a disk geometry is introduced in order to reduce the strength of the thermal lens in the laser gain crystal. This made it possible to build a longer, more complex cavity that facilitated measurements of the thermal lens in the Raman crystal, $BaWO_4$, via lateral shearing interferometry. The longer cavity made it easier to access the Raman crystal independently of the laser gain crystal and these measurements are, to the best of the author's knowledge, the first direct, *in situ*, measurements of the thermal lens in a CW intracavity Raman laser built around separate laser and Raman crystals. These measurements will be presented along with numerical modelling of the thermal lens in the laser gain disk. In Chapter 4, this information is used to refine the cavity design and experiments to power scale the laser will be described. The use of a coupled cavity configuration enabled experiments to further probe the thermal behaviour of these systems and partially disentangle the effects of the two thermal lenses and these will also be presented in Chapter 4.

In Chapter 5, an investigation into the spectral broadening often observed in intracavity Raman lasers will be presented. The extent of the broadening with and without SRS is measured and the dependence of the effect on the linewidth of the Raman transition is investigated. The potential impact of the broadening effect on the performance of the Raman laser is discussed and the possibility of using etalons to control the fundamental spectrum is investigated, again taking advantage of the coupled cavity configuration. All the work in the thesis will be summarised and conclusions and future prospects presented in Chapter 6.

# Bibliography

[1] T. H. Maiman, “Stimulated Optical Radiation in Ruby,” *Nature*, vol. 187, no. 4736, pp. 493–494, 1960.

[2] C. Raman, “A new radiation,” *Indian Journal of physics*, vol. 2, pp. 387–398, 1928.

[3] R. W. Boyd, *Nonlinear Optics.* Academic Press, 3rd ed., 2008.

[4] E. J. Woodbury and W. K. Ng, “Ruby laser operation in the near IR,” *Proceedings of the IRE*, vol. 50, no. 11, p. 2367, 1962.

[5] G. Eckhardt, R. W. Hellwarth, F. J. McClung, S. E. Schwarz, D. Weiner, and E. J. Woodbury, “Stimulated Raman Scattering From Organic Liquids,” *Physical Review Letters*, vol. 9, pp. 455–457, Dec 1962.

[6] G. Eckhardt, D. P. Bortfeld, and M. Geller, “Stimulated Emission of Stokes and Anti-Stokes Raman Lines from Diamond, Calcite, and $\alpha$-Sulfur Single Crystals,” *Applied Physics Letters*, vol. 3, no. 8, pp. 137–138, 1963.

[7] R. W. Minck, R. W. Terhune, and W. G. Rado, “Laser-Stimulated Raman Effect and Resonant Four-Photon Interactions in Gases $H_2$ $D_2$, and $CH_4$,” *Applied Physics Letters*, vol. 3, no. 10, pp. 181–184, 1963.

[8] H. M. Pask, “The design and operation of solid-state Raman lasers,” *Progress in Quantum Electronics*, vol. 27, no. 1, pp. 3–56, 2003.

[9] J. A. Piper and H. M. Pask, “Crystalline Raman Lasers,” *IEEE Journal of Selected Topics in Quantum Electronics*, vol. 13, no. 3, pp. 692–704, 2007.

[10] A. Penzkofer, A. Laubereau, and W. Kaiser, “High Intensity Raman Interactions,” *Progress in Quantum Electronics*, vol. 6, no. 2, pp. 56–140, 1979.

[11] S. M. Hooker and C. E. Webb, *Laser Physics.* Oxford University Press, 2010.

[12] J. T. Murray, W. L. Austin, and R. C. Powell, “Intracavity Raman conversion and Raman beam cleanup,” *Optical Materials*, vol. 11, no. 4, pp. 353 – 371, 1999.

[13] J. Lin, H. M. Pask, A. J. Lee, and D. J. Spence, “Study of relaxation oscillations in continuous-wave intracavity Raman lasers,” *Optics Express*, vol. 18, no. 11, pp. 11530–11536, 2010.

[14] Y. Feng, L. R. Taylor, and D. B. Calia, “150 W highly-efficient Raman fiber laser,” *Optics Express*, vol. 17, pp. 23678–23683, Dec 2009.

[15] J. K. Brasseur, K. S. Repasky, and J. L. Carlsten, “Continuous-wave Raman laser in $H_2$,” *Optics Letters*, vol. 23, no. 5, pp. 367–369, 1998.

[16] P. Černy, H. Jelínková, P. G. Zverev, and T. T. Basiev, “Solid state lasers with Raman frequency conversion,” *Progress in Quantum Electronics*, vol. 28, no. 2, pp. 113–143, 2004.

[17] J. M. Feve, K. E. Shortoff, M. J. Bohn, and J. K. Brasseur, “High average power diamond Raman laser,” *Optics Express*, vol. 19, no. 2, pp. 913–922, 2011.

[18] X. Chen, X. Zhang, Q. Wang, P. Li, S. Li, Z. Cong, Z. Liu, S. Fan, and H. Zhang, “Diode side-pumped actively Q-switched Nd:YAG/$SrWO_4$ Raman laser with high average output power of over 10 W at 1180 nm,” *Laser Physics Letters*, vol. 6, no. 5, pp. 363–366, 2009.

[19] D. J. Spence, E. Granados, and R. P. Mildren, “Mode-locked picosecond diamond Raman laser,” *Optics Letters*, vol. 35, no. 4, pp. 556–558, 2010.

[20] E. Granados, D. J. Spence, and R. P. Mildren, “Deep ultraviolet diamond Raman laser,” *Optics Express*, vol. 19, no. 11, pp. 10857–10863, 2011.

[21] E. Granados, H. M. Pask, E. Esposito, G. McConnell, and D. J. Spence, “Multi-wavelength, all-solid-state, continuous wave mode locked picosecond Raman laser,” *Optics Express*, vol. 18, pp. 5289–5294, Mar 2010.

[22] A. S. Grabtchikov, V. A. Lisinetskii, V. A. Orlovich, M. Schmitt, R. Maksimenka, and W. Kiefer, “Multimode pumped continuous-wave solid-state Raman laser,” *Optics Letters*, vol. 29, no. 21, pp. 2524–2526, 2004.

[23] A. S. Grabtchikov, V. A. Lisinetskii, V. A. Orlovich, M. Schmitt, S. Schluecker, B. Kuestner, and W. Kiefer, “Continuous-wave solid-state two-Stokes Raman laser,” *Quantum Electronics*, vol. 39, no. 7, pp. 624–626, 2009.

[24] O. Kitzler, A. McKay, and R. P. Mildren, “Continuous-wave wavelength conversion for high-power applications using an external cavity diamond Raman laser,” *Optics Letters*, vol. 37, pp. 2790–2792, Jul 2012.

[25] O. Kitzler, A. McKay, and R. P. Mildren, “Characterization of a Single-frequency-pumped Continuous-wave Extracavity Diamond Raman Laser,” in *Conference on Lasers and Electro-Optics Europe*, 2013.

[26] D. J. Spence, P. Dekker, and H. M. Pask, "Modeling of continuous wave intracavity Raman lasers," *IEEE Journal of Selected Topics in Quantum Electronics*, vol. 13, no. 3, pp. 756–763, 2007.

[27] A. A. Demidovich, A. S. Grabtchikov, V. A. Lisinetskii, V. N. Burakevich, V. A. Orlovich, and W. Kiefer, "Continuous-wave Raman generation in a diode-pumped $Nd^{3+}$:$KGd(WO_4)_2$ laser," *Optics Letters*, vol. 30, no. 13, pp. 1701–1703, 2005.

[28] H. M. Pask, "Continuous-wave, all solid-state Raman laser," *Optics Letters*, vol. 30, no. 18, pp. 2454–2456, 2005.

[29] T. T. Basiev, A. A. Sobol, P. G. Zverev, L. I. Ivleva, V. V. Osiko, and R. C. Powell, "Raman spectroscopy of crystals for stimulated Raman scattering," *Optical Materials*, vol. 11, no. 4, pp. 307–314, 1999.

[30] A. J. Lee, J. Lin, and H. M. Pask, "Near-infrared and orange-red emission from a continuous-wave, second-Stokes self-Raman Nd:$GdVO_4$ laser," *Optics Letters*, vol. 35, no. 18, pp. 3000–3002, 2010.

[31] A. J. Lee, H. M. Pask, T. Omatsu, P. Dekker, and J. A. Piper, "All-solid-state continuous-wave yellow laser based on intracavity frequency-doubled self-Raman laser action," *Applied Physics B*, vol. 88, no. 4, pp. 539–544, 2007.

[32] A. J. Lee, H. M. Pask, D. J. Spence, and J. A. Piper, "Efficient 5.3 W cw laser at 559 nm by intracavity frequency summation of fundamental and first-Stokes wavelengths in a self-Raman Nd:$GdVO_4$ laser," *Optics Letters*, vol. 35, no. 5, pp. 682–684, 2010.

[33] V. G. Savitski, I. Friel, J. E. Hastie, M. D. Dawson, D. Burns, and A. J. Kemp, "Characterization of Single-Crystal Synthetic Diamond for Multi-Watt Continuous-Wave Raman Lasers," *IEEE Journal of Quantum Electronics*, vol. 48, no. 3, pp. 328 –337, 2012.

[34] J. Lin and H. Pask, "Nd:$GdVO_4$ self-Raman laser using double-end polarised pumping at 880 nm for high power infrared and visible output," *Applied Physics B: Lasers and Optics*, vol. 108, no. 1, pp. 17–24, 2012.

[35] L. Fan, Y.-X. Fan, Y.-Q. Li, H. Zhang, Q. Wang, J. Wang, and H.-T. Wang, "High-efficiency continuous-wave Raman conversion with a $BaWO_4$ Raman crystal," *Optics Letters*, vol. 34, no. 11, pp. 1687–1689, 2009.

[36] W. Lubeigt, V. G. Savitski, G. M. Bonner, S. L. Geoghegan, I. Friel, J. E. Hastie, M. D. Dawson, D. Burns, and A. J. Kemp, "1.6 W continuous-wave Raman laser using low-loss synthetic diamond," *Optics Express*, vol. 19, no. 7, pp. 6938–6944, 2011.

[37] D. C. Parrotta, A. J. Kemp, M. D. Dawson, and J. E. Hastie, “Tunable continuous-wave diamond Raman laser,” *Optics Express*, vol. 19, no. 24, pp. 24165–24170, 2011.

[38] P. A. Apanasevich, A. A. Kananovich, A. A. Demidovich, M. B. Danailov, and V. A. Orlovich, “Stationary generation of diode-pumped self-Raman Nd:$YVO_4$/$YVO_4$ composite crystal laser,” *Journal of Applied Spectroscopy*, vol. 78, no. 1, pp. 43–49, 2011.

[39] Y. K. Bu, C. Q. Tan, and N. Chen, “Continuous-wave yellow light source at 579 nm based on intracavity frequency-doubled Nd:YLF/$SrWO_4$/LBO Raman laser,” *Laser Physics Letters*, vol. 8, no. 6, pp. 439–442, 2011.

[40] V. N. Burakevich, V. A. Lisinetskii, A. S. Grabtchikov, A. A. Demidovich, V. A. Orlovich, and V. N. Matrosov, “Diode-pumped continuous-wave Nd:$YVO_4$ laser with self-frequency Raman conversion,” *Applied Physics B*, vol. 86, no. 3, pp. 511–514, 2007.

[41] P. Dekker, H. M. Pask, D. J. Spence, and J. A. Piper, “Continuous-wave, intracavity doubled, self-Raman laser operation in Nd:$GdVO_4$ at 586.5 nm,” *Optics Express*, vol. 15, no. 11, pp. 7038–7046, 2007.

[42] P. Dekker, H. M. Pask, and J. A. Piper, “All-solid state 704 mW continuous-wave yellow source based on an intracavity frequency-doubled crystalline Raman laser,” *Optics Letters*, vol. 32, no. 9, pp. 1114–1116, 2007.

[43] Y. Duan, F. Yang, H. Zhu, Z. Zhu, Z. Huang, Chenghui amd You, Y. Wei, G. Zhang, and C. Tu, “Continuous-wave 560 nm light generated by intracavity $SrWO_4$ Raman and KTP sum-frequency mixing,” *Optics Communications*, vol. 283, no. 24, pp. 5135–5138, 2010.

[44] L. Fan, Y. X. Fan, Y. H. Duan, Q. Wang, H. T. Wang, G. H. Jia, and C. Y. Tu, “Continuous-wave intracavity Raman laser at 1179.5 nm with $SrWO_4$ Raman crystal in diode-end-pumped Nd:$YVO_4$ laser,” *Applied Physics B*, vol. 94, no. 4, pp. 553–557, 2009.

[45] L. Fan, Y. X. Fan, and H. T. Wang, “A compact efficient continuous-wave self-frequency Raman laser with a composite $YVO_4$/Nd:$YVO_4$/$YVO_4$ crystal,” *Applied Physics B*, vol. 101, no. 3, pp. 493–496, 2010.

[46] J. Jakutis-Neto, J. Lin, N. U. Wetter, and H. Pask, “Continuous-wave Watt-level Nd:YLF/KGW Raman laser operating at near-IR, yellow and lime-green wavelengths,” *Optics Express*, vol. 20, pp. 9841–9850, Apr 2012.

[47] A. J. Lee, D. J. Spence, J. A. Piper, and H. M. Pask, “A wavelength-versatile, continuous-wave, self-Raman solid-state laser operating in the visible,” *Optics Express*, vol. 18, no. 19, pp. 20013–20018, 2010.

[48] A. J. Lee, H. M. Pask, P. Dekker, and J. A. Piper, “High efficiency, multi-Watt CW yellow emission from an intracavity-doubled self-Raman laser using Nd:GdVO$_4$,” *Optics Express*, vol. 16, no. 26, pp. 21958–21963, 2008.

[49] A. J. Lee, H. M. Pask, J. A. Piper, H. Zhang, and J. Wang, “An intracavity, frequency-doubled BaWO$_4$ Raman laser generating multi-watt continuous-wave, yellow emission,” *Optics Express*, vol. 18, no. 6, pp. 5984–5992, 2010.

[50] X. Li, A. J. Lee, H. M. Pask, J. A. Piper, and Y. Huo, “Efficient, miniature cw yellow source based on an intracavity frequency-doubled Nd:YVO$_4$ self-Raman laser,” *Optics Letters*, vol. 36, no. 8, pp. 1428–1430, 2011.

[51] J. Lin, H. M. Pask, D. J. Spence, C. J. Hamilton, and G. P. A. Malcolm, “Continuous-wave VECSEL Raman laser with tunable lime-yellow-orange output,” *Optics Express*, vol. 20, pp. 5219–5224, Feb 2012.

[52] V. A. Lisinetskii, A. S. Grabtchikov, A. A. Demidovich, V. N. Burakevich, V. A. Orlovich, and A. N. Titov, “Nd:KGW/KGW crystal: efficient medium for continuous-wave intracavity Raman generation,” *Applied Physics B*, vol. 88, no. 4, pp. 499–501, 2007.

[53] X. Li, H. M. Pask, A. J. Lee, Y. Huo, J. A. Piper, and D. J. Spence, “Miniature wavelength-selectable Raman laser: new insights for optimizing performance,” *Optics Express*, vol. 19, no. 25, pp. 25623–25631, 2011.

[54] X. Li, A. J. Lee, Y. Huo, H. Zhang, J. Wang, J. A. Piper, H. M. Pask, and D. J. Spence, “Managing SRS competition in a miniature visible Nd:YVO$_4$/BaWO$_4$ Raman laser,” *Optics Express*, vol. 20, pp. 19305–19312, Aug 2012.

[55] W. Lubeigt, G. M. Bonner, J. E. Hastie, M. D. Dawson, D. Burns, and A. J. Kemp, “Continuous-wave diamond Raman laser,” *Optics Letters*, vol. 35, no. 17, pp. 2994–2996, 2010.

[56] Y. Lü, X. Zhang, S. Li, J. Xia, W. Cheng, and Z. Xiong, “All-solid-state cw sodium $D_2$ resonance radiation based on intracavity frequency-doubled self-Raman laser operation in double-end diffusion-bonded Nd$^{3+}$:LuVO$_4$ crystal,” *Optics Letters*, vol. 35, no. 17, pp. 2964–2966, 2010.

[57] Y. Lü, W. Cheng, Z. Xiong, J. Lu, L. Xu, G. Sun, and Z. Zhao, “Efficient CW laser at 559 nm by intracavity sum-frequency mixing in a self-Raman Nd:YVO$_4$ laser under direct 880 nm diode laser pumping,” *Laser Physics Letters*, vol. 7, no. 11, pp. 787–789, 2010.

[58] V. A. Orlovich, V. N. Burakevich, A. S. Grabtchikov, V. A. Lisinetskii, A. A. Demidovich, H. J. Eichler, and P. Turpin, "Continuous-wave intracavity Raman generation in $PbWO_4$ crystal in the Nd:$YVO_4$ laser," *Laser Physics Letters*, vol. 3, no. 2, pp. 71–74, 2006.

[59] D. C. Parrotta, W. Lubeigt, A. J. Kemp, D. Burns, M. D. Dawson, and J. E. Hastie, "Continuous-wave Raman laser pumped within a semiconductor disk laser cavity," *Optics Letters*, vol. 36, no. 7, pp. 1083–1085, 2011.

[60] J. Xia, Y. F. Lü, X. H. Zhang, W. B. Cheng, Z. Xiong, J. Lu, L. J. Xu, G. C. Sun, Z. M. Zhao, and Y. Tan, "All-solid-state CW Nd:$KGd(WO_4)_2$ self-Raman laser at 561 nm by intracavity sum-frequency mixing of fundamental and first-Stokes wavelengths," *Laser Physics Letters*, vol. 8, no. 1, pp. 21–23, 2011.

[61] F. G. Yang, Z. Y. You, Z. J. Zhu, Y. Wang, J. F. Li, and C. Y. Tu, "End-pumped continuous-wave intracavity yellow Raman laser at 590 nm with $SrWO_4$ Raman crystal," *Laser Physics Letters*, vol. 7, no. 1, pp. 14–16, 2010.

[62] H. Yu, Z. Li, A. J. Lee, J. Li, H. Zhang, J. Wang, H. M. Pask, J. A. Piper, and M. Jiang, "A continuous wave $SrMoO_4$ Raman laser," *Optics Letters*, vol. 36, no. 4, pp. 579–581, 2011.

[63] H. Y. Zhu, Y. M. Duan, G. Zhang, C. H. Huang, Y. Wei, W. D. Chen, L. X. Huang, and Y. D. Huang, "Efficient continuous-wave $YVO_4$/Nd:$YVO_4$ Raman laser at 1176 nm," *Applied Physics B*, vol. 103, no. 3, pp. 559–562, 2011.

[64] A. Lee, H. M. Pask, and D. J. Spence, "Control of cascading in multiple-order Raman lasers," *Optics Letters*, vol. 37, pp. 3840–3842, Sep 2012.

[65] D. J. Spence, X. Li, A. J. Lee, and H. M. Pask, "Modeling of wavelength-selectable visible Raman lasers," *Optics Communications*, vol. 285, no. 18, pp. 3849 – 3854, 2012.

[66] M. E. Innocenzi, H. T. Yura, C. L. Fincher, and R. A. Fields, "Thermal modelling of continuous-wave end-pumped solid-state lasers," *Applied Physics Letters*, vol. 56, no. 19, pp. 1831–1833, 1990.

[67] W. Koechner, *Solid-State Laser Engineering.* Springer, 6th ed., 2006.

[68] S. Chénais, F. Druron, S. Forget, F. Balembois, and P. Georges, "On thermal effects in solid-state lasers: The case of ytterbium-doped materials," *Progress in Quantum Electronics*, vol. 30, no. 4, pp. 89–153, 2006.

[69] T. Omatsu, M. Okida, A. Lee, and H. Pask, "Thermal lensing in a diode-end-pumped continuous-wave self-Raman Nd-doped $GdVO_4$ laser," *Applied Physics B: Lasers and Optics*, vol. 108, no. 1, pp. 73–79, 2012. 10.1007/s00340-012-4919-7.

[70] A. T. Georges, “Statistical theory of Raman amplification and spontaneous generation in dispersive media pumped with a broadband laser,” *Physical Review A*, vol. 39, pp. 1876–1886, Feb 1989.

[71] A. Giesen, H. Hugel, A. Voss, K. Wittig, U. Brauch, and H. Opower, “Scalable concept for diode-pumped high-power solid-state lasers,” *Applied Physics B*, vol. 58, no. 5, pp. 365–372, 1994.

[72] A. Giesen and J. Speiser, “Fifteen years of work on thin-disk lasers: results and scaling laws,” *IEEE Journal of Selected Topics in Quantum Electronics*, vol. 13, no. 3, pp. 598–609, 2007.

[73] P. Millar, R. B. Birch, A. J. Kemp, and D. Burns, “Synthetic diamond for intracavity thermal management in compact solid-state lasers,” *IEEE Journal of Quantum Electronics*, vol. 44, no. 8, pp. 709–717, 2008.

[74] A. J. Kemp, A. J. Maclean, J.-M. Hopkins, J. E. Hastie, S. Calvez, M. D. Dawson, and D. Burns, “Thermal management in disc lasers: doped-dielectric and semiconductor laser gain media in thin-disc and microchip format,” *Journal of Modern Optics*, vol. 54, no. 12, pp. 1669–1676, 2007.

[75] A. J. Kemp, G. J. Valentine, and D. Burns, “Progress towards high-power, high-brightness neodymium-based thin-disk lasers,” *Progress in Quantum Electronics*, vol. 28, no. 6, pp. 305–344, 2004.

[76] P. Millar, A. J. Kemp, and D. Burns, “Power scaling of Nd:$YVO_4$ and Nd:$GdVO_4$ disk lasers using synthetic diamond as a heat spreader,” *Optics Letters*, vol. 34, no. 6, pp. 782–784, 2009.

[77] Y. Sato and T. Taira, “The studies of thermal conductivity in $GdVO_4$, $YVO_4$ and $Y_3Al_5O_{12}$ measured by quasi-one-dimensional flash method,” *Optics Express*, vol. 14, no. 22, pp. 10528–10536, 2006.

[78] J. Didierjean, E. Herault, F. Balembois, and P. Georges, “Thermal conductivity measurements of laser crystals by infrared thermography. Application to Nd:doped crystals,” *Optics Express*, vol. 16, no. 12, pp. 8995–9010, 2008.

# Chapter 2

# Measurements of optical losses in synthetic diamond

In this chapter, experiments to measure the optical losses in synthetic diamond samples will be described. The goal of this work was to identify suitable diamond crystals for use as Raman gain media in CW intracavity Raman lasers. The experiments showed that some synthetic diamond crystals do have sufficiently low losses for such use; however, the supply of such material is not yet reliable and the diamonds that the author had access to for later laser work had much higher losses. Therefore, in the later chapters of this thesis attention is turned to Raman materials other than diamond.

In this chapter the remarkable properties of diamond, which make it an attractive material for laser engineering, will be discussed. Recent improvements in synthetic diamond growth techniques, which have made diamond a viable material for intracavity use, will then be briefly described, and demonstrations of diamond Raman lasers in both external cavity and intracavity configurations will be reviewed. The intracavity loss measurement techniques used in this work will then be described and the results for three diamond samples will be presented. These will be compared to calorimetric measurements of the losses made by colleagues of the author.

The work presented in this chapter aided in the characterisation of diamond samples which colleagues of the author were able to use to demonstrate several Raman laser systems [1–3].

## 2.1 Diamond as a Raman crystal

### 2.1.1 Properties of diamond

Diamond is a remarkable crystal, many of the properties of which lie at the extremes of the ranges for known materials [4]. Such properties make diamond an attractive material for use in lasers. Heat generation in solid state lasers is often the major barrier to improving the performance of such devices because it leads to changes in

**Table 2.1:** Thermal and mechanical properties of diamond compared to those of common laser hosts and Raman crystals [4–9].

| Material | Thermal conductivity /W m$^{-1}$ K$^{-1}$ | Young's modulus /GPa | Thermal expansion coefficient /10$^{-6}$ K$^{-1}$ | Tensile strength /MPa |
|---|---|---|---|---|
| Diamond | 2000 | 1100 | 1.0 | 2860 |
| YAG | 10.5 | 282 | 8 | 280 |
| $YVO_4$ | 6.5/5.5 (c/a) | 133 | 11.4/4.4 | 53 |
| $BaWO_4$ | 2.73/2.59 (c/a) | – | 35.1/11.0 | – |
| $KGd(WO_4)_2$ | 3.5/3.0/2.5 (g/m/p) | – | 17/11/2.4 | – |

the optical properties of the laser crystal and also to mechanical deformations and ultimately fracture of the crystal. These thermal problems, which will be discussed in more detail in Chapters 3 and 4, are influenced by various thermal and mechanical properties of the material, some of which are shown in Table 2.1 for diamond and several common laser hosts and Raman crystals.

Many of the properties of diamond are better than those of conventional laser materials, in some cases by orders of magnitude. In particular, its exceptionally high thermal conductivity greatly facilitates heat extraction. Furthermore, diamond has a very broad transparency window, from the ultraviolet (226 nm) to the terahertz region, interrupted only by a multiphonon absorption band at 2.5 to 6.5 μm [4]. Therefore, diamond is extremely attractive as a laser engineering material. Unfortunately, diamond does not have intrinsic laser gain. Furthermore, doping common active laser ions, such as rare earths, into the diamond lattice is difficult because such ions are large compared to the carbon-carbon spacing. Diamond has been exploited by bonding diamond heatspreaders to other materials which do have laser gain [10, 11], and there has been one demonstration of a diamond colour centre laser [12]. Another approach is to use diamond as a Raman material to convert the wavelength of other laser sources. There has been significant interest in diamond Raman lasers in the last five to ten years (see Section 2.2). Diamond has a very high Raman gain, in fact it was one of the first crystalline materials in which stimulated Raman scattering (SRS) was demonstrated [13]. However, it is only in the last five to ten years that improvements in diamond growth techniques (described in the next section) have led to significant interest in diamond as a practical Raman laser material.

Diamond has a strong Raman transition at 1332.5 cm$^{-1}$ [14], with gain of 17 cm GW$^{-1}$ at 1064 nm [15]. Comparison with commonly used Raman crystals such as $BaWO_4$ (8.5 cm GW$^{-1}$ at 925 cm$^{-1}$ [16]), $KGd(WO_4)_2$ (4.4 cm GW$^{-1}$ at 768 cm$^{-1}$ [17]) and $GdVO_4$ ($>$ 4.5 cm GW$^{-1}$ at 885 cm$^{-1}$ [17, 18]), shows that diamond has both a high gain, which facilitates the use of relatively short crystals, of order a few millimetres rather than tens of millimetres, and a large Raman shift, which means that diamond can be used to convert well-established 1 µm laser sources to different wavelengths than can be reached with vanadate and tungstate Raman lasers.

### 2.1.2 Improvements in diamond growth techniques

Natural diamonds are generally unsuitable for optical applications, especially intracavity laser applications, as defects and impurities, and the associated optical properties, vary widely from one crystal to another [11, 19, 20]. One way to grow diamonds synthetically is by chemical vapour deposition (CVD) [21]. Methane and hydrogen gas are passed over a diamond substrate under certain conditions of temperature and pressure. Methyl radicals add carbon to the substrate lattice, while the hydrogen suppresses the growth of graphitic ($sp^2$) carbon, resulting in the gradual deposition of more diamond layers on the substrate [21]. CVD growth of diamond is carried out at much lower pressures (less than 1 atm) than the widespread high pressure, high temperature (HPHT) method of diamond growth, and the ability to control the purity of the input gases makes it possible to improve the purity of the resulting diamonds. CVD diamond has found uses in many mechanical, thermal, and electronic applications [20]. While diamond has historically been viewed as too expensive, and difficult to synthesise with a high quality, for use in photonics applications, recent improvements in growth techniques have led to a substantial increase in the use of diamond for a wide variety of optical engineering applications, so much so that a book on “Optical Engineering of Diamond” has recently been published, containing reviews of many aspects of the growth, processing and use of diamond for optical applications [22].

For intracavity laser applications, the optical losses and birefringence of the diamond are crucial. Although a perfect diamond lattice is isotropic, natural and synthetic diamonds have dislocations which lead to strain in the lattice and non-uniform birefringence, (typically $\Delta n > 10^{-4}$) which cannot be easily compensated for [4, 23]. Control of such extended defects is particularly challenging for CVD growth of diamond. However, improvements in the technique have enabled the production of single crystal diamonds with low birefringence ($\Delta n < 10^{-5}$ or even $< 10^{-6}$) [24]. The key to this is to minimise the defect density and surface damage of the substrate on which the diamond is grown. This in turn leads to fewer dislocations propagating through the diamond as it grows on the substrate, resulting in diamonds with low birefringence [24]. Such low birefringence diamond has been shown to perform well as an intracavity heatspreader in disk lasers [11].

Low birefringence is important for many intracavity applications of diamond; however, for CW intracavity Raman lasers the optical loss must also be kept to a minimum since such systems operate with very low output coupling, as discussed in Chapter 1. Losses in CVD-grown diamond in the near IR region are thought to be primarily due to nitrogen impurities [4], and the measurement of loss in such diamonds is the subject of this chapter. Turri *et al* have previously studied CVD diamonds from Element Six

Ltd with losses as low as 0.003 cm$^{-1}$ [25], but these samples had relatively high birefringence. The diamonds studied in this thesis were either grown specifically for low birefringence, or selected because they happened to have low birefringence. Element Six Ltd are the dominant supplier of high quality CVD-grown diamond, and all the diamonds used in the work presented in this thesis were grown by Element Six Ltd. A review of diamond Raman laser systems demonstrated to date will now be given, before the loss measurement experiments are presented.

## 2.2 Review of diamond Raman laser systems

The first demonstration of a diamond Raman laser was reported at the 2005 Conference on Lasers and Electro-Optics Europe [26]. This was a picosecond pulsed system, but few other details are given in the proceedings. In 2008, Mildren *et al* [27] demonstrated an external cavity diamond Raman laser pumped with a frequency-doubled, Q-switched Nd:YAG laser at 532 nm. The uncoated diamond was inserted into the cavity at Brewster's angle but the performance was limited by losses at the surfaces of the diamond due to birefringence in the crystal - reflected beams from the crystal faces were significantly stronger than the beam transmitted through the output coupler. However, 0.05 mJ pulses at the 1st Stokes wavelength of 573 nm were detected in a single reflection from one facet of the diamond. This represents 2.1 % of the pulse energy at 1064 nm. The Mildren group later demonstrated a similar system [28] using a diamond with much lower birefringence ($\Delta n \sim 1.0 \times 10^{-7}$). This laser produced 1.2 W at the 1st Stokes wavelength of 573 nm with a slope efficiency of 75 %. The same authors have also demonstrated external cavity diamond Raman lasers pumped with Q-switched lasers at 1064 nm, producing output at the both the 1st Stokes wavelength (1240 nm) [29] and the 2nd Stokes wavelength (1485 nm) [30]. Jelíneck *et al* [31] also generated output in the eyesafe region, but via a single Stokes shift, going from a pump wavelength of 1.34 µm (from a Q-switched Nd:YAP rod) to an output wavelength of 1.63 µm. The highest average power diamond Raman laser to date was demonstrated by Feve *et al* [32], who obtained 24.5 W at 1193 nm by pumping an external cavity diamond Raman laser with a cryogenically cooled, Q-switched Yb:YAG laser. The maximum conversion efficiency was 13 %.

Two diamond Raman lasers synchronously pumped by picosecond modelocked lasers have been demonstrated, one operating at 573 nm [33] and one at 275.7 nm [34]. These were pumped by the second and fourth harmonics of a Nd laser respectively.

As discussed in Chapter 1, continuous wave (CW) operation of Raman lasers is usually only possible in an intracavity system. However, by taking advantage of diamond's high Raman gain and excellent thermal properties (which permit the use of very small mode sizes in the crystal), Kitzler *et al* [35] were able to demonstrate a CW external cavity diamond Raman laser producing 10.1 W at 1240 nm for 31 W pump at 1064 nm. More recently, the same group reported 15 W output power from an external cavity diamond Raman laser pumped with 42 W from a single longitudinal mode Yb-based fibre laser [36].

Most intracavity diamond Raman laser work has been performed by colleagues of the author at the University of Strathclyde. Lubeigt *et al* [1] demonstrated a Q-switched, Nd:$YVO_4$/diamond Raman laser which produced 375 mW at 1240 nm for 9.5 W absorbed diode laser pump power at 808 nm. This system was limited by thermal lensing in the Nd:$YVO_4$ laser gain rod and by losses in the diamond (~0.8 % to 1 % per single pass, see results for diamond A in Section 2.3). Using the same diamond, Lubeigt *et al* built the first CW intracavity diamond Raman laser [2] which produced 200 mW at 1240 nm for 10 W absorbed pump power at 808 nm. Again, thermal lensing in the Nd:$YVO_4$ rod and losses in the diamond severely limited the performance of this system. The intracavity measurements of losses in various diamond samples presented in this chapter, in conjunction with calorimetric loss measurement performed by other researchers, made it possible to quantitatively evaluate nominally low loss diamond supplied by Element Six Ltd. Using a low loss diamond, selected by Dr Ian Friel of Element Six Ltd on the basis of the work presented in this chapter, Lubeigt *et al* were able to obtain 1.6 W CW at 1240 nm for 15 W absorbed pump power, using a disk geometry (of the kind described in Section 1.5) to minimise the thermal lens in the Nd:$YVO_4$ laser gain crystal [3]. Using one of the diamonds characterised by the author in the present work (diamond B in Section 2.3), Parrotta *et al* [37] built a tunable diamond Raman laser by using a semiconductor disk laser (SDL) to provide tunable laser gain at fundamental wavelengths ranging from 1047 nm - 1067 nm, resulting in 1st Stokes output from 1217 nm - 1244 nm. The maximum output power of 1.3 W occurred at a wavelength of 1227 nm for an absorbed pump power of 9 W.

The highest power to date from a CW intracavity diamond Raman laser was obtained by Savtiski *et al* [38] using a side-pumped commercial Nd:YLF module as the laser gain material. Operating the Nd:YLF laser at 1047 nm led to 5.1 W at 1217 nm for 153 W incident diode pump power. While the diode-Stokes conversion efficiency of this system is low, it should be noted that the beam quality of the Stokes output is much higher than the beam quality of the 1047 nm output from Nd:YLF laser in a simple two mirror configuration. In the latter case, the side-pumping of the laser rod leads to $M^2$ parameters of $14 \times 19$ in the horizontal and vertical planes respectively, while the $M^2$ parameters of the Stokes output beam from the Raman laser were $1.1 \times 1.2$. Thus the Raman laser provides a 43-fold brightness enhancement compared to the Nd:YLF laser [38]. Again, this system was built around the least lossy of the diamonds studied by the author in the present work (diamond B in Section 2.3).

## 2.3 Intracavity loss measurements

As mentioned in Section 2.1.2, the use of diamond as an intracavity Raman crystal requires material with low optical losses. Experiments were undertaken to measure the losses in three diamond samples, in order to identify suitable material for use in Raman lasers and to determine the diamond specification required for practical Raman laser systems. Intracavity loss measurement techniques were used, in which the losses in the sample were determined by measuring the difference in performance of a Nd:$YVO_4$ laser with and without the sample present in the cavity. The details of the samples used will now be presented, and then experimental methods and the laser cavity will be described, before the results are presented.

### 2.3.1 Details of samples

Three diamond samples, grown by Element Six Ltd via chemical vapour deposition, were studied. One of these had anti-reflection (AR) coatings for 1064 nm and 1240 nm, while the other two were uncoated and therefore had to be inserted into the cavity at Brewster's angle. In these cases, it was necessary to propagate along an axis parallel to one of the shorter edges of the crystal to avoid clipping the beam at the crystal edges. When diamond B was subsequently used by colleagues of the author in diamond Raman lasers [37, 38], it was coated for propagation parallel to the longest edge. The losses in an AR coated piece of $KGd(WO_4)_2$ were also measured. Details of these samples are given in Table 2.2. Loss measurements were also made for an uncoated fused silica window (FS) – this was expected to have very low losses and hence was used to test the experimental method.

**Table 2.2:** Properties of the samples; diamond birefringence data from Element Six Ltd. Dimensions of samples are denoted by a, b and c. Beam propagated through face ab during experiments.

| Sample ID | Details | a/mm | b/mm | c/mm |
|---|---|---|---|---|
| A | Coated diamond [1] | 2 $\langle 100 \rangle$ | 3.0 $\langle 100 \rangle$ | 3.3 $\langle 100 \rangle$ |
| B | Uncoated diamond [2] | 6.5 $\langle 110 \rangle$ | 1.5 $\langle 100 \rangle$ | 3.0 $\langle 110 \rangle$ |
| C | Uncoated diamond [3] | 3.5 $\langle 110 \rangle$ | 0.5 $\langle 100 \rangle$ | 1.2 $\langle 110 \rangle$ |
| KGW | Coated $KGd(WO_4)_2$ | 5 | 5 | 41.5 |
| FS | Uncoated fused silica window | Diameter = 25 mm | | 5 |

[1] Low birefringence $\Delta n < 5 \times 10^{-7}$.

[2] "Low absorption" material; large birefringence at edges; $\Delta n < 5 \times 10^{-6}$ at centre.

[3] Not grown for low birefringence, but $\Delta n \approx 3.7 \times 10^{-6}$.

### 2.3.2 Loss measurement techniques

Since CW intracavity Raman lasers are so sensitive to loss, practical Raman crystals must have very low losses, on the order of 0.5 % or less per single pass. This makes it challenging to characterise such crystals because accurately measuring such small losses is not trivial. Simply measuring the power of a laser beam transmitted through the crystal is not sufficient as the difference between incident and transmitted power would be too small to determine accurately. Calorimetric techniques determine the optical power absorbed by the crystal be measuring the heat deposited in the crystal. This can be done in a variety of ways – by measuring the variation of temperature with time during and after irradiation [25], by measuring the current required for a thermo-electric cooler to keep the diamond temperature constant during irradiation [3], and by measuring the voltage drop across a thermo-electric cooler which is placed between the diamond and a fixed-temperature heat sink [38].

Such calorimetric techniques can be simple to implement, but they are only sensitive to absorption of the laser light, not to scattering. For purposes of building a laser, scattering losses are also important. Intracavity loss measurement techniques, which determine loss by placing the sample inside a laser cavity and analysing the effect this has on the behaviour of the laser, are sensitive to all sources of loss that affect laser performance. While these techniques are more difficult to implement, they determine the total loss parameter that is of interest for laser engineering. In this work, two intracavity loss measurements techniques have been used (Caird analysis and Findlay-Clay analysis [39, 40]). The results of these experiments will be compared to a calorimetric experiment performed by a colleague of the author in Section 2.4.1. The theory behind the Caird and Findlay-Clay analyses will now be described.

In a Caird analysis [39], the round trip parasitic losses in the cavity, $L$, are determined by measuring the slope efficiency of the laser for output couplers of varying transmission. Applying a standard analysis of the rate equations for a four level system, Svelto [41] shows that the slope efficiency of a laser is given by

$$\eta = \eta_0 \frac{T}{T+L} \tag{2.1}$$

where $T$ is the transmission of the output coupler and $\eta_0$ takes account of such factors as the quantum defect and the absorption and quantum efficiencies of the gain material [41]. Rearranging Equation 2.1 yields

$$\frac{1}{\eta} = \frac{1}{\eta_0}\left(\frac{L}{T}+1\right) \tag{2.2}$$

from which it can be seen that if the inverse of the slope efficiency is plotted against the inverse of the output coupler transmission, then a straight line is obtained, and the round trip parasitic losses are given by the ratio of the gradient of the line to the y-intercept.

In a Findlay-Clay analysis [40], the threshold pump power is measured for various output couplers. It can be shown [41] that the threshold pump power, $P_{\mathrm{th}}$, is related to the round trip losses, $L$, and the reflectivity of the output coupler, $R = 1 - T$, by

$$P_{\mathrm{th}} = \frac{-\ln(1-L) - \ln R}{K} \tag{2.3}$$

where K is a constant that takes account of the pump and cavity mode spot sizes, $w_{\mathrm{p}}$ and $w_0$, the pump photon energy, $h\nu_{\mathrm{p}}$, the stimulated emission cross-section, $\sigma$, and the upper level lifetime, $\tau$ of the gain material [41]:

$$K = \frac{\tau}{h\nu_{\mathrm{p}}} \frac{2\sigma}{\pi \left( w_0^2 + w_{\mathrm{p}}^2 \right)} \tag{2.4}$$

If the round trip losses are small ($L < 0.05$), as is the case for the laser systems of interest here, then $\ln(1 - L) \approx -L$ and

$$-\ln R = \mathrm{K} \cdot P_{\mathrm{th}} - L. \tag{2.5}$$

Therefore, if $-\ln R$ is plotted against $P_{\mathrm{th}}$ for various output couplers, the round trip parasitic losses are equal to the absolute value of the y-intercept of the straight line obtained. It should be noted that both the Caird and Findlay-Clay analyses are derived from an ideal four-level rate equation model of laser behaviour, and therefore where a real laser departs from this ideal there is scope for error in the results.

### 2.3.3 Laser cavity for loss measurements

A 3 mirror Nd:YVO$_4$ laser was constructed as shown in Figure 2.1. A 10 W, 808 nm fibre-coupled laser diode (fibre core diameter = 100 µm, numerical aperture = 0.22) was used as the pump source. An attenuator, consisting of two polarising beamsplitting cubes and a half-wave plate (consisting of two quarter-wave plates mounted together), was used to vary the pump power incident on the gain medium over approximately 0 to 4 W, without any of the variations in wavelength and mode-content that would have been caused by changing the current passing through the diode laser. An 8.4 mm long, a-cut Nd:YVO$_4$ crystal was wrapped in indium foil and placed in a water-cooled copper

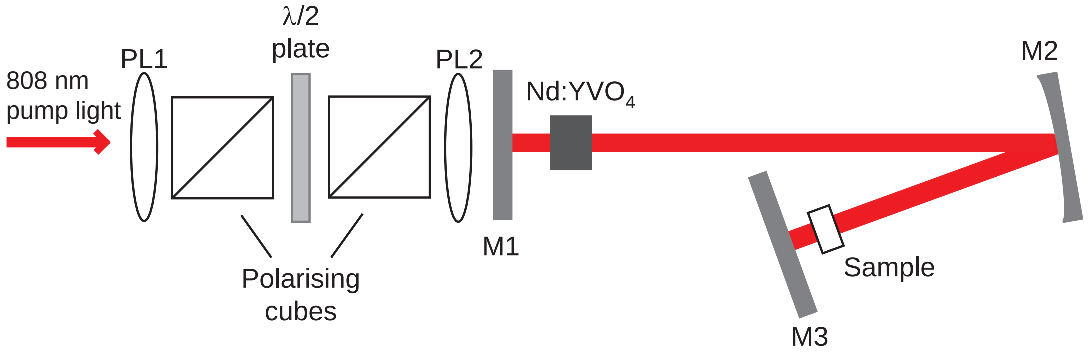

**Figure 2.1:** Schematic of laser cavity showing position of the sample when present. The pump laser was a 10 W fibre-coupled diode laser. M1 was a plane highly reflecting (HR) mirror while M2 was a curved HR mirror (radius of curvature = 100 mm). M3 was a plane output coupler for light at 1064 nm.

mount. The c-axis of the Nd:$YVO_4$ was oriented horizontally.

The pump lenses PL1 and PL2, with focal lengths of 14 mm and 75.6 mm respectively, focussed the pump beam to a spot of radius 270 µm in the gain crystal. The $TEM_{00}$ radius of the 1064 nm cavity mode was calculated to be 250 µm in the Nd:$YVO_4$ and 50 to 100 µm in the sample. The cavity was adjusted for each sample to keep the mode radius in the Nd:$YVO_4$ approximately constant - this resulted in various mode radii in the different samples. The samples were placed close to the output coupler, where the cavity mode radius was smallest so as to avoid any clipping on the edges of the crystals, some of which had small dimensions (see Table 2.2).

### 2.3.4 Experimental method

The transmissions of the six output couplers used in the experiments were measured at 1064 nm using the output beam of the laser itself. The transmissions were found to be: 1.9 %, 2.9 %, 3.4 %, 4.1 %, 8.1 % and 9.1 %.

For each sample, the fold angle of the cavity and the distance between M2 and the output coupler were adjusted in order to ensure the spot size in the gain crystal remained approximately constant. In the case of those samples that had to be inserted at Brewster's angle (ie the fused silica window and the uncoated diamond samples), the position and orientation of the sample was carefully adjusted to maximise the output power and minimise the Fresnel reflections. Small reflections (generally 0.1 - 0.2% of the intracavity power per round trip) were still observed and had to be taken into account when determining the loss due to scatter and absorption in the sample.

For each output coupler, the orientation of the output coupler and the position of 2nd pump lens (PL2 in Figure 2.1) were optimised at a low pump power (0.6 W absorbed). The threshold was then measured. The laser was then re-optimised at full pump power (4.2 W absorbed), again adjusting only the output coupler orientation and the position of PL2. The output power of the laser was then measured as a function of absorbed pump power. (Note that the absorbed pump power was determined by measuring the residual pump power transmitted through the Nd:$YVO_4$ crystal. This involved blocking the cavity with the power meter and so the absorbed pump power was measured under non-lasing conditions. However, calculations showed that even at maximum pump power, the population density in the upper laser level under non-lasing conditions was only 2 % of the total Nd ion density and therefore absorption saturation was not a concern. More than 99 % of the incident pump power was absorbed.)

A sample power transfer for the baseline case (no sample in the cavity) using an output coupler of $T = 9.10\,\%$ is shown in Figure 2.2. The slope efficiency was determined by fitting a straight line to the points for absorbed pump powers $\geq 1.5\,\mathrm{W}$ as shown in the figure. Data points near threshold were omitted to prevent any nonlinearities near threshold affecting the measured slope efficiency.

In the case of uncoated samples, the residual Fresnel reflections were measured at

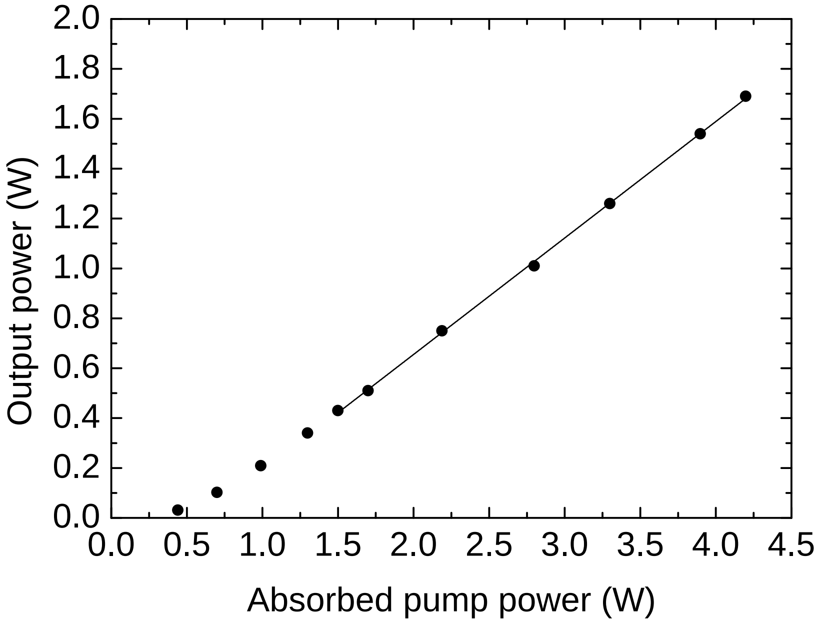

**Figure 2.2:** Sample power transfer showing performance of the laser with no sample in the cavity, using an output coupler of $T = 9.10\,\%$. The line indicates the linear fit used to determine the slope efficiency.

maximum pump power for each output coupler and the mean calculated. Note that the laser was optimised separately for the threshold (ie Findlay-Clay) measurements and the power transfer (ie Caird) measurements in case the thermal lens changed enough between low and high power to affect the optimal alignment.

### 2.3.5 Loss measurement results

The Caird and Findlay-Clay plots are shown in Figures 2.3 and 2.4. The total round-trip losses were calculated using Equations 2.2 and 2.5. By subtracting off the losses measured for the "empty" cavity (ie the baseline data) and reflection losses (for the uncoated samples), the round-trip losses due to the samples were determined and attenuation coefficients calculated.

To estimate the uncertainties in the slope efficiency and threshold measurements, repeated measurements of these were made for a single output coupler ($T = 2.9\,\%$). The output coupler was removed and replaced between each set of measurements so as to replicate the procedure used in the Caird and Findlay-Clay analyses. In this way, a measure was obtained of the variation in laser performance caused by slight alignment changes that occurred when changing output coupler. This led to an estimate of the uncertainty in the slope efficiency of $\pm 2\,\%$ (of the value of the slope efficiency) and in the threshold of $\pm 3\,\%$ (of the value of the threshold). The transmission of each output coupler was measured 5 times (using the output of the laser constructed for the loss measurements) and the standard deviation of these measurements (which was on the order of the resolution of the experiment) was taken to be the uncertainty. In this way

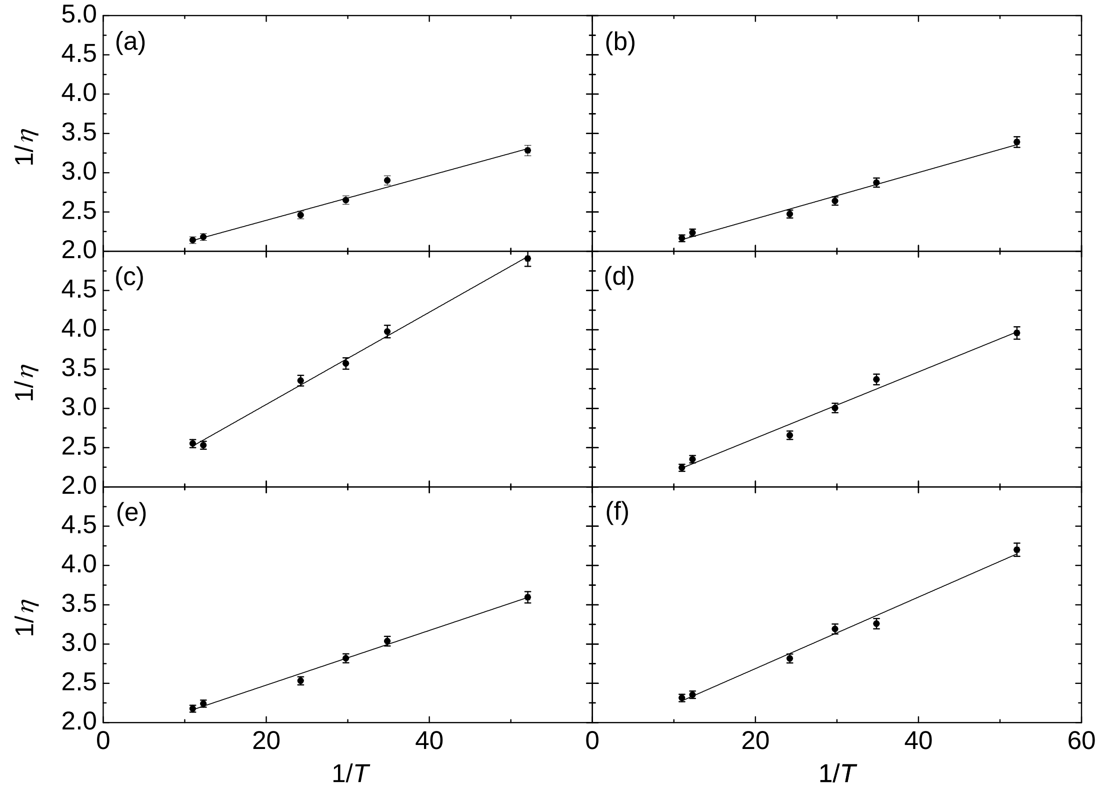

**Figure 2.3:** Caird analysis plots for (a) baseline (no sample in cavity), (b) fused silica window, (c) diamond A, (d) diamond B, (e) diamond C and (f) KGd(WO$_4$)$_2$. $\eta$ is the slope efficiency and $T$ is the transmission of the output coupler. Lines indicate least squares linear fits from which the total round trip losses were determined.

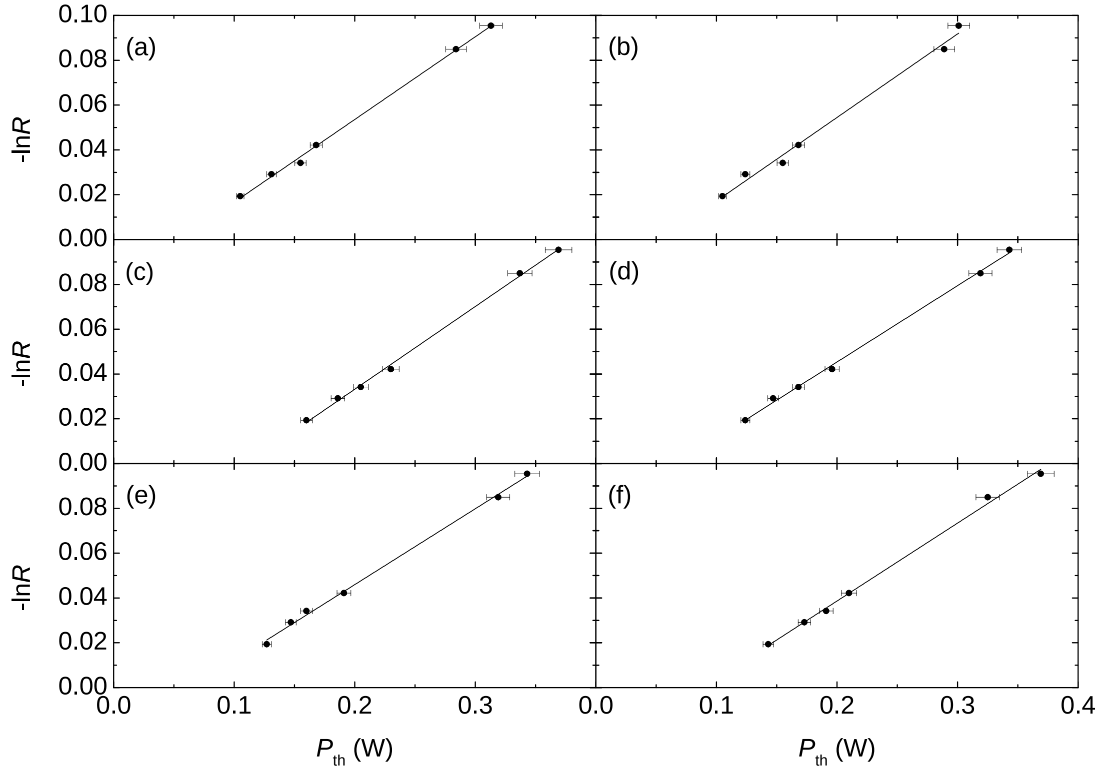

**Figure 2.4:** Findlay-Clay analysis plots for (a) baseline (no sample in cavity), (b) fused silica window, (c) diamond A, (d) diamond B, (e) diamond C and (f) $KGd(WO_4)_2$. $P_{\mathrm{th}}$ is the threshold absorbed pump power and $R$ is the reflectivity of the output coupler. Lines indicate least squares linear fits from which the total round trip losses were determined.

**Table 2.3:** Summary of results ($L_s$ is the round-trip loss due to the sample, excluding reflection losses from the uncoated samples). The losses at 1064 nm were measured via both the Caird [39] and Findlay-Clay [40] techniques. Baseline round-trip losses are given for the cavity without any sample present.

| | Caird | | Findlay-Clay | |
|---|---|---|---|---|
| Sample | $L_s$ (%) | $\alpha_C/\mathrm{cm}^{-1}$ | $L_s$ (%) | $\alpha_{FC}/\mathrm{cm}^{-1}$ |
| Baseline | $1.56 \pm 0.11$ | n/a | $2.03 \pm 0.20$ | n/a |
| A | $1.57 \pm 0.21$ | $0.024 \pm 0.004$ | $2.0 \pm 0.4$ | $0.031 \pm 0.007$ |
| B | $0.67 \pm 0.19$ | $0.010 \pm 0.003$ | $0.1 \pm 0.3$ | $0.002 \pm 0.005$ |
| C | $0.33 \pm 0.15$ | $0.013 \pm 0.006$ | $0.1 \pm 0.3$ | $0.003 \pm 0.012$ |
| KGW | $1.01 \pm 0.19$ | $0.0012 \pm 0.0002$ | $1.1 \pm 0.3$ | $0.0013 \pm 0.0004$ |
| FS | $0.01 \pm 0.16$ | $0.00007 \pm 0.0013$ | $-0.07 \pm 0.30$ | $-0.0005 \pm 0.0025$ |

the error bars shown in Figures 2.3 and 2.4 were determined (note that the error bars related to the transmission of the output couplers are very small compared to the error bars related to either the slope efficiency or threshold and in fact are barely visible on the graphs). Minimum and maximum slope straight line fits were then obtained by plotting lines to and from the extremes of the error bars on first and last point on each graph. Minimum and maximum values for the total cavity loss were then calculated from these lines and compared to the value obtained from the line of best fit. The uncertainty in the total loss was then taken to be the average difference between the minimum and maximum losses and the best value, divided by $(n-2)^{\frac{1}{2}}$ (where $n$ is the number of points on the graph) by analogy with [42]. In this way, the uncertainty in the total cavity round-trip loss was calculated for each case.

In order to estimate the uncertainty in the attenuation coefficient, the uncertainty in the total cavity loss was combined with that in the reflection loss measurements where applicable (estimated from the spread of the measurements of the reflection loss with each output coupler) and the uncertainty in the length of the sample (estimated to be ±0.5 mm based on generally good agreement between vernier calliper measurements and the manufacturer specification). It was found that the uncertainty in the total cavity loss was the dominant uncertainty.

The round-trip losses due to the samples and the corresponding attenuation coefficients are shown in Table 2.3. The results show that the losses in the fused silica window are too small to measure with the present techniques, suggesting that the sensitivity of the current methodology is at absolute best 0.05% loss per round-trip (the reflection loss measured for the fused silica sample), with the uncertainties in determining the slope efficiencies and thresholds actually making the overall uncertainty substantially greater than this. There is substantial difference between the Caird and Findlay-Clay results for both diamonds B and C, although it is only for diamond B that the measurements fail to agree within the uncertainty bounds. Diamonds B and C were uncoated and hence had to be inserted at Brewster's angle, and therefore insertion of these diamonds changed the cavity more than did the insertion of the AR coated diamond A at normal incidence.

Experience suggests that Findlay-Clay may be the less accurate technique given the relatively few raw measurements made (compared to the Caird) - any inconsistencies in measuring the threshold would lead to a large error in the final result. The calculated uncertainties are also much larger for the Findlay-Clay analysis – in some cases the uncertainties are larger than the measured quantity. For this reason, the Caird analysis results were deemed more reliable for this application.

## 2.4 Implications and consequences

### 2.4.1 Comparison to calorimetric loss measurements

The losses in diamonds A, B and C were also measured by Dr Walter Lubeigt using a calorimetric approach. In this experiment [3], Dr Lubeigt illuminated each sample with laser light at 1064 nm and determined the fraction absorbed by measuring the current required by a thermo-electric cooler (TEC) to keep the diamond at a constant temperature. Dr Lubeigt's measurements are presented in Table 2.4, alongside the author's Caird analysis results, which were presented above.

**Table 2.4:** The author's Caird analysis results are compared to calorimetric measurements performed by Dr Walter Lubeigt. Note that the Caird analysis is sensitive to both absorption and scattering losses, while the calorimetry detects only absorption and scatter in one direction (ie downwards into the TEC).

| Sample | $\alpha_{\text{Caird}}/\text{cm}^{-1}$ | $\alpha_{\text{calorimetry}}/\text{cm}^{-1}$ |
|---|---|---|
| A | $0.024 \pm 0.004$ | $0.030 \pm 0.002$ |
| B | $0.010 \pm 0.003$ | $0.010 \pm 0.002$ |
| C | $0.013 \pm 0.006$ | $0.045 \pm 0.004$ |

The results of the Caird analysis broadly agree with the results of a calorimetry experiment for diamonds A and B, but there is significant disagreement for diamond C. Diamond C was only 0.5 mm thick and therefore was challenging to work with as it presented a small aperture to the laser beam. When performing the calorimetry Dr Lubeigt found that it was difficult to ensure that the probe beam didn't clip the mount or thermistor, which would give an additional heat load and hence lead to an overestimate of the loss. Both techniques agree on that diamond B has the lowest losses, and taking into account the issues described, the techniques broadly agree on the absolute magnitude of the loss. This further strengthens the argument that the Caird analysis was the better of the two intracavity techniques used. The broad agreement between the Caird and the calorimetry also shows that the dominant losses in the diamonds are due to absorption, not scatter, and therefore the experimentally simpler calorimetric approach may be the most efficient way to characterise diamond loss coefficients in future.

### 2.4.2 Performance of diamond samples in intracavity Raman lasers

Diamond A was used by Dr Walter Lubeigt in the first demonstrations of Q-switched [1] and CW [2] intracavity Raman lasers based on synthetic diamond Raman lasers. However, the performance of these systems was fairly limited, a fact explained by the high losses found in diamond A. Diamond B was used much more successfully by Dr Vasili Savitski [38] and Mr Daniele Parrotta [37] in some of the systems reviewed in Section 2.2.

These results are entirely consistent with the loss measurements presented in this chapter. They show that diamonds for use in CW intracavity Raman lasers should have loss coefficients less than $0.01\,\mathrm{cm}^{-1}$.

### 2.4.3 New diamond samples

The Caird analysis showed that diamond B was the least lossy of the samples, and this was backed up by Dr Lubeigt's calorimetry experiments. This identification of diamond B as a promising sample for use in a Raman laser also informed further purchases of diamonds from Element Six Ltd. Diamonds were ordered to a similar specification as diamond B; in particular it was important that the nitrogen content be less than or equal to that of diamond B since nitrogen impurities are thought to be the main source of loss in the infrared region [4]. These other diamonds are described in Table 2.5.

**Table 2.5:** Details of diamond samples obtained subsequent to the experiments reported above.

| Sample ID | Details | a/mm | b/mm | c/mm |
|---|---|---|---|---|
| D | Uncoated diamond [1] | 1.6 $\langle 100 \rangle$ | 3.1 $\langle 110 \rangle$ | 4.1 $\langle 110 \rangle$ |
| E | Coated diamond [2] | 2 $\langle 100 \rangle$ | 2 $\langle 110 \rangle$ | 4 $\langle 110 \rangle$ |
| F | Coated diamond [2] | 2 $\langle 100 \rangle$ | 2 $\langle 110 \rangle$ | 6 $\langle 110 \rangle$ |

[1] This diamond was coated when used in the laser reported in [3] but uncoated when the calorimetric loss measurements described in Section 2.4.4 below were carried out by Dr Vasili Savitski.

[2] These diamonds were purchased for use in Raman lasers by the author, however as described below, performance was very poor. Calorimetric loss measurements were performed by Dr Vasili Savitski.

Diamond D [3] was used by Dr Walter Lubeigt to demonstrate the 1.6 W CW Raman laser described in Section 2.2. This was the first Watt-level CW diamond Raman laser. Diamonds E and F were purchased for use by the author in CW intracavity Raman lasers. However, no SRS could be obtained from diamond E, while the system using diamond F performed extremely poorly. High losses were suspected and subsequently confirmed by calorimetry measurements (performed by Dr Vasili Savitski), which will now be described.

### 2.4.4 Calorimetric measurements of losses in new diamonds

Dr Savitski performed calorimetric measurements of the losses in diamonds B, D, E and F using a slightly different technique [38] from that described in Section 2.4.1. In this case, a TEC was mounted between the diamond and a water-cooled brass mount, which was held at a fixed temperature. The temperature difference created between the two sides of the TEC by absorption of laser radiation in the diamond led to a voltage drop across the TEC, from which the heat load in the diamond could be determined. Dr Savitski's results are summarised in Table 2.6.

**Table 2.6:** Calorimetric measurements of losses in new diamond samples, performed by Dr Vasili Savitski.

| Sample | $\alpha_{\text{calorimetry}}/\text{cm}^{-1}$ |
|---|---|
| B | 0.004 |
| D | 0.006 |
| E | 0.017 |
| F | 0.013 |

Diamonds E and F have significantly higher losses than diamond B, which explains why the author was unable to build practical intracavity Raman lasers using these samples. The fact that these diamonds did not meet the requested specification shows that, while diamond can be grown to suitable quality for intracavity Raman lasers, there are still problems with the reliability of the supply of such material.

## 2.5 Conclusions

The results of the intracavity loss measurements performed by the author, in conjunction with calorimetry experiments performed by colleagues, have shown that diamond can be grown by CVD techniques with losses low enough to make it a practical Raman crystal for use in CW intracavity Raman lasers. However, the reliability of the commercial supply of such low loss diamond needs to be improved. Unfortunately, the diamonds obtained for use in the author's laser work turned out to have high losses and no useful CW Raman lasers could be built using these crystals. For this reason, greater attention was given to managing the thermal problems in other Raman crystals, and such work is described in the rest of this thesis.

# Bibliography

[1] W. Lubeigt, G. M. Bonner, J. E. Hastie, M. D. Dawson, D. Burns, and A. J. Kemp, “An Intra-cavity Raman Laser using Synthetic Single-crystal Diamond,” *Optics Express*, vol. 18, no. 16, pp. 16765–16770, 2010.

[2] W. Lubeigt, G. M. Bonner, J. E. Hastie, M. D. Dawson, D. Burns, and A. J. Kemp, “Continuous-wave diamond Raman laser,” *Optics Letters*, vol. 35, no. 17, pp. 2994–2996, 2010.

[3] W. Lubeigt, V. G. Savitski, G. M. Bonner, S. L. Geoghegan, I. Friel, J. E. Hastie, M. D. Dawson, D. Burns, and A. J. Kemp, “1.6 W continuous-wave Raman laser using low-loss synthetic diamond,” *Optics Express*, vol. 19, no. 7, pp. 6938–6944, 2011.

[4] I. Friel, S. L. Geoghegan, D. J. Twitchen, and G. A. Scarsbrook, “Development of high quality single crystal diamond for novel laser applications,” in *Optics and Photonics for Counterterrorism and Crime Fighting VI and Optical Materials in Defence Systems Technology VII* (C. Lewis, D. Burgess, R. Zamboni, F. Kajzar, and E. M. Heckman, eds.), vol. 7838, p. 783819, SPIE, 2010.

[5] J. Didierjean, E. Herault, F. Balembois, and P. Georges, “Thermal conductivity measurements of laser crystals by infrared thermography. Application to Nd:doped crystals,” *Optics Express*, vol. 16, no. 12, pp. 8995–9010, 2008.

[6] X. Peng, A. Asundi, Y. Chen, and Z. Xiong, “Study of the Mechanical Properties of Nd:$YVO_4$ Crystal by use of Laser Interferometry and Finite-Element Analysis,” *Applied Optics*, vol. 40, pp. 1396–1403, Mar 2001.

[7] VLOC Inc., *YAG: Yttrium Aluminium Garnate Laser Materials Datasheet*, 2003, available at http://www.vloc.com/PDFs/YAGBrochure.pdf.

[8] D. Ran, H. Xia, S. Sun, Z. Ling, W. Ge, and H. Zhang, “Thermal conductivity of $BaWO_4$ single crystal,” *Materials Science and Engineering: B*, vol. 130, no. 1-3, pp. 206–209, 2006.

[9] S. Biswal, S. P. O’Connor, and S. R. Bowman, “Thermo-optical parameters measured in ytterbium-doped potassium gadolinium tungstate,” *Applied Optics*, vol. 44, no. 15, pp. 3093–3097, 2005.

[10] A. J. Kemp, A. J. Maclean, J.-M. Hopkins, J. E. Hastie, S. Calvez, M. D. Dawson, and D. Burns, "Thermal management in disc lasers: doped-dielectric and semiconductor laser gain media in thin-disc and microchip format," *Journal of Modern Optics*, vol. 54, no. 12, pp. 1669–1676, 2007.

[11] P. Millar, R. B. Birch, A. J. Kemp, and D. Burns, "Synthetic diamond for intracavity thermal management in compact solid-state lasers," *IEEE Journal of Quantum Electronics*, vol. 44, no. 8, pp. 709–717, 2008.

[12] S. C. Rand and L. G. DeShazer, "Visible color-center laser in diamond," *Optics Letters*, vol. 10, no. 10, pp. 481–483, 1985.

[13] G. Eckhardt, D. P. Bortfeld, and M. Geller, "Stimulated Emission of Stokes and Anti-Stokes Raman Lines from Diamond, Calcite, and $\alpha$-Sulfur Single Crystals," *Applied Physics Letters*, vol. 3, no. 8, pp. 137–138, 1963.

[14] A. M. Zaitsev, *Optical Properties of Diamond: A Data Handbook*. Springer, 2001.

[15] V. G. Savitski, S. Reilly, and A. J. Kemp, "Steady-State Raman Gain in Diamond as a Function of Pump Wavelength," *IEEE Journal of Quantum Electronics*, vol. 49, no. 2, pp. 218–223, 2013.

[16] P. G. Zverev, T. T. Basiev, A. A. Sobol, V. V. Skornyakov, L. I. Ivleva, N. M. Polozkov, and V. V. Osiko, "Stimulated Raman scattering in alkaline-earth tungstate crystals," *Quantum Electronics*, vol. 30, no. 1, p. 55, 2000.

[17] J. A. Piper and H. M. Pask, "Crystalline Raman Lasers," *IEEE Journal of Selected Topics in Quantum Electronics*, vol. 13, no. 3, pp. 692–704, 2007.

[18] A. A. Kaminskii, K. Ueda, H. J. Eichler, Y. Kuwano, H. Kouta, S. M. Bagaev, T. H. Chyba, J. C. Barnes, G. M. A. Gad, T. Murai, and J. Lu, "Tetragonal vanadates $YVO_4$ and $GdVO_4$ - new efficient $\chi^{(3)}$-materials for Raman lasers," *Optics Communications*, vol. 194, no. 1-3, pp. 201–206, 2001.

[19] F. van Loon, A. J. Kemp, A. J. Maclean, S. Calvez, J.-M. Hopkins, J. E. Hastie, M. D. Dawson, and D. Burns, "Intracavity diamond heatspreaders in lasers: the effects of birefringence," *Optics Express*, vol. 14, pp. 9250–9260, Oct 2006.

[20] R. S. Balmer, J. R. Brandon, S. L. Clewes, H. K. Dhillon, J. M. Dodson, I. Friel, P. N. Inglis, T. D. Madgwick, M. L. Markham, T. P. Mollart, N. Perkins, G. A. Scarsbrook, D. J. Twitchen, A. J. Whitehead, J. J. Wilman, and S. M. Woollard, "Chemical vapour deposition synthetic diamond: materials, technology and applications," *Journal of Physics: Condensed Matter*, vol. 21, no. 36, p. 364221, 2009.

[21] J. E. Butler, R. L. Woodin, L. M. Brown, and P. Fallon, "Thin film diamond growth mechanisms," *Philosophical Transactions: Physical Sciences and Engineering*, vol. 342, no. 1664, pp. 209–224, 1993.

[22] R. P. Mildren and J. R. Rabeau, eds., *Optical Engineering of Diamond.* Wiley-VCH, 2013.

[23] A. R. Lang, "Causes of birefringence in diamond," *Nature*, vol. 213, no. 5073, pp. 248–251, 1967.

[24] I. Friel, S. Clewes, H. Dhillon, N. Perkins, D. Twitchen, and G. Scarsbrook, "Control of surface and bulk crystalline quality in single crystal diamond grown by chemical vapour deposition," *Diamond and Related Materials*, vol. 18, no. 58, pp. 808 – 815, 2009. Proceedings of Diamond 2008, the 19th European Conference on Diamond, Diamond-Like Materials, Carbon Nanotubes, Nitrides and Silicon Carbide.

[25] G. Turri, Y. Chen, M. Bass, D. Orchard, J. E. Butler, S. Magana, T. Feygelson, D. Thiel, K. Fourspring, R. V. Dewees, J. M. Bennett, J. Pentony, S. Hawkins, M. Baronowski, A. Guenthner, D. Seltzer, Michael, D. C. Harris, and C. M. Stickley, "Optical absorption, depolarization, and scatter of epitaxial single-crystal chemical-vapor-deposited diamond at 1.064 $\mu$m," *Optical Engineering*, vol. 46, no. 6, p. 064002, 2007.

[26] A. A. Demidovich, A. S. Grabtchikov, V. A. Orlovich, M. B. Danailov, and W. Kiefer, "Diode pumped diamond Raman microchip laser," in *Conference on Lasers and Electro-Optics Europe*, 2005.

[27] R. P. Mildren, "Side-pumped crystalline Raman laser," *Optics Letters*, vol. 36, no. 2, pp. 235–237, 2011.

[28] R. P. Mildren and A. Sabella, "Highly efficient diamond Raman laser," *Optics Letters*, vol. 34, no. 18, pp. 2811–2813, 2009.

[29] A. Sabella, J. A. Piper, and R. P. Mildren, "1240 nm diamond Raman laser operating near the quantum limit," *Optics Letters*, vol. 35, no. 23, pp. 3874–3876, 2010.

[30] A. Sabella, J. A. Piper, and R. P. Mildren, "Efficient conversion of a 1.064 $\mu$m Nd:YAG laser to the eye-safe region using a diamond Raman laser," *Optics Express*, vol. 19, no. 23, pp. 23554–23560, 2011.

[31] M. Jelíneck, O. Kitzler, H. Jelínková, J. Šulc, and M. Němec, "CVD-diamond external cavity nanosecond Raman laser operating at 1.63 $\mu$m pumped by 1.34 $\mu$m Nd:YAP laser," *Laser Physics Letters*, vol. 9, no. 1, pp. 35–38, 2012.

[32] J. M. Feve, K. E. Shortoff, M. J. Bohn, and J. K. Brasseur, “High average power diamond Raman laser,” *Optics Express*, vol. 19, no. 2, pp. 913–922, 2011.

[33] D. J. Spence, E. Granados, and R. P. Mildren, “Mode-locked picosecond diamond Raman laser,” *Optics Letters*, vol. 35, no. 4, pp. 556–558, 2010.

[34] E. Granados, D. J. Spence, and R. P. Mildren, “Deep ultraviolet diamond Raman laser,” *Optics Express*, vol. 19, no. 11, pp. 10857–10863, 2011.

[35] O. Kitzler, A. McKay, and R. P. Mildren, “Continuous-wave wavelength conversion for high-power applications using an external cavity diamond Raman laser,” *Optics Letters*, vol. 37, pp. 2790–2792, Jul 2012.

[36] O. Kitzler, A. McKay, and R. P. Mildren, “Characterization of a Single-frequency-pumped Continuous-wave Extracavity Diamond Raman Laser,” in *Conference on Lasers and Electro-Optics Europe*, 2013.

[37] D. C. Parrotta, A. J. Kemp, M. D. Dawson, and J. E. Hastie, “Tunable continuous-wave diamond Raman laser,” *Optics Express*, vol. 19, no. 24, pp. 24165–24170, 2011.

[38] V. G. Savitski, I. Friel, J. E. Hastie, M. D. Dawson, D. Burns, and A. J. Kemp, “Characterization of Single-Crystal Synthetic Diamond for Multi-Watt Continuous-Wave Raman Lasers,” *IEEE Journal of Quantum Electronics*, vol. 48, no. 3, pp. 328 –337, 2012.

[39] J. A. Caird, S. A. Payne, P. R. Staver, A. J. Ramponi, L. L. Chase, and W. F. Krupke, “Quantum Electronic Properties of the $Na_3Ga_2Li_3F_{12}$:$Cr^{3+}$ Laser,” *IEEE Journal of Quantum Electronics*, vol. 24, no. 6, pp. 1077–1099, 1988.

[40] D. Findlay and R. A. Clay, “The measurement of internal losses in 4-level lasers,” *Physics Letters*, vol. 20, no. 3, pp. 277–278, 1966.

[41] O. Svelto, *Principles of Lasers*. Plenum Press, 4th ed., 1998.

[42] J. L. Safko, “Error analysis of straight line plots in the undergradute physics laboratory,” *American Journal of Phyics*, vol. 33, no. 5, pp. 379–382, 1965.

# Chapter 3

# Determining the thermal lens strengths

In this chapter, experimental and theoretical approaches to determining the strengths of the thermal lenses in a CW intracavity Raman laser will be presented. Direct, in situ measurements of the thermal lens in the $BaWO_4$ Raman crystal in a CW intracavity Raman laser will be reported, and a finite element analysis approach to estimating the thermal lens in the laser gain material, a Nd:$YVO_4$ disk, will be described. First, the theory describing the formation and behaviour of thermal lenses will be described. Certain issues specific to Raman lasers will be noted and previous measurements of thermal lenses in Raman lasers will be reviewed. The experimental technique used here to measure the thermal lens in the $BaWO_4$ crystal, lateral shearing interferometry, will then be explained. In order to build a longer cavity, better suited to the thermal lens measurement technique, a disk geometry was used for the laser gain crystal. The performance of the disk laser at the fundamental wavelength of 1064 nm will be presented and then the Raman laser and diagnostic set-up for the lateral shearing interferometry experiment will be described. The results of this experiment will be presented and discussed with reference to the material properties of $BaWO_4$. The modelling technique used to determine the thermal lens in the Nd:$YVO_4$ disk will then be described and the results reported. Finally, the implications for Raman laser design of the experimental results and the numerical calculations will be discussed.

The lateral shearing interferometry experiments presented in this chapter were undertaken in collaboration with Professor Takashige Omatsu of Chiba University, Japan, while Prof. Omatsu was visiting Macquarie University. The author constructed the laser and then the measurements were carried out jointly by the author and Prof. Omatsu. Analysis and interpretation of the lateral shearing interferograms was performed by Prof. Omatsu using his own custom software that he has developed over many years.

Much of the work reported in this chapter has been published in a journal paper (G. M. Bonner, H. M. Pask, A. J. Lee, A. J. Kemp, J. Wang, H. Zhang, and T. Omatsu, "Measurement of thermal lensing in a CW $BaWO_4$ intracavity Raman laser," *Optics*

*Express*, vol. 20, pp. 9810–9818, Apr 2012) [1].

## 3.1 Thermal lenses

As mentioned in Chapter 1, thermal problems often limit the performance of solid state lasers, and can be particularly acute in Raman lasers. Energy dissipated as heat in the material can cause a variety of problems. The temperature of the material rises, which can affect parameters such as energy level lifetimes, re-absorption losses (in three level systems), and thermal conductivity. Even more problematically, the temperature rise is usually non-uniform, leading to temperature gradients throughout the crystal. These gradients give rise to lensing effects and other detrimental phenomena. In this section, the sources of heat in a laser gain crystal will be outlined. The effects of the resulting temperature gradients will then be discussed – these are the same for both laser and Raman crystals. The inelastic nature of stimulated Raman scattering (SRS) has implications for the generation and effects of heat in the Raman crystal. These Raman-specific details will be presented in Section 3.2.

### 3.1.1 Heat sources and temperature profiles

The difference in energy between the pump and emitted photons in a laser is known as the quantum defect and sets the minimum heat load [2]. In a four level system (for example the 1064 nm transition in $Nd^{3+}$ pumped with light at 808 nm), a pump photon excites an ion up to the pump level, from which it drops down to the upper laser level via a non-radiative decay, dissipating the excess energy as heat. After the decay to the lower laser level via stimulated emission, another non-radiative decay takes the ion from the lower laser level back to the ground state.

The quantum defect is the principal source of heating in solid-state lasers [2] but it does not account for the full heat load observed in many systems. Several parasitic processes can add to the heat load [2, 3]. Any non-radiative path from the pump or upper laser levels back to the ground state will add to the heat load. Excited state absorptions [4], whereby ions in the pump level or upper laser level absorb pump or emitted photons again to reach higher levels can lead to increased heating if the ions subsequently decay non-radiatively from these very high energy levels. Upconversion [3, 5, 6] can lead to a similar situation, for example if the extra energy comes from a neighbouring excited ion, which decays to a lower state while its partner is raised to a higher level. Concentration quenching [3, 5], whereby neighbouring ions exchange energy and move to different, sometimes intermediate, levels can also result in more non-radiative decays. Concentration quenching can also reduce the lifetime of the upper laser level, thereby reducing the gain and increasing the threshold of the laser. Concentration quenching and upconversion become more problematic at high doping concentrations, at which there are many laser ions close together in the host lattice. Dead sites are laser ions which absorb pump light but do not contribute to the population inversion - the absorbed energy is dissipated as heat [2, 7]. Any impurities in the crystal which absorb at the pump or emission wavelengths will also contribute to the heat load [2].

For a Nd:YVO$_4$ laser, pumped at 808 nm and emitting at 1064 nm, the fractional thermal loading (the ratio of heat energy deposited to the energy of the fundamental or pump photon [2]), due to the quantum defect alone is 0.24 [2], but Sennaroglu determined the total fractional thermal loading to be 0.40 for a crystal with a doping concentration of 3 at.% [8].

As mentioned above, absolute temperature rises can have some effect on the laser. However, for most diode-pumped solid-state lasers it is the temperature gradients created in the crystal that cause the most severe problems and therefore we must consider the cooling geometry and resultant heat flow in order to analyse the thermal lens effects in a laser. In particular, variations in temperature in the directions transverse to the propagation axis of the cavity lead to transverse variations in the optical path length, and hence cause the medium to act like a lens. If an infinitely long cylindrical rod is uniformly pumped (that is to say that heat is generated uniformly throughout the volume of the rod) and cooled through its curved surface, then the resultant transverse temperature profile is parabolic [2]. This results in a parabolic phase change across a beam passing through the material - in other words, the rod acts like a perfect lens. However, uniform pumping of the gain material often leads to the oscillation of higher order transverse modes.

End-pumping makes it possible to deposit the pump energy into just the central area of the crystal, where it can be extracted by primarily (or indeed only) the lowest order transverse mode. However, end-pumping leads to non-parabolic temperature profiles and non-parabolic phases changes, ie an aberrated lens [5, 9, 10]. In the case of a top hat pump profile, the thermal lens is spherical, with a constant focal length, over the radius of the top hat but outside that radius the focal length is itself a function of radius [5]. A Gaussian-pump profile provides better mode-matching, but in this case the focal length of the thermal lens varies with radius across the entire cross-section of the crystal, so the thermal lens is more highly aberrated [5].

As mentioned in Section 1.5, disk-shaped laser gain crystals develop much weaker thermal lenses than rod-shaped crystals. This is because the extraction of heat through the large rear face of the disk (and in some cases through some portion of the front face) leads to primarily axial heat flow and axial temperature gradients, with significantly reduced transverse temperature gradients [11]. In the case of thin disks, where the thickness of the disk is less than the radius, the heat flow is almost entirely axial and the contribution to the thermal lens from transverse temperature gradients is almost negligible. In such cases, the dominant contribution to the thermal lens is bowing of the disk caused by the temperature difference between the front and rear faces [12]. The slightly thicker disk lasers used in this work (described in Section 1.5) are an intermediate case between rod and thin disk geometries from a thermal point of view, with the diamond heatspreader helping to promote disk-like temperature gradients even while the thickness of the disk is still larger than radius.

The optical effects of the temperature gradients which arise in laser crystals will now be considered in more detail.

### 3.1.2 Optical effects of non-uniform temperature rises

The non-uniform temperature rises in the crystal alter its optical properties in several ways [2, 13], which are summarised in Figure 3.1. Thermal expansion causes the hotter central parts of the crystal to expand more than the cooler edges, resulting in stresses and strains in the material and deformation of the end faces. These bulge outwards, creating a positive lensing effect. The stresses and strains in the material have several effects. In the extreme case, the crystal will fracture if the stress exceeds the tensile strength of the material. Refractive index also varies with strain via the photoelastic effect. Gradients in the strain therefore lead to gradients in the refractive index and hence further lensing effects, which can be positive or negative depending on the elasto-optic coefficients. This modification of the refractive index is usually anisotropic, leading to strain-induced birefringence even in materials that have no intrinsic optical axis such as YAG [2, 5]. The refractive index itself varies directly with temperature also, and hence the temperature gradients also lead to refractive index gradients and hence lensing effects. Again this contribution to the thermal lens can be positive or negative.

Such changes in the shape and refractive index of the crystal impact on laser performance in a number of ways. The thermal lens changes the stability range of the cavity, causing the operating point of the cavity in the $g_1$-$g_2$ stability plane to vary with power. This means that the cavity will only be stable for a certain range of pump powers. Changes in the mode size and divergence of the field at various points in

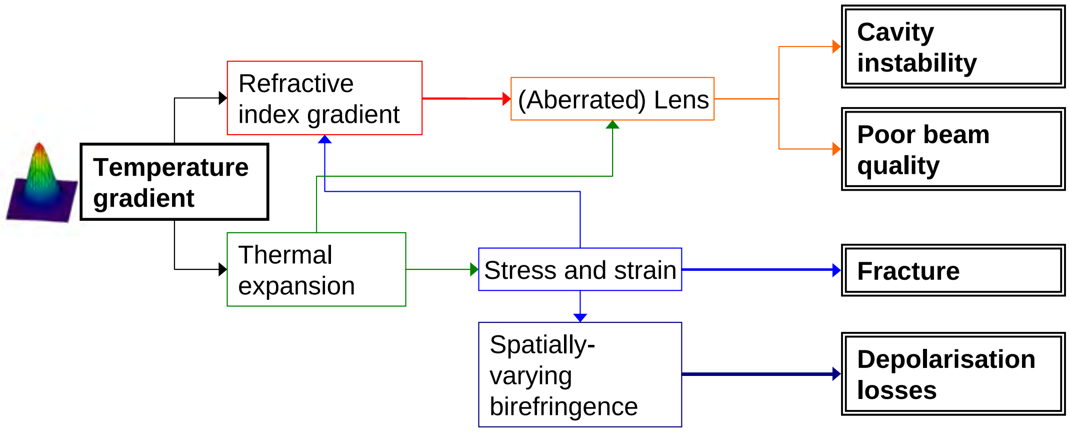

**Figure 3.1:** The effects of heat deposition in laser crystals.

the cavity can change the quality of the mode-matching between the cavity and pump fields, affecting the efficiency and transverse mode of the laser. If the phase change profile is parabolic, then the crystal acts like a spherical lens. However, if there are non-parabolic features (as is the case in end-pumped systems) then the thermal lens will have aberrations which can degrade the beam quality of the laser [5]. All these effects are complicated by strain-induced birefringence, which causes different polarisations to experience different lensing effects, resulting in degraded beam quality and depolarisation losses at polarisation-sensitive elements in the cavity [2, 5, 13]. The above description indicates the complex interactions between heating, mechanical and optical effects. The material properties and cavity design parameters that influence these phenomena will now be considered.

### 3.1.3 Key parameters that impact on thermal lens strength

Complete modelling of thermal lenses often requires finite element analysis to account for heat flow, stress and strain in the three dimensional (and possibly anisotropic) crystal. Accurate knowledge of the mechanical, thermal and optical properties of the crystal is also needed, but this information is not available for many crystals. However, analytical solutions derived for certain simple cases can be instructive and provide insight into the effect of changing key parameters. Koechner [2] derives the following expression for the focal length of the thermal lens in a uniformly pumped, side-cooled cylindrical rod:

$$f = \frac{\kappa A}{P_{\mathrm{h}}} \left( \frac{1}{2} \frac{\mathrm{d}n}{\mathrm{d}T} + \alpha_{\mathrm{t}} C_{\mathrm{r},\phi} n_0^3 + \frac{\alpha_{\mathrm{t}} r_0 \left( n_0 - 1 \right)}{l} \right)^{-1} \tag{3.1}$$

where $\kappa$ is the thermal conductivity, $A$ is the cross-sectional area of the rod, $P_{\mathrm{h}}$ is the total heat dissipated in the rod, $\mathrm{d}n/\,\mathrm{d}T$ is the rate of change of refractive index with temperature, $\alpha_{\mathrm{t}}$ is the thermal expansion coefficient, $C_{\mathrm{r},\phi}$ are functions of the elasto-optical coefficients for the radial and tangential directions respectively, $n_0$ is the refractive index at the centre of the rod, $r_0$ is the radius of the rod and $l$ is the length of the rod. The first term in the brackets in Equation 3.1 represents the lens due to the variation of refractive index with temperature, the second term represents the strain-induced component of the lens and the third term represents the bulging of the end faces of the rod.

The situation becomes more complicated for end-pumped systems, as there will be non-parabolic components to the temperature profile and hence the thermal lens will have aberrations. Innocenzi *et al* [9] give the focal length of the spherical component of the thermal lens in a rod end-pumped with a Gaussian profile pump beam as:

$$f = \frac{\pi \kappa \omega_{\mathrm{p}}^2}{P_{\mathrm{ph}} \left( \frac{\mathrm{d}n}{\mathrm{d}T} \right)} \left( \frac{1}{1 - \exp\left( -\alpha l \right)} \right) \tag{3.2}$$

where $\omega_\mathrm{p}$ is the $1/\mathrm{e}^2$ radius of the pump beam, $P_\mathrm{ph}$ is the incident pump power multiplied by the fraction of the pump power that is dissipated as heat and $\alpha$ is the absorption coefficient.

These equations illustrate why, as was discussed in Chapter 2, the thermal conductivity is so important – the focal length of the thermal lens is proportional to the thermal conductivity. It can also be seen that the thermal expansion coefficient affects both the strain and bulging terms, and therefore $\alpha_\mathrm{t}$ is another important material property. It can be seen from Equation 3.2 that the pump spot size is also a crucial parameter and to minimise the thermal lens, it is desirable to work with the largest possible spot size. Unfortunately the pump spot size is usually limited by mode-matching concerns, and by the fact that the threshold of the laser also increases with the square of the radius of the pump beam [14].

Full calculation of the stress and strain fields in the crystal requires knowledge of the elasto-optical, compliance and thermal expansion tensors, perhaps as many as 36 elements for some crystals [13]. This number decreases for crystals with particularly simple symmetries in the lattice but even so, these parameters have been measured for only a very few laser crystals (YAG is one notable example [2, 13]). For this reason, the strain-induced component of the thermal lens is often neglected. So also is the bulging component, and in some systems this is acceptable since the temperature-dependence of the refractive index is the dominant factor in the thermal lens (representing 74 % of the optical distortion in a uniformly pumped, cylindrical Nd:YAG rod [2]). However, the bulging of the end faces must be considered in some systems, especially end-pumped devices [2].

As mentioned above, thermal expansion contributes to $\mathrm{d}n/\mathrm{d}T$, and this makes it difficult to separate strain and $\mathrm{d}n/\mathrm{d}T$ effects. Chénais *et al* [13] have raised questions over the definition of $\mathrm{d}n/\mathrm{d}T$, and the way this parameter is measured and then applied in thermal lens calculations. Another difficulty is that parameters like $\mathrm{d}n/\mathrm{d}T$ and even thermal conductivity are often not known with good accuracy (for example, [15] and [16] disagree on not only the magnitude but also the sign of $\mathrm{d}n/\mathrm{d}T$ for various axes in $\mathrm{KGd(WO_4)_2}$, while [17] and [18] disagree as to whether Nd:$\mathrm{YVO_4}$ or Nd:$\mathrm{GdVO_4}$ has the higher thermal conductivity). In short, models of thermal lensing can be useful as indicators of trends but, if accurate absolute values are desired, it is much preferable to measure the thermal lens directly, under operating conditions if possible.

## 3.2 Thermal lensing in Raman lasers

### 3.2.1 Issues specific to Raman lasers

Temperature gradients in a Raman crystal have the same effects as described above for laser gain crystals. However, the main source of heat in the Raman crystal is SRS and this has several implications for the effects of the thermal lens in the Raman material.

In the laser gain crystal, the deposition of heat is related primarily to the absorption of pump radiation, some of the energy of which is dispersed as heat. The total amount of heat deposited can vary under lasing and non-lasing conditions, but it remains the case that it is primarily the parameters of the pump beam (power, spot size etc) that determine the strength of the thermal lens.

In contrast, the primary source of heating in the Raman crystal is the inelastic Raman scattering process: every time a Stokes photon is generated, a phonon has necessarily been created also, and furthermore, if a Stokes photon is not generated, ie if no scattering event occurs, then no phonon is created and hence no heat is deposited. (There may also be absorptions or other parasitic process involving fundamental and/or Stokes photons. One notable phenomenon is the strong blue fluorescence that is observed in many Raman crystals above Raman threshold [19]. This fluorescence is thought to be due to thulium impurities in the Raman crystal [20], and it has been estimated that the fluorescence process makes a modest contribution to the heat load in the Raman crystal – an increase in the heat load of around 16 % has been calculated for $KGd(WO_4)_2$ [20].)

This direct link between the emission of Stokes photons and the deposition of heat has several consequences for the thermal effects in the Raman crystal. Firstly the strength of the thermal lens depends on the Stokes power generated in the laser, and on the mode radius of the Stokes field in the Raman crystal [21]. Since mode radii at different points in the cavity depend on the strength of any thermal lenses in the cavity, and since the conversion efficiency, and hence the Stokes power, depend on mode radii, a complex interdependency exists between the performance of the laser and the strength of the thermal lens in the Raman crystal. Secondly, heat is deposited in precisely the volume occupied by the Stokes field. In a conventional laser gain crystal, it is possible to avoid aberrated regions of the thermal lens by varying the fundamental field mode area relative to that of the pump beam [5] (albeit at the expense of poorer mode-matching). This is not possible in the Raman crystal, since the field of interest (the Stokes field) is the very field which primarily determines the temperature distribution in the crystal. A related issue is that since it is desirable to have a long interaction length for the nonlinear SRS process, it is not easy to design geometries with favourable heat flow such as thin disks.

As noted in Chapter 2, many common Raman materials have poor thermal conductivities. The quantum defect between the fundamental and Stokes wavelength is compared to that between pump and fundamental photons in some common laser gain materials in Table 3.1. The fractional thermal loading due to the quantum defect (the ratio of heat energy deposited to the energy of the fundamental or pump photon [2]) is given by

$$\eta_{\mathrm{h}} = 1 - \frac{\lambda_{\mathrm{in}}}{\lambda_{\mathrm{out}}} \tag{3.3}$$

where, for the laser gain material, $\lambda_{\mathrm{in}} = \lambda_{\mathrm{P}}$, the pump wavelength and $\lambda_{\mathrm{out}} = \lambda_{\mathrm{F}}$,

**Table 3.1:** Fractional thermal loading due to the quantum defect for several laser and Raman materials. $KGd(WO_4)_2$ has two strong Raman shifts, one of which can be selected by appropriate choice of crystal orientation. Note that $\eta_h$ will vary for a given Raman material depending on the fundamental wavelength since it is the frequency shift that is fixed, while the fundamental wavelength can be chosen freely.

| Material | Process | $\lambda_P$/nm | $\lambda_F$/nm | $\lambda_S$/nm | $\eta_h$ |
|---|---|---|---|---|---|
| $Nd:YVO_4$ | laser | 808 | 1064 | — | 0.24 |
| $Nd:YVO_4$ | laser | 880 | 1064 | — | 0.17 |
| Yb:YAG | laser | 943 | 1030 | — | 0.084 |
| $BaWO_4$ | Raman | — | 1064 | 1180 | 0.098 |
| $KGd(WO_4)_2$ ($901\,\mathrm{cm}^{-1}$) | Raman | — | 1064 | 1177 | 0.096 |
| $KGd(WO_4)_2$ ($768\,\mathrm{cm}^{-1}$) | Raman | — | 1064 | 1159 | 0.082 |
| $Nd:GdVO_4$ | self-Raman | 808 | 1063 | 1173 | 0.31 |

the fundamental wavelength, and for the Raman material, $\lambda_{\text{in}} = \lambda_F$ and $\lambda_{\text{out}} = \lambda_S$, the Stokes wavelength. Values of $\eta_h$ for several common laser and Raman materials are shown in Table 3.1. It can be seen that the quantum defect for the SRS process in common Raman crystals is typically smaller than that for conventional pumping schemes in a Nd-based laser material, and is comparable to that in Yb, a prominent, low quantum defect laser material. (It should be noted however that the heat load in the Raman crystal rises rapidly if the SRS process is cascaded to 2nd or higher orders - a phonon is deposited for each shift [22].)

As described in Chapter 1, intracavity Raman lasers can either consist of separate laser and Raman crystals, or, if a Raman active host is used for the laser ions (for example $YVO_4$ or $GdVO_4$), then a single crystal can act as both laser and Raman material in a "self-Raman" laser. Self-Raman laser cavities can be very compact and simple, and have low losses since the number of surfaces is minimised. However, a very large heat load and strong thermal lens is created in the one crystal. By separating the laser gain and SRS processes, the heat load is spread over two crystals and there is more flexibility when designing the cavity to cope with the two thermal lenses.

### 3.2.2 Previous measurements of thermal lenses in Raman lasers

Dekker *et al* [19] estimated the thermal lens in a CW $Nd:GdVO_4$ self-Raman laser to have a focal length of only 17 mm for 18 W pump power and 1.1 W Stokes output power, with a pump spot radius of 200 µm, based on the onset of cavity instability. Kananovich *et al* [23] used a similar approach, calculating the thermal lens in a quasi-CW $Nd:YVO_4$ self-Raman laser to have a focal length of 60 mm for 23 W pump power when the system was operated at 10 % duty-cycle, with a pump spot radius of 200 µm. Such strong thermal lenses can be problematic even in very short cavities (24 mm in the case of [19]). Dekker *et al* also compared their measurements to calculations of the thermal lens based on the quantum defect expected for the laser gain and SRS processes. While they found good agreement between calculation and experiment for the case when the laser was operating at the fundamental wavelength (no SRS), the thermal lens found experimentally when SRS was occurring was significantly stronger than that predicted by the calculations [19]. This was attributed to additional heat load arising from processes such as impurity absorption or excited state absorption involving the Stokes wavelength. As mentioned in Section 3.2.1, strong blue fluorescence is observed in many Raman crystals above Raman threshold and there could be additional heating associated with this process.

Determining the thermal lens from cavity stability measurements has the disadvantage that it probes the thermal lens at the stability edge of the laser, a regime in which the laser would not normally be operated and in which the behaviour of the laser may be different. Furthermore, it only provides an estimate of the focal length of the strongest plane of an astigmatic lens (ie the focal length in whichever plane of the cavity becomes unstable first). If possible it is better to measure thermal lenses more directly. Wang *et al* [24] passed a collimated probe beam from a HeNe laser through the Nd:GdVO$_4$ crystal in a Q-switched self-Raman laser and determined the thermal lens strength by finding the focus of the probe beam after the crystal. They found the focal length of the thermal lens to be 180 mm for 18 W pump power at 30 kHz pump repetition frequency (0.95 W Stokes output power, pump spot radius 160 µm). The accuracy of this technique depends on how accurately the focus of the probe beam can be located, which is challenging for weak thermal lenses.

Recently the technique applied in the present work, lateral shearing interferometry, was used to measure the thermal lens in a Nd:GdVO$_4$ self-Raman laser. In that system, the focal length of the thermal lens was found to be as short as 28 mm [25], for 16.2 W pump power at 808 nm, 0.54 W Stokes output power, 200 µm pump spot radius. Omatsu *et al* also compared 808 nm and 880 nm pumping, finding a weaker lens of 36 mm, for 17.5 W pump power, 0.70 W Stokes output power in the latter case. A significant difference between the strength of the thermal lensing above and below Raman threshold again suggested additional heat loading processes associated with SRS, beyond the quantum defect between fundamental and Stokes photons [25]. Lateral shearing interferometry is described in detail in Sections 3.3 and 3.5 below.

All of the above measurements were for self-Raman systems. It is also interesting to study thermal lensing in systems using separate laser and Raman gain media. Sun *et al* [26] studied the thermal lens in a Q-switched Nd:YAG/BaWO$_4$ Raman laser operating on the 332 cm$^{-1}$ shift of BaWO$_4$ by measuring the radius and divergence of the output beam, and calculating the intracavity mode size. By comparing this to ABCD resonator modelling, and calculating the thermal lens in the Nd:YAG using the theory described in [27], they inferred a focal length of −1100 mm in the BaWO$_4$ crystal at a pump power of 7.55 W and an output power of 1.23 W at a pulse repetition frequency of 17 kHz and a Stokes mode radius of 240 µm, which is assumed here to be in the BaWO$_4$ crystal. The accuracy of this technique will be heavily influenced by how accurately the lens in the laser gain medium can be determined. Basiev *et al* [28] also studied the thermal lens in $BaWO_4$, but in an external cavity Raman laser. They analysed the interference of the reflections of a HeNe laser beam from the front and rear surfaces of the $BaWO_4$ crystal and found a weak (8.3 m), *positive* lens. Sun *et al* specify that the crystal they used was a-cut [26], but no indication of the cut of the crystal is given in [28]. It is possible that a different cut of crystal was used, leading to a different sign in the thermal lens strength.

In the work presented here, lateral shearing interferometry is used to directly measure the thermal lens in a $BaWO_4$ crystal in a CW intracavity system. To the best of the author's knowledge, this is the first direct measurement of the thermal lens in a CW intracavity Raman laser constructed around separate laser and Raman crystals.

## 3.3 Lateral shearing interferometry

Lateral shearing interferometry is a convenient way to measure the phase distortions created when a collimated beam of light passes through a focussing element, such as a bulk lens or a thermally loaded laser crystal. A shearing plate is used to create two copies of the distorted probe beam, which then interfere with each other. The strength of the thermal lens can be calculated by analysing the interference fringes. Lateral shearing interferometry has been used to measure thermal lensing in various laser systems [25, 29–33], including the Nd:$GdVO_4$ self-Raman laser [25] described in Section 3.2.2. The technique is insensitive to vibration and there is no requirement for perfect spatial overlap between the probe beam and the pumped volume within the crystal (a collimated probe beam is used to illuminate the entire surface of the crystal under study). For these reasons, it is reasonably straightforward to implement.

The experimental set-up for lateral shearing interferometry is shown schematically in Figure 3.2. A collimated probe beam is directed through the sample under study, and then lenses are used to image the beam exiting the sample onto a CCD camera. Before reaching the camera, the probe beam passes through a shearing plate, which has two diffraction gratings holographically written into it. The two gratings have slightly different spatial frequencies and therefore the first order diffracted beams from each grating propagate at slightly different angles. In this way, two copies of the wave front are created; these are slightly tilted with respect to each other and pick up an increasing lateral separation (shear) as they propagate. These two beams then interfere with each other on the CCD. If the initially plane phase fronts of the collimated beam have passed through the sample undistorted then straight interference fringes will be observed, with a spatial frequency related to the tilt between the sheared copies. If, however, the sample has any focussing or defocussing effect on the probe beam, then the phase fronts will be curved and this will manifest as distortions in the fringe pattern.

A Fourier transform technique is used to analyse the fringes [34]. The tilt between the phase fronts leads to straight fringes in the case of plane phase fronts. By taking the Fourier transform of the fringe pattern, filtering out the spatial frequency of the

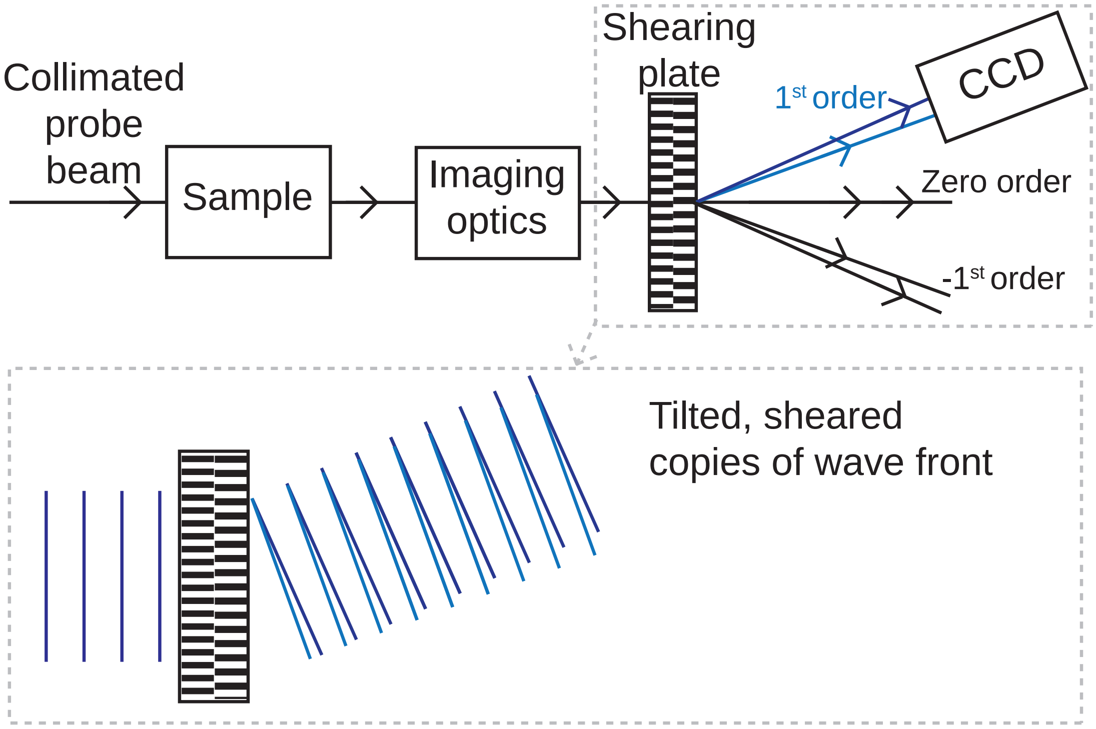

**Figure 3.2:** Schematic of lateral shearing interferometry.

fringes and then taking the inverse Fourier transform, it becomes possible to calculate the difference in phase between the phase front and its laterally-shifted duplicate, as indicated in Figure 3.3. With knowledge of the shearing distance, which can be calculated from the specification of the shearing plate and the distance between the plate and the CCD, we can then calculate the spatial derivative of the phase front. Lateral shearing interferometry is therefore a differential technique. When an initially collimated beam passes through a spherical lens, it acquires a parabolic phase front, and therefore the spatial derivative is linear. The strength of the lens can be obtained from the gradient of the derivative.

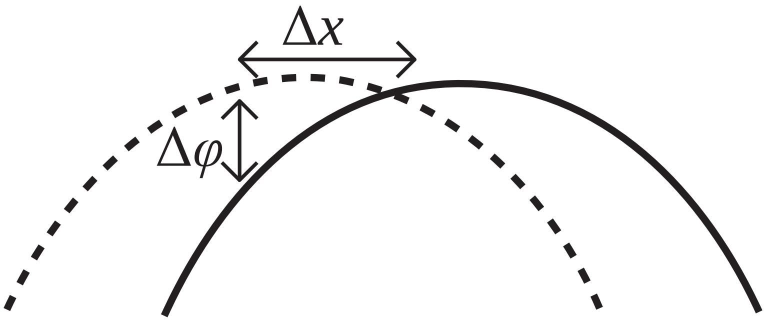

**Figure 3.3:** Lateral shearing interferometry measures the derivative of the phase front of the probe beam by comparing it to a laterally-shifted copy of itself. $\Delta\phi$ is the difference in phase, and $\Delta x$ is the lateral separation of the wavefronts (the shearing distance).

## 3.4 $Nd:YVO_4$ disk laser operating at 1064 nm

In order to build longer and more flexible cavities, the Raman lasers described in the rest of this thesis were constructed using $Nd:YVO_4$ disks bonded to diamond heatspreaders as the laser gain media. The design and operating principles of this style of disk laser were presented in Section 1.5. This disk geometry was chosen because the relatively weak thermal lens enabled the construction of a longer cavity, which in the context of the lateral shearing interferometry made it possible to access the laser and Raman crystals separately. The performance of the disk laser operating at 1064 nm will be described in this section, while the design of the Raman laser and the lateral shearing interferometry experiment itself will be described in the next section.

A 3 mm × 3 mm × 0.5 mm piece of a-cut, 1 at.% $Nd:YVO_4$ was capillary bonded [35] to a 0.5 mm thick, 4 mm diameter CVD-grown single crystal diamond heatspreader. The vanadate-diamond unit was sandwiched between sheets of indium foil and held in a water-cooled brass mount. There was a hole in the sheet of indium foil in front of the diamond heatspreader to permit passage of the pump and cavity beams. The rear surface of the $Nd:YVO_4$ crystal had a coating that was highly reflecting (HR) at 1064 nm and 1180 nm, while the front surface of the diamond heatspreader had an anti-reflection coating for 1064 nm and 1180 nm. (Strictly, the coating on the diamond was specified for 1240 nm, it had a reflectivity of approximately 1 % at 1180 nm. This issue is dealt with in the following section.)

The disk laser was pumped with light at 808 nm from a fibre-coupled diode laser (fibre core diameter = 100 µm, numerical aperture = 0.22) was focussed to a 290 µm radius spot in the $Nd:YVO_4$. The laser cavity design is shown in Figure 3.4. ABCD matrix modelling of the cavity predicts a cold cavity $TEM_{00}$ mode radius of 220 µm in the $Nd:YVO_4$ disk. The power transfer of the laser is shown in Figure 3.5. A maximum output power of 5.1 W at 1064 nm was obtained for an incident pump power of 12.9 W.

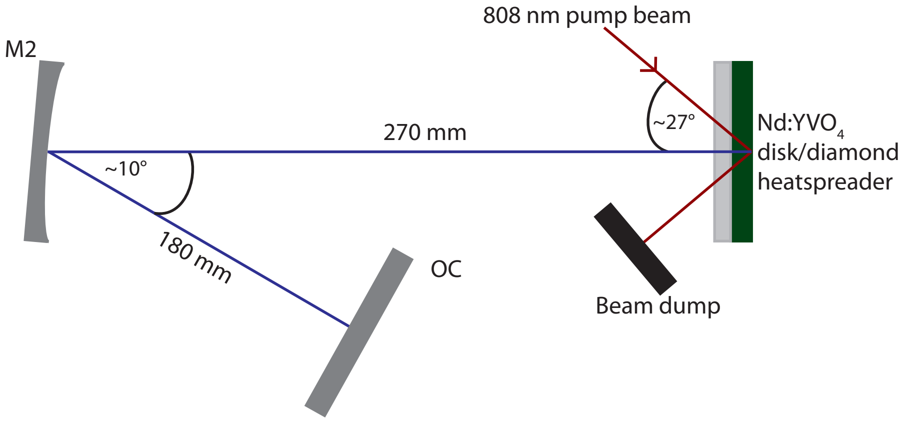

**Figure 3.4:** Cavity design for testing baseline performance of $Nd:YVO_4$ disk laser at 1064 nm. M2 was a concave mirror with radius of curvature 250 mm, coated to be highly reflecting at 1064 nm. OC was a plane output coupler which had a transmission of 9.1 % at 1064 nm.

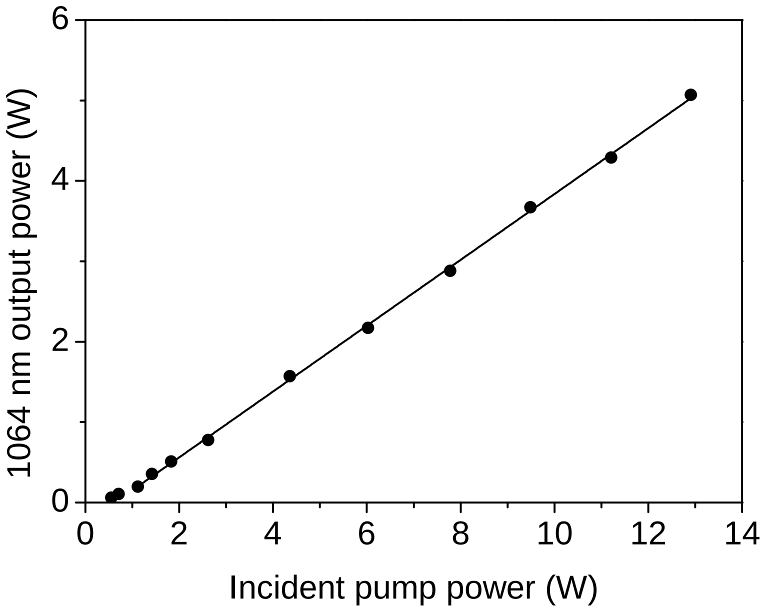

**Figure 3.5:** Power transfer for disk laser operating at fundamental wavelength of 1064 nm.

The slope efficiency of 41 % with respect to incident power compares favourably with the 39 % slope efficiency achieved by Millar *et al* for a very similar laser [36]. The pump power was limited to 12.9 W at first to avoid any risk of crystal fracture during the early stages of the work. Measurements of the absorbed pump power will be described in the next section. The $M^2$ parameter of the output beam was measured to be 2.0 using a Coherent Beam Master.

The work described so far was performed at the University of Strathclyde during the first year of the PhD project. At the end of the first year, the work was transferred to Macquarie University. The Nd:YVO$_4$/diamond unit was transported to Macquarie University and used as the laser gain crystal in the Raman laser experiments that will now be described.

## 3.5 Measurement of thermal lens in barium tungstate

### 3.5.1 Design of Raman laser cavity

A Nd:YVO$_4$-disk/BaWO$_4$-rod Raman laser cavity was designed to enable measurements to be made of the thermal lens in the BaWO$_4$ using lateral shearing interferometry.

The disk laser was pumped using an 808 nm fibre-coupled laser diode (fibre core diameter = 100 µm, numerical aperture = 0.22). To minimise the unabsorbed pump light exiting the disk, a polariser and half-wave plate were placed in the pump beam, such that up to 14 W of 808 nm light polarised parallel to the c-axis of the Nd:YVO$_4$ crystal was incident on the vanadate-diamond unit. (The c-axis of the Nd:YVO$_4$ crystal was oriented vertically.) The unabsorbed pump power reflected from the Nd:YVO$_4$/diamond unit was measured under laser conditions. It was found that approximately 88 % of the pump power incident on the Nd:YVO$_4$/diamond unit was absorbed in the Nd:YVO$_4$ disk. This led to an absorbed pump power of up to 12.2 W. The pump spot radius was 180 µm.

An a-cut 4 mm × 4 mm × 25 mm BaWO$_4$ crystal, grown at the State Key Laboratory of Crystal Materials, Shandong University, China, was wrapped in indium foil and placed in a water-cooled copper mount with the a-axis oriented vertically.

The laser cavity and probe beam optics are shown in Figure 3.6. (Note that the transmission/reflectivity curves for the mirrors and crystals used in the Raman lasers presented in this thesis are reproduced in Appendix A.) The initial intention was to use lateral shearing interferometry to measure both the lens in the BaWO$_4$ and that in the Nd:YVO$_4$. Ultimately the latter experiment was unsuccessful (for reasons discussed below). It was with this goal in mind that a z-fold resonator design was chosen, permitting access for the probe beam to both crystals without any intervening curved optics. (The phase front curvature introduced by propagation through such elements would have complicated the analysis of the interferograms.) The only curved mirror in the cavity was M3, which was concave with a radius of curvature of 100 mm. ABCD matrix modelling of the cavity predicts length-averaged 1064 nm TEM$_{00}$ mode radii of 220 µm and 80 µm in the Nd:YVO$_4$ and BaWO$_4$ crystals respectively for cold cavity conditions. Mirrors M2 and M3 had coatings which were highly reflecting (HR) at 1064 nm and 1180 nm, while the output coupler, OC, was HR at 1064 nm but had a transmission of 0.4 % at 1180 nm. Both surfaces of the BaWO$_4$ crystal were anti-reflection (AR) coated at 1064 nm and 1180 nm, but the diamond heatspreader AR coating was specified for 1064 nm and 1240 nm. It had a reflectivity of ∼ 1 % at 1180 nm. This necessitated the use of a coupled cavity configuration to avoid the Stokes field

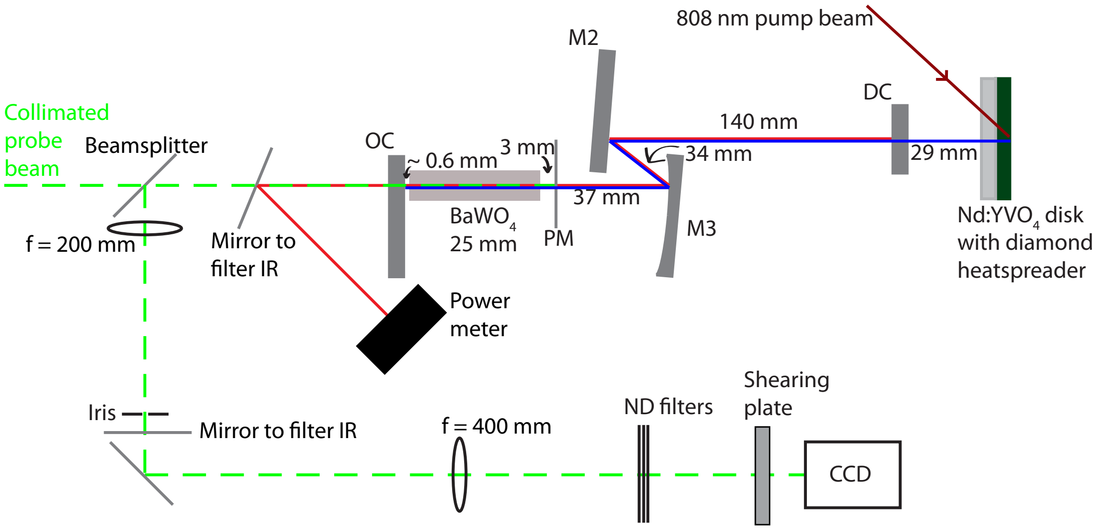

**Figure 3.6:** Experimental set-up for the measurement of the thermal lens in the BaWO$_4$ crystal. Cavity optic separations are shown in mm.

experiencing detrimental losses at the diamond surface. Therefore a dichroic mirror, DC, was used to complete the Stokes field cavity in front of the vanadate-diamond unit.

### 3.5.2 Lateral shearing interferometry set-up

A 532 nm laser (Innolight $\mu$flare) used to generate the probe beam for the lateral shearing interferometry. This probe beam was polarised parallel to the fundamental and Stokes cavity fields, that is parallel to the [vertical] a-axis of the $BaWO_4$ crystal. To measure the thermal lens in the $BaWO_4$, the collimated probe beam was passed through the plane output coupler, OC, and then double-passed through the $BaWO_4$ crystal via a dichroic probe mirror, PM, which reflected visible light but was highly transmissive for the infrared cavity fields. This double-pass configuration was used so as to avoid passing the probe beam through the curved mirror M3. Outside of the laser cavity, a beamsplitter was used to separate the incoming and outgoing probe beams. After passing through the $BaWO_4$, the distorted probe beam was imaged onto the CCD (Cohu 4800) using lenses of 200 and 400 mm focal length to give a magnification factor of 2. This magnification was chosen so that the image of the near surface of the $BaWO_4$ crystal filled most of the area of the CCD sensor. The probe beam passed through the shear plate between the second imaging lens and the CCD. The gratings in the shear plate had a spatial frequency of fringes of $\sim 4\,\mathrm{line\,mm^{-1}}$, and a diffraction efficiency $\sim 5\,\%$. By rotating the shear plate through 90°, the focussing power of the thermal lens in the horizontal and vertical planes could be measured. (When rotating the shear plate, the CCD was also rotated by 90° to avoid having to modify the analysis to account for the camera's rectangular pixels.)

Multiple reflections were observed due to the large number of surfaces encountered by the probe beam. An iris was placed between the lenses to select the beam that had made the double pass through the $BaWO_4$ crystal. It was also important to filter out all the infrared Stokes radiation exiting the cavity so as to protect the CCD. An infrared HR mirror, which transmitted the visible probe beam, was used to reflect the Stokes beam on to a power meter, thus protecting the CCD and making it possible to monitor the output power of the laser throughout the experiment. A second infrared HR mirror was placed in the path of the probe beam to ensure no infrared radiation would interfere with the measurement. Finally, neutral density filters were used in the probe beam to avoid saturation of the CCD.

### 3.5.3 Raman laser performance

When the laser was optimised without the intracavity probe mirror, PM, in place, a maximum output power of 1.05 W at 1180 nm was obtained for an absorbed diode laser pump power of 11.4 W, corresponding to a diode-Stokes conversion efficiency of 9.2 %. The Raman threshold was around 1.7 W of absorbed pump power. The insertion of PM increased the cavity losses and reduced the maximum output power to 0.67 W,

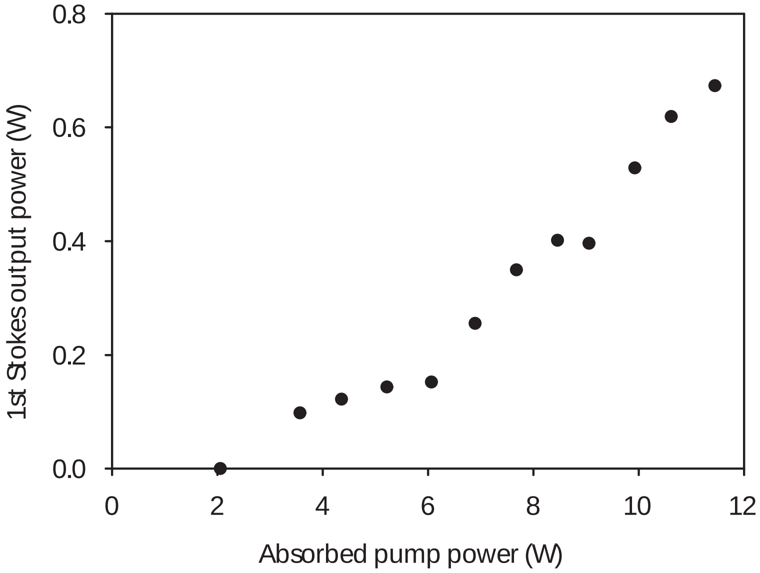

**Figure 3.7:** Raman laser power transfer with probe mirror (PM) in cavity.

corresponding to a diode-Stokes conversion efficiency of 5.9 %. The threshold increased to 2.1 W. With PM in place the beam quality $M^2$ factor of the output Stokes radiation was 1.5 in both planes, and based on this the length-averaged Stokes mode radius in the $BaWO_4$ crystal was estimated to be 98 µm (that is, the $TEM_{00}$ mode radius multiplied by $M$). Figure 3.7 shows a sample power transfer with the PM in place in the cavity.

### 3.5.4 Thermal lens measurements

Interferograms were recorded for zero pump power and for various pump powers above the Raman threshold. At each pump power the Stokes output power was also noted. This was done separately for the horizontal and vertical planes, rotating the shear plate and CCD as described above. Interferograms are shown for both planes in Figure 3.8, for maximum absorbed pump power (11.4 W) and for the reference case (zero pump power). The fringes were analysed as described above, using a fitting region of 300 µm diameter. The shape of the distortion of the fringes indicated that the thermal lens was negative (ie a diverging lens) and that the lens in the horizontal plane was much stronger than that in the vertical plane (as can be seen in Figure 3.8(c), the distortion in the vertical plane is very weak). The strength of the lens in each plane is plotted against the Stokes output power in Figure 3.9.

An uncertainty of ±5 % in the strength of the lens is estimated for the thermal lens strengths measured in the horizontal plane, primarily due to uncertainties in the fringe analysis process. (Note that in order to calibrate for the magnification of the imaging system, measurements were made of the strength of bulk lenses placed in a probe beam path equivalent to that taken through the $BaWO_4$. Bulk lenses of focal length 500 mm and 1000 mm were used as the calibration samples.) The very weak fringe distortions observed in the vertical plane led to considerably larger uncertainties, perhaps as large

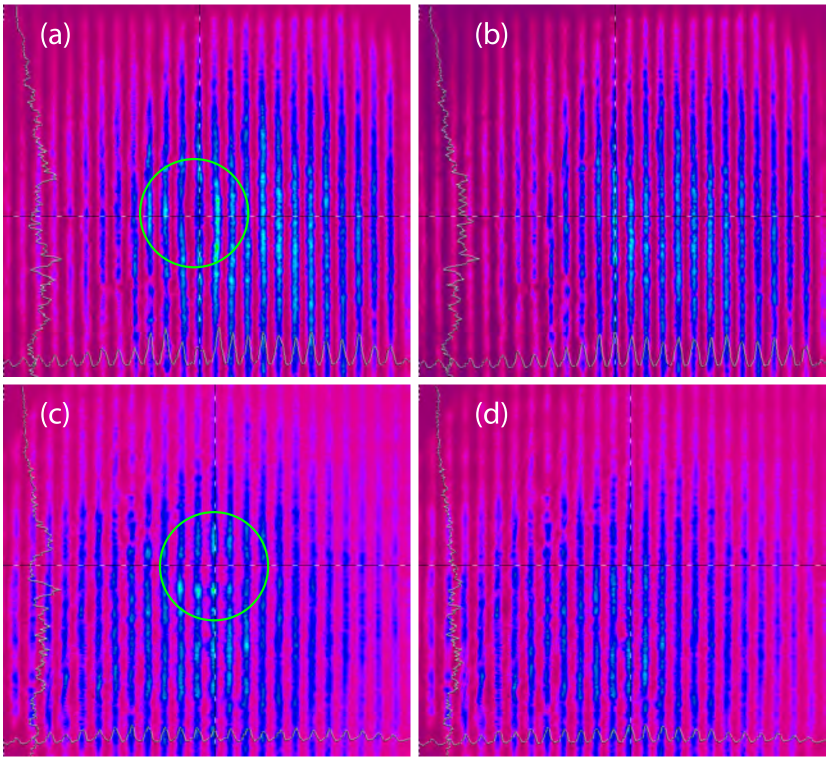

**Figure 3.8:** Lateral shearing interferograms for (a) horizontal plane, maximum power (11.45 W absorbed pump power, 0.67 W Stokes output power); (b) horizontal plane, references fringes (pump off); (c) vertical plane, maximum power (11.45 W absorbed pump power, 0.56 W Stokes output power  lower than for the horizontal case due to drift in laser performance between experiments); (d) vertical plane, reference fringes (pump off).

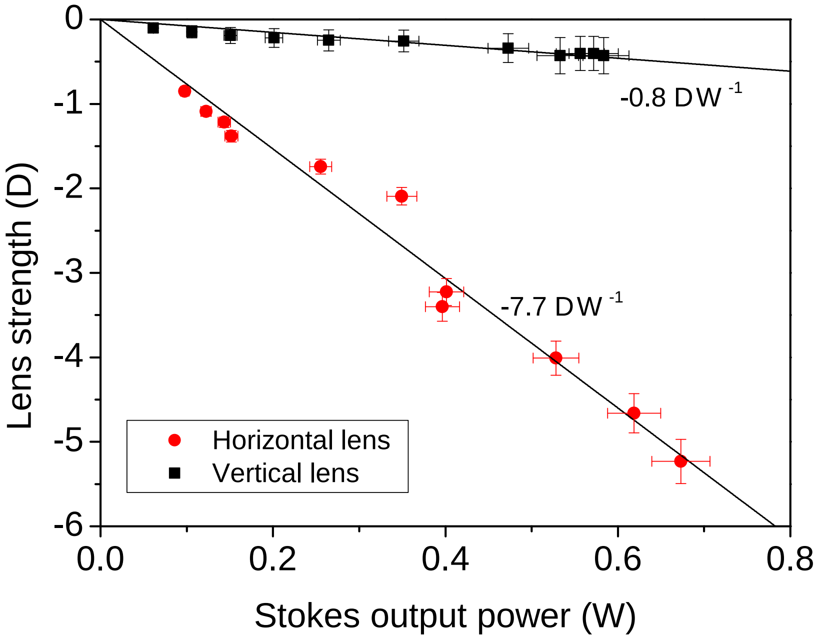

**Figure 3.9:** Strength of thermal lens in $BaWO_4$ in the horizontal and vertical planes (containing the c- and a-axes respectively), plotted as functions of Stokes output power.

as ±50 %.

The data show that the strength of the thermal lens in the $BaWO_4$ crystal is linearly proportional to the output Stokes power. This implies that the area of the Stokes mode in the $BaWO_4$ does not vary significantly with pump power in this cavity design, an observation which is consistent with ABCD modelling of the resonator. The astigmatism of the lens is substantial – in the horizontal direction (the c-axis of the $BaWO_4$) the gradient of the lens strength with respect to the Stokes output power is $(-7.7 \pm 0.3)\,\mathrm{D\,W^{-1}}$, while in the vertical direction it is only $(-0.8 \pm 0.1)\,\mathrm{D\,W^{-1}}$, where the uncertainties in the gradients of the fitted lines were estimated using the technique described in Section 2.3.5. The value for the vertical direction should be treated with some caution since any small undetected systematic error would be much more significant for such weak values of the thermal lens.

### 3.5.5 Thermal properties of $BaWO_4$

The thermal conductivity and thermal expansion coefficient for each axis of $BaWO_4$ are shown in Table 3.2. To the best of the author's knowledge, no measurement of $\mathrm{d}n/\,\mathrm{d}T$ has been made.

**Table 3.2:** Thermal properties of $BaWO_4$ [37].

| | Crystal axis | |
|---|---|---|
| Property | a | c |
| Thermal conductivity/$\mathrm{W\,m^{-1}\,K^{-1}}$ | 2.59 | 2.73 |
| Thermal expansion coefficient/$10^{-6}\,\mathrm{K^{-1}}$ | 11.0 | 35.1 |

As described in Section 3.1, the various contributions to the thermal lens are difficult to disentangle experimentally. In the present case, the marked astigmatism of the thermal lens is particularly noteworthy. A linearly polarised field will experience only a single value of $\mathrm{d}n/\,\mathrm{d}T$ ($\mathrm{d}n_\mathrm{a}/\,\mathrm{d}T$ here), and similarly the end-face bulging component of the thermal lens depends primarily on the thermal expansion coefficient along the propagation axis of the crystal. Therefore, the astigmatism of the thermal lens is likely due to the stress-induced component – the large anisotropy of the thermal expansions coefficients will lead to anisotropic stresses, and the unknown elasto-optic coefficients may also be anisotropic. These results indicate that the stress component of the thermal lens in $BaWO_4$ must be comparable to the $\mathrm{d}n/\,\mathrm{d}T$ and end-face bulging components, and therefore cannot be neglected in this material although it often is in the modelling of the thermal lens in other materials [2, 5].

Given that the sign of the elasto-optic coefficients is unknown, the question remained as to whether $\mathrm{d}n/\,\mathrm{d}T$ in $BaWO_4$ is positive or negative. To determine this, the $BaWO_4$ crystal was placed in one arm of a Rayleigh interferometer and the movement of fringes at 633 nm was examined while the temperature of the crystal was changed using a resistive heater placed beneath the $BaWO_4$. In this experiment, thermal expansion of the crystal always leads to an increase in optical path length with increasing temperature, while the variation of refractive index with temperature can lead to an increase or decrease in the optical path length. The experiment was also performed using a material of known positive $\mathrm{d}n/\mathrm{d}T$ (Nd:$YVO_4$). The direction of movement of the interference fringes indicated that in $BaWO_4$ there was a net decrease in optical path length with increasing temperature, which means that $\mathrm{d}n/\mathrm{d}T$ must be sufficiently large and negative so as to cancel out the positive contribution from thermal expansion. Using the data on thermal expansion in $BaWO_4$ from [37], it was calculated that $\mathrm{d}n/\mathrm{d}T$ must be negative and have a magnitude of at least $9 \times 10^{-6}\,\mathrm{K}^{-1}$. This is a lower limit on the magnitude – the experiment was not precise enough to give an absolute value. It should be noted that this is in the regime for which questions have been raised over the definition, measurement and application of $\mathrm{d}n/\mathrm{d}T$ [13], demonstrating once again the value of making direct, in situ measurements of the thermal lens in a laser under operating conditions.

Attempts to compensate for the $BaWO_4$ lens will be complicated by its strong astigmatism. It is likely that c-cut $BaWO_4$(as opposed to the a-cut material used here) will exhibit lower astigmatism. This would increase the positive bulging component of the thermal lens (which is influenced mainly by the thermal expansion along the axis of propagation) but would lead to more symmetric transverse behaviour, and possibly even a reduction in the maximum thermal lens strength, depending upon the balance of the dn/dT and end face bulging components against the stress component in the new orientation. It is notable that the measurements reported here are in agreement with Sun *et al* with regards to the negative sign of the thermal lens in a-cut $BaWO_4$ [26]. As discussed in Section 3.2.2, Basiev *et al* [28] found a positive lens in their $BaWO_4$, but give no indication of the cut of the crystal they used. It is possible the $BaWO_4$ crystal in that experiment was c-cut.

## 3.6 Finite element modelling of thermal lens in Nd:$YVO_4$ disk

Attempts were made to use lateral shearing interferometry to measure the thermal lens in the Nd:$YVO_4$ disk, but these were ultimately unsuccessful. While it is certainly possible in principle to do this, difficulties arose due to the multiple reflections from the vanadate-diamond unit. Therefore, numerical modelling has been used to obtain some indication of the strength of the lens in the disk. The simulations for the 180 µm pump spot radius case (ie the case for the laser presented in this chapter) were performed by Dr Alan Kemp of the University of Strathclyde. Calculations for the larger pump spots used in later chapters are also presented here – these were performed by the author, who also adapted the simulation to account for the double-pass of the pump beam in

**Table 3.3:** Materials properties for Nd:YVO$_4$ (a/c-axis) and diamond used for FEA simulations.

| Material | Thermal conductivity /W m$^{-1}$ K$^{-1}$ | Thermal expansion coefficient /10$^{-6}$ K$^{-1}$ | Young's modulus /GPa | Poisson ratio |
|---|---|---|---|---|
| Nd:YVO$_4$ | 5.5/6.5 [18] | 4.4/11.4 [38] | 133 [38] | 0.33 [38] |
| Diamond | 2000 [39] | 1 [39] | 1100 [39] | 0.2 [40] |

those systems (described in Section 4.4.2).

Commercial finite element analysis (FEA) software (Comsol Multiphysics) was used to model the flow of heat and consequent temperature distribution and thermal expansion in the Nd:YVO$_4$/diamond unit. In a finite element analysis, the object of interest is divided up into a mesh of small, discrete volumes. The flow of heat between these volumes (the elements) and the change in the temperature and dimensions of each volume is calculated and iterated until a self-consistent steady state solution is found. The focal length of the $\mathrm{d}n/\mathrm{d}T$ component of the thermal lens and the radius of curvature of the deformed rear mirror can then be calculated from the temperature distribution and the deformation of the Nd:YVO$_4$ disk. The material properties used in the simulations are listed in Table 3.3.

An axially symmetric model of the Nd:YVO$_4$/diamond unit and brass mount was used to reduce the computing resources required. The values of the thermal conductivity and thermal expansion coefficient for the a-cut Nd:YVO$_4$ crystal were averaged to obtain a single value for the transverse direction for use in the axially symmetric model. Comparison of axi-symmetric and full 3D models of a simpler structure suggest that the error introduced by the symmetry approximation is $< 5\,\%$ for the focal length of the $\mathrm{d}n/\mathrm{d}T$ component of the thermal lens and $< 15\,\%$ for the radius of curvature of the end face [1].

The FEA modelling was carried out for pump spot radii of 180 µm, 300 µm and 400 µm, corresponding to the pump spots used in the experiments reported in this and the following chapter. A Gaussian transverse profile for the pump beam was assumed. In the case of the 300 µm and 400 µm pump spots, the doping of the Nd:YVO$_4$ disk was 0.5 at.% and a double-pass pump geometry was use to match the experiments described in the next chapter - the effect of theses changes on the axial pump distribution was accounted for in the FEA model. The fractional thermal loading coefficient (ie the fraction of the absorbed pump power converted to heat) was taken to be 0.28 for 1 at.% Nd:YVO$_4$ and 0.24 for 0.5 at.% Nd:YVO$_4$ [2]. In each case, the modelling was performed for several pump powers. A sample plot of the output of the FEA modelling is shown in Figure 3.10, showing the temperature distribution and the deformation (magnified 250 times for clarity) for the case of a 300 µm radius pump spot and 43.6 W absorbed pump power.

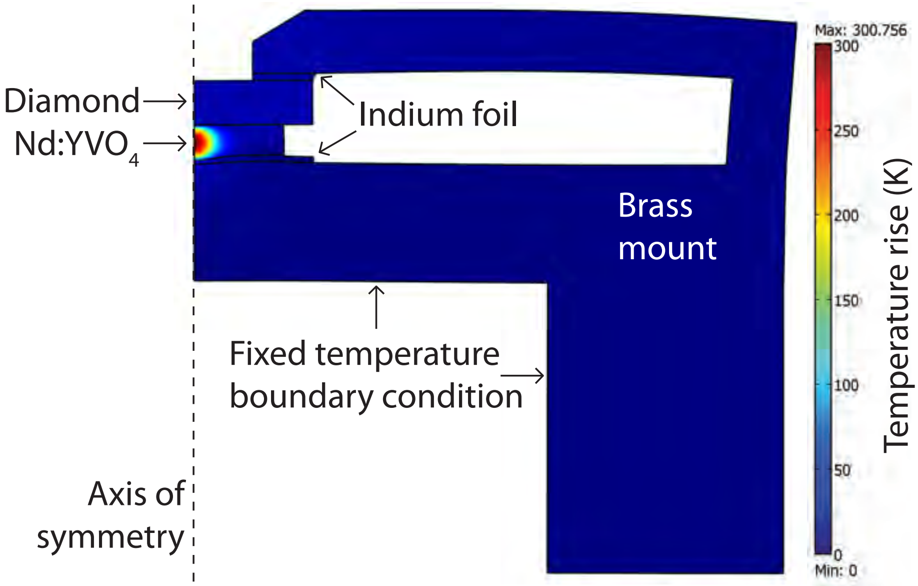

**Figure 3.10:** Sample surface plot of the results of FEA modelling for a 300 µm pump spot radius and an absorbed pump power of 43.6 W. The Nd:YVO$_4$ disk is 0.5 mm thick and the diamond heatspreader is 0.75 mm thick. The distortion is magnified by a factor of 250 to make it visible.

The optical effect of the temperature distribution and the deformation must next be determined. The $\mathrm{d}n/\mathrm{d}T$ component of the thermal lens can be determined as follows. The phase change associated with a spherical lens of focal length $f$ is given by [9]

$$\Delta\phi(r) = \frac{kr^2}{2f} \tag{3.4}$$

where $k$ is the wavenumber and $r$ is the radial (transverse) coordinate. The phase change caused by propagation through the disk is given by

$$\Delta\phi(r) = \int_0^t k\Delta n(r,z)\,\mathrm{d}z = k\frac{\mathrm{d}n}{\mathrm{d}T}\int_0^t \Delta T(r,z)\,\mathrm{d}z \tag{3.5}$$

where $\Delta T(r,z)$ is the temperature rise in the crystal and t is the thickness of the crystal [9]. Therefore, if it is assumed that $\int_0^t \Delta T(r,z)\,\mathrm{d}z$ is quadratic in $r$, then the focal length of the thermal lens is

$$f = \frac{r^2}{2\,\mathrm{d}n/\mathrm{d}T\int_0^t \Delta T(r,z)\,\mathrm{d}z}. \tag{3.6}$$

As an example, the integrated temperature change ($\int_0^t \Delta T(r,z)\,\mathrm{d}z$) is plotted as a function of $r^2$ in Figure 3.11 for the case of a 300 µm radius pump spot and 43.6 W absorbed pump power. Note that the y-axis has been shifted such that the graph passes through the origin for visual clarity - the temperature change is actually positive across the whole crystal and highest at the centre. It can be seen that towards the

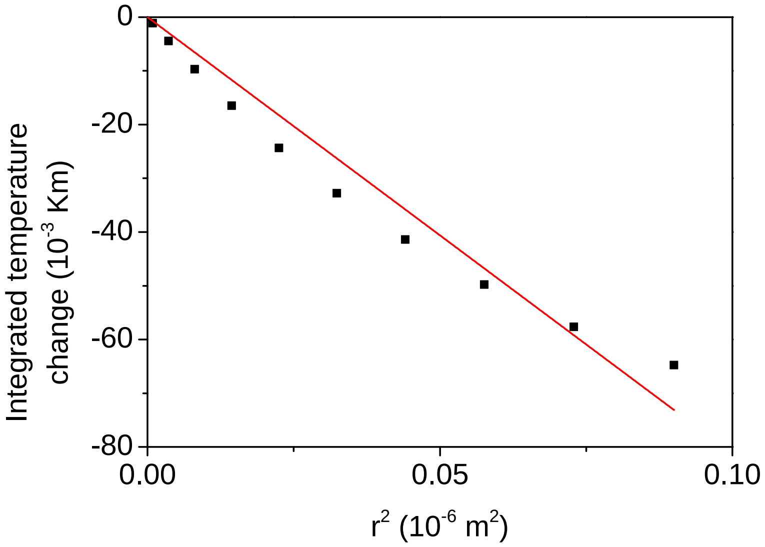

**Figure 3.11:** Sample plot of the integrated temperature change as a function of the square of the radial coordinate, from which the $\mathrm{d}n/\mathrm{d}T$ component of the thermal lens can be calculated. The linear fit is applied over the pump spot radius, in this example 300 µm. The absorbed pump power was 43.6 W for the case shown.

edges of the pump spot, the temperature profile, and hence the phase change, is not purely quadratic but contains higher order aberrations as expected for a Gaussian pump intensity distribution [5]. As a first approximation, a linear fit has been calculated over the pump spot radius, ignoring these aberrations. From the gradient of this line, the focal length of the $\mathrm{d}n/\mathrm{d}T$ component of the thermal lens was calculated using Equation 3.6.

The radius of curvature of the deformed rear mirror on the Nd:$YVO_4$ disk can be calculated from the displacement calculated by the FEA modelling. If this displacement, $\delta$, is small close to the centre of the distortion, then the radius of curvature can be calculated by considering a circle as shown in Figure 3.12. The radius of curvature, $R$, the radial coordinate, $r$, and the displacement, $\delta$, are related as follows:

$$R^2 = r^2 + (R - \delta)^2 \tag{3.7}$$

For small values of $\delta$, this reduces to

$$\delta = \frac{r^2}{2R} \tag{3.8}$$

and so the radius of curvature can be calculated from the gradient of a plot of $\delta$ against $r^2$. One such plot is shown in Figure 3.13 for the case of a 300 µm radius pump spot and 43.6 W absorbed pump power. Again, the thermally induced-distortion is non-quadratic towards the edges of the pumped region, but these distortions are neglected here.

The results of the FEA modelling are shown in Figure 3.14. Note that for the

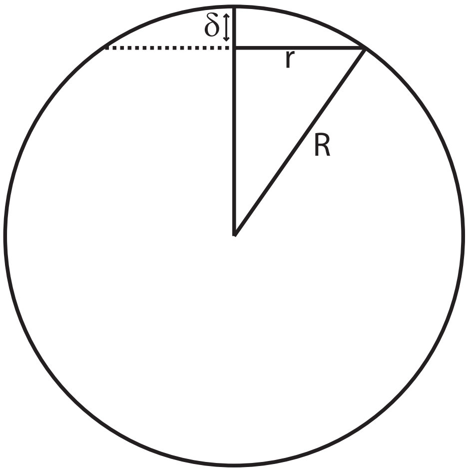

**Figure 3.12:** Geometry for determining radius of curvature of end mirror from thermally-induced distortion.

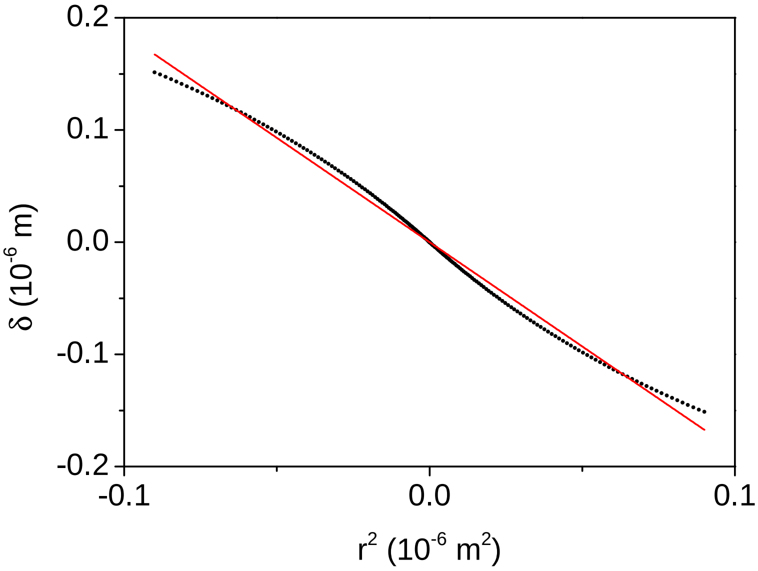

**Figure 3.13:** Sample plot of distortion as a function of the square of the radial coordinate, from which the radius of curvature of the end mirror can be calculated. The linear fit is applied over the pump spot radius, in this example 300 µm. The absorbed pump power was 43.6 W for the case shown.

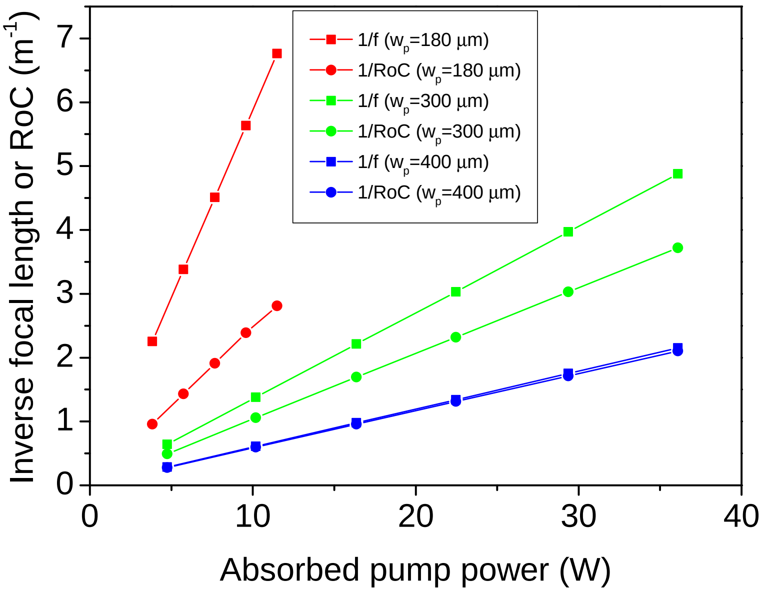

**Figure 3.14:** Inverse focal lengths of the $\mathrm{d}n/\,\mathrm{d}T$ component of the thermal lens (squares) and inverse radii of curvature (RoC) of the deformed disk (circles) for pump spot radii of 180 µm (red symbols), 300 µm (green symbols) and 400 µm (blue symbols).

case of a 180 µm pump spot radius, the thermal lens strengths were only modelled up to an absorbed pump power of 11.5 W in line with the experiments described in this chapter. Increasing the pump spot size leads to significantly weaker thermal lenses. For small pump spots, the $\mathrm{d}n/\,\mathrm{d}T$ component of the thermal lens is stronger than the end-face deformation component, but as the pump spot size increases, this difference also decreases as the system moves from rod-like to disk-like thermal behaviour.

The focal length of the $\mathrm{d}n/\,\mathrm{d}T$ component of the thermal lens, $f$, and the radius of curvature of the deformed end mirror, $R$, are given by the following equations for each pump spot radius, $w_\mathrm{P}$, in terms of the absorbed pump power, $P_\mathrm{abs}$:

$$\begin{aligned} w_\mathrm{P} = 180\,\mu\mathrm{m}: \quad & f = \tfrac{1.7}{P_\mathrm{abs}} \quad R = \tfrac{4.0}{P_\mathrm{abs}} \\ w_\mathrm{P} = 300\,\mu\mathrm{m}: \quad & f = \tfrac{7.4}{P_\mathrm{abs}} \quad R = \tfrac{9.7}{P_\mathrm{abs}} \\ w_\mathrm{P} = 400\,\mu\mathrm{m}: \quad & f = \tfrac{16.8}{P_\mathrm{abs}} \quad R = \tfrac{17.1}{P_\mathrm{abs}} \end{aligned} \tag{3.9}$$

Note that in the above equations, the absorbed pump power should be given in units of watts, to obtain the focal length or radius of curvature in units of metres. Note also that both $f$ and $R$ are positive, meaning that the $\mathrm{d}n/\,\mathrm{d}T$ component of the thermal lens is a converging lens, and that the rear mirror on the disk becomes concave and hence also has a positive focussing effect.

The two components of the thermal lens in the Nd:YVO$_4$ disk were included separately in the ABCD matrix modelling of the cavity described in the next chapter. However, it is useful to combine them into a single number for intuitive comparison to the thermal lens in the BaWO$_4$ crystal. Since the disk is thin, the two components can

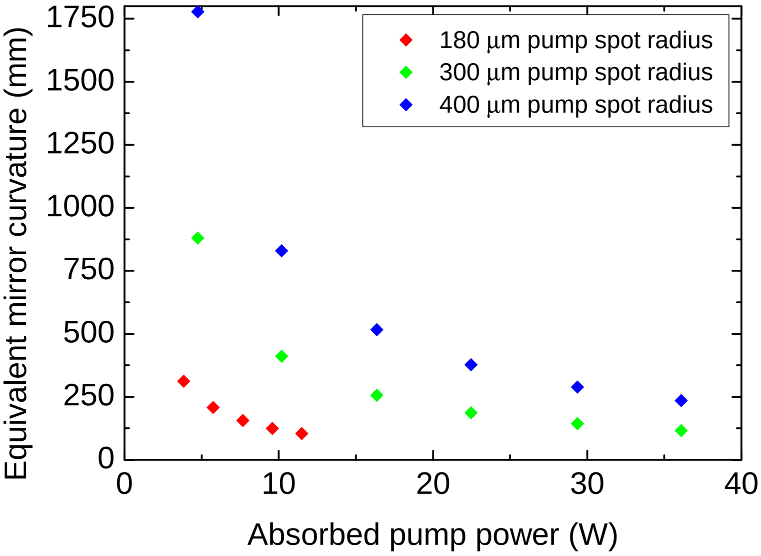

**Figure 3.15:** An equivalent radius of curvature for the end mirror, taking account of both the bulging and the $dn/dT$ components of the thermal lens for pump spot radii of 180 µm (red diamonds), 300 µm (green diamonds) and 400 µm (blue diamonds).

be combined into a single effective radius of curvature for the end mirror on the back of the disk. This equivalent end mirror curvature is plotted as a function of pump power for the three pump spot radii in Figure 3.15. The relative strengths of the Nd:$YVO_4$ and $BaWO_4$ thermal lenses are compared in the next section and the implications for cavity design are discussed.

## 3.7 Conclusions

Lateral shearing interferometric measurements of the thermal lens in a $BaWO_4$ rod in a CW intracavity Raman laser have been presented. The use of a disk geometry for the Nd:$YVO_4$ laser gain crystal made it possible to build a longer Raman laser cavity than is conventional, which in turn made it easier to probe the thermal lens in the $BaWO_4$ Raman crystal. To the best of the author's knowledge these are the first direct, in situ, measurements of the Raman thermal lens in a CW intracavity Raman laser based on separate laser and Raman crystals. The thermal lens in the a-cut $BaWO_4$ was found to be negative and highly astigmatic. Possible reasons for this astigmatism were inferred from the known material properties of $BaWO_4$.

Attempts to measure the thermal lens in the Nd:$YVO_4$ disk using lateral shearing interferometry were frustrated by multiple reflections from the Nd:$YVO_4$/diamond unit. A finite element approach was used to model the heat flow and thermal expansion in the disk and from this the strength of the thermal lens in the disk was estimated.

It is instructive to compare the thermal lenses in the Nd:$YVO_4$ disk and the $BaWO_4$ crystal. If the laser system presented in this chapter was operated at an absorbed pump power of 11.4 W, then the calculated focal length of the thermal lens resulting from thermally induced changes in refractive index would be 149 mm and the radius of curvature of the rear mirror on the Nd:$YVO_4$ caused by thermal expansion would be 351 mm. These two effects can be combined into a single equivalent radius of curvature for the end mirror of 105 mm. The focal length of the corresponding lens in the $BaWO_4$ crystal (based on the observed output power of 0.67 W) would be $-194$ mm in the plane parallel to the c-axis and $-1866$ mm in the plane parallel to the a-axis. Therefore, the lens in the plane of the c-axis of the $BaWO_4$ is comparable to that in the Nd:$YVO_4$ disk and it could be even more significant if a higher conversion efficiency were obtained (since generating a higher Stokes power for the same pump power would result in a stronger thermal lens in the $BaWO_4$ crystal while the thermal lens in the Nd:$YVO_4$ disk would remain the same). Therefore, both lenses need to be taken into account when designing such laser cavities. It is noteworthy that the thermal lens in $BaWO_4$ has a negative focal length, while many common laser gain materials develop postive thermal lens (eg Nd-doped $YVO_4$, $GdVO_4$ and YAG); the impact of this on resonator behaviour will be discussed in Chapter 4. As it happens a number of other common Raman crystals also develop negative thermal lenses, for example, $LiIO_3$ [21], $Ba(NO_3)_2$ [21], and, depending on the crystal cut and orientation, $KGd(WO_4)_2$ [41]. $CaWO_4$ has also been calculated to have a negative thermal lens [21]. This is, however, by no means a general rule - $YVO_4$ and $GdVO_4$ would be prominent examples of Raman crystals that develop positive thermal lenses.

The thermal lenses in both crystals in the laser described here have focal lengths similar to the total cavity length ($\sim 240$ mm), and these focal lengths will become even shorter if the laser is operated at higher pump and output power levels. The FEA modelling indicates that increasing the pump spot size will significantly reduce the thermal lens in the Nd:$YVO_4$ disk, and experiments involving larger pump spots will be presented in the next chapter. Carefully designed cavities will have to be employed to cope with the thermal lens in the $BaWO_4$ crystal. Again, work on such cavity designs will be presented in the next chapter.

# Bibliography

[1] G. M. Bonner, H. M. Pask, A. J. Lee, A. J. Kemp, J. Wang, H. Zhang, and T. Omatsu, "Measurement of thermal lensing in a CW $BaWO_4$ intracavity Raman laser," *Optics Express*, vol. 20, pp. 9810–9818, Apr 2012.

[2] W. Koechner, *Solid-State Laser Engineering.* Springer, 6th ed., 2006.

[3] D. Brown, "Heat, fluorescence, and stimulated-emission power densities and fractions in Nd:YAG," *IEEE Journal of Quantum Electronics*, vol. 34, pp. 560–572, Mar 1998.

[4] Y. Guyot, H. Manaa, J. Y. Rivoire, R. Moncorgé, N. Garnier, E. Descroix, M. Bon, and P. Laporte, "Excited-state-absorption and upconversion studies of $Nd^{3+}$-doped single crystals $Y_3Al_5O_{12}$, $YLiF_4$, and $LaMgAl_{11}O_{19}$," *Physical Review B*, vol. 51, pp. 784–799, Jan 1995.

[5] W. A. Clarkson, "Thermal effects and their mitigation in end-pumped solid-state lasers," *Journal of Physics D - Applied Physics*, vol. 34, no. 16, pp. 2381–2395, 2001.

[6] S. Guy, C. Bonner, D. Shepherd, D. Hanna, A. Tropper, and B. Ferrand, "High-inversion densities in Nd:YAG-upconversion and bleaching," *IEEE Journal of Quantum Electronics*, vol. 34, pp. 900 – 909, May 1998.

[7] T. Fan, "Heat generation in Nd:YAG and Yb:YAG," *IEEE Journal of Quantum Electronics*, vol. 29, pp. 1457–1459, Jun 1993.

[8] A. Sennaroglu, "Experimental Determination of Fractional Thermal Loading in an Operating Diode-Pumped Nd:$YVO_4$ Minilaser at 1064 nm," *Applied Optics*, vol. 38, pp. 3253–3257, May 1999.

[9] M. E. Innocenzi, H. T. Yura, C. L. Fincher, and R. A. Fields, "Thermal modelling of continuous-wave end-pumped solid-state lasers," *Applied Physics Letters*, vol. 56, no. 19, pp. 1831–1833, 1990.

[10] A. K. Cousins, "Temperature and thermal stress scaling in finite-length end-pumped laser rods," *IEEE Journal of Quantum Electronics*, vol. 28, no. 4, pp. 1057–1069, 1992.

[11] A. Giesen, H. Hugel, A. Voss, K. Wittig, U. Brauch, and H. Opower, "Scalable concept for diode-pumped high-power solid-state lasers," *Applied Physics B*, vol. 58, no. 5, pp. 365–372, 1994.

[12] A. J. Kemp, G. J. Valentine, and D. Burns, "Progress towards high-power, high-brightness neodymium-based thin-disk lasers," *Progress in Quantum Electronics*, vol. 28, no. 6, pp. 305–344, 2004.

[13] S. Chénais, F. Druron, S. Forget, F. Balembois, and P. Georges, "On thermal effects in solid-state lasers: The case of ytterbium-doped materials," *Progress in Quantum Electronics*, vol. 30, no. 4, pp. 89–153, 2006.

[14] O. Svelto, *Principles of Lasers.* Plenum Press, 4th ed., 1998.

[15] S. Biswal, S. P. O'Connor, and S. R. Bowman, "Thermo-optical parameters measured in ytterbium-doped potassium gadolinium tungstate," *Applied Optics*, vol. 44, no. 15, pp. 3093–3097, 2005.

[16] V. V. Filippov, N. V. Kuleshov, and I. T. Bodnar, "Negative thermo-optical coefficients and athermal directions in monoclinic $KGd(WO_4)_2$ and $KY(WO_4)_2$ laser host crystals in the visible region," *Applied Physics B*, vol. 87, no. 4, pp. 611–614, 2007.

[17] Y. Sato and T. Taira, "The studies of thermal conductivity in $GdVO_4$, $YVO_4$ and $Y_3Al_5O_{12}$ measured by quasi-one-dimensional flash method," *Optics Express*, vol. 14, no. 22, pp. 10528–10536, 2006.

[18] J. Didierjean, E. Herault, F. Balembois, and P. Georges, "Thermal conductivity measurements of laser crystals by infrared thermography. Application to Nd:doped crystals," *Optics Express*, vol. 16, no. 12, pp. 8995–9010, 2008.

[19] P. Dekker, H. M. Pask, D. J. Spence, and J. A. Piper, "Continuous-wave, intracavity doubled, self-Raman laser operation in Nd:$GdVO_4$ at 586.5 nm," *Optics Express*, vol. 15, no. 11, pp. 7038–7046, 2007.

[20] J. Jakutis-Neto, *Low gain Nd:YLF lasers operating in the quasi-three level transition and in Raman lasers.* PhD thesis, Macquarie University, 2012.

[21] H. M. Pask, "The design and operation of solid-state Raman lasers," *Progress in Quantum Electronics*, vol. 27, no. 1, pp. 3–56, 2003.

[22] A. J. Lee, J. Lin, and H. M. Pask, "Near-infrared and orange-red emission from a continuous-wave, second-Stokes self-Raman Nd:$GdVO_4$ laser," *Optics Letters*, vol. 35, no. 18, pp. 3000–3002, 2010.

[23] A. Kananovich, A. Demidovich, M. Danailov, A. Grabtchikov, and V. Orlovich, "All-solid-state quasi-CW yellow laser with intracavity self-Raman conversion and sum frequency generation," *Laser Physics Letters*, vol. 7, no. 8, pp. 573–578, 2010.

[24] Z. Wang, C. Du, S. Ruan, and L. Zhang, "Thermal lens measurements in a Nd:GdVO$_4$ self-Raman laser," *Optics & Laser Technology*, vol. 42, no. 6, pp. 873–877, 2010.

[25] T. Omatsu, M. Okida, A. Lee, and H. Pask, "Thermal lensing in a diode-end-pumped continuous-wave self-Raman Nd-doped GdVO$_4$ laser," *Applied Physics B: Lasers and Optics*, vol. 108, no. 1, pp. 73–79, 2012. 10.1007/s00340-012-4919-7.

[26] W. J. Sun, Q. P. Wang, Z. J. Liu, X. Y. Zhang, G. T. Wang, F. Bai, W. X. Lan, X. B. Wan, and H. J. Zhang, "An efficient 1103 nm Nd:YAG/BaWO$_4$ Raman laser," *Laser Physics Letters*, vol. 8, no. 7, pp. 512–515, 2011.

[27] S. Fan, X. Zhang, Q. Wang, S. Li, S. Ding, and F. Su, "More precise determination of thermal lens focal length for end-pumped solid-state lasers," *Optics Communications*, vol. 266, no. 2, pp. 620 – 626, 2006.

[28] T. T. Basiev, A. V. Gavrilov, V. V. Osiko, S. N. Smetanin, and A. V. Fedin, "High-average-power SRS conversion of radiation in a BaWO$_4$ crystal," *Quantum Electronics*, vol. 34, no. 7, pp. 649–651, 2004.

[29] M. Shimosegawa, T. Omatsu, A. Hasegawa, M. Tateta, and I. Ogura, "Transient thermal lensing measurement in a laser diode pumped Nd$_x$Y$_{1-x}$Al$_3$(BO$_3$)$_4$ laser using a holographic shearing interferometer," *Optics Communications*, vol. 140, no. 4-6, pp. 237 – 241, 1997.

[30] J. L. Blows, T. Omatsu, J. Dawes, H. Pask, and M. Tateda, "Heat generation in Nd:YVO$_4$ with and without laser action," *IEEE Photonics Technology Letters*, vol. 10, no. 12, pp. 1727–1729, 1998.

[31] J. L. Blows, J. M. Dawes, and T. Omatsu, "Thermal lensing measurements in line-focus end-pumped neodymium yttrium aluminium garnet using holographic lateral shearing interferometry," *Journal of Applied Physics*, vol. 83, no. 6, pp. 2901–2906, 1998.

[32] M. Okida, M. Itoh, T. Yatagai, H. Ogilvy, J. Piper, and T. Omatsu, "Heat generation in Nd doped vanadate crystals with 1.34 $\mu$m laser action," *Optics Express*, vol. 13, no. 13, pp. 4909–4915, 2005.

[33] M. Okida, A. Tonouchi, M. Itoh, T. Yatagai, and T. Omatsu, "Thermal-lens measurement in a side-pumped 1.3 $\mu$m Nd:YVO$_4$ bounce laser," *Optics Communications*, vol. 277, no. 1, pp. 125–129, 2007.

[34] M. Takeda, H. Ina, and S. Kobayashi, “Fourier-transform method of fringe-pattern analysis for computer-based topography and interferometry,” *Journal of the Optical Society of America B*, vol. 72, no. 1, pp. 156–160, 1982.

[35] Z. L. Liau, “Semiconductor wafer bonding via liquid capillarity,” *Applied Physics Letters*, vol. 77, no. 5, pp. 651–653, 2000.

[36] P. Millar, A. J. Kemp, and D. Burns, “Power scaling of Nd:$YVO_4$ and Nd:$GdVO_4$ disk lasers using synthetic diamond as a heat spreader,” *Optics Letters*, vol. 34, no. 6, pp. 782–784, 2009.

[37] D. Ran, H. Xia, S. Sun, Z. Ling, W. Ge, and H. Zhang, “Thermal conductivity of $BaWO_4$ single crystal,” *Materials Science and Engineering: B*, vol. 130, no. 1-3, pp. 206–209, 2006.

[38] X. Peng, A. Asundi, Y. Chen, and Z. Xiong, “Study of the Mechanical Properties of Nd:$YVO_4$ Crystal by use of Laser Interferometry and Finite-Element Analysis,” *Applied Optics*, vol. 40, pp. 1396–1403, Mar 2001.

[39] I. Friel, S. L. Geoghegan, D. J. Twitchen, and G. A. Scarsbrook, “Development of high quality single crystal diamond for novel laser applications,” in *Optics and Photonics for Counterterrorism and Crime Fighting VI and Optical Materials in Defence Systems Technology VII* (C. Lewis, D. Burgess, R. Zamboni, F. Kajzar, and E. M. Heckman, eds.), vol. 7838, p. 783819, SPIE, 2010.

[40] K. E. Spear and J. P. Dismukes, *Synthetic diamond: emerging CVD science and technology.* Wiley-Interscience, 1994.

[41] P. A. Loiko, I. A. Denisov, K. V. Yumashev, N. V. Kuleshov, and A. A. Pavlyuk, “Laser performance and thermal lensing in flashlamp pumped $n_p$- and $n_g$-cut Nd:KGW crystals,” *Applied Physics B*, vol. 100, no. 3, pp. 477–483, 2010.

# Chapter 4

# Managing the thermal lenses

In the previous chapter, experiments and modelling were used to determine the strengths of the thermal lenses in the intracavity Raman laser. In this chapter, work will be presented on increasing the output power of the system by improving the cavity design to better cope with the thermal lenses. It will be shown how the measurements of the thermal lens in $BaWO_4$ crystal and the modelling of the thermal lens in the Nd:$YVO_4$ disk in the previous chapter can be used as initial data for cavity modelling that can then inform the design of the laser. Gradual improvements to the cavity design will be laid out, along with the modelling and experiments that motivated these design changes.

## 4.1 Effect of thermal lenses on a laser cavity

The effect of a thermal lens on a laser cavity was outlined briefly in Section 3.1.2. The mode size and divergence of the cavity field(s) will change as the pump power, and hence the strength of the thermal lens, changes. This will change the overlap between the cavity and pump fields, impacting on the efficiency and transverse mode of the laser. The $g_1$-$g_2$ stability parameters [1] of the cavity also become functions of pump power. In this chapter, cavity modelling will be used to investigate the extent of these effects in intracavity Raman lasers, and the results of the modelling will guide experimental improvements to the cavity design. Aberrations and polarisation effects can also be introduced by the thermal lens, but these are more difficult to quantify and will not be dealt with here.

The phenomena described above become more complex in intracavity Raman lasers because of the thermal lens in the Raman crystal. In a conventional laser with a single gain crystal, the single thermal lens causes the cavity to move along a straight line in the $g_1$-$g_2$ plane as the pump power increases [2]. When there are multiple gain crystals, and hence multiple thermal lenses, in the cavity the situation is more complicated. Driedger *et al* model laser cavities with multiple, identical laser gain rods [3] and find that a laser cavity with two such gain crystals moves along a parabola in the $g_1$-$g_2$

plane, and along a more complicated path when more crystals are used. However, in an intracavity Raman laser, the two crystals are not identical. Not only do the crystals usually have different thermal properties, the processes occurring in each are different such that the two thermal lenses scale differently as the power of the laser is increased. The strength of the thermal lens in the laser gain crystal is proportional to the pump power [4], but the strength of the lens in the Raman crystal is proportional to the Stokes output power [5], and hence is only present above the Raman threshold and thereafter varies in a different manner from the lens in the laser gain crystal. This means that the laser cavity moves along a complex path in the $g_1$-$g_2$ plane, and to determine whether or not a cavity will be stable at a given pump power it is necessary to estimate what the output Stokes power will be at that pump power.

The changes in the mode sizes of the fundamental and Stokes fields are also very important. Not only will the change in the overlap between the pump field and the fundamental field in the laser gain crystal affect the efficiency and transverse mode content of the fundamental field, as in a conventional laser, but the change in overlap between the fundamental and Stokes fields in the Raman crystal will affect the efficiency of the SRS process [6], which in turn will affect the strength of the thermal lens in the Raman crystal, creating a complex feedback loop. The transverse mode content of the Stokes field will also depend on the overlap of the Stokes and fundamental fields. In the case of the coupled cavity configuration used in this work, the set of transverse modes for the fundamental field can potentially be different from that for the Stokes field, creating the potential for more significant mode mismatch between the fundamental and Stokes fields and therefore mode overlap is something that must be taken careful account of when designing such cavities.

In order to model the impact of the thermal lenses on the laser cavity, the measured experimental power transfers were used to generate values of the thermal lens strengths (based on the measurements and modelling presented in Chapter 3) and these were then used as inputs for ABCD cavity modelling to determine the variation of the stability parameters and mode overlap as functions of pump power. The cavity modelling techniques used will now be described.

## 4.2 Approaches to analysing cavity behaviour

The two main criteria for analysing the behaviour of the Raman laser cavities presented in this Chapter were (1) the mode overlap of the fundamental and Stokes fields in the Raman crystal and (2) the optical stability of the resonators. The methods used to calculate these parameters are described below.

### 4.2.1 Determining the fundamental/Stokes mode overlap

The use of a coupled cavity configuration means that the overlap of the fundamental and Stokes modes in the Raman crystal can vary with the diode laser pump power, since the mode radii of the $\mathrm{TEM}_{00}$ and higher order modes of the two cavities may be different and since the fundamental field experiences both thermal lenses, while the Stokes field experiences only the thermal lens in the Raman crystal. The mode overlap influences the transfer of power from the fundamental field to the Stokes field [6] and therefore this variation in overlap as a function of diode laser pump power will affect the performance of the laser.

The $\mathrm{TEM}_{00}$ mode radii in the $\mathrm{BaWO_4}$ crystal were calculated using ABCD cavity modelling software (LASCAD). The thermal lens in the $\mathrm{Nd{:}YVO_4}$ disk was accounted for by placing a mirror immediately behind the disk (to model the effect of the bulging of the disk) and a thin lens at the centre of the disk (to model the $\mathrm{d}n/\mathrm{d}T$ component of the lens). The radius of curvature of the end mirror and the focal length of the lens were determined from the FEA modelling as described in the previous chapter. The thermal lens in the Raman crystal was modelled as a thin lens at the centre of the $\mathrm{BaWO_4}$ crystal, in line with Prof. Omatsu's analysis of the lateral shearing interferometry results. The lens was assigned different focal lengths in the horizontal (tangential) and vertical (sagittal) planes, to account for the astigmatism of the thermal lens. The length-averaged mode radius for each field in the $\mathrm{BaWO_4}$ crystal was approximated as the average of the values of the radius at each end of the crystal. Since there is a focus in the cavity near one end of the $\mathrm{BaWO_4}$ crystal, this method slightly over-estimates the length-averaged mode radius but since it was the ratio of the mode radii that was of interest, it was used as a reasonable first order approximation.

Note that this approach only provides information about the overlap of the $\mathrm{TEM}_{00}$ modes of each field. In reality one or both of the fields may be operating on one or more higher order transverse modes, leading to a larger beam radius. In general, the Stokes field usually has better spatial beam quality than the fundamental field – the "Raman beam clean-up" effect [7].

### 4.2.2 Determining the cavity stability parameters

It can be shown [2] that the single-pass ABCD matrix for a multi-mirror cavity has the same form as that of an equivalent two mirror cavity with stability parameters $(g_1, g_2) = (A, D)$. In this way, the stability parameters of the fundamental and Stokes cavities were calculated from the single-pass ray transfer matrix of each cavity [2].

The ABCD matrices for each element in the cavity were constructed in a MATLAB script, and a set of thermal lens strengths for the two thermal lenses for various pump powers, calculated as above, were passed to the script as an input. For each pump power, the total single-pass ray transfer ABCD matrix was calculated, generating the values of $(g_1, g_2) = (A, D)$ as a function of pump power for each plane of each cavity [2].

The MATLAB script is given in Appendix B.

As mentioned above, Driedger *et al* [3] have analytically modelled the stability parameters as functions of pump power for cavities involving multiple, identical, laser gain crystals. However, here the approach used is to calculate the thermal lens strengths for the laser and Raman crystals based on the experimentally measured pump power and Stokes output power and use these values to determine the path of the cavity through the $g_1$-$g_2$ plane. This approach is particularly well suited to intracavity Raman lasers, since such devices involve two thermal lenses, one of which scales with the pump power and the other of which scales with the output power.

## 4.3 Evaluation of cavities using a 180 µm radius pump spot

### 4.3.1 Summary of cavities

A number of resonator designs have been investigated with the overall goal of optimising the output power and efficiency. The modelling approaches described above were applied to each system to gain insight into the effects of the thermal lenses. The results of this modelling, along with experimental investigations that will be described below, were used to determine the next step in the refinement of the cavity design. This process of design, testing, modelling and re-design of each cavity will now be presented sequentially in this and the following sections. For reference, a summary of the Raman laser cavities tested is given in Table 4.1.

**Table 4.1:** Summary of Raman laser cavities tested in this chapter. Nominal maximum pump powers for the diode pump lasers are given but full pump power was not always used. Pump double-pass geometry will be explained later in the chapter.

| | Pump laser (nominal max power) | Pump spot radius | Pump double-pass | Stokes cavity |
|---|---|---|---|---|
| Cavity 1 | 30 W[†*] | 180 µm | No | 3 mirror |
| Cavity 2 | 30 W[†*] | 180 µm | No | 4 mirror |
| Cavity 3 | 30 W[†] | 300 µm | Yes | 4 mirror |
| Cavity 4 | 90 W[‡] | 300 µm | Yes | 4 mirror |
| Cavity 5 | 90 W[‡] | 400 µm | Yes | 4 mirror |

[†] LIMO30-F100-DL808-EX1320, fibre core ⌀ = 100 µm, NA= 0.22

[‡] LIMO90-F200-DL808, fibre core ⌀ = 200 µm, NA= 0.22

[*] A polariser was placed in the output of this pump laser such that beam was polarised parallel to the c-axis of the Nd:YVO$_4$. Therefore the maximum available pump power was nominally 15 W.

### 4.3.2 Cavity 1: Three mirror Stokes cavity

Cavity 1 was a similar laser cavity to that used in the lateral shearing interferometry experiments, but the flat folding mirror (M3 in Figure 3.6), which was previously used to facilitate easy access to both crystals for the probe beam, was omitted. The layout of Cavity 1 is shown in Figure 4.1. The same crystals were used, and the pump spot radius in the Nd:$YVO_4$ was again 180 µm. ABCD matrix modelling of the cavity indicated that the cold cavity $TEM_{00}$ mode radius of the fundamental field in the tangential (sagittal) plane was 264 µm (300 µm) in the Nd:$YVO_4$ disk and 79.5 µm (79.5 µm) in the $BaWO_4$ crystal. The cold cavity $TEM_{00}$ mode radius of the Stokes field was 84.5 µm (84 µm) in the $BaWO_4$ crystal. The power transfer of this laser is shown in Figure 4.2. An output power of 1.52 W at 1180 nm was obtained for an absorbed diode laser pump power of 10.6 W. The Raman threshold was approximately 1.2 W of absorbed diode pump power and the slope efficiency up to the roll-over point was 16.5 %. The maximum diode-Stokes conversion efficiency, just before the roll-over, was 14.3 %.

To investigate whether the roll-over was caused by the thermal lenses, the pump beam was chopped immediately after the diode laser fibre, using a 50 % duty cycle chopper at 500 Hz. It can be seen in Figure 4.2 that the laser does not roll-over in the quasi-continuous wave (QCW) case, suggesting that the roll-over is indeed a thermal problem.

Here it has been assumed that the on-time periods were sufficiently short such that the temperature profile in each crystal did not have time to build up to a steady state and hence the strengths of the thermal lenses were significantly reduced when the chopper was used. To justify this, the thermal time constants of the Nd:$YVO_4$ disk and the $BaWO_4$ crystal were calculated using the approach given by Koechner [4], who

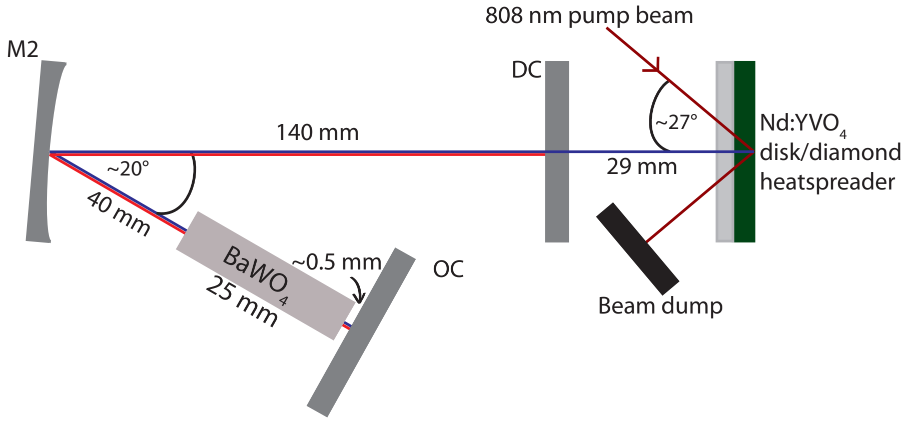

**Figure 4.1:** Cavity 1 – three mirror coupled cavity laser design. DC was a plane dichroic mirror, highly transmissive at 1064 nm and highly reflective at 1180 nm. M2 was a concave mirror with radius of curvature 100 mm and was highly reflecting at both wavelengths. OC was a plane output coupler, highly reflecting at 1064 nm but with a transmission of 0.4 % at 1180 nm.

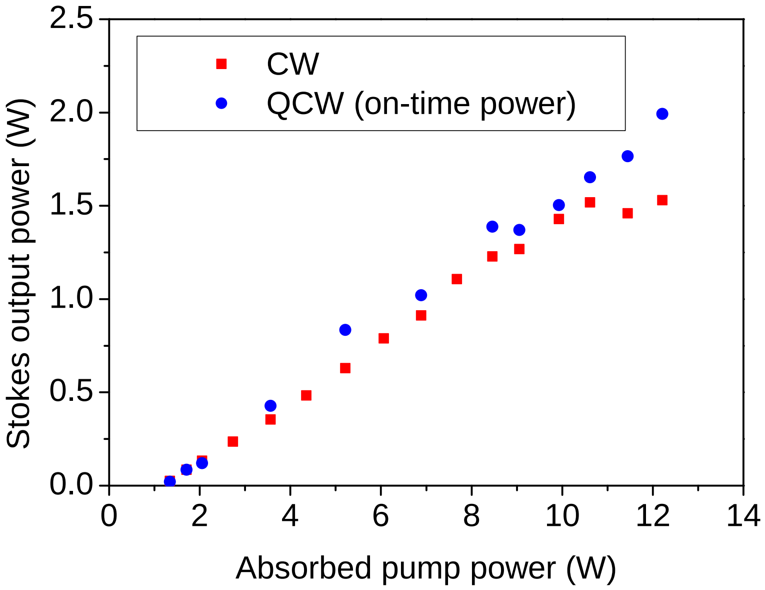

**Figure 4.2:** Power transfers for Cavity 1, for continuous wave (CW) and quasi-continuous wave (QCW) operation. On-time power is shown for QCW case, for which pump beam was chopped at 500 Hz with a 50 % duty-cycle.

gives the thermal time constant of a uniformly pumped rod as

$$\tau_{\mathrm{th}} = \frac{r_0^2 C\gamma}{\kappa} \tag{4.1}$$

where $r_0$ is the radius of the rod, $C$ is the specific heat, $\gamma$ is the mass density and $\kappa$ is the thermal conductivity [4]. In order to apply this equation to the lasers described in this thesis, $r_0$ was taken to be the distance the heat had to flow to reach the heat sink. This was assumed to be the radius of the pump beam in the Nd:$YVO_4$ disk (180 µm in the smallest case) and the radius of the Stokes mode in the $BaWO_4$ rod ($\sim$ 100 µm). If anything, using these values will lead to an underestimate of the thermal time constant. Using values for the material properties obtained from [8–12], the thermal time constants of the Nd:$YVO_4$ disk and the $BaWO_4$ rod were calculated to be 17 ms and 7 ms respectively. Throughout this chapter, the chopper was operated with a 50 % duty cycle, at a frequency of either 500 Hz or 1 kHz leading to “on-times” of 1 ms or 0.5 ms respectively. Therefore, it can be seen that the on-time periods were in fact sufficiently short such that the temperature profile in each crystal did not have time to build up to a steady state and thermal lensing was significantly reduced when the chopper was used. Note that the temporal dynamics of the laser were not monitored (eg relaxation oscillations, variation of the thermal lens strength during the on-time period of the chopper).

To investigate the thermal behaviour of the system in more detail, the cavity modelling techniques described in Section 4.2 above were applied to the laser cavity. A linear fit to the linear section of the CW power transfer in Figure 4.2 was calculated and extrapolated a few points beyond the roll-over. These pump and Stokes powers were then used to create table of thermal lens strengths (for the Nd:YVO$_4$ disk and BaWO$_4$ crystal), which were fed into the modelling calculations. The ratio of the fundamental TEM$_{00}$ mode radius to the Stokes TEM$_{00}$ mode radius is plotted as a function pump power in Figure 4.3, while the movement of the fundamental and Stokes cavities through the $g_1$-$g_2$ plane is shown in Figures 4.4 and 4.5 respectively.

There are several important features to note in Figures 4.3 and 4.4. Firstly the behaviour of the laser is quite different in the two planes, which is unsurprising given the marked astigmatism of the thermal lens in the BaWO$_4$ crystal. The stability parameter analysis shows that the positive thermal lens in the Nd:YVO$_4$ disk moves the fundamental cavity in the direction of negative $g_2$ (downwards in Figure 4.4), while the negative thermal lens in the BaWO$_4$ crystal moves the cavity in the direction of positive $g_1$ (towards the right in Figure 4.4). (Note therefore that the sharp bend in the data points occurs at the Raman threshold.) In this way, the thermal lens in the BaWO$_4$ actually helps to keep the cavity stable as the pump power is increased, and the problem is that the BaWO$_4$ lens is too weak in the plane parallel to the a-axis (the sagittal plane of the cavity), and the modelling predicts that the cavity will become unstable in this plane at around 11 W absorbed pump power. In fact it is found experimentally that the cavity continues to oscillate above this pump power, as can be seen in Figure 4.2 but it is around 11 W absorbed pump power that the Stokes output power begins to roll-over, showing that it is around this point that the thermal lenses start to become particularly problematic. Given the assumptions and uncertainties in the modelling this level of agreement is reasonable: the modelling should be used to determine general trends, but the absolute values predicted should be treated with

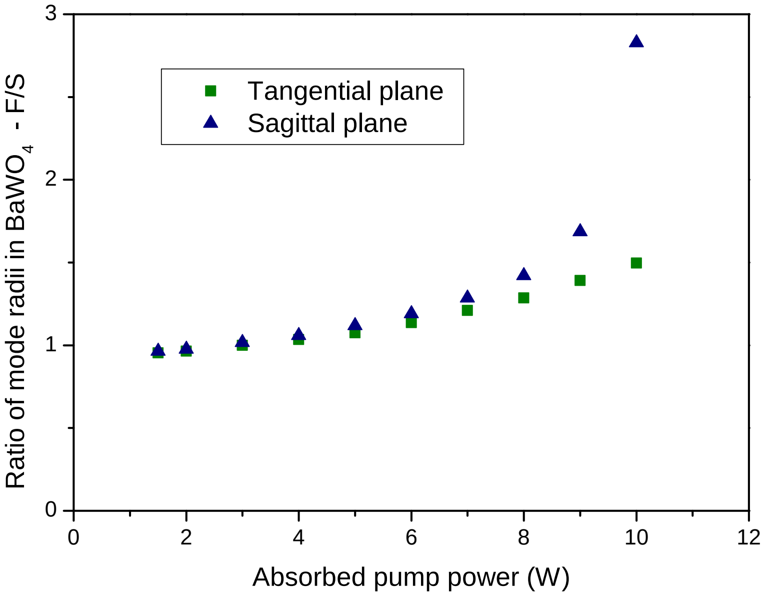

**Figure 4.3:** Ratio of TEM$_{00}$ mode radii of the fundamental and Stokes fields in the BaWO$_4$ crystal as a function of pump power for Cavity 1.

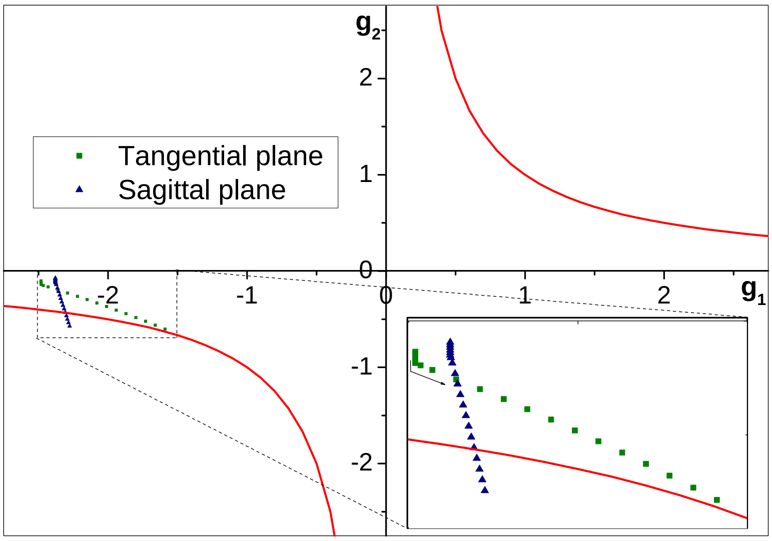

**Figure 4.4:** Variation of the $g_1$-$g_2$ stability parameters for the fundamental cavity with pump power for Cavity 1. The red lines show the stability limit $g_1g_2 = 1$. The inset shows a magnified version of the region of interest, and the arrow in the inset indicates the direction of increasing pump power. The sharp bend in the data occurs at the Raman threshold.

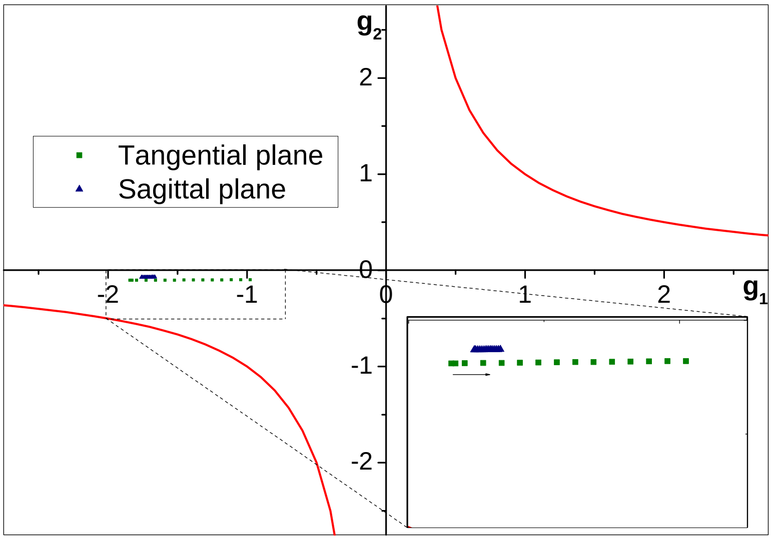

**Figure 4.5:** Variation of the $g_1$-$g_2$ stability parameters for the Stokes cavity with pump power for Cavity 1. The red lines show the stability limit $g_1g_2 = 1$. The inset shows a magnified version of the region of interest, and the arrow in the inset indicates the direction of increasing pump power.

caution. However, the general trends are arguably the most useful piece of information for determining how to improve the cavity design.

As can be seen in Figure 4.5, the Stokes cavity remains well away from the stability limits. When discussing the other cavity designs presented later in this chapter, the stability parameters for the Stokes cavity are only plotted if the Stokes cavity approaches any of the stability limits.

Figure 4.3 shows that the $\mathrm{TEM}_{00}$ mode radii of the fundamental and Stokes fields in the $\mathrm{BaWO}_4$ crystal begin to diverge rapidly at high pump powers. This is mainly due to the fundamental mode size increasing rapidly, especially in the sagittal plane – the Stokes mode size changes only slowly. The coupled cavity arrangement means that the Stokes field only experiences the thermal lens in the $\mathrm{BaWO}_4$ crystal, while the fundamental field experiences both thermal lenses, leading to these potentially large discrepancies in the mode sizes of the two fields.

*Key findings* – These experiments and calculations suggested two approaches to improving the performance of the laser. Firstly, folding the Stokes cavity at the flat dichroic mirror and adding a concave end mirror that would simulate the effect of the Nd:$\mathrm{YVO}_4$ thermal lens at high power, and secondly increasing the pump spot size so as to reduce the strength of the thermal lens in the Nd:$\mathrm{YVO}_4$ and thereby increase the range of pump powers over which the fundamental cavity remains stable. These first of these changes was implemented in the form of Cavity 2, which will now be discussed.

### 4.3.3 Cavity 2: Four mirror Stokes cavity

In order to improve the overlap of the fundamental and Stokes modes at high pump powers, the Stokes cavity was folded at the dichroic mirror and a curved end mirror added, which would have a similar effect on the Stokes field as the thermal lens in the Nd:$\mathrm{YVO}_4$ disk had on the fundamental field, albeit for one pump power only. The resulting layout of Cavity 2 is shown in Figure 4.6. The cold cavity $\mathrm{TEM}_{00}$ mode radius of the fundamental field in the tangential (sagittal) plane was 211 µm (233 µm) in the Nd:$\mathrm{YVO}_4$ disk and 80 µm (80 µm) in the $\mathrm{BaWO}_4$ crystal. The cold cavity $\mathrm{TEM}_{00}$ mode radius of the Stokes field was 112 µm (117 µm) in the $\mathrm{BaWO}_4$ crystal. The curvature of the Stokes cavity end mirror (M3 in Figure 4.6) and its separation from the dichroic mirror were chosen in order to emulate the effect of the thermal lens in the Nd:$\mathrm{YVO}_4$ disk at high powers. This was done by calculating the total ABCD matrix for all the optical elements in the fundamental cavity after the dichroic, for an absorbed pump power of 10.6 W, and adjusting the focal length and position of the new Stokes cavity end mirror to create the same total ABCD matrix for the path of the Stokes beam after the dichroic. The addition of a Stokes-only arm to the cavity (ie DC-M3) also makes it possible to chop the Stokes cavity only, thereby reducing the thermal lens in the Raman crystal but not that in the laser gain material. This can partially disentangle the effects of the two thermal lenses and several such experiments will be presented in

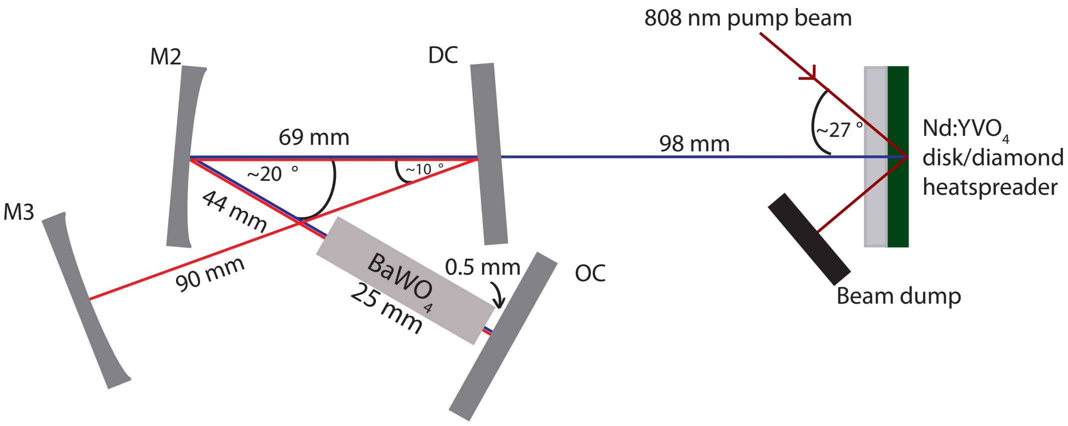

**Figure 4.6:** Cavity 2 – coupled cavity laser design with separate end mirror for the Stokes cavity. DC was a plane dichroic mirror, highly transmissive at 1064 nm and highly reflective at 1180 nm. M2 and M3 were highly reflecting at both wavelengths and were concave with radii of curvature equal to 100 mm and 150 mm respectively. OC was a plane output coupler, highly reflecting at 1064 nm but with a transmission of 0.4 % at 1180 nm. The pump spot radius was again 180 µm.

this chapter.

Power transfers for the CW, QCW and chopped Stokes cavity regimes are shown in Figures 4.7 and 4.8. In the CW regime, the slope efficiency is 16 % and the threshold was 0.74 W absorbed pump power. A maximum output power of 1.71 W was obtained at 1180 nm for 12.2 W absorbed pump power. The diode to Stokes conversion efficiency at maximum pump power was 14 %. Comparison of Figure 4.7 to Figure 4.2 reveals that the addition of a separate Stokes end mirror may have made the roll-over in the output power somewhat less severe – there is a slight curvature of the power transfer in Figure 4.8 – but higher pump powers than were available at the time would be required to check this. It can be seen in Figure 4.7 that chopping the pump beam, and thereby reducing the strength of both thermal lenses, increases the on-time Stokes output power somewhat, although the improvement is not as significant was the case with the previous cavity design (see Figure 4.2). The CW power transfer in Figure 4.7 curves slightly as if a roll-over is imminent, and indeed it was found that occasionally the laser did roll-over slightly depending upon the precise alignment of the optics, as can be seen in the CW power transfer in Figure 4.8. The data shown in Figures 4.7 and 4.8 were collected on the same day, but the laser was re-optimised in between the experiments because the performance of the laser varied over the timescale of the experiments.

The power transfer for the case where the Stokes cavity was chopped is instructive. As can be seen in Figure 4.8, the Stokes output power rolls over much earlier when the Stokes cavity is chopped. This indicates that the SRS-induced thermal lens in the BaWO$_4$ crystal is in some way beneficial for the performance of the laser. This is consistent with the modelling described in the previous section, which indicated that the negative lens in the BaWO$_4$ kept the previous fundamental cavity stable against

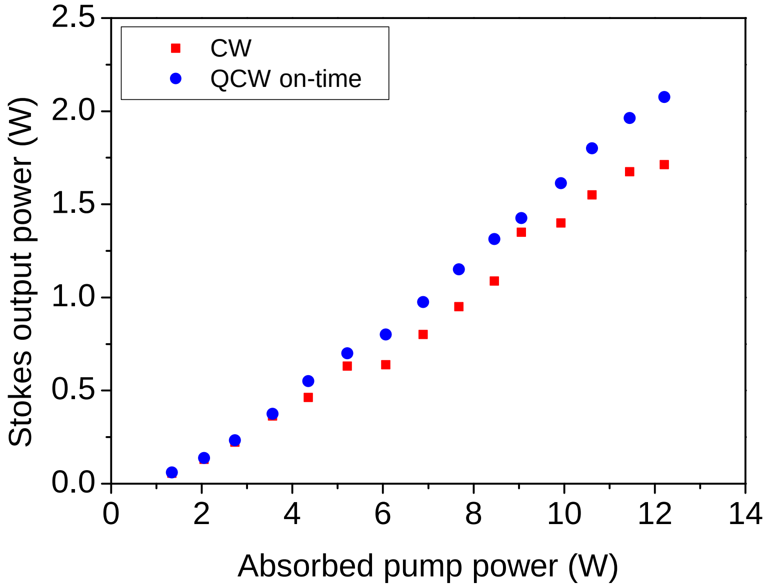

**Figure 4.7:** Power transfers for Cavity 2, for continuous wave (CW) and quasi-continuous wave (QCW) operation. On-time power is shown for QCW case, for which pump beam was chopped at 1 kHz with a 50 % duty-cycle.

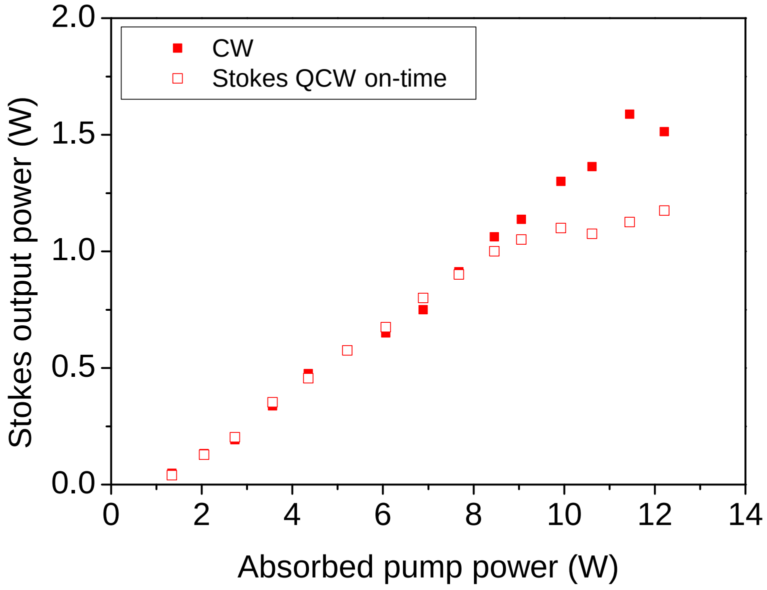

**Figure 4.8:** Power transfers for Cavity 2, for continuous wave (CW) operation, and for the case when the Stokes cavity was chopped just in front of M3 (Stokes QCW). On-time power is shown for QCW case, for which Stokes cavity was chopped at 1 kHz with a 50 % duty-cycle.

the effects of the positive lens in the Nd:YVO$_4$ disk.

Another diagnostic for the behaviour of intracavity Raman is the residual power at the fundamental wavelength. Measurements of this are shown in Figure 4.9. Both the Stokes and fundamental powers were measured (separately) behind the output coupler, using either a long pass 1100 nm or a narrow band pass 1064 nm filter as appropriate to select the desired wavelength. The fundamental power was measured with and without the Stokes cavity blocked. There are several features of this data to note. Firstly, the fundamental power does not clamp at its Raman threshold value. In theory, since the Raman gain is proportional to the fundamental intensity, this should remain constant after the Raman threshold is reached, in order to maintain a steady state. Such clamping of the fundamental power has been observed in some intracavity Raman lasers [13–15], but not in others [16–18]. In the system presented here, the rate of increase of fundamental power with pump power does decrease at the Raman threshold, but it does not level off completely. This could be due to energy being coupled into higher order spatial or spectral modes of the fundamental cavity [17, 18]. The fundamental power does level off more at higher pump powers, before increasing again somewhat as the Stokes output power starts to roll over. The point at which the fundamental power levels off is around 6 W to 7 W absorbed pump power, and at this point a change in the slope efficiency of the Stokes output power can be observed in both Figures 4.7 and 4.9, suggesting that something is changing in the laser around this pump power - again, transverse and spectral modes are possibilities.

When the Stokes cavity is blocked, suppressing SRS, the fundamental reaches higher powers with a different roll-over near the maximum pump power. However, at low powers the fundamental power does not increase much compared to the case when the Stokes field is oscillating which suggests that the coupling of energy from the funda-

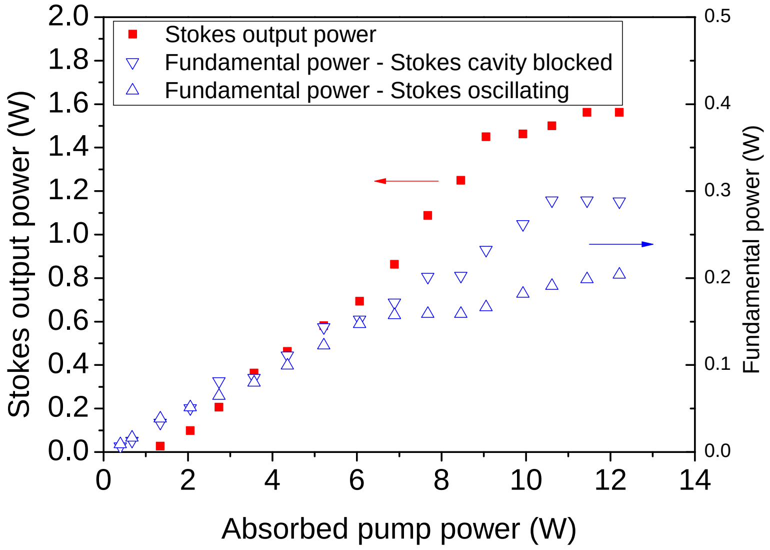

**Figure 4.9:** Output power and residual power at 1064 nm, measured behind the output coupler, for Cavity 2, with and without the Stokes cavity blocked.

mental field to the Stokes field is sub-optimal. Furthermore, although the fundamental field rolls over at high powers it does continue to oscillate even when the Stokes cavity is blocked, showing that the fundamental cavity does not actually become unstable when the thermal lens in the $BaWO_4$ crystal is removed, even if it does approach the stability edge.

The mode overlap in the $BaWO_4$ crystal and the $g_1$-$g_2$ parameters were modelled as functions of pump power as before. A linear fit to the CW power transfer in Figure 4.7 was calculated and extrapolated a few points beyond the roll-over and these pump and Stokes powers were then used to determine the thermal lens strengths as before. The ratio of the fundamental $TEM_{00}$ mode radius to the Stokes $TEM_{00}$ mode radius is plotted as a function pump power in Figure 4.10, while the movement of the fundamental cavity through the $g_1$-$g_2$ plane is shown in Figure 4.11.

It can be seen from Figure 4.10 that adding the separate, curved end mirror to the Stokes cavity has achieved the goal of improving the mode overlap in the $BaWO_4$ crystal at high pump powers - the ratio of the mode radii now varies over a smaller range, and passes through 1 closer to the maximum pump power than before. This may be the main reason why the roll-over is less severe in Figure 4.8 than in Figure 4.2. However, as was noted above there is little difference in the maximum output power, and so there may be other effects that need to be accounted for.

There is relatively little change in movement of the fundamental cavity through the stability zone - once again the modelling predicts that the fundamental cavity will become unstable at lower pump powers (10 W to 11 W) than is the case experimentally, showing the limitations of such calculations for predicting absolute values of various parameters. However, the general trends are in line with what is observed experimen-

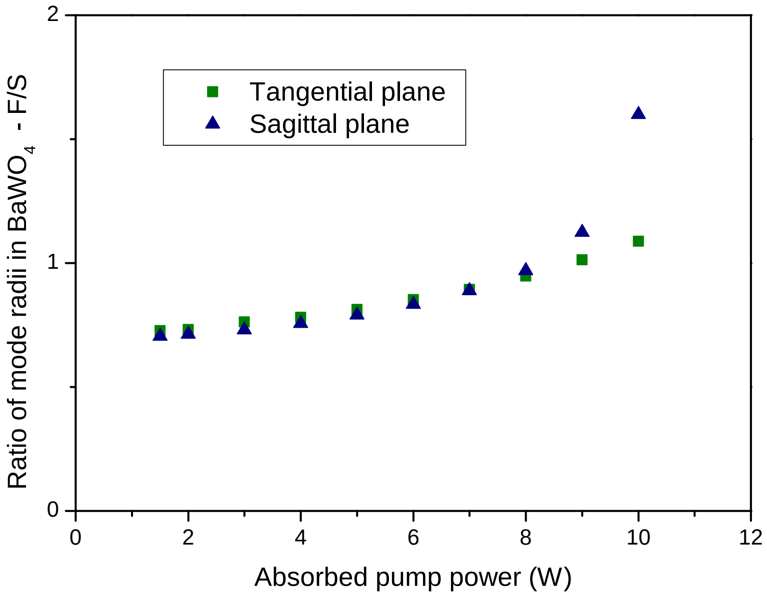

**Figure 4.10:** Ratio of $TEM_{00}$ mode radii of the fundamental and Stokes fields in the $BaWO_4$ crystal as a function of pump power for Cavity 2.

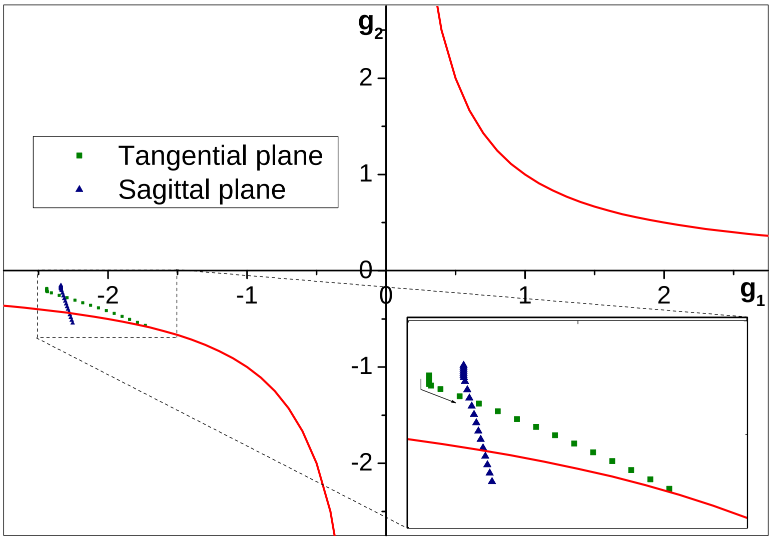

**Figure 4.11:** Variation of the $g_1$-$g_2$ stability parameters for the fundamental cavity with pump power for Cavity 2. The arrow in the inset shows the direction of increasing pump power.

tally, and these make it clear that the thermal lens in the disk is the limiting factor for this cavity design.

*Key findings* – Curved mirror M3 was effective for improving the mode matching between the fundamental and Stokes fields in the $BaWO_4$ crystal. The thermal lens in the Nd:$YVO_4$ disk makes the cavity unstable at high pump powers. This is delayed in the tangential plane by the strong negative thermal lens in the $BaWO_4$ crystal, but in the sagittal plane the thermal lens in the $BaWO_4$ is too weak to have a significant effect. Therefore, it is necessary to reduce the strength of the thermal lens in the Nd:$YVO_4$ disk relative to that in the $BaWO_4$ crystal in order to further increase the output power of the laser. The thermal lens in the disk can be reduced by increasing the pump spot radius, and experiments involving a larger pump spot will be described in the next section.

## 4.4 Evaluation of cavities using a 300 µm radius pump spot

### 4.4.1 Cavity 3: Cavity design – convex end mirror

The pump spot radius used in the Raman lasers described so far in this thesis, 180 µm, is small for a disk laser. It was chosen at first to improve the beam quality and lower the Raman threshold, making it easier to obtain Raman oscillation. However, to take advantage of the disk geometry's favourable thermal behaviour, it is essential to move to a larger pump spot radius approaching, or preferably exceeding, the thickness of the disk (0.5 mm here). As a first step in this direction, the pump spot radius was increased to 300 µm and the cavity was redesigned so as to match the fundamental and pump modes in the Nd:$YVO_4$ disk, while maintaining as small a spot size as

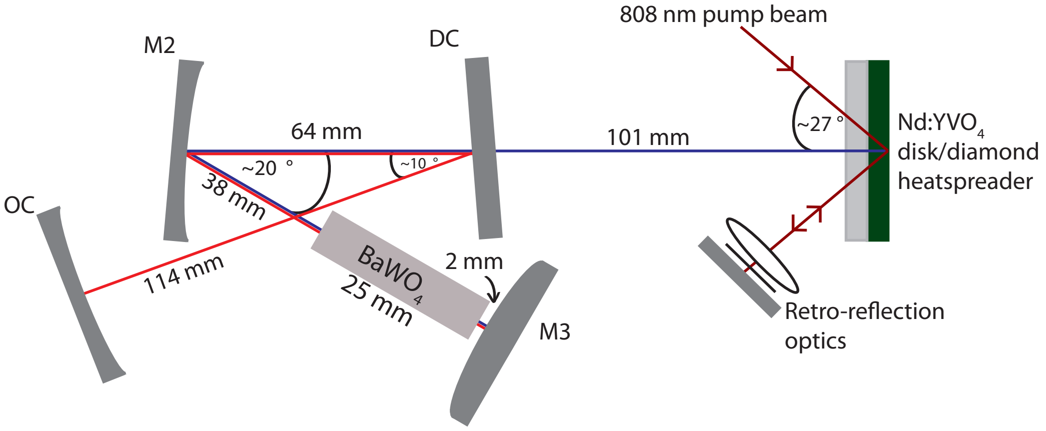

**Figure 4.12:** Cavity 3 – coupled cavity laser design for a pump spot of radius $w_P = 300\,\mu\text{m}$. DC was a plane dichroic mirror, highly transmissive at 1064 nm and highly reflective at 1180 nm. M2 and M3 were highly reflecting at both wavelengths. M2 was concave with radius of curvature 100 mm, while M3 was convex with radius of curvature −100 mm. OC was a concave output coupler with radius of curvature 250 mm, highly reflecting at 1064 nm but with a transmission of 0.4 % at 1180 nm. The pump retro-reflection optics are described in Section 4.4.2.

possible in the BaWO$_4$ crystal. The design of Cavity 3 is shown in Figure 4.12. This requirement for a large mode size in one crystal and a small mode size in another makes it more difficult to design a cavity that will be stable over a large range of pump powers. The stability parameter analyses presented in the preceding sections indicated that the positive thermal lens in the Nd:YVO$_4$ disk drove the cavity towards more negative values of $g_2$, while the negative thermal lens in the BaWO$_4$ crystal drove it towards more positive values of $g_1$, and due to the starting position of the cavity in the $g_1$-$g_2$ plane, the negative BaWO$_4$ lens actually helped to stabilise the cavity against the influence of the positive Nd:YVO$_4$ lens. Therefore, when the cavity was redesigned for a 300 µm radius pump spot, a convex end mirror was introduced so as to increase the total defocussing effect at the end of the cavity, and thereby to move the cavity into a broader region of the stability zone. The cold cavity TEM$_{00}$ mode radius of the fundamental field in the tangential (sagittal) plane was 257 µm (293 µm) in the Nd:YVO$_4$ disk and 87 µm (87 µm) in the BaWO$_4$ crystal. The cold cavity TEM$_{00}$ mode radius of the Stokes field was 102.5 µm (105.5 µm) in the BaWO$_4$ crystal.

### 4.4.2 Double-passing the pump beam

Since the roll-over was not completely clear in Figure 4.7 at the maximum absorbed pump power available in the single-pass, polarised pump arrangement, a double-pass arrangement was introduced. Previously (see Section 3.5.1) the disk laser was pumped using the output of an 808 nm fibre-coupled laser diode, which first passed through a polariser and half-wave plate, such that up to 14 W of 808 nm light polarised parallel to the c-axis of the Nd:YVO$_4$ crystal was incident on the vanadate-diamond unit. This led to an absorbed pump power of up to 12.2 W. The polariser and half-wave-plate were used to ensure that the Nd:YVO$_4$ disk was pumped with light polarised parallel to the c-axis in order to minimise the unabsorbed pump light exiting the disk unit. In this arrangement, approximately 88 % of the pump power incident on the Nd:YVO$_4$/diamond unit was absorbed in the Nd:YVO$_4$ disk. Most of the unabsorbed light was that which was reflected from the AR coating on the front surface of the diamond heatspreader (which had a reflectivity of 11.5 % at the pump wavelength) – in other words, 98 % to 99 % of the pump light which passed through the coated diamond heatspreader and reached the Nd:YVO$_4$ disk was then absorbed over the single-pass (defined here as one trip from the front surface to the rear mirror and back to the front surface again).

To increase the maximum absorbed pump power accessible using the same laser diode (which had a nominal maximum power of 30 W), the polariser and half-wave plate were removed so that up to 28.3 W unpolarised radiation at 808 nm was incident on the Nd:YVO$_4$/diamond unit. The unabsorbed pump light reflected from the unit was retro-reflected back along its path so that it would pass through the Nd:YVO$_4$ disk a second time. As noted above, most of the c-polarised light was absorbed on the first pass and therefore the unabsorbed light was mainly a-polarised, apart from the small component that reflected from the front surface of the diamond heatspreader, which remained largely unpolarised. To maximise the benefit of the second pass, the polarisation of the unabsorbed light was first rotated before it was re-focussed into the Nd:YVO$_4$ disk. This was achieved as follows: a 50 mm focal length lens was used to collect and collimate the diverging, unabsorbed, pump beam after the first pass. The beam then passed through a quarter-wave plate, and reflected off a plane, broadband reflector before passing through the quarter-wave plate again. The returning beam, having had its original polarisation state rotated by 90° was then focussed by the same 50 mm focal length lens back onto the same spot in the Nd:YVO$_4$ crystal. These retro-reflection optics are shown in Figure 4.12. This unconventional approach made it possible to achieve reasonable pump absorption using only a simple double-pass arrangement.

Initially, no measurements were made of the absorbed pump power since it was difficult to access the unabsorbed pump light that was travelling back towards the diode laser fibre. Therefore the laser performance is reported with respect to the incident pump power in Section 4.4.3. The challenges of determining the absorbed pump power in the double-pass arrangement were subsequently overcome and measurements were made. These measurements were made when using a different pump laser diode, and therefore will be presented later in the chapter. However, based on those measurements, it is likely that at least 90 % of the pump power incident on the Nd:YVO$_4$/diamond unit was absorbed in the Nd:YVO$_4$ disk in the present case.

### 4.4.3 Cavity 3: Raman laser performance

The CW power transfer for Cavity 3 is shown in Figure 4.13. The Raman threshold was 3.5 W incident pump power, and the maximum output power at the Stokes wavelength was 2.11 W for an incident pump power of 28.3 W, representing a diode-Stokes conversion efficiency of 7.5 % (with respect to incident pump power). The cavity remained stable over a large range of pump powers, as was one of the goals of the cavity design. The slope efficiency gradually decreased as the pump power was increased, it is not clear why this was the case. However, a complete roll-over in the power was not observed at the maximum available pump power and therefore a more powerful diode laser was required to fully explore the limits of this cavity design.

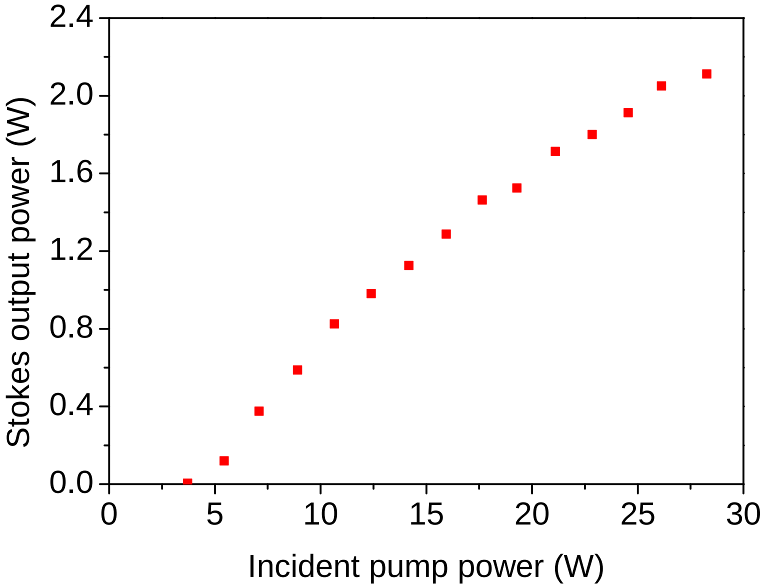

**Figure 4.13:** CW power transfer for Cavity 3. Note that the x-axis is the pump power incident on the Nd:$YVO_4$/diamond unit.

### 4.4.4 90 W diode pump laser

The work described so far in this chapter was carried out at Macquarie University. The Raman laser was then moved back to the University of Strathclyde, where a 90 W fibre-coupled diode laser at 808 nm (200 µm diameter fibre core, numerical aperture of 0.22) was used to pump the Nd:$YVO_4$ disk. The absorbed pump power in the double-pass arrangement was determined by placing a non-polarising beam-splitter cube between the pump lenses, as shown in Figure 4.14. This picked off approximately half of the unabsorbed pump light and from this the fraction of the incident pump light that was absorbed was determined. This was then used to calculate the absolute absorbed power when the beam-splitter was not present. These measurements were carried out under lasing conditions. The measurements were initially carried out using a 0.5 mm thick, 1 at.% doped Nd:$YVO_4$ disk and a 0.75 mm thick diamond heatspreader. Note that

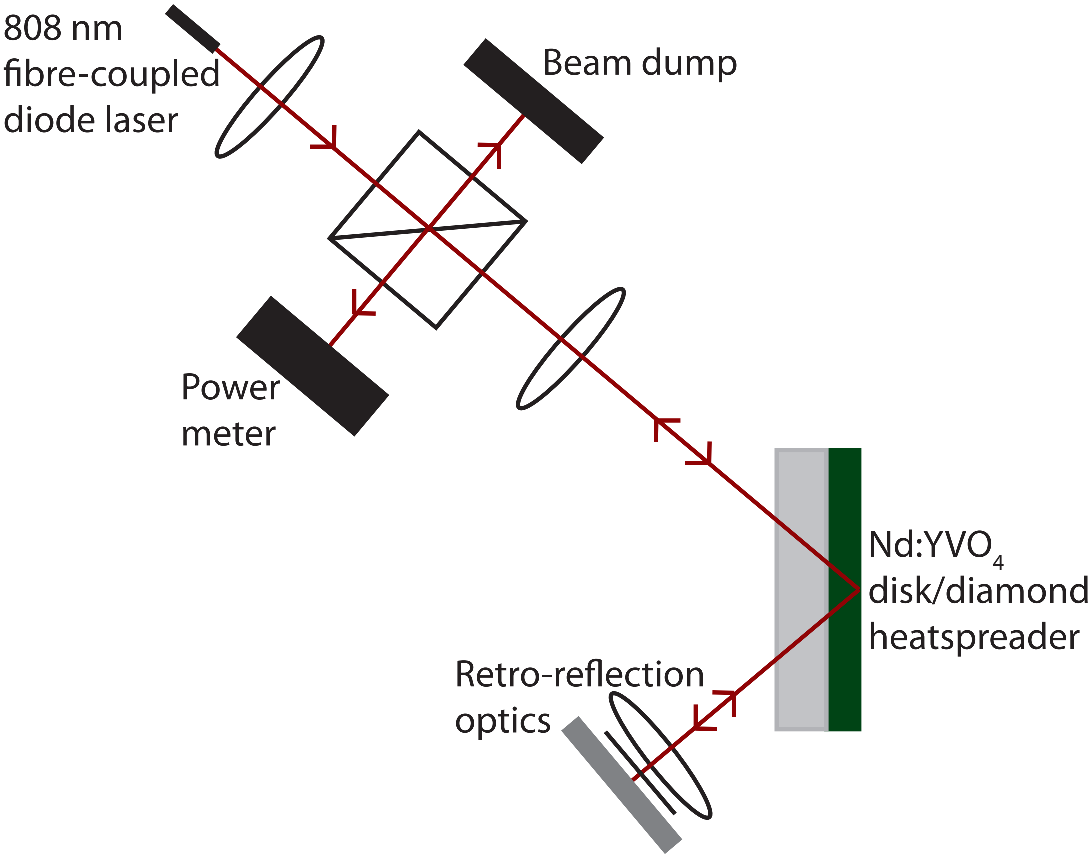

**Figure 4.14:** Experimental setup for measuring the absorbed pump power under the double pass scheme. A non-polarising beam-splitting cube was placed between the pump imaging lenses to pick off a portion of the unabsorbed pump light after the second pass. Note that the beam-splitting cube was removed for normal operation of the laser.

these crystals had slightly different coatings compared to those used previously – the original Nd:YVO$_4$ disk had fractured. In this case, 93 % of the pump power incident on the Nd:YVO$_4$/diamond unit was absorbed in the Nd:YVO$_4$ disk. This setup was used for most of the experiments described in Chapter 5, but before further power-scaling work could be done another disk fracture occurred and (separately) the BaWO$_4$ crystal also fractured and had to be re-polished.

### 4.4.5 Cavity 4: New crystals

No more 1 at.% doped Nd:YVO$_4$ disks were available, and therefore a 0.5 mm thick, 0.5 at.% doped Nd:YVO$_4$ disk was used, bonded to a 0.75 mm thick diamond heat-spreader. The absorbed pump power was measured again using the technique described in the previous section, and it was found that 82 % of the pump power incident on the Nd:YVO$_4$/diamond unit was absorbed in the Nd:YVO$_4$ disk.

After the 25 mm long BaWO$_4$ crystal fractured, it was re-polished to a length of 16.4 mm and re-coated. The cavity length was adjusted to account for the shorter length of BaWO$_4$. The revised cavity design (Cavity 4) is shown in Figure 4.15. The cold cavity TEM$_{00}$ mode radius of the fundamental field in the tangential (sagittal) plane was 262 µm (292 µm) in the Nd:YVO$_4$ disk and 71.5 µm (70.5 µm) in the BaWO$_4$ crystal. The cold cavity TEM$_{00}$ mode radius of the Stokes field was 91.5 µm (95 µm) in the BaWO$_4$ crystal.

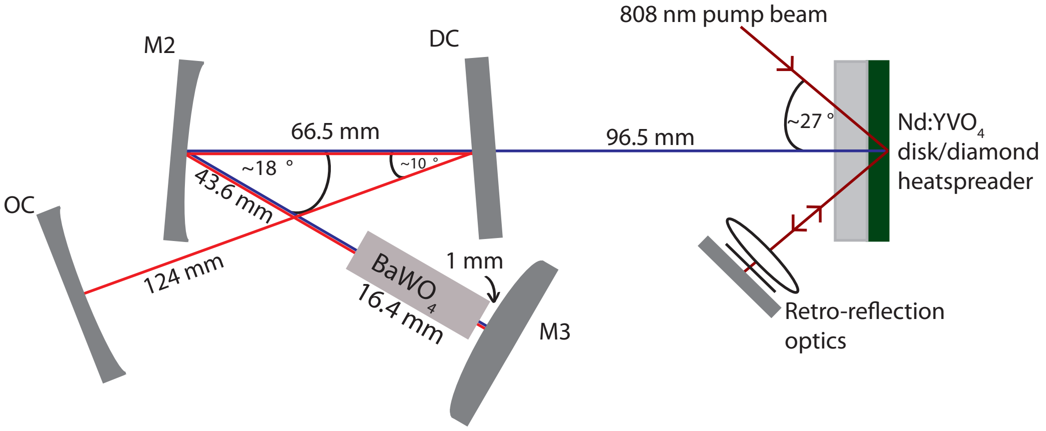

**Figure 4.15:** Cavity 4 – coupled cavity laser design for a pump spot of radius $w_P = 300\,\mu\text{m}$, using 0.5 at.% Nd:YVO$_4$ disk and shorter, re-polished BaWO$_4$ crystal. DC was a plane dichroic mirror, highly transmissive at 1064 nm and highly reflective at 1180 nm. M2 and M3 were highly reflecting at both wavelengths. M2 was concave with radius of curvature 100 mm, while M3 was convex with radius of curvature −100 mm. OC was a concave output coupler with radius of curvature 250 mm, highly reflecting at 1064 nm but with a transmission of 0.4 % at 1180 nm.

### 4.4.6 Cavity 4: Experimental data and cavity modelling

Power transfers were measured for CW operation, and when chopping either the pump beam or the Stokes cavity (just in front of the output coupler OC) at 1 kHz, with a

50 % duty-cycle. Simultaneously, the residual power at the fundamental wavelength, 1064 nm, was measured behind mirror M2. These measurements are shown in Figures 4.16 and 4.17. In the CW regime, the maximum Stokes output power is 3.15 W for an absorbed pump power of 33.9 W, representing a diode-to-Stokes conversion efficiency of 9.3 %. The Raman threshold was 4.7 W. The slope efficiency was 11.5 %, omitting the final point from the linear fit. The $M^2$ of the output Stokes beam was measured to be $< 1.1$ in both axes, while the beam profile of the residual fundamental beam was complex. It is typical of Raman lasers that the Stokes beam has better beam quality than the fundamental beam, due to the Raman beam cleanup effect [7].

In the disk laser presented here, the QCW power transfer remains linear at all pump powers, and gives a higher on-time power of 4.26 W. This suggests that there are still some thermal problems to be overcome although these are not nearly so severe as when a 180 µm radius pump spot was used, since the output power does not begin to roll-over until the absorbed pump power is about 25 W, whereas the CW power transfers in Figures 4.7 and 4.8 started to roll over at around 12 W absorbed pump power. Once again chopping the Stokes cavity leads to a slightly more severe roll-over, but only at the highest pump powers used.

It can be seen from Figure 4.17 that once again the fundamental power does not clamp at the Raman threshold – there is a decrease in the slope of the fundamental power transfers, but the fundamental power continues to rise. The decrease in the slope is larger for the QCW case, which is consistent with the fact that higher Stokes output power are obtained for this regime – SRS is more strongly depleting the fundamental under QCW operation. There is very little difference between the CW and Stokes

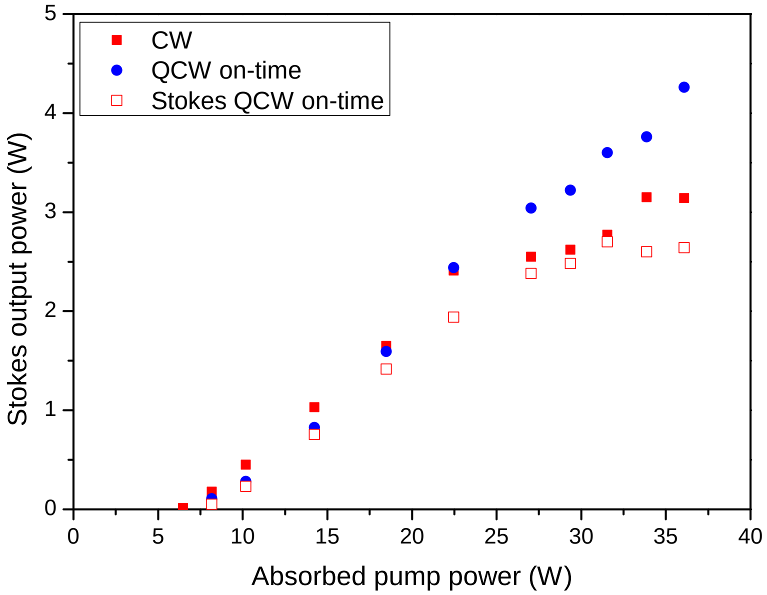

**Figure 4.16:** Power transfers for CW operation and with the pump beam or Stokes cavity chopped (QCW and Stokes QCW respectively) for Cavity 4. On-time powers are shown for the QCW cases.

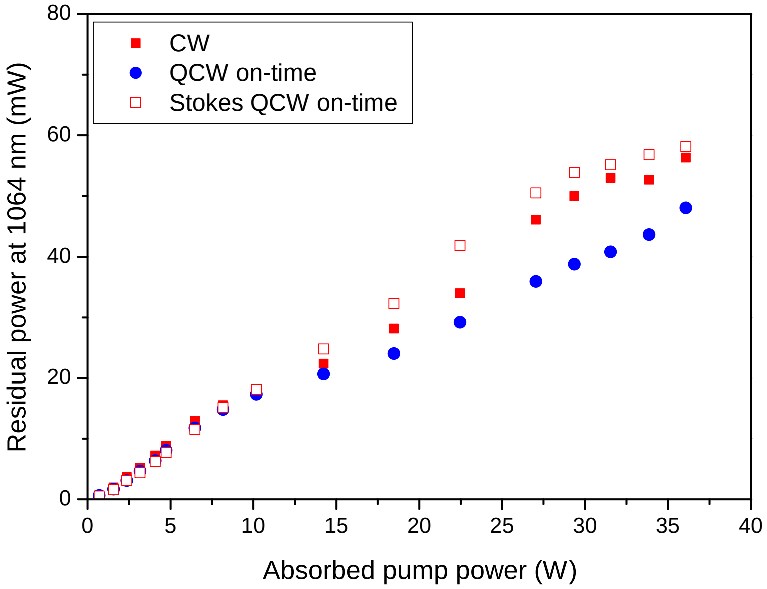

**Figure 4.17:** Residual power at 1064 nm, measured behind mirror M2, for Cavity 5 for CW operation and with the pump beam or Stokes cavity chopped (QCW and Stokes QCW respectively) for Cavity 4.

QCW regimes.

The mode overlap and stability parameter calculations were performed for Cavity 4. As described in Chapter 3, finite element analysis was used to calculate the new values of the thermal lens in the Nd:YVO$_4$ disk, taking account of the larger pump spot size and the double-pass geometry (which changes the axial heat distribution in the disk slightly). The strength of the thermal lens in the BaWO$_4$ crystal was calculated as a function of pump power by extrapolating a linear fit of the CW power transfer in Figure 4.16, ie the data points up to and including an absorbed pump power of 33.9 W. The fit was extrapolated to an absorbed pump power of 40 W. It should be noted that the reduction in the length of the BaWO$_4$ crystal makes it more difficult to calculate the thermal lens strength using the lateral shearing interferometry measurements for the longer crystal. The reduction in length will make the [positive] bulging component of the lens stronger, but will not affect the other contributions [4]. For the BaWO$_4$ crystal, this means that the lens will be more weakly negative. However, it is not trivial to disentangle the various contributions to the total thermal lens strength and therefore this change had to be neglected in the calculations. The lens strengths used in the modelling therefore represent an upper limit to the magnitude of the [negative] thermal lens strength. The results of the modelling are shown in Figures 4.18 and 4.19.

*Key findings* – It can be seen from Figure 4.19 that using the convex end mirror has ensured that the fundamental cavity remains stable over a large range of pump powers, against the destabilising influence of the positive thermal lens in the Nd:YVO$_4$, which itself is also weaker thanks to the larger pump spot size. However, the astigmatism of the thermal lens in the BaWO$_4$ crystal is becoming more problematic - the cavity is

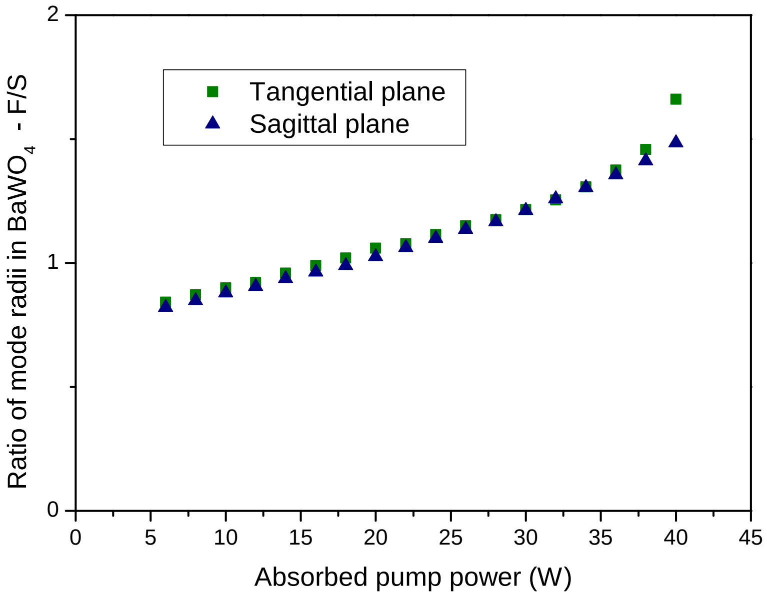

**Figure 4.18:** Ratio of $TEM_{00}$ mode radii of the fundamental and Stokes fields in the $BaWO_4$ crystal as a function of pump power, for Cavity 4.

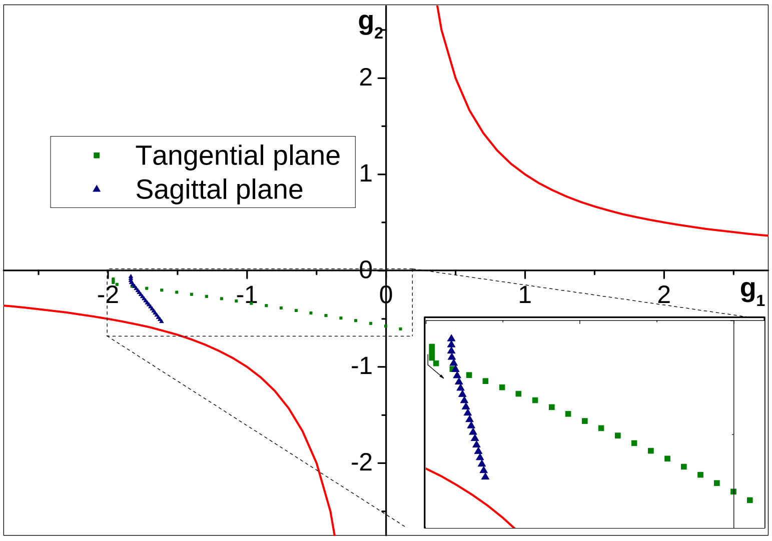

**Figure 4.19:** Variation of the $g_1$-$g_2$ stability parameters for Cavity 4. The arrow in the inset shows the direction of increasing pump power. Note that the calculations were performed for a larger range of pump powers than was the case for the previous laser cavity designs (0 W to 44 W absorbed pump power compared to 0 W to 14 W previously).

now being driven towards a stability edge (the $g_2$ axis) by the strong negative $BaWO_4$ thermal lens in the tangential plane, while the $BaWO_4$ lens in the sagittal plane is only just strong enough to effectively counter the effects of the positive Nd:$YVO_4$ thermal lens. (Note that the pump and Stokes output powers have been extrapolated to a maximum absorbed pump power of 44 W, and that the lens in the $BaWO_4$ only makes the cavity unstable at an absorbed pump power of 42 W and a hypothetical Stokes output power of 4.18 W, beyond the operational parameters of the experimental system.) Further major improvements to the system may require the use of cylindrical optic to compensate for the astigmatism of the thermal lens in the $BaWO_4$. Another option is to increase the pump spot size to further reduce the strength of the thermal lens in the Nd:$YVO_4$ disk - this will reduce the need to rely on the negative thermal lens in the $BaWO_4$ and open up other options for the cavity design. Experiments involving a larger pump spot size will be described in the next section.

## 4.5 Evaluation of cavity using a 400 µm radius pump spot

In order to further reduce the thermal lens in the Nd:$YVO_4$ disk, the pump spot radius was increased to 400 µm. The cavity was redesigned to increase the mode radius of the fundamental field in the Nd:$YVO_4$ disk also, in order to match the pump and cavity modes. The design of Cavity 5 is shown in Figure 4.20. The cold cavity $TEM_{00}$ mode radius of the fundamental field in the tangential (sagittal) plane was 405 µm (650 µm) in the Nd:$YVO_4$ disk and 66.5 µm (77 µm) in the $BaWO_4$ crystal. The cold cavity $TEM_{00}$ mode radius of the Stokes field was 95.5 µm (98 µm) in the $BaWO_4$ crystal.

The Stokes output power and residual fundamental power were measured as before, for the CW, QCW and Stokes QCW regimes. The measurements are plotted in Fig-

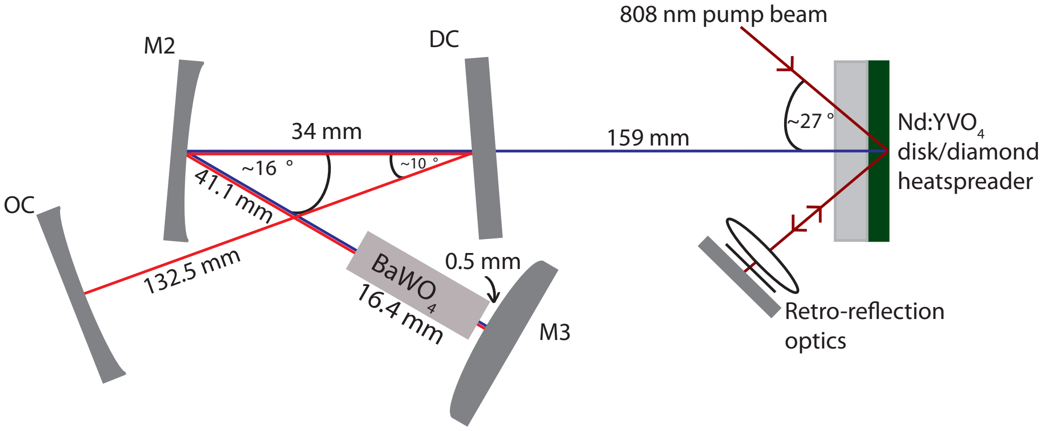

**Figure 4.20:** Cavity 5 – coupled cavity laser design for a pump spot of radius $w_P = 400\,\mu m$. DC was a plane dichroic mirror, highly transmissive at 1064 nm and highly reflective at 1180 nm. M2 and M3 were highly reflecting at both wavelengths. M2 was concave with radius of curvature 100 mm, while M3 was convex with radius of curvature −100 mm. OC was a concave output coupler with radius of curvature 250 mm, highly reflecting at 1064 nm but with a transmission of 0.4 % at 1180 nm.

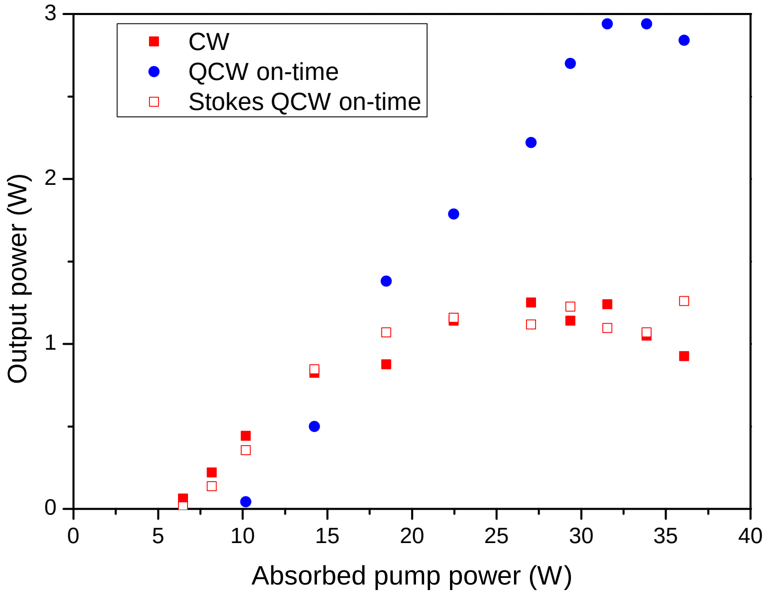

**Figure 4.21:** Power transfers for CW operation and with the pump beam or Stokes cavity chopped (QCW and Stokes QCW respectively) for Cavity 5. On-time powers are shown for the QCW cases.

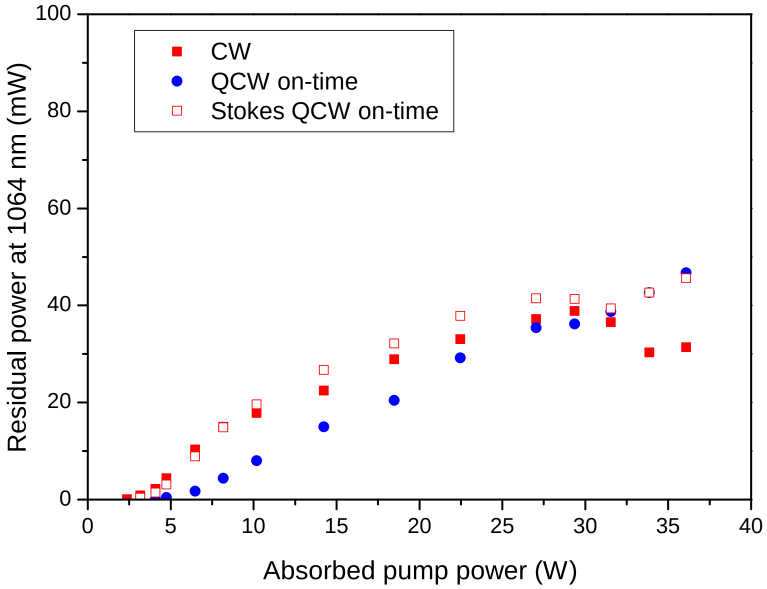

**Figure 4.22:** Residual power at 1064 nm, measured behind mirror M2, for Cavity 5 for CW operation and with the pump beam or Stokes cavity chopped (QCW and Stokes QCW respectively).

ures 4.21 and 4.22. The CW performance of the laser is much poorer than that of the 300 µm pump spot radius system described in the previous section, exhibiting a roll-over in output power at less than 20 W absorbed pump power. The QCW performance is better, but still not as good as that of the 300 µm pump spot radius system.

To investigate possible reasons for the poor performance, the mode overlap and stability parameter modelling were performed again for this cavity. Initially, a linear extrapolation of the low power region of the CW power transfer (the first four points in Figure 4.21) was used to investigate what would happen if the Stokes output power did *not* roll over, up to an absorbed pump power of 44 W. The mode overlap (the ratio of the fundamental $\mathrm{TEM}_{00}$ mode radius to the Stokes $\mathrm{TEM}_{00}$ mode radius) and the fundamental and Stokes cavity $g_1$-$g_2$ parameters are shown in Figures 4.23, 4.24 and 4.25 respectively.

It can be seen from Figure 4.24 that the fundamental cavity remains stable over a large range of pump powers and Stokes output powers. However, Figure 4.25 shows that now the stability of the Stokes cavity is potentially an issue - at a Stokes output power of 3.8 W, the thermal lens in the $\mathrm{BaWO}_4$ has a focal length of only 33 mm in the tangential (horizontal) plane and this puts the cavity on the edge of stability. The effect of the thermal lens in the $\mathrm{BaWO}_4$ crystal on the Stokes cavity is also important for the mode overlap. In the previous cavity designs, the Stokes mode size in the $\mathrm{BaWO}_4$ crystal varied only slightly with the thermal lens in the $\mathrm{BaWO}_4$, and it was the variation of the mode size of the fundamental field that dominated the variation in mode overlap. However, the change in the mode overlap shown in Figure 4.23 is due to both the increase in the mode size of the fundamental in the $\mathrm{BaWO}_4$ crystal,

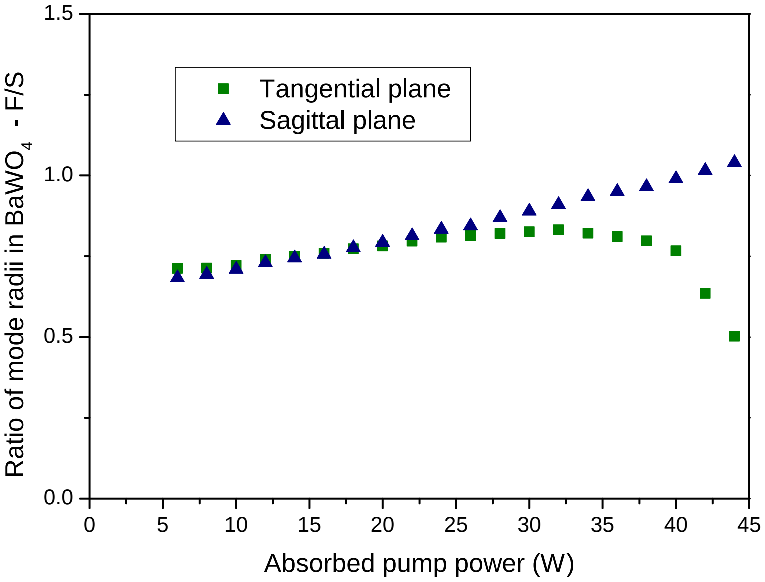

**Figure 4.23:** Ratio of $\mathrm{TEM}_{00}$ mode radii of the fundamental and Stokes fields in the $\mathrm{BaWO}_4$ crystal as a function of pump power, for Cavity 5. The thermal lenses were calculated using a linear extrapolation of the Stokes power transfer of the laser.

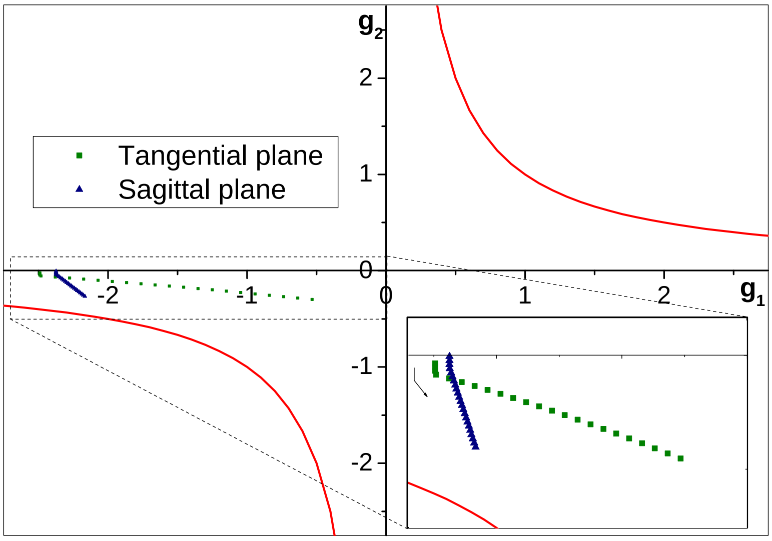

**Figure 4.24:** Variation of the $g_1$-$g_2$ stability parameters for the fundamental resonator in Cavity 5. The arrow in the inset shows the direction of increasing pump power. The thermal lenses were calculated using a linear extrapolation of the Stokes power transfer of the laser.

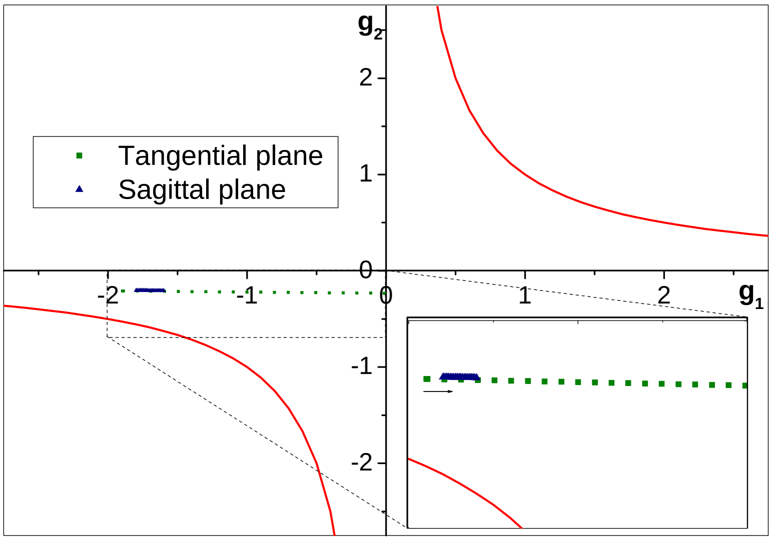

**Figure 4.25:** Variation of the $g_1$-$g_2$ stability parameters for the Stokes resonator in Cavity 5. The arrow in the inset shows the direction of increasing pump power. The thermal lenses were calculated using a linear extrapolation of the Stokes power transfer of the laser.

and, at high powers, the rapid increase in the Stokes mode radius (in the tangential plane). It must be remembered, however, that the mode overlap has been calculated assuming $TEM_{00}$ modes for both the fundamental and Stokes fields. In the case of the fundamental, this assumption is unlikely to be accurate because both the decrease in the radius of the fundamental mode in the Nd:$YVO_4$ disk with increasing pump power and the SRS conversion itself will lead to deterioration of the beam quality of the fundamental field.

The above modelling was carried out using a linear extrapolation of the Stokes power transfer to calculate the thermal lenses strengths for the $BaWO_4$ crystal. While this was a reasonable approach for previous cavity designs (which exhibited linear behaviour over a large range of pump powers), it is less appropriate for the 400 µm pump spot radius cavity, since the output power rolls over much earlier. Therefore the modelling was repeated using the measured Stokes output powers to calculated the $BaWO_4$ thermal lens strengths. The mode overlap (the ratio of the fundamental $TEM_{00}$ mode radius to the Stokes $TEM_{00}$ mode radius) and the fundamental and Stokes cavity $g_1$-$g_2$ parameters are shown in Figures 4.26, 4.27 and 4.28 respectively.

Figure 4.28 shows that the stability of the Stokes cavity is not a problem at the low Stokes output powers observed. The complex shape of the plots in Figure 4.27 highlights the complications for cavity design caused by the fact that the thermal lens in the Raman crystal is proportional to the Stokes output power, which itself depends on many factors including the strength of the thermal lens in the Raman crystal – this tight feedback can be seen in the weaving path taken by the cavity through the $g_1$-$g_2$ plane. However, it appears that the fundamental cavity also remains stable over the

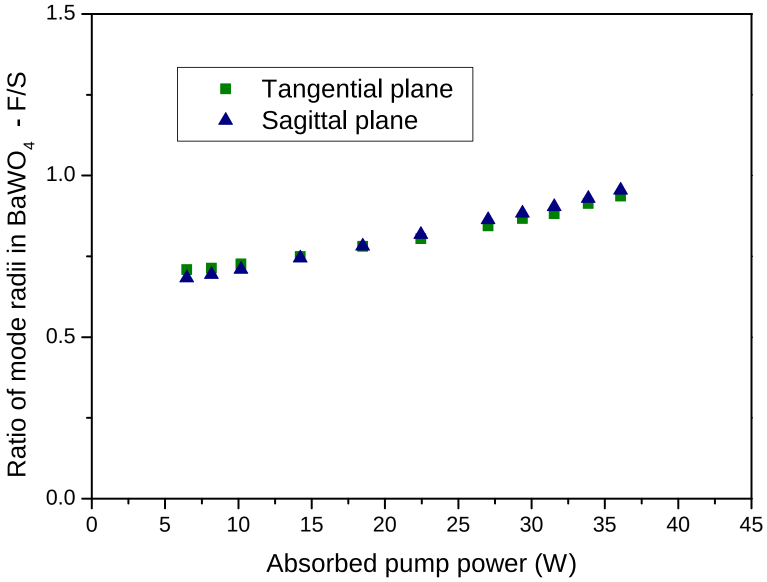

**Figure 4.26:** Ratio of $TEM_{00}$ mode radii of the fundamental and Stokes fields in the $BaWO_4$ crystal as a function of pump power, for Cavity 5. The thermal lenses were calculated using the experimentally measured Stokes power transfer of the laser.

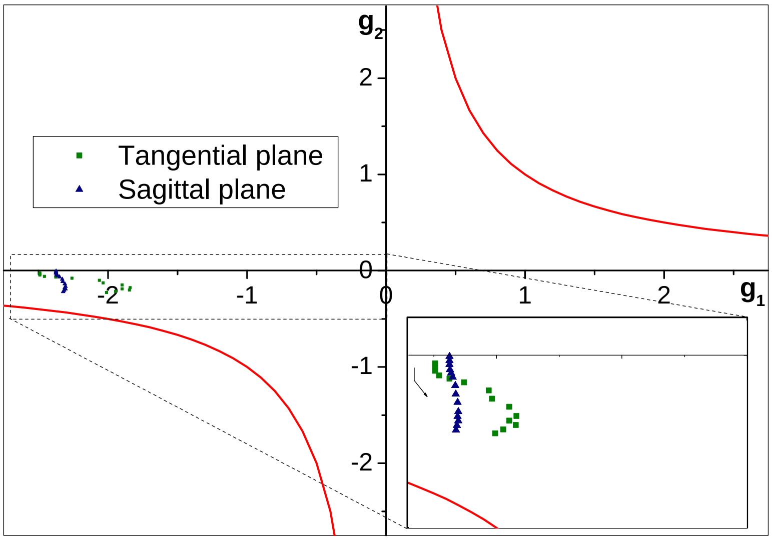

**Figure 4.27:** Variation of the $g_1$-$g_2$ stability parameters for the fundamental resonator in Cavity 5. The arrow in the inset shows the direction of increasing pump power. The thermal lenses were calculated using the experimentally measured Stokes power transfer of the laser.

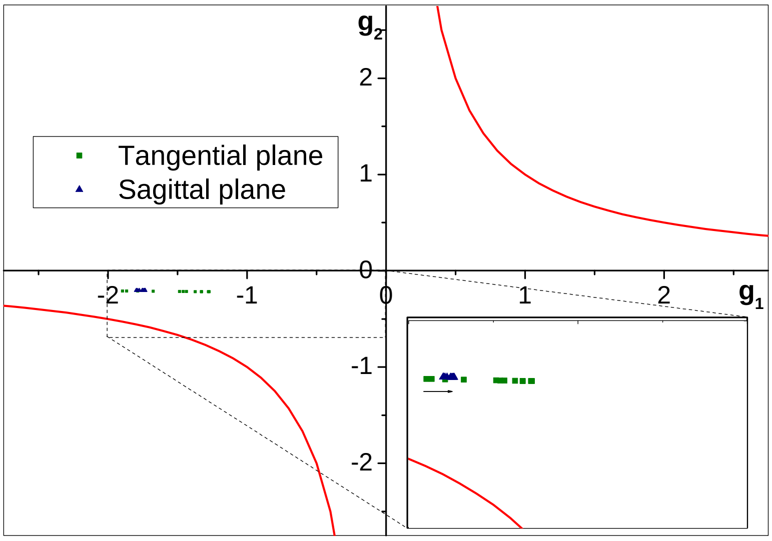

**Figure 4.28:** Variation of the $g_1$-$g_2$ stability parameters for the Stokes resonator in Cavity 5. The arrow in the inset shows the direction of increasing pump power. The thermal lenses were calculated using the experimentally measured Stokes power transfer of the laser.

range of powers considered. The mode overlap in the $BaWO_4$ crystal gradually changes, driven largely by changes in the mode size of the fundamental field – the thermal lens in the $BaWO_4$ crystal is sufficiently weak that the Stokes mode size varies only slightly.

It remains unclear why the 400 µm pump spot radius system performs much more poorly than the 300 µm pump spot radius system. There are many constraints on the cavity design - the fundamental field must have a large radius in the Nd:$YVO_4$ disk, to match the pump spot radius and obtain good beam quality, but a small radius in the $BaWO_4$ crystal to obtain a low Raman threshold. Meeting these requirements while avoiding operating the cavity close to the stability limits can be difficult, and in such cavities the mode sizes are often very sensitive to the thermal lens strengths. Unfortunately there was insufficient time to test out different cavity designs with a 400 µm pump spot radius. With further work, and more detailed investigation of some of the issues described above, it might be possible to improve the performance of the 400 µm pump spot radius system, in order to take full advantage of the weak thermal lens in the Nd:$YVO_4$ disk.

## 4.6 Discussion

A summary of the performance of Raman lasers described in this chapter is given in Table 4.2. A number of insights into the thermal behaviour of intracavity Raman lasers can be drawn from the work presented in this chapter. The disk laser has been shown to be a useful test-bed for investigating the thermal effects in intracavity Raman lasers. The ability to build longer cavities than can be constructed using rod geometries makes it easier to probe the thermal lens in the Raman crystal, as was described in the previous

**Table 4.2:** Summary of Raman laser performance for the cavities tested in this chapter. The Raman thresholds are given in terms of absorbed pump power except where otherwise noted.

| | Raman Threshold/W | Output power/W | Conversion efficiency | Notes |
|---|---|---|---|---|
| Cavity 1 | 1.2 | 1.52 | 14.3 % | At high powers, mode overlap deteriorated. |
| Cavity 2 | 0.74 | 1.71 | 14.0 % | Nd:$YVO_4$ thermal lens drives cavity towards stability limit. |
| Cavity 3 | $3.5^\dagger$ | 2.11 | 7.5 % | Pump power limited |
| Cavity 4 | 4.7 | 3.15 | 9.3 % | Astigmatism of $BaWO_4$ thermal lens may need to be compensated for further improvements. |
| Cavity 5 | 5.6 | 1.25 | 4.6 % | Output power rolled over ∼ 27 W pump power. |

$^\dagger$ Incident pump power.

chapter, and, with the use of a coupled cavity arrangement, makes it possible to chop the Stokes cavity separately, thereby providing information that helps to distinguish the effects of the two thermal lenses. When such experiments are combined with the modelling described here, a picture can be built up of how the cavity changes as the pump power is varied.

This information can then be used to inform the design of improved cavities. It was shown that the negative thermal lens in the $BaWO_4$ crystal helped to stabilise the cavity against the effects of the positive thermal lens in the $Nd{:}YVO_4$ disk. In fact, the problem was generally that the thermal lens in one plane of the $BaWO_4$ crystal was too weak to fulfil this role properly. Since the thermal lens in the $BaWO_4$ is proportional to the Stokes output power, it would be better not to depend on it for cavity stability. Therefore efforts were made to reduce the reliance of the cavity on the $BaWO_4$ thermal lens both by reducing the sensitivity of the cavity to thermal lens in the $Nd{:}YVO_4$ disk (by using a convex end mirror which moved the cavity to a broader region of the stability zone) and by reducing the strength of the thermal lens in the $Nd{:}YVO_4$ disk itself.

To minimise the thermal lens in the $Nd{:}YVO_4$ disk, it is important to use a large a pump spot radius as possible. However, this presents additional challenges to the cavity design, since it becomes necessary to have a large cavity mode size in the $Nd{:}YVO_4$ (to match the pump spot) and a small cavity mode size in the $BaWO_4$ crystal (to keep the Raman threshold low). Such cavities tend to be sensitive to changes in the thermal lens strengths. Another way to reduce the thermal lens in the $Nd{:}YVO_4$ would be to use a thinner disk. With the relatively simple double-pass system used in this work, it should be possible to use a 250 µm thick, 1 at.% $Nd{:}YVO_4$ disk while maintaining a reasonably level of pump absorption ($\sim 82\,\%$, similar to the case of the 500 µm thick, 0.5 at.% $Nd{:}YVO_4$ disk presented in Section 4.4.5). A 250 µm thick disk would have a fairly weak thermal lens even for a 300 µm radius pump spot.

Once the thermal lens in the $Nd{:}YVO_4$ disk has been reduced further, the lens in the $BaWO_4$ crystal will become the limiting factor and some way of dealing with this will need to be found. Prospects for future work are described in the next section.

## 4.7 Conclusions

The process of improving the design of a $Nd{:}YVO_4$-disk/$BaWO_4$-rod CW intracavity Raman laser has been presented. Approaches to modelling the effects of the two thermal lenses on the behaviour of the cavity have been described and applied to provide insight into the physics underlying the experimental observations. The disk geometry reduced the thermal lens in the laser gain crystal, making it possible to construct longer and more complex cavities than are conventionally used for intracavity Raman lasers. This provided flexibility of cavity design when attempting to manage the effects of the thermal lenses and also made it easier to probe the thermal behaviour of the laser.

In particular, advantage has been taken of a coupled cavity configuration to partially disentangle the effects of the two thermal lenses by chopping the Stokes cavity only.

The best performance was achieved from a 300 µm pump spot radius system, which produced a maximum Stokes output power of 3.15 W for an absorbed pump power of 33.9 W, representing a diode-to-Stokes conversion efficiency of 9.3 %. The Raman threshold was 4.7 W and the slope efficiency was 11.5 %.

This performance is comparable to many multi-Watt CW crystalline intracavity Raman lasers. For example, the highest reported output power at 1180 nm from a CW intracavity Raman laser based on $BaWO_4$ was demonstrated by Fan *et al* [16], who obtained 3.36 W for an incident pump power of 25.5 W, with a Raman threshold of 3.6 W. Their laser was a conventional rod-based geometry, using Nd:$YVO_4$ as the gain medium and a simple two mirror cavity. The highest CW 1st Stokes output power reported to date from an end-pumped system is 4.1 W from a double-end pumped Nd:$GdVO_4$ self-Raman laser [19], representing a diode-Stokes conversion efficiency of 11.2 % with respect to incident pump power (although the authors calculated that almost all the incident pump power should have been absorbed under the double-end pumping scheme [19]). Meanwhile the highest CW 1st Stokes output power reported to date from any intracavity Raman laser is 6.1 W, from a $KGd(WO_4)_2$ Raman laser in which the laser gain medium was a side-pumped Nd:YLF rod [20]. The conversion efficiency was 4 % with respect to incident pump power in the commercial side-pumped Nd:YLF module.

In summary it has been demonstrated that a Nd:$YVO_4$-disk/$BaWO_4$-rod Raman laser can provide respectable CW performance at the 1st Stokes wavelength, but further work would be required to exceed the performance given by state-of-the-art systems. The experimental and numerical techniques presented here for analysing the behaviour of the system may in future provide a route to higher output powers. In particular, further work to develop a suitable cavity design for a pump spot radius of 400 µm or more could make it possible to take full advantage of the disk geometry, yielding a very weak thermal lens in the laser gain crystal. However, as discussed above, designing a cavity that can mode-match a large pump spot while remaining relatively insensitive to even weak thermal lenses is challenging. Hanna *et al* investigated telescopic resonators to obtain large, and thermally insensitive, $TEM_{00}$ mode radii in a laser gain crystal close to one end mirror of a cavity [21]. Such cavity designs could be applicable to the disk lasers here; however the work of Hanna *et al* only dealt with the single thermal lens in the laser gain material [21] and application of such cavity designs to Raman lasers would have to take account of the thermal lens in the Raman crystal. If cavities could be designed to mode-match large pump spots while maintaining small mode sizes in the Raman crystal then the lens in the Raman crystal would become the limiting factor. Continued power-scaling of a $BaWO_4$-based system would likely require the use of a cylindrical optic in the cavity, or some other mechanism to compensate for astigmatism of the thermal lens in the $BaWO_4$. If high quality diamond could be obtained, as discussed in Chapter 2, then the thermal lens in the Raman crystal would be greatly reduced. If the challenges of designing a suitable cavity for the large pump spot and obtaining low loss diamond can be overcome, then the combination of diamond as a Raman crystal with a large pump spot disk geometry for the laser gain crystal could be an effective way to obtain output powers around 10 W.

# Bibliography

[1] S. M. Hooker and C. E. Webb, *Laser Physics.* Oxford University Press, 2010.

[2] N. Hodgson and H. Weber, *Laser resonators and beam propagation: fundamentals, advanced concepts and applications.* Springer Series in Optical Sciences, Vol 108, Springer, 2nd ed., 2005.

[3] K. Driedger, R. Ifflander, and H. Weber, "Multirod resonators for high-power solid-state lasers with improved beam quality," *IEEE Journal of Quantum Electronics*, vol. 24, pp. 665 –674, Apr 1988.

[4] W. Koechner, *Solid-State Laser Engineering.* Springer, 6th ed., 2006.

[5] H. M. Pask, "The design and operation of solid-state Raman lasers," *Progress in Quantum Electronics*, vol. 27, no. 1, pp. 3–56, 2003.

[6] D. J. Spence, P. Dekker, and H. M. Pask, "Modeling of continuous wave intracavity Raman lasers," *IEEE Journal of Selected Topics in Quantum Electronics*, vol. 13, no. 3, pp. 756–763, 2007.

[7] J. T. Murray, W. L. Austin, and R. C. Powell, "Intracavity Raman conversion and Raman beam cleanup," *Optical Materials*, vol. 11, no. 4, pp. 353 – 371, 1999.

[8] X. Peng, A. Asundi, Y. Chen, and Z. Xiong, "Study of the Mechanical Properties of Nd:$YVO_4$ Crystal by use of Laser Interferometry and Finite-Element Analysis," *Applied Optics*, vol. 40, pp. 1396–1403, Mar 2001.

[9] J. Didierjean, E. Herault, F. Balembois, and P. Georges, "Thermal conductivity measurements of laser crystals by infrared thermography. Application to Nd:doped crystals," *Optics Express*, vol. 16, no. 12, pp. 8995–9010, 2008.

[10] W. Ge, H. Zhang, J. Wang, J. Liu, H. Li, X. Cheng, H. Xu, X. Xu, X. Hu, and M. Jiang, "The thermal and optical properties of $BaWO_4$ single crystal," *Journal of Crystal Growth*, vol. 276, no. 1-2, pp. 208–214, 2005.

[11] W. W. Ge, H. J. Zhang, J. Y. Wang, J. H. Liu, X. G. Xu, X. B. Hu, M. H. Jiang, D. G. Ran, S. Q. Sun, H. R. Xia, and R. I. Boughton, "Thermal and mechanical properties of $BaWO_4$ crystal," *Journal of Applied Physics*, vol. 98, no. 1, p. 013542, 2005.

[12] D. Ran, H. Xia, S. Sun, Z. Ling, W. Ge, and H. Zhang, "Thermal conductivity of $BaWO_4$ single crystal," *Materials Science and Engineering: B*, vol. 130, no. 1-3, pp. 206–209, 2006.

[13] V. A. Orlovich, V. N. Burakevich, A. S. Grabtchikov, V. A. Lisinetskii, A. A. Demidovich, H. J. Eichler, and P. Turpin, "Continuous-wave intracavity Raman generation in $PbWO_4$ crystal in the Nd:$YVO_4$ laser," *Laser Physics Letters*, vol. 3, no. 2, pp. 71–74, 2006.

[14] D. C. Parrotta, A. J. Kemp, M. D. Dawson, and J. E. Hastie, "Tunable continuous-wave diamond Raman laser," *Optics Express*, vol. 19, no. 24, pp. 24165–24170, 2011.

[15] J. Lin, H. M. Pask, D. J. Spence, C. J. Hamilton, and G. P. A. Malcolm, "Continuous-wave VECSEL Raman laser with tunable lime-yellow-orange output," *Optics Express*, vol. 20, pp. 5219–5224, Feb 2012.

[16] L. Fan, Y.-X. Fan, Y.-Q. Li, H. Zhang, Q. Wang, J. Wang, and H.-T. Wang, "High-efficiency continuous-wave Raman conversion with a $BaWO_4$ Raman crystal," *Optics Letters*, vol. 34, no. 11, pp. 1687–1689, 2009.

[17] V. A. Lisinetskii, A. S. Grabtchikov, A. A. Demidovich, V. N. Burakevich, V. A. Orlovich, and A. N. Titov, "Nd:KGW/KGW crystal: efficient medium for continuous-wave intracavity Raman generation," *Applied Physics B*, vol. 88, no. 4, pp. 499–501, 2007.

[18] V. N. Burakevich, V. A. Lisinetskii, A. S. Grabtchikov, A. A. Demidovich, V. A. Orlovich, and V. N. Matrosov, "Diode-pumped continuous-wave Nd:$YVO_4$ laser with self-frequency Raman conversion," *Applied Physics B*, vol. 86, no. 3, pp. 511–514, 2007.

[19] J. Lin and H. Pask, "Nd:$GdVO_4$ self-Raman laser using double-end polarised pumping at 880 nm for high power infrared and visible output," *Applied Physics B: Lasers and Optics*, vol. 108, no. 1, pp. 17–24, 2012.

[20] V. G. Savitski, I. Friel, J. E. Hastie, M. D. Dawson, D. Burns, and A. J. Kemp, "Characterization of Single-Crystal Synthetic Diamond for Multi-Watt Continuous-Wave Raman Lasers," *IEEE Journal of Quantum Electronics*, vol. 48, no. 3, pp. 328 –337, 2012.

[21] D. C. Hanna, C. G. Sawyers, and M. A. Yuratich, "Telescopic resonators for large-volume $TEM_{00}$-mode operation," *Optical and Quantum Electronics*, vol. 13, pp. 493–507, 1981.

# Chapter 5

# Spectral broadening in intracavity Raman lasers

In this chapter, work will be presented on the widely-observed broadening of the fundamental spectrum in intracavity Raman lasers. The mechanism behind this broadening will be outlined, and experimental observations comparing the fundamental spectrum of a laser with and without Raman conversion will be presented. An investigation into the effect of the Raman linewidth by comparing two materials with substantially different Raman linewidths, $BaWO_4$ and $KGd(WO_4)_2$, will be presented. The impact of the spectral broadening on the effective Raman gain will be analysed numerically, and experiments to assess the benefits of controlling the spectral behaviour of the laser with etalons will be presented. Much of the theoretical work in Section 5.2 was developed with the assistance of Associate Professor David Spence of Macquarie University and it is presented to here to lay out the context for the experimental work in this chapter, all of which was carried out by the author.

## 5.1 Previous observations of spectral broadening

Broadening of the fundamental spectrum has been observed in a number of intracavity Raman lasers. Dekker *et al* [1] observed complex structure developing in the fundamental and Stokes spectra of their frequency-doubled $Nd:GdVO_4$ self-Raman laser, with a second fundamental peak at 1066 nm appearing at high powers. This was attributed to the SRS-induced loss for the main transition at 1063 nm permitting the orthogonal 1066 nm transition to reach threshold [1]. The same group also observed spectral broadening in a frequency-doubled $Nd:GdVO_4/KGd(WO_4)_2$ system [2], with the fundamental field reaching a bandwidth of approximately 1 nm. The authors noted that the spectrum was most stable when the SRS conversion process strongly depleted the circulating fundamental field. Fan *et al* [3] noted that the fundamental bandwidth varied from 0.15 nm to 0.55 nm in their $Nd:YVO_4/SrWO_4$ Raman laser, while the Stokes bandwidth varied from 0.05 nm to 0.35 nm, although the authors did not explicitly state the pump powers at which these measurements were made. Some of the same researchers observed similar broadening in a $YVO_4$/Nd:$YVO_4$/$YVO_4$ Raman laser [4], with the fundamental spectrum broadening from 0.23 nm at the Raman threshold to 1.09 nm at maximum power, while the Stokes spectral width varied from 0.14 nm to 0.52 nm. Some complex spectral structure was noted [4]. The same group also observed spectral broadening in a Nd:$YVO_4$/$BaWO_4$ laser [5], in which the fundamental peak broadened from 0.2 nm at the Raman threshold to 1.05 nm at maximum pump power, whilst the Stokes peak broadened from 0.15 nm to 0.5 nm. Lisinetskii *et al* [6] observed that the fundamental field in their Nd:$KGd(WO_4)_2$/$KGd(WO_4)_2$ laser broadened from $5\,\mathrm{cm}^{-1}$ to $24\,\mathrm{cm}^{-1}$ (0.6 nm to 2.7 nm)

Such spectral broadening is therefore often observed in intracavity Raman lasers, but, to the best of the author's knowledge, there has not been any detailed study of this phenomenon.

## 5.2 Theory of spectral broadening

### 5.2.1 Simple model of an ideal Raman laser

In order to understand the interplay between the fundamental and Stokes fields and the Raman crystal, it is useful to first consider an idealised picture of the behaviour of an intracavity Raman laser. As the pump power is increased from zero, the small signal fundamental gain coefficient increases. Once the fundamental gain equals the round-trip losses at the fundamental wavelength, the fundamental field oscillates in the cavity. As the pump power is increased further, the intracavity field saturates the gain such that the fundamental gain coefficient is clamped to its threshold value. Meanwhile the intensity of the fundamental field increases. Now the Raman gain at the Stokes wavelength is proportional to the intensity of the fundamental field and therefore increases also. Eventually the intensity of the fundamental field is high enough that the Raman gain equals the losses at the Stokes wavelength and the Stokes field will oscillate. As the pump power is increased further, the intensity of the Stokes field now grows. To maintain a steady state, the Raman gain must be clamped equal to the round-trip losses at the Stokes wavelength, which means that the intensity of the fundamental field must be clamped at the value it has at the Raman threshold. However, since the loss presented to the fundamental field due to the stimulated Raman scattering (SRS) is proportional to the rising Stokes intensity, the gain at the fundamental also rises so as to balance out the round-trip losses. The variation of the fundamental and Stokes gain and intensity with pump power is illustrated in Figure 5.1.

It was noted in Chapter 4 that in the laser systems described in this thesis, the intensity of the fundamental field did not clamp at the Raman threshold value (for example see Figure 4.9). This suggests that energy is “leaking” into other modes of the fundamental – spectral, spatial or both. Other researchers have observed clamping of

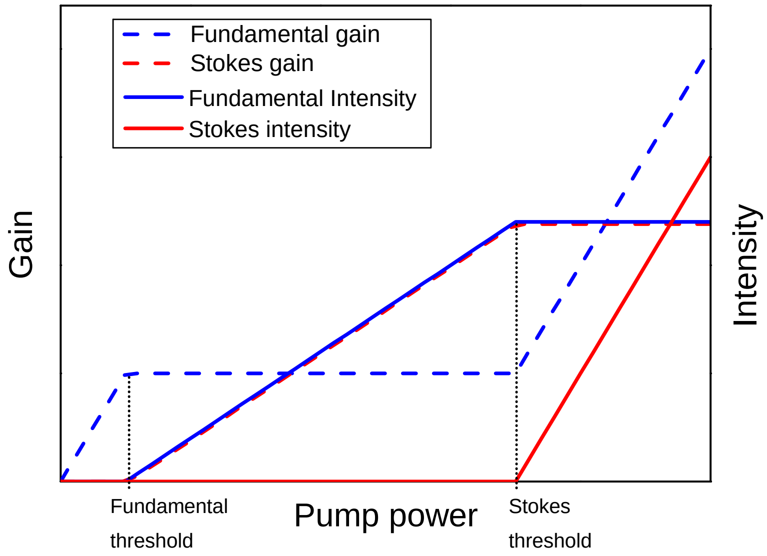

**Figure 5.1:** The variation of the gain and intensity at the fundamental and Stokes wavelengths in an idealised model Raman laser.

the fundamental intensity in some systems [7–9], but in other devices the fundamental intensity continued to increase above the Raman threshold [5, 6, 10]. In some cases this was attributed to broadening of the fundamental spectrum [6, 10]. In this chapter, the spectral behaviour of intracavity Raman lasers will be considered in much more detail.

### 5.2.2 Spectral broadening mechanism

The above description assumes that the laser and Raman transitions, and fundamental and Stokes fields are all delta functions in frequency. However, in reality the fundamental gain and the Raman transition have some finite width, and so the spectral width of the fields depends upon the material properties of the crystals involved and the details and operational parameters of the particular laser cavity, which together determine how many axial modes of the cavity can oscillate. If the laser gain is homogeneously broadened, and if spatial hole burning is neglected, then the first axial mode of the fundamental field to reach threshold (usually the mode closest to the central frequency of the transition) clamps the gain and thus prevents other modes from oscillating. This is also the situation in an intracavity Raman laser below the Raman threshold (again assuming homogeneous broadening of the laser transition and no spatial hole burning), and it is illustrated in Figure 5.2 (a), where a Lorentzian gain profile and spectrally flat losses have been assumed.

Above the Raman threshold, SRS presents a spectrally-varying loss to the fundamental field over and above the spectrally flat parasitic losses in the cavity. This SRS-induced loss is the fraction of the fundamental radiation converted to Stokes radiation on each round trip, and is related to the second term on the right hand side of the rate equation for the fundamental power given in Chapter 1 (Equation 1.11b). The spectral profile of this loss depends on the profile of the Raman transition (a material property) and the spectral profile of the fundamental and Stokes fields. If both the fields are single mode and treated as delta functions, then the profile of the loss to the fundamental due to Raman conversion is the same as that of the Raman transition. In order to maintain a steady state, the fundamental gain at the frequency of the oscillating mode must increase such that the gain ($\alpha_{\mathrm{F}}$) equals the parasitic loss ($\gamma_{\mathrm{F}}$) plus the loss to the fundamental due to Raman conversion ($\Gamma$). This is shown in Figure 5.2 (b)-(d) for various ratios of the fundamental gain bandwidth, $\Delta\nu_{\mathrm{F}}$, and the Raman linewidth, $\Delta\nu_{\mathrm{R}}$, which are defined here as the full widths at half maximum (FWHM) of the stimulated emission cross-section of the laser gain crystal and the Raman peak of the Raman crystal respectively. Lorentzian lineshapes have been assumed for both the fundamental gain and the Raman transition. It can be seen that if the Raman line is narrow

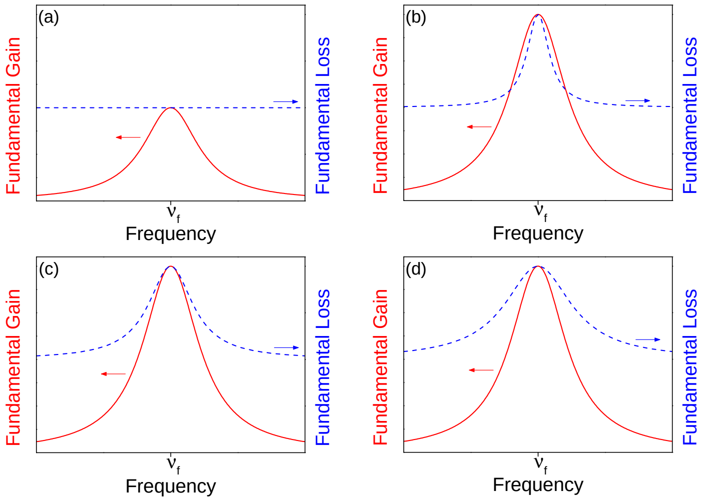

**Figure 5.2:** Gain and loss at the fundamental frequency (a) below Raman threshold and (b)-(d) above Raman threshold for various ratios of the fundamental gain bandwidth ($\Delta\nu_{\mathrm{F}}$) and the Raman linewidth ($\Delta\nu_{\mathrm{R}}$). (b) $^{\Delta\nu_{\mathrm{R}}}/_{\Delta\nu_{\mathrm{F}}} = 0.2$, (c) $^{\Delta\nu_{\mathrm{R}}}/_{\Delta\nu_{\mathrm{F}}} = 0.8$, (d) $^{\Delta\nu_{\mathrm{R}}}/_{\Delta\nu_{\mathrm{F}}} = 1.2$.

compared to the laser gain (Figure 5.2 (b)) then modes of the fundamental adjacent to the central mode will also have gain greater than the round-trip loss and hence can oscillate, leading to broadening of the fundamental spectrum. On the other hand, if the Raman line is broad compared to the laser gain (Figure 5.2 (d)), then this broadening of the fundamental spectrum does not occur. Figure 5.2 (c) shows an intermediate case, where the Raman line is only slightly narrower than the laser gain. In this case there will be a regime above the Raman threshold where no SRS-induced broadening occurs, but as the power is increased such broadening will eventually occur.

A more detailed analysis of this phenomenon will now be presented, with a view to understanding the regimes in which it is significant. The potential for spectral broadening of the fundamental can be determined by considering the net gain for the fundamental. The net gain for the fundamental is the gain minus the total losses, and

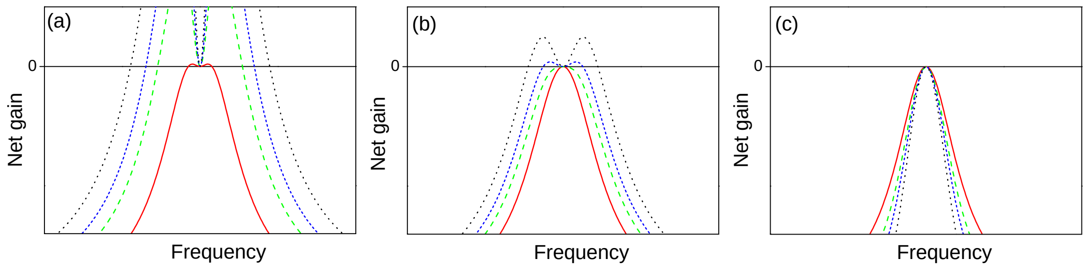

**Figure 5.3:** The net fundamental gain as a function of frequency for various ratios of the fundamental gain bandwidth and the Raman linewidth (a) $\Delta\nu_\mathrm{R}/\Delta\nu_\mathrm{F} = 0.2$, (b) $\Delta\nu_\mathrm{R}/\Delta\nu_\mathrm{F} = 0.8$, (c) $\Delta\nu_\mathrm{R}/\Delta\nu_\mathrm{F} = 1.2$. The different lines on each graph show the net gain for various pump powers above the fundamental threshold: solid red line, $\alpha_\mathrm{F}/\gamma_\mathrm{F} = 1.3$; green dashes, $\alpha_\mathrm{F}/\gamma_\mathrm{F} = 2.6$; short blue dashes, $\alpha_\mathrm{F}/\gamma_\mathrm{F} = 3.5$; and black dots, $\alpha_\mathrm{F}/\gamma_\mathrm{F} = 5$.

is shown here as a function of frequency:

$$\text{Net gain} = \alpha_\mathrm{F}(\nu) - \Gamma(\nu) - \gamma_\mathrm{F} \tag{5.1}$$

where $\alpha_\mathrm{F}(\nu)$ is the fundamental gain, $\Gamma(\nu)$ is the loss to the fundamental due to SRS and $\gamma_\mathrm{F}$ is the parasitic loss to the fundamental. The net gain must be zero (or less in the case of non-oscillating modes) in order for a steady state to be maintained in the laser. The net gain is plotted in Figure 5.3 for various laser gain and Raman linewidths and for various values of $\alpha_\mathrm{F}/\gamma_\mathrm{F}$. It can be seen in Figure 5.3 (a) and (b) that when the Raman line is narrower than the fundamental gain, broadening of the fundamental spectrum will eventually occur as the pump power is increased. The narrower the Raman line, the lower the value of $\alpha_\mathrm{F}/\gamma_\mathrm{F}$ at which broadening of the spectrum can occur (for example in Figure 5.3 (a), for a linewidth ratio of $\Delta\nu_\mathrm{R}/\Delta\nu_\mathrm{F} = 0.2$, broadening can occur when $\alpha_\mathrm{F}/\gamma_\mathrm{F} = 1.3$). If the Raman line is broader than the laser gain (as in Figure 5.3 (c)), then broadening will not occur no matter how far above threshold the laser is pumped. It should be noted that $\alpha_\mathrm{F}$ is the saturated gain coefficient, not the small signal gain coefficient, and therefore the ratio $\alpha_\mathrm{F}/\gamma_\mathrm{F}$ is *not* exactly equivalent to the number of times above threshold that the laser is being pumped but is simply indicative of how far above the fundamental threshold the laser is operating.

The situation can be analysed more quantitatively by differentiating Equation 5.1 twice with respect to frequency and setting the derivative equal to zero at the centre of the fundamental transition [11]. This represents the point at which the curvature of the net gain curve changes from positive to negative, and hence the point beyond which the wings of the curve may be above zero. If we do this then we find that broadening may occur when

$$\frac{\alpha_\mathrm{F}}{\gamma_\mathrm{F}} \geq \frac{1}{1 - \left(\frac{\Delta\nu_\mathrm{R}}{\Delta\nu_\mathrm{F}}\right)^2} \tag{5.2}$$

or equivalently

$$\frac{\Gamma}{\gamma_{\mathrm{F}}} \geq \frac{1}{1-\left(\frac{\Delta\nu_{\mathrm{R}}}{\Delta\nu_{\mathrm{F}}}\right)^2} - 1. \tag{5.3}$$

The ratio $\Gamma/\gamma_{\mathrm{F}}$ is the ratio of the fraction of the fundamental radiation converted to Stokes radiation to the fraction of the fundamental radiation lost to parasitic losses. Since $\Gamma$ is proportional to the Stokes intensity, this ratio increases as pump power is increased above the Raman threshold (assuming a linear increase in Stokes intensity above the Raman threshold) and for an intracavity Raman laser to be efficient it needs to be operated in a regime where $\Gamma/\gamma_{\mathrm{F}} \gg 1$. Therefore, if Equation 5.3 gives a value of $\Gamma/\gamma_{\mathrm{F}}$ that is much greater than 1, then the Raman laser can be operated efficiently without SRS-induced spectral broadening occurring. However, if Equation 5.3 gives a value of $\Gamma/\gamma_{\mathrm{F}}$ that is close to or less than 1, then spectral broadening will have an effect before the Raman laser reaches an efficient operating point.

It should be noted that this simplified analysis breaks down as soon as the wings of the gain profile reach threshold, since these neighbouring modes may themselves be Raman-shifted, leading to complex behaviour as the SRS process "follows" the fundamental spectrum. In other words, this analysis gives no indication of the likely extent of the spectral broadening, merely the point at which spectral broadening is likely to occur.

The Raman linewidths of several Raman crystals are given in Table 5.1 along with the gain bandwidth of the laser gain material used in this thesis, Nd:$YVO_4$, and several other common Nd-doped laser crystals. The ratio of $\Gamma/\gamma_{\mathrm{F}}$ above which SRS-induced broadening is to be expected is plotted as a function of Raman linewidth in Figure 5.4, for a variety of Nd-doped laser gain crystals. The Raman linewidths of $BaWO_4$, diamond and $KGd(WO_4)_2$ are noted on the graph. In order to avoid SRS-induced spectral

**Table 5.1:** Laser gain and Raman linewidths of various crystals. Values given are full widths at half maximum (FWHM).

| | Wavelength/nm | Laser gain bandwidth/cm$^{-1}$ |
|---|---|---|
| Nd:$YVO_4$ | 1064 | 9.7 [12] |
| Nd:$GdVO_4$ | 1063 | 8.8 [13] |
| Nd:YAG | 1064 | 5.3 [14] |
| Nd:YLF | 1047/1053 | 12 [15] |
| | **Stokes shift/cm$^{-1}$** | **Raman linewidth/cm$^{-1}$** |
| $BaWO_4$ | 925 | 1.6 [16] |
| Diamond | 1333 | 2.7 [17] |
| $KGd(WO_4)_2$ | 901 | 5.4 [17] |
| $KGd(WO_4)_2$ | 768 | 6.4 [17] |
| $LiNbO_3$ | 872 | 21.4 [17] |

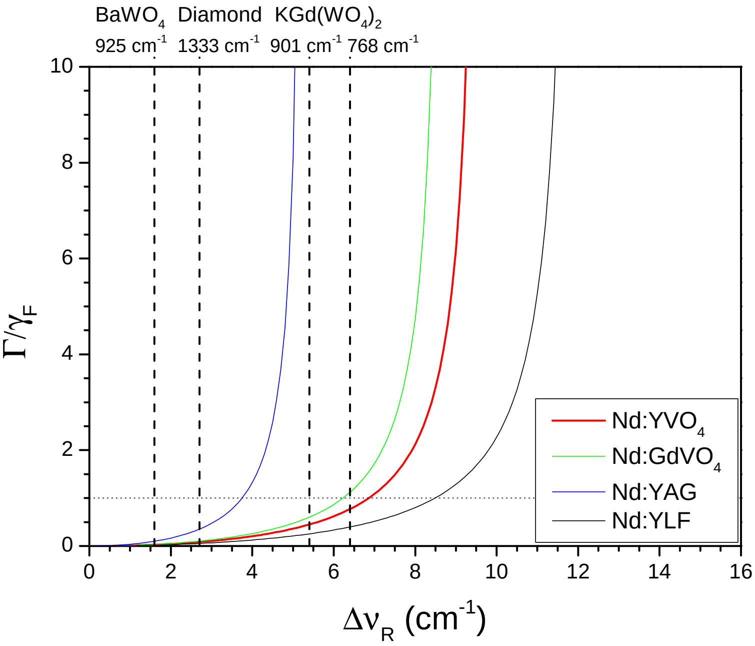

**Figure 5.4:** The ratio of $\Gamma/\gamma_F$ above which SRS-induced broadening of the fundamental field would be expected for a variety of Nd-doped laser gain crystals as a function of Raman linewidth. The linewidths of several Raman crystals are highlighted: $BaWO_4$, diamond and $KGd(WO_4)_2$ (for which both main Raman transitions are shown).

broadening, it is desirable for the curve for the laser gain crystal to cross the line for the Raman linewidth at as high a value as possible, preferably a value much greater than 1.

It can be seen from Figure 5.4 that SRS-induced broadening is practically unavoidable when using $BaWO_4$ or diamond as the Raman crystal, since these have very narrow Raman transitions. On the other hand, SRS-induced spectral broadening is unlikely to occur in a Nd:YAG/$KGd(WO_4)_2$ Raman laser, especially if the 768 $cm^{-1}$ Raman-shift is used, since Nd:YAG has a relatively narrow gain bandwidth and the 768 $cm^{-1}$ transition in $KGd(WO_4)_2$ is relatively broad. However, on the whole, most combinations of common Nd-doped laser crystals and common Raman crystals will create the potential for SRS-induced broadening since the main transitions of most Raman crystals have linewidths of only a few wavenumbers. $LiNbO_3$ is unusual in having an exceptionally broad Raman transition around 872 $cm^{-1}$ with a linewidth of 21.4 $cm^{-1}$ [17], which is off the x-axis scale in Figure 5.4. The above analysis would predict that a Raman laser based on Nd:$YVO_4$ and $LiNbO_3$ would not exhibit SRS-induced broadening of the fundamental spectrum.

### 5.2.3 Effective Raman gain for broadband fundamental field

The impact of spectral broadening on the effective Raman gain will now be considered. The theoretical analysis in this section is based on as yet unpublished work by A/Prof. David Spence of Macquarie University [11]. It is given here to set out the context and motivation for the work of the author presented in the rest of this chapter, in which a detailed experimental investigation of spectral broadening effects was undertaken.

In Chapter 1, the results of the standard theory of SRS were briefly outlined. In particular it was stated that

$$\frac{\mathrm{d}I_{\mathrm{S}}}{\mathrm{d}z} = g_{\mathrm{R}} I_{\mathrm{F}} I_{\mathrm{S}} \tag{5.4}$$

where $I_{\mathrm{F}}$ and $I_{\mathrm{S}}$ are the local fundamental and Stokes intensities and $g_{\mathrm{R}}$ is the Raman gain coefficient.

The standard theory of SRS [18] assumes a narrow fundamental spectrum, which means that the Raman gain takes on the spectral profile of the Raman transition, which is assumed to be homogeneously broadened and therefore Lorentzian [18]. However, the situation becomes more complicated if the fundamental spectrum is broad. The finite bandwidth of the Raman transition means that a given mode of the fundamental can contribute to the growth of several Stokes modes. Conversely, a given Stokes mode can be amplified by gain arising from several modes of the fundamental.

The effect of this on the Raman gain depends on the degree of dispersion in the material. A broad spectral bandwidth corresponds, in the time domain, to fast amplitude and phase fluctuations. In the absence of dispersion, the amplitude and phase fluctuations in the Stokes field are driven to reproduce those in the fundamental field and so the Raman gain is unaffected [19]. However, in the presence of dispersion, the fundamental and Stokes fields have different group velocities and therefore corresponding features in the fields walk off each other as the fields propagate. If the intensity is sufficiently high that the amplitude and phase fluctuations of the fundamental are imprinted on the Stokes field before this walk-off occurs, then the effects of dispersion can be ignored. However, if the intensity is low, then the structure in the fields misaligns before significant energy transfer has occurred, and the structures in the Stokes field and the fundamental field remain uncorrelated. The fast phase fluctuations between the Stokes and fundamental fields prevent the phonon field reaching its steady-state value and the effective Raman gain is reduced [11, 20, 21]. A critical fundamental intensity can be defined, which provides an indication of whether dispersion is significant or not in a given case [11, 21]:

$$I_{\mathrm{cr}} = \frac{\left(n_{\mathrm{S}}^{\mathrm{g}} - n_{\mathrm{F}}^{\mathrm{g}}\right)}{c g_{\mathrm{R}}} \Delta\omega_{\mathrm{F}} = \frac{2\pi \left(n_{\mathrm{S}}^{\mathrm{g}} - n_{\mathrm{F}}^{\mathrm{g}}\right)}{g_{\mathrm{R}}} \frac{\Delta\lambda_{\mathrm{F}}}{\lambda_{\mathrm{F}}^{2}} \tag{5.5}$$

where $n_{\mathrm{F}}^{\mathrm{g}}$ and $n_{\mathrm{S}}^{\mathrm{g}}$ are the group indexes at the fundamental and Stokes wavelengths, $c$ is the speed of light, and $\Delta\omega_{\mathrm{F}}$ and $\Delta\lambda_{\mathrm{F}}$ are the FWHM of the fundamental spectrum in frequency and wavelength space respectively. If the fundamental intensity is much greater than $I_{\mathrm{cr}}$, then the effects of dispersion are negligible; however, if the fundamental intensity is much less than $I_{\mathrm{cr}}$, then the effective Raman gain will be reduced.

Much of the work in the literature on SRS with broadband pump/fundamental fields applies to gas lasers, with no dispersion (for example [20]). However, in crystalline CW intracavity Raman lasers, dispersion needs to be taken into account. For example, if Equation 5.5 is evaluated for a $\mathrm{BaWO_4}$ Raman laser with $g_\mathrm{R} = 8.5\,\mathrm{cm\,GW^{-1}}$, operating at 1064 nm with a fundamental spectral width of 1 nm, then the critical intensity is found to be $28\,\mathrm{MW\,cm^{-2}}$, while the fundamental intensity in the $\mathrm{BaWO_4}$ crystal in the CW systems described in the previous chapter is approximately $1\,\mathrm{MW\,cm^{-2}}$ (based on the data presented in Figure 4.9). Therefore, dispersion is significant and the effective Raman gain will be reduced when the fundamental spectrum is broad. Georges [21] derived the result that for the high dispersion regime, the Raman gain is reduced by a factor of $\Delta\tilde{\nu}_\mathrm{R}/\left(\Delta\tilde{\nu}_\mathrm{R} + \Delta\tilde{\nu}_\mathrm{F}\right)$ where $\Delta\tilde{\nu}_\mathrm{F}$ is the FWHM of the fundamental field. This result was derived for the case of a delta function Stokes spectrum, but in fact broad Stokes spectra are also often observed in the Raman lasers of interest here. The fuller treatment of the CW crystalline Raman laser case developed by A/Prof. David Spence of Macquarie University [11] will now be summarised.

In this regime, the effect can best be analysed in the frequency domain. SRS can be viewed as a $\chi^{(3)}$ four-wave-mixing process [18], in which the four waves are two longitudinal modes of the fundamental field and two longitudinal modes of the Stokes field. One of the fundamental modes beats together with one of the Stokes modes, driving the coherent phonon field. The other fundamental wave then scatters off this phonon field, driving the fourth wave - the Stokes mode experiencing gain. If the fields are single mode then we can write this as [11, 18]

$$\frac{\mathrm{d}E_\mathrm{S}}{\mathrm{d}z} \propto (E_\mathrm{S}E_\mathrm{F}^*)E_\mathrm{F} \tag{5.6}$$

where $E_\mathrm{F}$ and $E_\mathrm{S}$ are the complex amplitudes of the fundamental and Stokes fields respectively. The term in the brackets can be considered to be the phonon field. This equation demonstrates the “automatic phase-matching” of SRS - the phase of the fundamental field drops out, since the complex amplitude of the field is multiplied by its complex conjugate, and hence the Stokes field is driven coherently for any phase of the fundamental field.

When the fundamental and Stokes fields are multimode, a given Stokes mode can be driven by many combinations of fundamental and Stokes modes. In this case, the sum of all these contributions must be taken and the rate of change of a particular Stokes mode, $s_k$, is given by [11, 19]

$$\dot{s_k} \propto \sum_{ij} g_j (s_i f_{i-j}^*) f_{k-j} \tag{5.7}$$

where $f_i$ is the complex amplitude of the $i$-th fundamental mode. The sum is taken over all combinations of $i$ and $j$ such that energy is conserved, and $g_j$ gives the Raman gain. For terms that are resonant ($j = 0$), $g_j = g_\mathrm{R}$, while $g_j < g_\mathrm{R}$ off-resonance.

If there is no dispersion, then all combinations of two fundamental and two Stokes modes that conserve energy will contribute to the gain. However, in CW crystalline

Raman lasers dispersion causes the modes within the fundamental spectrum to change phase relative to one another, and the same thing happens to the modes within the Stokes spectrum. This limits which combinations of fundamental and Stokes modes can coherently drive the Stokes field and results in a reduction in the effective Raman gain. In this case only the degenerate terms in Equation 5.7 ($k = i$) contribute significantly to the overall gain:

$$\dot{s_k} \propto s_k \sum_j g_j |f_{k-j}|^2. \tag{5.8}$$

This means that if we wish to use the spectrally integrated intensities in Equation 5.4 then we must modify the Raman gain coefficient. Equation 5.8 is a sum of the intensities of the fundamental modes weighted by the Raman transition profile. With narrowly spaced modes, we can generalise this discrete sum to a convolution of the Raman gain profile with the fundamental spectrum. Therefore, if $g_{\mathrm{R}}$ is the conventional steady state Raman gain coefficient then the effective gain coefficient is

$$g_{\mathrm{eff}} = \varepsilon g_{\mathrm{R}} \tag{5.9}$$

where

$$\varepsilon = \int \left(\bar{R}(\tilde{\nu}) \otimes \bar{F}(\tilde{\nu})\right) \cdot \bar{S}(\tilde{\nu})\,\mathrm{d}\tilde{\nu}. \tag{5.10}$$

$\bar{F}(\tilde{\nu})$ and $\bar{S}(\tilde{\nu})$ are the fundamental and Stokes spectra respectively, normalised to area, and $\bar{R}(\tilde{\nu})$ is the Raman lineshape, normalised to have a peak value of 1. $\tilde{\nu}$ is the wavenumber. The term in brackets in Equation 5.10 (the convolution of the Raman lineshape with the fundamental spectrum) is the gain available to the Stokes field as a function of frequency. By taking the overlap integral of this spectral gain with the Stokes spectrum, the total effective Raman gain can be calculated. In this way, Equation 5.10 can be used to calculate the reduction in the effective Raman gain due to spectral broadening for a real laser, by using measured fundamental and Stokes spectra [11].

It is instructive to consider the simple case where the fundamental spectrum, the Stokes spectrum and the Raman peak are all Lorentzians, with FWHM of $\Delta\tilde{\nu}_{\mathrm{F}}$, $\Delta\tilde{\nu}_{\mathrm{S}}$ and $\Delta\tilde{\nu}_{\mathrm{R}}$, respectively. If Equation 5.10 is evaluated for this simple case, then it is found that the gain is reduced by a factor of

$$\varepsilon = \frac{\Delta\tilde{\nu}_{\mathrm{R}}}{\Delta\tilde{\nu}_{\mathrm{F}} + \Delta\tilde{\nu}_{\mathrm{S}} + \Delta\tilde{\nu}_{\mathrm{R}}}. \tag{5.11}$$

To get an approximate indication of the potential impact of this effect, it is useful to consider the laser described in [5]. In this paper, Fan *et al* reported the highest power CW intracavity Raman laser based on $BaWO_4$ to date, demonstrating an output power of 3.36 W for an incident diode pump power of 25.5 W [5]. The laser gain material was Nd:$YVO_4$, as in the lasers described in this thesis. The authors of [5] reported fundamental and Stokes linewidths of 1.05 nm (9.3 $\mathrm{cm}^{-1}$) and 0.5 nm (4.4 $\mathrm{cm}^{-1}$) respectively at maximum pump power. Inserting these values into Equation 5.11, along with the Raman linewidth for $\mathrm{BaWO_4}$ from Table 5.1 (1.6 $\mathrm{cm}^{-1}$), $\varepsilon$ can be calculated to be 0.1, representing an order of magnitude reduction in the Raman gain. Note that here it has been assumed that Fan *et al* [5] quoted the spectral widths as FWHM values, and that the spectral peaks were Lorentzian. This latter assumption in particular is likely to represent something of an approximation, given that complex spectral structure has been noted by a number of researchers [1, 4] and therefore to accurately calculate $\varepsilon$ it would be necessary to perform the convolution and overlap integral of Equation 5.10 on the full spectral data. Nonetheless, it is clear that the reduction in the effective Raman gain due to spectral broadening could be a very significant effect, and more detailed experimental investigation is warranted. In the following sections, experiments investigating spectral broadening in Raman lasers using different Raman crystals will be presented, along with an investigation into the effect of using etalons to control the fundamental bandwidth.

## 5.3 Observations of spectral broadening in a Nd:$\mathrm{YVO_4}$ /$\mathrm{BaWO_4}$ laser

### 5.3.1 Experimental setup

The laser cavity used in these experiments is shown in Figure 5.5. The disk laser and pump geometry were of the design described in previous chapters. The Nd:$\mathrm{YVO_4}$ disk was 0.5 mm thick and had a doping concentration of 1 at.%, whilst the diamond heatspreader was 0.75 mm thick. The pump spot radius was 300 µm. A typical power transfer is shown in Figure 5.6.

The spectrum of the laser was measured using an Ocean Optics HR4000 spectrometer, with an optical resolution of 0.08 nm over 1050 nm to 1190 nm. Light was coupled

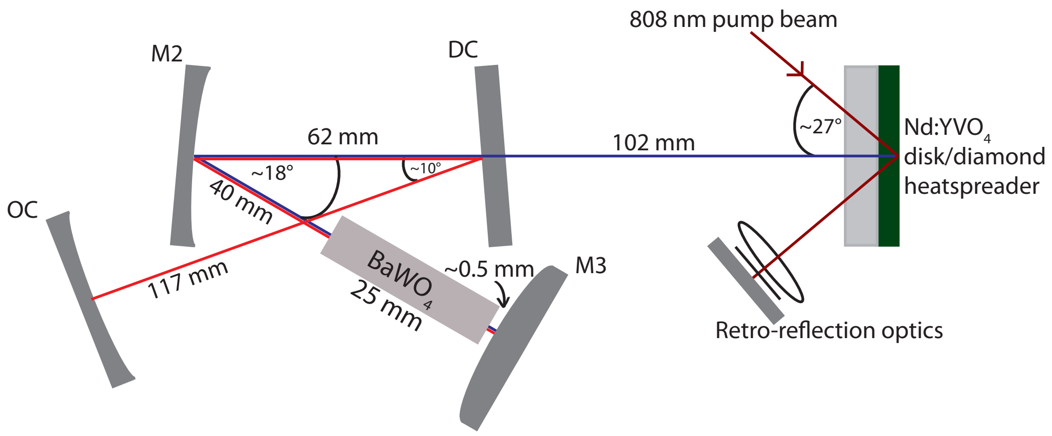

**Figure 5.5:** Cavity design for measurements of spectral broadening in $\mathrm{BaWO_4}$ Raman laser.

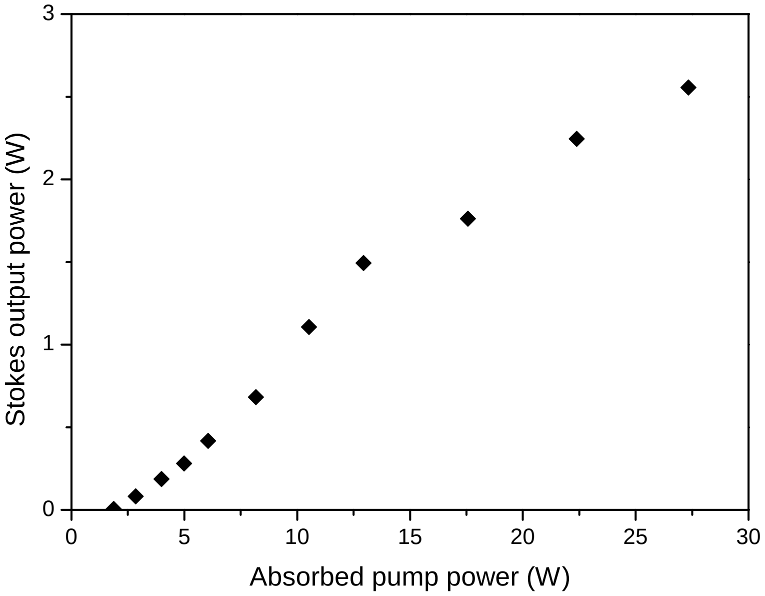

**Figure 5.6:** Typical power transfer for the $BaWO_4$ Raman laser.

into the spectrometer using a 200 µm diameter fibre. The detection optics are shown in Figure 5.7. Due to the coupled cavity configuration and the extremely high reflectivity of mirror M2 at the Stokes wavelength of 1180 nm, there was no single beam from the laser that contained measurable amounts of both the fundamental and Stokes wavelengths. Therefore the fundamental was measured using the radiation leaking through M2, and a glass wedge was used to pick off a small fraction of the output Stokes beam. A series of highly reflecting mirrors and a dichroic mirror were used to make the Stokes beam pick-off and the fundamental beam collinear. After this both beams were focussed into the spectrometer fibre using a 75 mm focal length lens. A ground glass diffuser

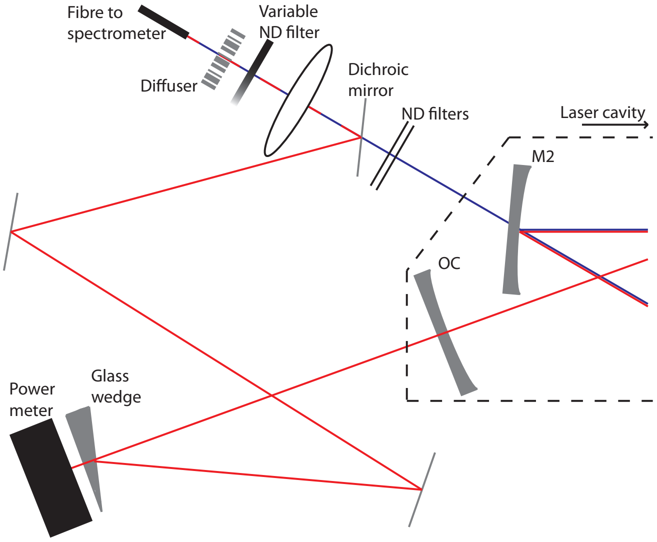

**Figure 5.7:** Experimental apparatus for coupling both fundamental and Stokes beams into HR4000 spectrometer while monitoring the Stokes output power.

was placed in front of the fibre to minimise any dependence of the measured spectrum on the spatial coupling of the two beams into the fibre. Fixed neutral density (ND) filters were used to balance the power of the detected beams, while a variable ND filter was used to keep the maximum intensity incident on the spectrometer approximately constant over the range of pump powers used.

### 5.3.2 Spectral data

The spectra of the $BaWO_4$ Raman laser for various output powers are shown in Figure 5.8. Note that the power transfer in Figure 5.6 was measured simultaneously with the spectra in Figure 5.8. All the spectra shown in this chapter were recorded with an integration time of 80 ms and averaged over 40 scans. The fundamental and Stokes spectra have each been separately normalised to area over ranges of about 10 nm, so that each trace represents the frequency spectrum of essentially the same number of fundamental or Stokes photons as appropriate. Accordingly, a decrease in the peak height can be interpreted as a general broadening of the spectrum. Note that the spectra are plotted with respect to a linear wavenumber axis at the bottom of each plot, while the corresponding (nonlinear) wavelength axis is shown at the top. The origins of the fundamental and Stokes plots are separated in wavenumber by the nominal Stokes shift. Therefore, features in corresponding fundamental and Stokes plots which line up vertically are separated by the Stokes shift. The MATLAB script for the normalisation routine is reproduced in Appendix B.

It can be seen that the fundamental spectrum broadens significantly as the pump power increases, from approximately $2.5\,\mathrm{cm}^{-1}$ below Raman threshold to over $9\,\mathrm{cm}^{-1}$ at high pump powers. These spectral widths are similar to those observed by Fan *et al* in another $Nd{:}YVO_4/BaWO_4$ Raman laser [5]. In order to investigate the extent to which this broadening is due to SRS, spectra were also taken with the Stokes cavity blocked, such that no SRS occurred and the fundamental field oscillated in a high Q cavity, and also for a simple 3 mirror cavity with an output coupler of 10 % transmission at 1064 nm. These spectra are shown in Figures 5.9 and 5.10 respectively. In Figure 5.9, the fundamental spectra for normal Raman laser operation (from Figure 5.8) are re-plotted as a black overlay for comparison. In all three cases, a red-shift of the fundamental emission was observed as the pump power was increased. This small shift ($\sim 2\,\mathrm{cm}^{-1}$ to $3\,\mathrm{cm}^{-1}$ or 0.2 nm to 0.4 nm) is not due to SRS, but rather to the increase in the peak wavelength of the stimulated emission cross-section of $Nd{:}YVO_4$ with increasing temperature observed in several studies [14, 22, 23]. Délen *et al* [23] also noted a broadening of the emission spectrum with increasing temperature.

The full widths at half maximum (FWHM) of the fundamental peaks are plotted as functions of pump power for the three cases in Figure 5.11. The irregular shape of the spectral peaks makes it difficult to define a measure of the width that is appropriate for all cases. The FWHM gives deceptively small values for the width of the funda-

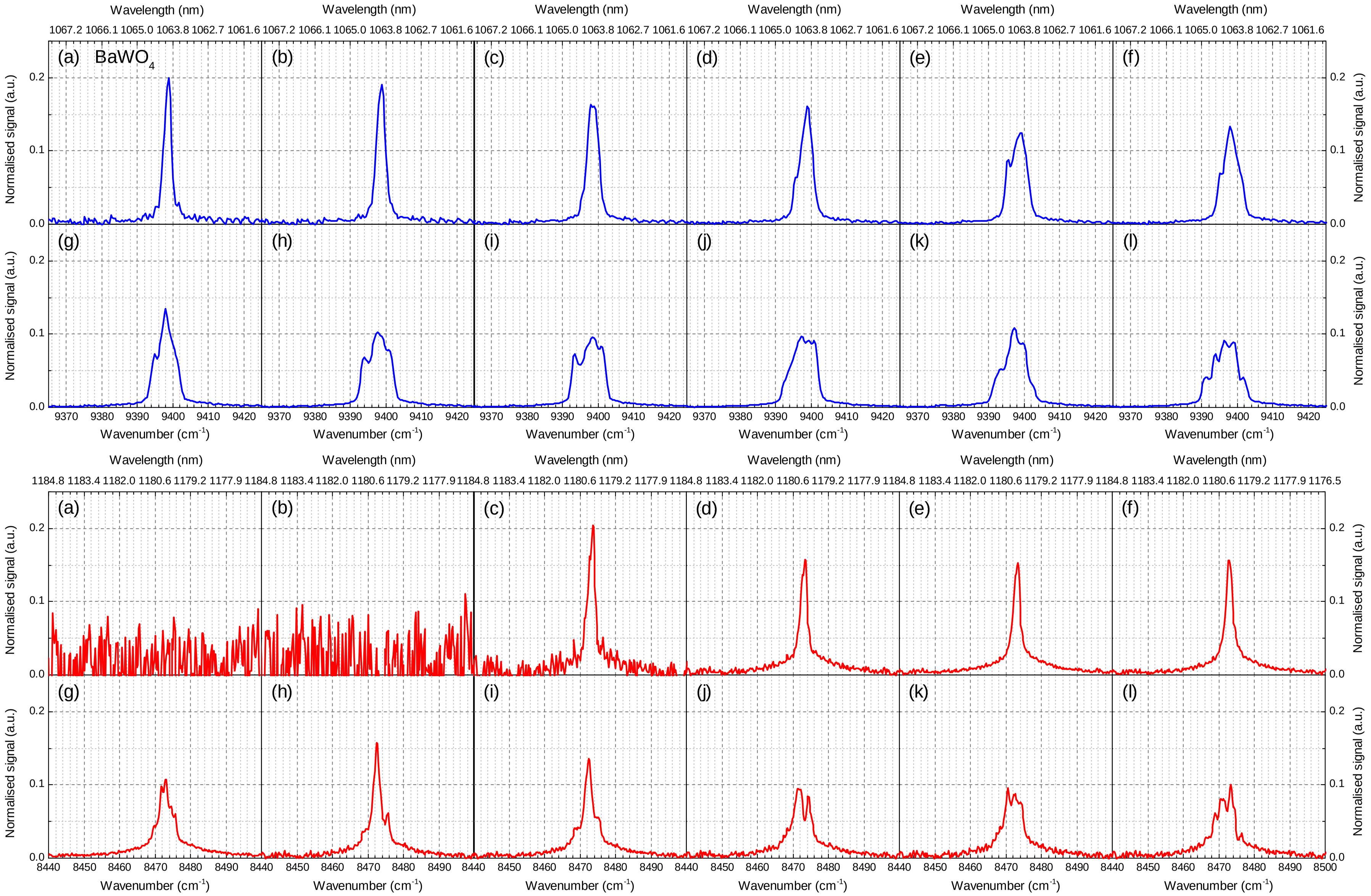

**Figure 5.8:** Spectra of BaWO$_4$ Raman laser. Upper plots (blue) show the fundamental spectra, lower plots (red) show the corresponding Stokes spectra. $P_{\text{abs}} =$ (a) 0.90 W (below Raman threshold), (b) 1.86 W (below Raman threshold), (c) 2.85 W, (d) 3.98 W, (e) 4.99 W, (f) 6.06 W, (g) 8.17 W, (h) 10.52 W, (i) 12.94 W, (j) 17.57 W, (k) 22.39 W, (l) 27.33 W.

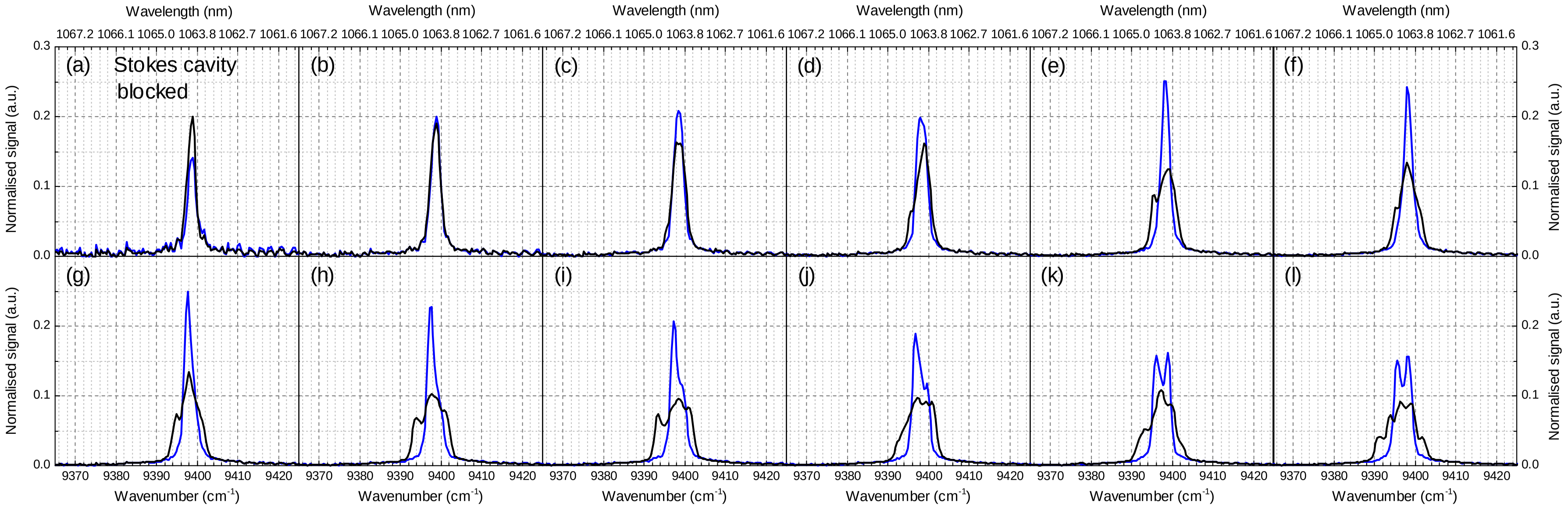

**Figure 5.9:** Spectra of $BaWO_4$ Raman laser with the Stokes cavity blocked (blue lines). Spectra from Figure 5.8 for normal Raman laser operation are also plotted for comparison (black lines). All mirrors are highly reflecting at the fundamental wavelength. $P_{\mathrm{abs}}$ = (a) 0.90 W, (b) 1.86 W, (c) 2.85 W, (d) 3.98 W, (e) 4.99 W, (f) 6.06 W, (g) 8.17 W, (h) 10.52 W, (i) 12.94 W, (j) 17.57 W, (k) 22.39 W, (l) 27.33 W.

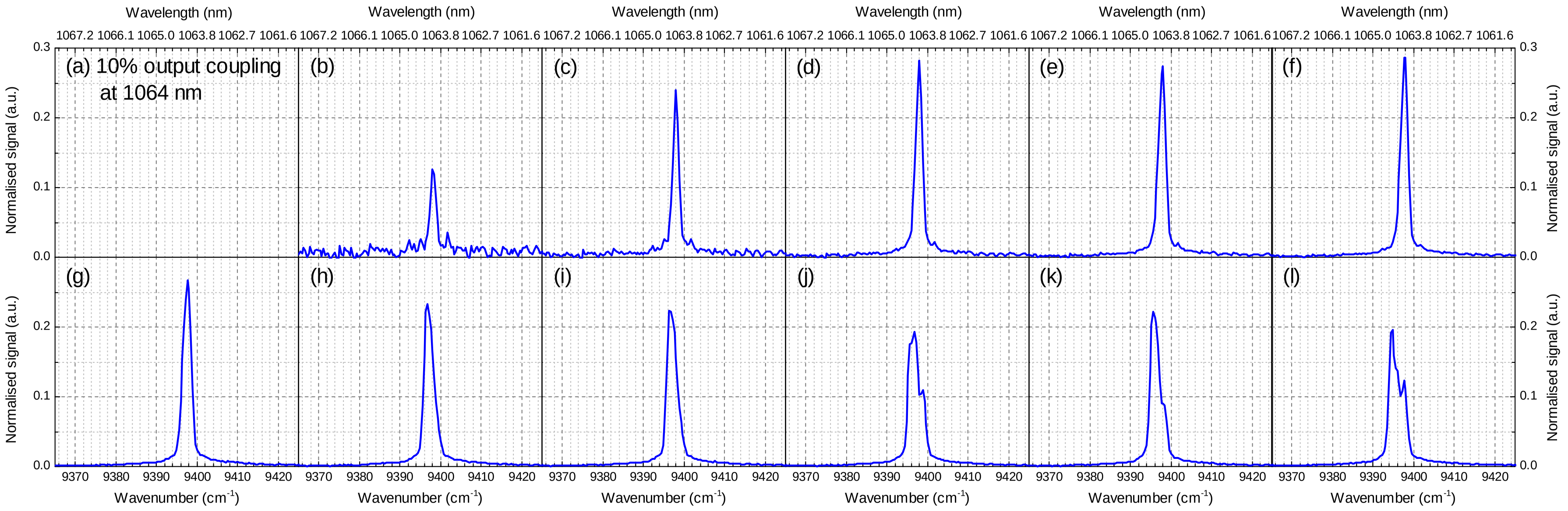

**Figure 5.10:** Spectra of disk laser using an output coupler with 10 % transmission at the fundamental wavelength. $P_{\text{abs}}$ = (a) 0.90 W (below threshold), (b) 1.86 W, (c) 2.85 W, (d) 3.98 W, (e) 4.99 W, (f) 6.06 W, (g) 8.17 W, (h) 10.52 W, (i) 12.94 W, (j) 17.57 W, (k) 22.39 W, (l) 27.33 W.

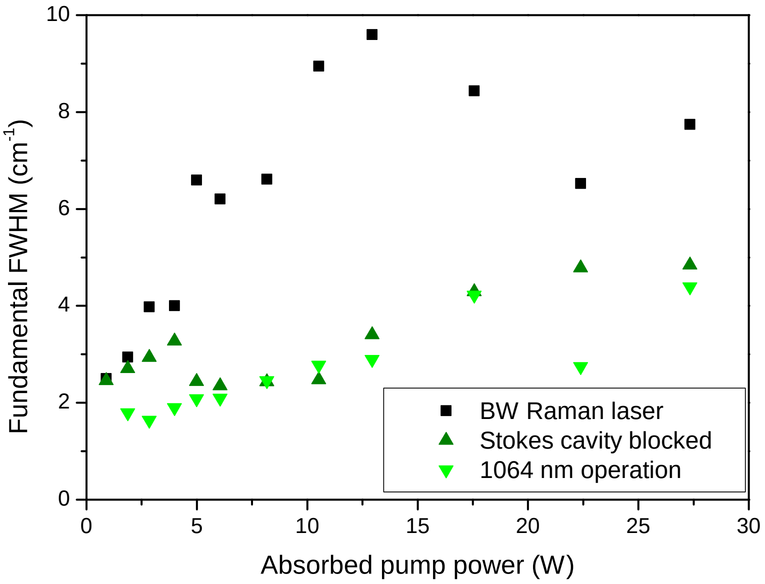

**Figure 5.11:** FWHM of the fundamental spectrum as a function of pump power for the BaWO$_4$ (BW) Raman laser (black squares), the same laser but with the Stokes cavity blocked to suppress SRS (dark green upright triangles) and for a cavity with 10 % output coupling at 1064 nm (light green inverted triangles).

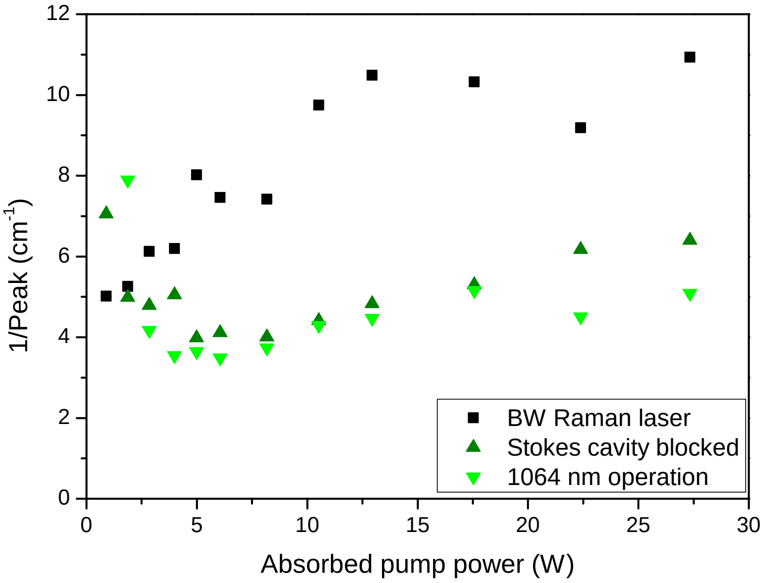

**Figure 5.12:** Inverse peak value of the normalised fundamental spectrum as a function of pump power for the BaWO$_4$ (BW) Raman laser (black squares), the same laser but with the Stokes cavity blocked to suppress SRS (dark green upright triangles) and for a cavity with 10 % output coupling at 1064 nm (light green inverted triangles).

mental spectrum of the $BaWO_4$ Raman laser with no etalon in cavity at high powers because those spectra contain significant structure below the half maximum level (see Figure 5.8(j), (k) and (l)). The possibility of using the inverse of the peak value of the normalised spectrum was also considered and this metric is plotted in Figure 5.12 but the low signal to noise ratio in the spectra at low powers (for example, see Figure 5.8(a)) led to unreasonably high values of the peak width at low powers when using this parameter as a measure of the peak width. The most important point of this exercise was to identify general trends in the spectral behaviour rather than determining an accurate absolute measure of the spectral width, and therefore the FWHM was selected for its simplicity, with the caveat that it can give misleading values for individual spectra if those spectra have a particularly complex structure.

From Figure 5.11, it can be seen that while the fundamental broadens slightly even when there is no SRS, the broadening is much more significant when SRS is occurring. The dip in the data at high pump powers for the SRS case is due to the difficulties of defining the width of the peak discussed above. It is however evident that there is significant broadening of the fundamental spectrum associated with the SRS process.

### 5.3.3 Spatial hole burning in Nd:$YVO_4$ disk laser

The broadening of the fundamental spectrum observed even in the absence of SRS is most likely due to spatial hole burning. Spatial hole burning occurs because the standing wave created by the counter-propagating cavity fields saturates the gain medium only near the anti-nodes of the field. Around the nodes of the standing wave the laser gain remains unsaturated, and since axial modes of slightly different frequencies will form standing waves with anti-nodes in slightly different places, this induced spatial inhomogeneity allows multiple axial modes to reach threshold even in a homogeneously broadened gain material [24].

Since the gain material in the lasers presented here is a disk at one end of the cavity, the potential for spatial hole burning would be expected to be less than is the case in systems where the laser gain rod is in the middle of the cavity. The reason for this is that all axial modes of the cavity must have a node at the end mirror, and when that mirror is coated directly on to one end of a thin laser gain crystal, the variation in the overlap of different axial modes with unsaturated regions of the gain material is reduced. However the situation is not so simple in the present case since the disk lasers used here are face-pumped rather than end-pumped, meaning that the gain is greatest at the uncoated end of the Nd:$YVO_4$, where the axial modes are not constrained. To clarify the situation, and assess whether the spectral broadening observed in the absence of SRS could be attributed to spatial hole burning, calculations were performed to assess the potential for spatial hole burning in the Nd:$YVO_4$ disk laser using the approach described by Zayhowski [25]. A simplified model of the cavity was used, containing only the Nd:$YVO_4$ disk and an end mirror. The length of the modelled cavity was chosen to roughly match the optical length of the real laser cavity (including the diamond heatspreader, dichroic mirror and $\mathrm{BaWO_4}$ crystal), and was fine tuned to 255.800063 mm so that an axial mode lay at exactly the peak of the laser gain profile (1064.1 nm as measured by Sato and Taira [13]).

Zayhowski derives an expression for the ratio of the maximum single-longitudinal-mode inversion density to the threshold inversion density. $\zeta(m,n)$ is the ratio of the inversion density at which mode $n$ will oscillate to the threshold inversion density for the first mode to oscillate, mode $m$, assuming that mode $m$, and only mode $m$, is already oscillating. This ratio is given by

$$\zeta(m,n) = \left(\frac{\beta(m,n)-1}{1-\langle\psi(m,n)\rangle}+1\right)\cdot\left(\frac{2\left[\beta(m,n)-1\right]}{1-\langle\psi(m,n)\rangle}+1\right) \tag{5.12}$$

where $\beta(m,n)$ is the discrimination factor and is given by

$$\beta(m,n) = \frac{\sigma_m\gamma_n}{\sigma_n\gamma_m} \tag{5.13}$$

where $\sigma_m$ and $\gamma_m$ are the stimulated emission cross-section and round trip loss respectively, at the frequency of mode m.

$\langle\psi(m,n)\rangle$ is the correlation factor and gives a measure of the overlap of the standing wave patterns for modes $m$ and $n$.

$$\langle\psi(m,n)\rangle = \frac{1}{l\langle N_0\rangle}\int_0^l N_0(z)\cos\left[2\left(k_{\mathrm{m}}-k_{\mathrm{n}}\right)z+2\left(\theta_{\mathrm{m}}-\theta_{\mathrm{n}}\right)\right]\,\mathrm{d}z \tag{5.14}$$

where $l$ is the length of the crystal, $k$ and $\theta$ are the wavenumber and phase of the modes respectively (determined by the cavity geometry), and $N_0(z)$ is the inversion density in the absence of saturation. $\langle N_0\rangle$ is the length-averaged value of $N_0(z)$ and is given by

$$\langle N_0\rangle = \frac{1}{l}\int_0^l N_0(z)\,\mathrm{d}z\,. \tag{5.15}$$

If $\langle\psi(m,n)\rangle = 1$, then the modes are perfectly correlated and mode $n$ will never oscillate once mode $m$ is oscillating. If $\langle\psi(m,n)\rangle = -1$ then the modes are anti-correlated, with the anti-nodes of mode $n$ aligned with the nodes of mode $m$, giving the most favourable conditions for mode $n$ to oscillate.

$\zeta(m,n)$ was calculated for the simplified model of the disk laser described above. As previously mentioned, the length of the model cavity was fine tuned so that an axial mode lay at exactly the centre of the gain profile (1064.1 nm) [13]. This mode, $m$, was therefore the first to oscillate. $\zeta(m,n)$ was then calculated for each possible second mode $n$. The mode $n$ with the lowest value of $\zeta(m,n)$ would be the second mode to oscillate in the laser. (Note that after a second mode is oscillating the calculation breaks down because the correlation factor would have to be modified to take into account the depletion of the gain by both oscillating modes.) A Lorentzian gain profile

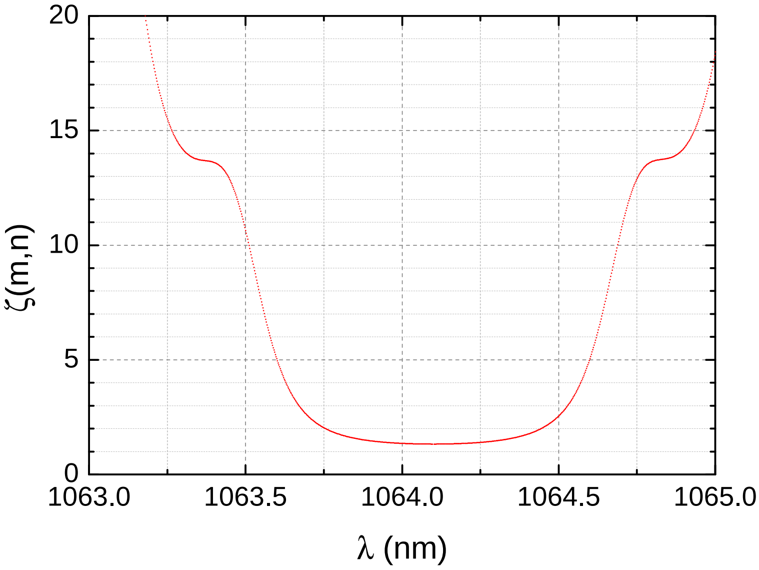

**Figure 5.13:** Ratio of the maximum single-longitudinal-mode inversion density to the threshold inversion density calculated for a simplified model of the disk laser using the Zayhowski approach [25].

was assumed, with a FWHM of 1.1 nm [13]. The losses were assumed to be spectrally flat over the region of interest (a few nanometres around 1064 nm). $\zeta(m,n)$ is plotted as a function of wavelength in Figure 5.13, for $m = 480782$ such that the first mode to oscillate has a wavelength of 1064.1 nm. Note that $\zeta(m,n)$ appears to be a continuous function in some sections of the plot. This is due to the small separation of the points – the free spectral range of the cavity is just 2.2 pm – in reality $\zeta(m,n)$ is of course a discrete function.

$\zeta(m,n)$ is very flat around 1064.1 nm. This means that there are many modes in this region that could be the second mode to oscillate, and is probably due to a balance between the decreasing emission cross section and increasing overlap with unsaturated regions of the gain material as one moves away from the central wavelength. As mentioned above, the calculation breaks down once a second mode is oscillating; however, the propensity of many modes to oscillate at relatively small multiples of the threshold inversion density (less than a factor of 2 over a range of approximately 0.75 nm) suggests that there is a significant potential for spectral broadening due to spatial hole burning, even despite the fact that the gain is located at one end of the cavity. This will be particularly true in the case of the Raman laser, in which all the mirrors are highly reflecting at the fundamental wavelength and therefore the threshold inversion density is small - in such a system the laser will usually be pumped tens of times above the fundamental threshold level just to reach the Raman threshold, while at maximum power the laser may be being pumped hundreds of times above the fundamental threshold level.

Potential etalon effects from the diamond heatspreader have been neglected in this analysis, as has energy diffusion [25]. Etalon effects would introduce spectral variations in the loss, making $\zeta(m, n)$ less flat, while energy diffusion tends to smooth out the spatial inhomogeneities in the gain thus increasing $\zeta(m, n)$. However, the propensity for spatial hole burning predicted by this simplified calculation suggests that spatial hole burning is responsible for the (relatively modest) spectral broadening observed in the disk laser when SRS is suppressed.

## 5.4 Effect of Raman linewidth

As discussed in Section 5.2, the relative widths of the fundamental laser gain and the Raman peak affect the broadening process such that the narrower the Raman peak (relative to the fundamental peak), the more severe the SRS-induced broadening. In order to test this, a Raman laser was constructed using $KGd(WO_4)_2$ and its spectral behaviour was compared to that of the $BaWO_4$ Raman laser described above. The same $Nd{:}YVO_4$ disk was used as the laser gain material, so the fundamental gain bandwidth was unchanged. The Raman linewidths of $BaWO_4$ and $KGd(WO_4)_2$ were given in Table 5.1 – $1.6\,\mathrm{cm}^{-1}$ [16] and $6.4\,\mathrm{cm}^{-1}$ [17] respectively (for the $768\,\mathrm{cm}^{-1}$ transition in the case of $KGd(WO_4)_2$). It would have been ideal to try $LiNbO_3$ also, since its Raman transition is so broad that no SRS-induced broadening would have been expected, but no suitably coated $LiNbO_3$ was available. The Raman spectra of $BaWO_4$ and $KGd(WO_4)_2$ are shown in Figure 5.14. These spectra were collected using a Renishaw InVia Reflex Raman spectrometer with resolution $2\,\mathrm{cm}^{-1}$.

The $BaWO_4$ Raman lasers described so far operated on the strong, narrow peak at $925\,\mathrm{cm}^{-1}$. The Raman spectrum of $KGd(WO_4)_2$ is much more complex, with strong lines at $768\,\mathrm{cm}^{-1}$ and $901\,\mathrm{cm}^{-1}$ and numerous weaker lines at lower wavenumbers. Either of the two main Stokes shifts ($768\,\mathrm{cm}^{-1}$ or $901\,\mathrm{cm}^{-1}$) can be accessed by rotating the $KGd(WO_4)_2$ crystal. The $768\,\mathrm{cm}^{-1}$ shift was chosen since it is the broader of the two main peaks. The Raman spectrum shown in Figure 5.14(b) was collected using an excitation beam propagating along the $N_p$ axis, polarised parallel to the $N_g$-axis such that the $768\,\mathrm{cm}^{-1}$ peak was strongest. This crystal orientation was also used in the Raman laser, in other words the $N_g$-axis of the $KGd(WO_4)_2$ crystal was oriented parallel to the c-axis of the $Nd{:}YVO_4$ crystal and hence parallel to the polarisation of the fundamental field.

The cavity design for the $KGd(WO_4)_2$ Raman laser is shown in Figure 5.15. A 25 mm long, $N_p$-cut $KGd(WO_4)_2$ crystal was used, wrapped in indium foil and mounted in a water-cooled brass mount that permitted the crystal to be rotated. The cavity was almost identical to that of the $BaWO_4$ Raman laser; the distance between M2 and the Raman crystal was adjusted slightly to compensate for the difference in refractive index between $BaWO_4$ and $KGd(WO_4)_2$. A typical power transfer is shown in Figure 5.16.

Spectra were collected at various pump powers in the manner described above for the $BaWO_4$ Raman laser. The fundamental and Stokes peaks were normalised to area over ranges of about 10 nm. The spectra are shown in Figure 5.17. Note that

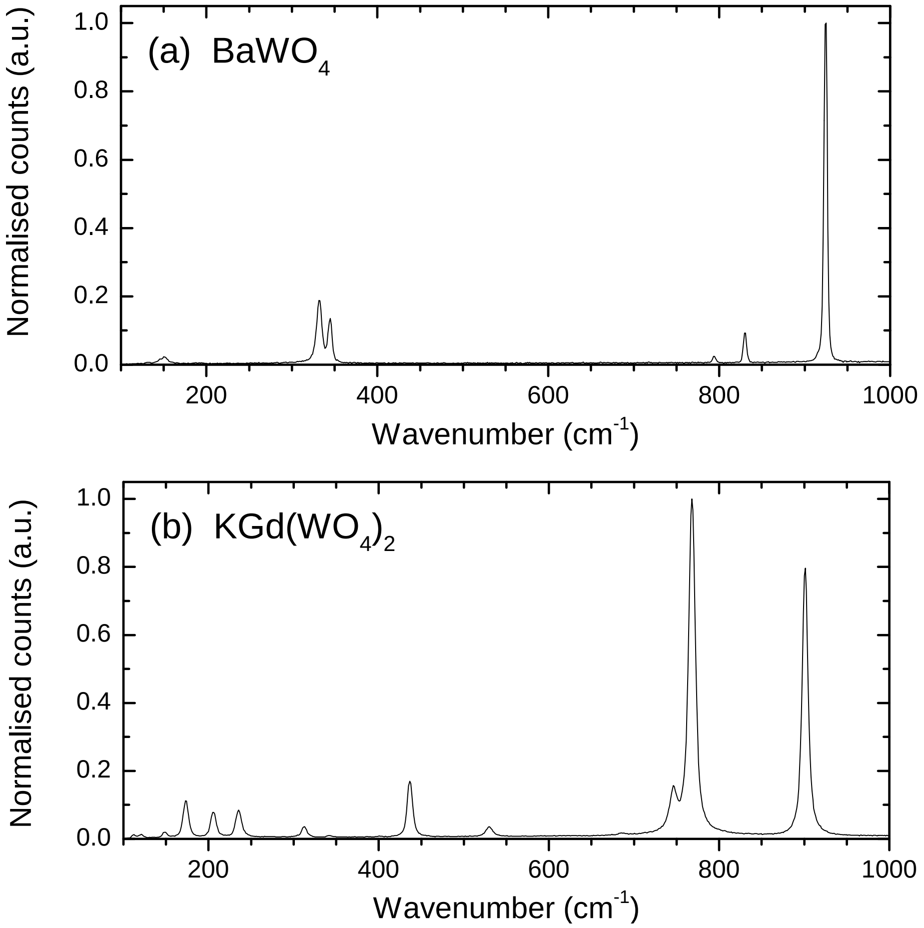

**Figure 5.14:** Raman spectra for (a) $BaWO_4$ and (b) $KGd(WO_4)_2$. The excitation laser was polarised parallel to the a-axis of the a-cut $BaWO_4$ and parallel to the $N_g$-axis of the $N_p$-cut $KGd(WO_4)_2$. In both cases only the light scattered with polarisation parallel to that of the excitation laser was collected - this is the configuration of most relevance for the Raman lasers considered here.

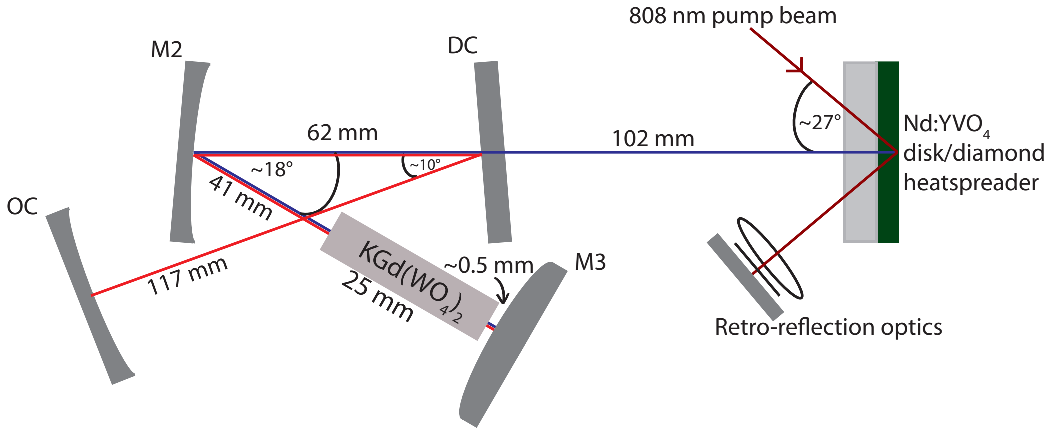

**Figure 5.15:** Cavity design for measurements of spectral broadening in $KGd(WO_4)_2$ Raman laser.

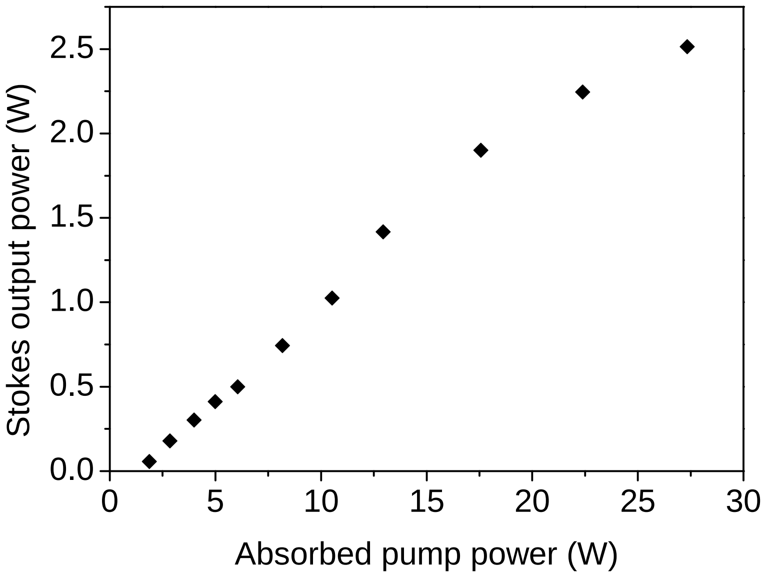

**Figure 5.16:** Typical power transfer for the KGd(WO$_4$)$_2$ Raman laser.

the power transfer in Figure 5.16 was measured simultaneously with the spectra in Figure 5.17. Multiple Stokes peaks were observed - the main one at about 8630 cm$^{-1}$ ($\sim$ 1159 nm), corresponding to the 768 cm$^{-1}$ shift of the fundamental, and also another around 8546 cm$^{-1}$ ($\sim$ 1170 nm). This peak is due to a combination Stokes shift, whereby the fundamental field is shifted via the 768 cm$^{-1}$ peak and then again by a peak at 84 cm$^{-1}$. This latter Raman peak at 84 cm$^{-1}$ is not shown in the Raman spectrum in Figure 5.14 but has been observed previously [26]. This additional Stokes peak was not included in the normalisation range for the Stokes spectra.

The FWHM of the main fundamental peak is plotted as a function of pump power in Figure 5.18. The data for the BaWO$_4$ Raman laser with and without the Stokes cavity blocked, originally shown in Figure 5.11, are also replotted for comparison. It can be seen that the observed spectral broadening is much less significant in the KGd(WO$_4$)$_2$ Raman laser than in the BaWO$_4$ system, and that in the KGd(WO$_4$)$_2$ Raman laser, the main fundamental peak does not broaden beyond the extent observed when SRS is suppressed. However, it can be seen in Figure 5.17 that as well as the main peak around 9398 cm$^{-1}$ ($\sim$ 1064 nm), a small peak around 9377 cm$^{-1}$ ($\sim$ 1066 nm) appears at higher pump powers. This behaviour is consistent with the broadening mechanism described in Section 5.2, since the Raman linewidth of KGd(WO$_4$)$_2$ is greater than that of BaWO$_4$ but still less than the gain bandwidth of Nd:YVO$_4$ (see Table 5.1). The broader Raman line of KGd(WO$_4$)$_2$ will present a broader loss to the fundamental field, reducing the propensity for broadening of the fundamental spectrum. However, at sufficiently high pump powers, modes in the wings of the laser gain bandwidth will still be able to reach threshold leading to a distinct fundamental peak separate from the relatively narrow main fundamental peak.

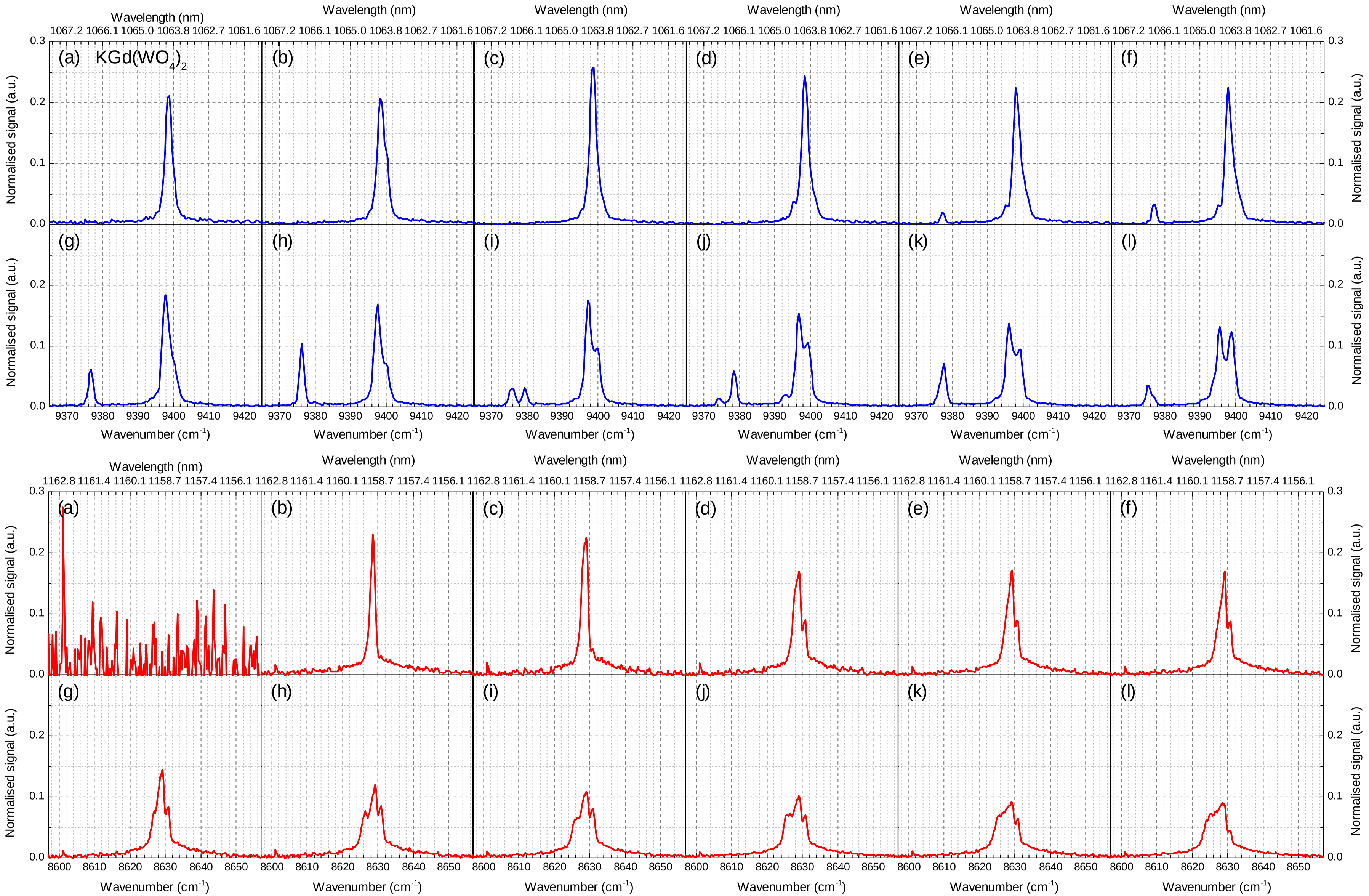

**Figure 5.17:** Spectra of KGd(WO$_4$)$_2$ Raman laser. $P_{\text{abs}}$ = (a) 0.90 W (below Raman threshold), (b) 1.86 W, (c) 2.85 W, (d) 3.98 W, (e) 4.99 W, (f) 6.06 W, (g) 8.17 W, (h) 10.52 W, (i) 12.94 W, (j) 17.57 W, (k) 22.39 W, (l) 27.33 W.

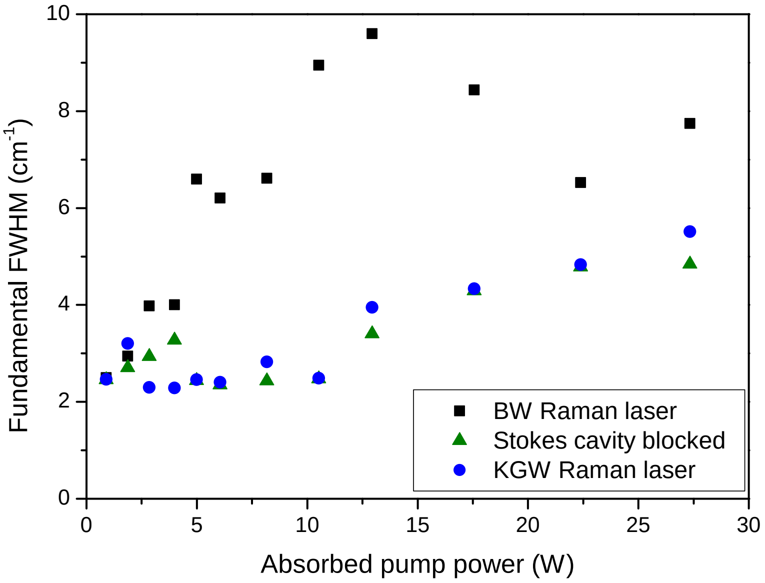

**Figure 5.18:** FWHM of the main fundamental peak as a function of pump power for the $KGd(WO_4)_2$ (KGW) Raman laser (blue circles). The data shown previously for the $BaWO_4$ (BW) Raman laser (black squares) and the same laser but with the Stokes cavity blocked to suppress SRS (green triangles) are also re-plotted here for comparison.

## 5.5 Use of etalons to control broadening

Since the broadening of the fundamental spectrum leads to a decrease in effective Raman gain, experiments were performed to investigate whether or not the performance of the laser could be improved by controlling the spectral width of the fundamental. Spectral control was achieved by inserting etalons into the fundamental cavity, between the laser gain crystal and the dichroic mirror such that only the fundamental field was affected by the presence of the etalon(s). This simplified the interpretation of the results and minimised the impact of any detrimental side effects of inserting the etalon since only the fundamental field was affected by these. (This approach was facilitated by use of the disk geometry for the laser gain material - the weaker thermal lens permitted the construction of a relatively long pair of coupled cavities, thereby making it possible to place optical elements such as etalons into one cavity only.)

Interference between the reflections from each surface of a solid etalon leads to a periodic spectral transmission in which the separation of the transmission peaks, the free spectral range, is determined by the optical thickness of the etalon and the width of the peaks is determine by the reflectivity of the surfaces (the finesse of the etalon). The thinner the etalon, the broader the free spectral range; the higher the reflectivity of the surfaces, the higher the finesse and the narrower the transmission peaks. The precise position of the transmission peaks in frequency space can be adjusted by tilting the etalon slightly.

Three different etalons were used, two coated glass etalons and an uncoated YAG etalon. The details of these etalons are given in Table 5.2. The abbreviations given in

**Table 5.2:** Details of etalons used to control fundamental spectral width. The abbreviations given are used to refer to these etalons throughout the rest of this thesis.

| Material | Thickness/µm | Coated | Surface Reflectivity (%) | Abbreviation |
|---|---|---|---|---|
| Fused silica | 290 | Yes | 30 | E30 |
| Fused silica | 290 | Yes | 60 | E60 |
| YAG | 50 | No | 8.4 | YAG[1] |

[1] The YAG etalon is mainly used in combination with the E30 etalon, in which case the abbreviation E30Y is used to refer to both etalons together.

the table are used to refer to the etalons and experiments in which the etalons were used throughout the rest of this thesis. For cases when no etalon was used, the abbreviation "NE" is used.

The theoretical transmission curves of the etalons were calculated using the equations given by Koechner in [27]:

$$T = \frac{(1-R)^2}{1+R^2-2R\cos\varphi} \tag{5.16}$$

where

$$\varphi = \left(\frac{2\pi}{\lambda}\right) 2nt\cos\theta. \tag{5.17}$$

$R$ is the reflectivity of the etalon surfaces, assumed equal for both surfaces, $\lambda$ is the wavelength, $n$ is the refractive index of the etalon, $t$ is the thickness of the etalon and $\theta$ is the angle of the beam to the surface normal inside the etalon [27]. The theoretical transmission curves are plotted in Figure 5.19.

These curves were calculated assuming perfect surface quality and flatness, and negligible walk-off of the beam passing through the tilted etalon. The tilt angle was chosen to place a transmission peak at 1064.1 nm, the peak of the Nd:YVO$_4$ stimulated

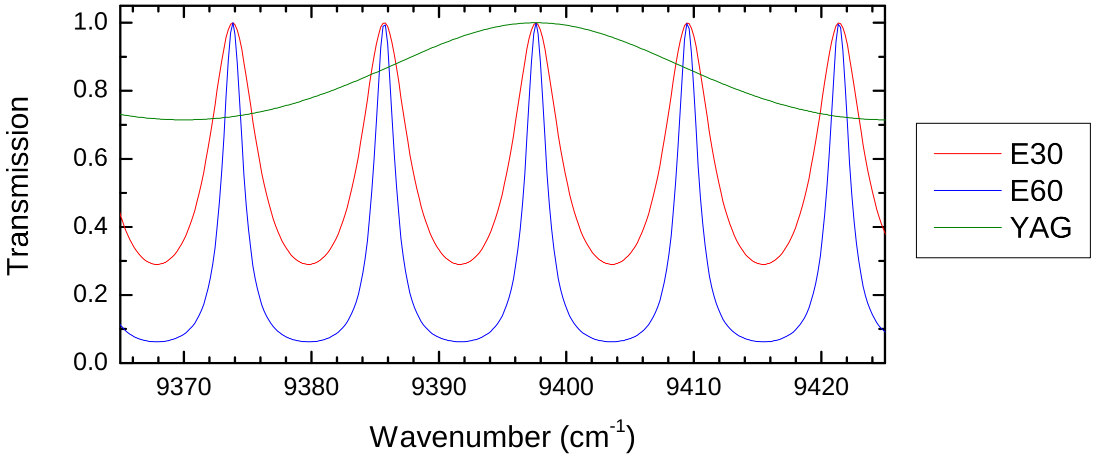

**Figure 5.19:** Theoretical transmission curves for the etalons, assuming perfect surface quality and parallelism, and negligible beam-walk-off.

emission cross section [13]. These assumptions lead to a transmission of 100 % at the transmission peaks - in reality, the maximum transmission might be slightly less. The manufacturers' specifications for the etalons are given in Appendix A.

### 5.5.1 Effect of etalon on $BaWO_4$ Raman laser

The E30 and E60 coated glass etalons were separately inserted into the fundamental-only arm of the cavity of the $BaWO_4$ Raman laser and the spectrum and output power were measured as functions of pump power. Figures 5.20 and 5.21 show the spectra for the laser running with the E30 and E60 etalons respectively, while Figure 5.22 shows the spectra for the laser with the E30 etalon when the Stokes cavity was blocked to suppress SRS. (The spectra were very similar when the Stokes cavity was blocked with the E60 etalon in place.) Comparison of Figure 5.22 to Figure 5.9 demonstrates that the etalon effectively controls the spectral broadening caused by spatial hole burning.

In the cases where SRS was occurring (Figures 5.20 and 5.21), both the etalons keep the fundamental peak narrow across the entire range of pump powers (the FWHM of the fundamental is about $1.5\,\mathrm{cm}^{-1}$ to $2\,\mathrm{cm}^{-1}$). However, several satellite peaks appear in the fundamental spectrum, separated by the free spectral range of the etalons (1.35 nm or $12\,\mathrm{cm}^{-1}$). It was surprising to observe laser oscillation so far from the peak of the laser gain spectrum; however, the very high reflectivity of all the cavity mirrors at the fundamental wavelength may have made it possible for these satellite peaks to reach threshold when the SRS was presenting a loss to the main peak. These satellite peaks never become intense enough to reach the threshold for Raman conversion, and therefore the Stokes output consists of a single, narrow peak. However, the fact that energy is being lost to these satellite peaks is undesirable and efforts to suppress the oscillation of these modes with a second etalon are described in Section 5.5.3 below.

The output power and Stokes FWMH are shown in Figures 5.23 and 5.24 respectively. Comparable output powers can be obtained with and without the E30 etalon, while the E60 etalon reduces the output power somewhat, particularly at high power. Both etalons result in a narrow Stokes output spectrum, and therefore the E30 etalon can be said to increase the spectral brightness even though it does not increase the output power itself.

There are several possible reasons why the etalons did not yield an improvement in output power. As previously discussed, CW intracavity Raman lasers are very sensitive to even small increases in the round-trip loss. Due to the fragility of the etalons, they were cleaned less frequently than the other optics, so it is possible that small dust particles on their surface may have increased the loss. The etalons themselves may not have had perfectly smooth, flat, parallel surfaces - any imperfections will reduce the peak transmission from 100 %. Also, the peak transmission of an etalon reduces slowly with the tilt angle as the etalon is tilted to tune the wavelength of the transmission peaks, because the multiple reflections of the beam gradually become

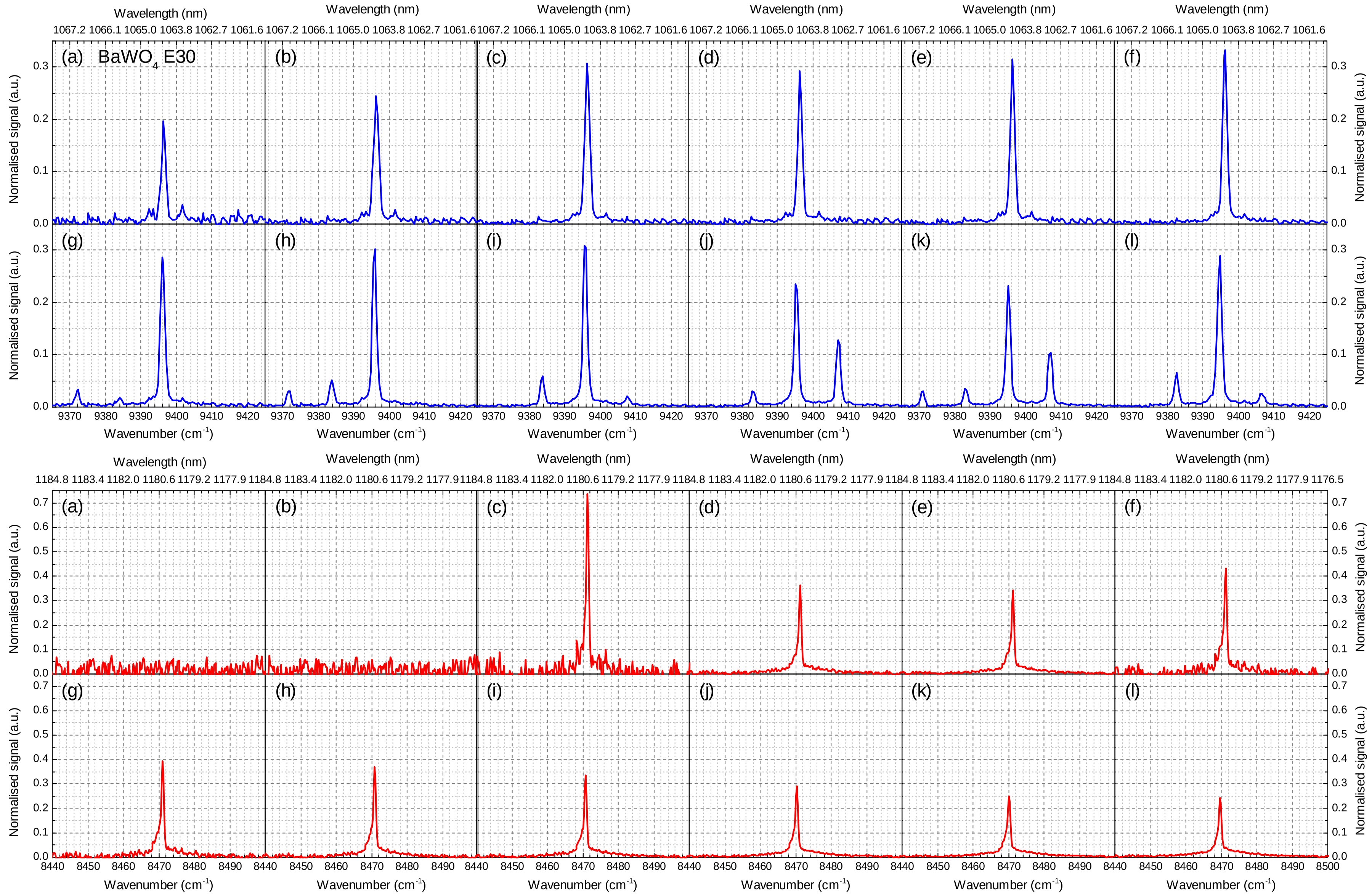

**Figure 5.20:** Spectra of BaWO$_4$ Raman laser with the E30 etalon in the fundamental cavity. $P_{\text{abs}}$ = (a) 0.90 W (below Raman threshold), (b) 1.86 W (below Raman threshold), (c) 2.85 W, (d) 3.98 W, (e) 4.99 W, (f) 6.06 W, (g) 8.17 W, (h) 10.52 W, (i) 12.94 W, (j) 17.57 W, (k) 22.39 W, (l) 27.33 W.

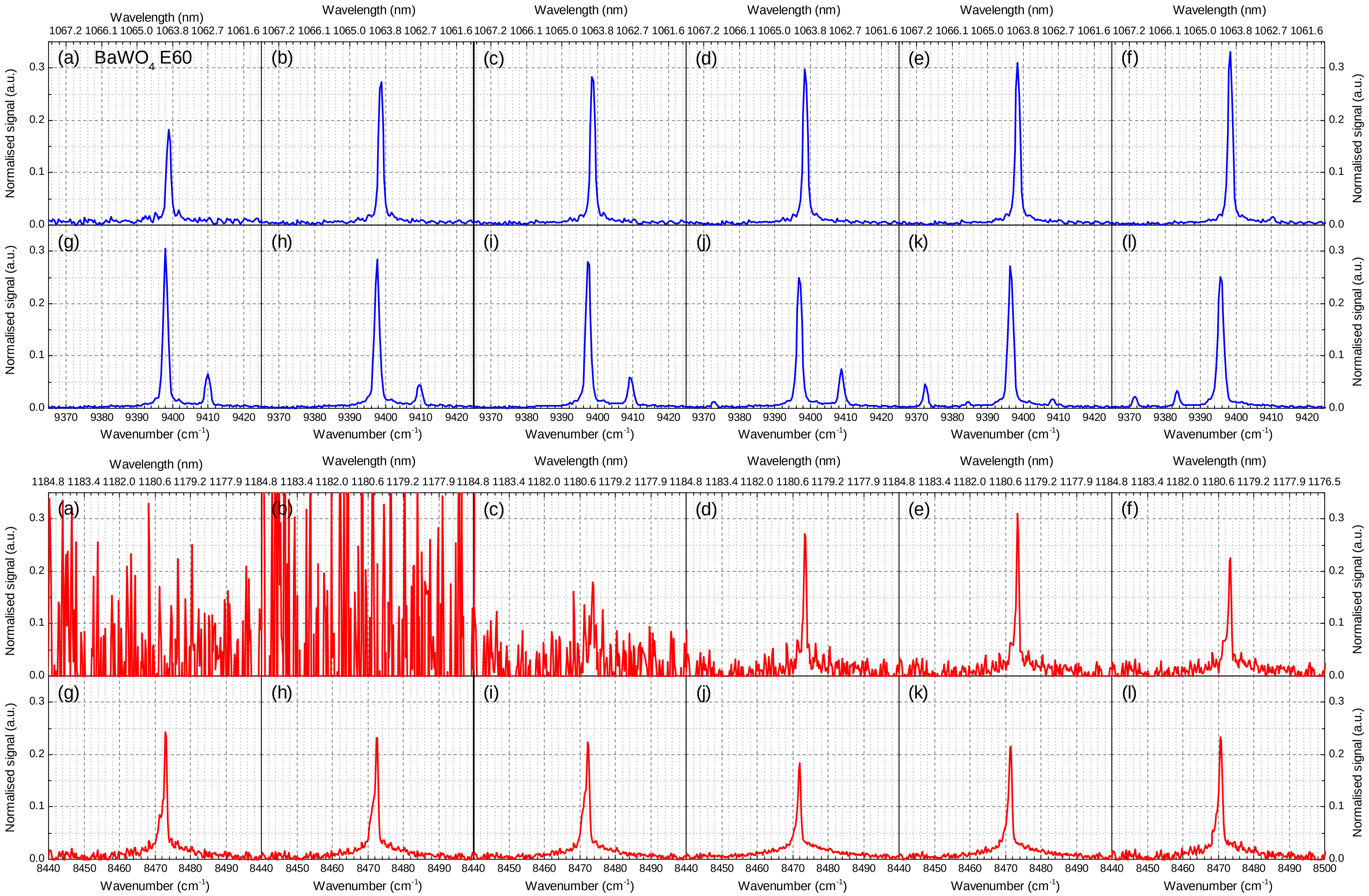

**Figure 5.21:** Spectra of BaWO$_4$ Raman laser with the E60 etalon in the fundamental cavity. $P_{\rm abs}$ = (a) 0.90 W (below Raman threshold), (b) 1.86 W (below Raman threshold), (c) 2.85 W, (d) 3.98 W, (e) 4.99 W, (f) 6.06 W, (g) 8.17 W, (h) 10.52 W, (i) 12.94 W, (j) 17.57 W, (k) 22.39 W, (l) 27.33 W.

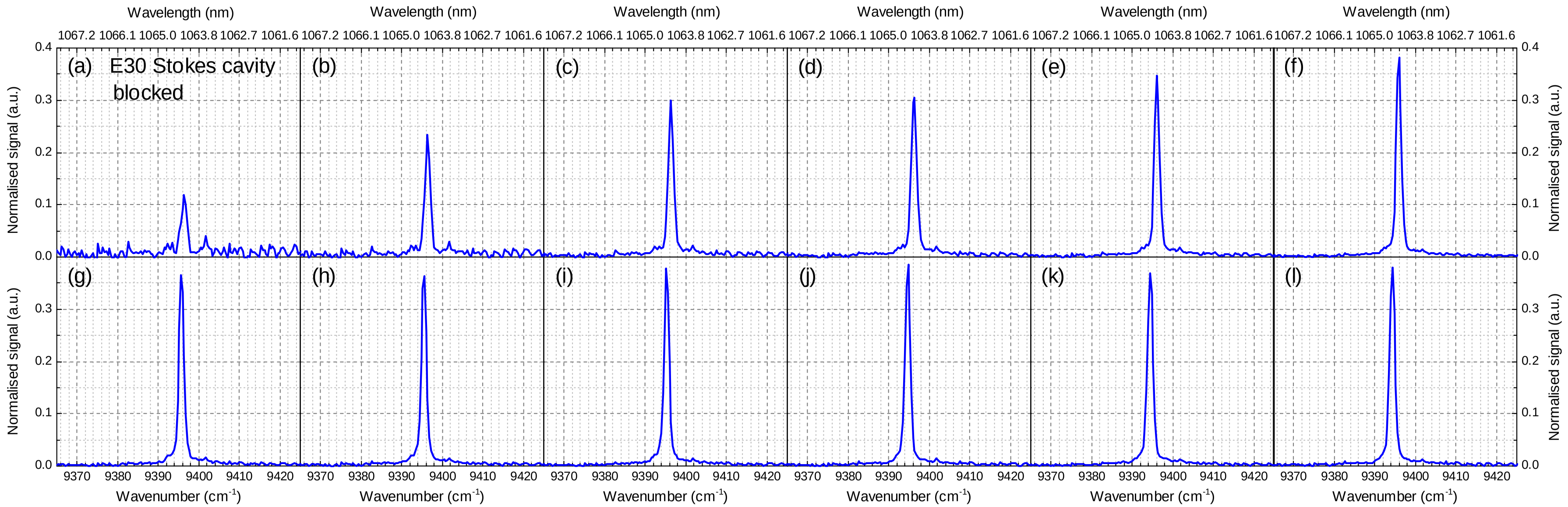

**Figure 5.22:** Spectra of BaWO$_4$ Raman laser with the E30 etalon in the fundamental cavity and the Stokes cavity blocked. $P_{\mathrm{abs}}$ = (a) 0.90 W, (b) 1.86 W, (c) 2.85 W, (d) 3.98 W, (e) 4.99 W, (f) 6.06 W, (g) 8.17 W, (h) 10.52 W, (i) 12.94 W, (j) 17.57 W, (k) 22.39 W, (l) 27.33 W.

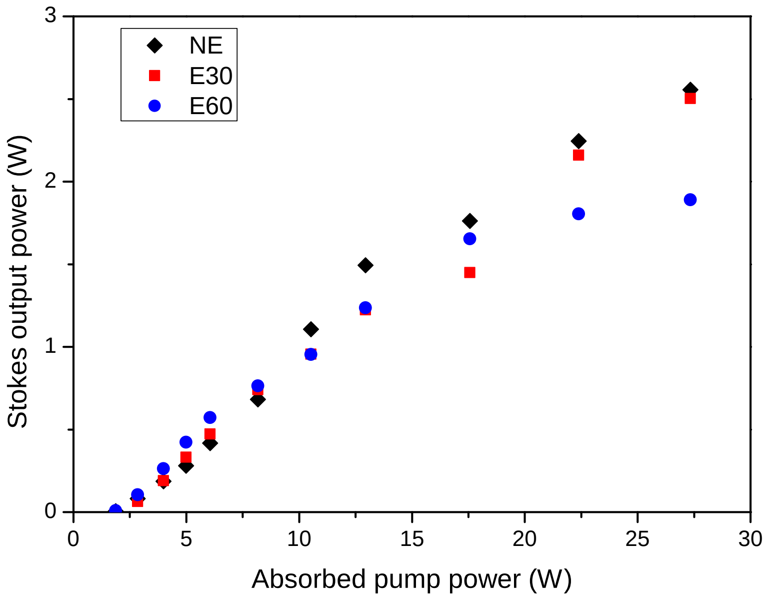

**Figure 5.23:** Power transfers for $BaWO_4$ Raman laser with and without etalons.

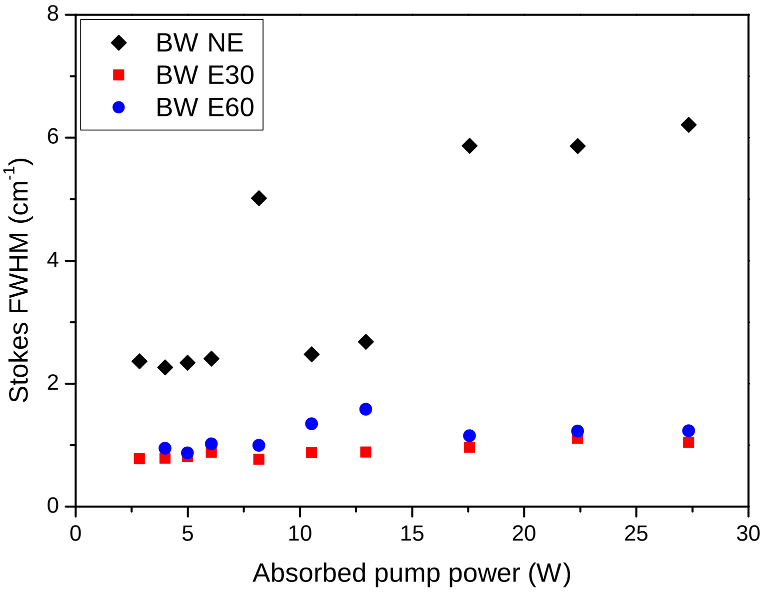

**Figure 5.24:** FWHM of the Stokes output spectrum as a function of pump power for the $BaWO_4$ Raman laser with no etalon in the cavity and with the E30 and $R = 30\,\%$ etalons in the fundamental cavity (E30 and E60 respectively).

misaligned, reducing the interference effect. All these issues would be exacerbated in the E60 etalon due to the higher number of reflections the beam would undergo in this higher finesse etalon. The higher number of round trips would also increase the total loss caused by any absorption or scattering within the etalon. Finally, the presence of the satellite peaks in the fundamental may be limiting the benefits of using the etalons. This is dealt with in Section 5.5.3 below.

### 5.5.2 Effect of etalon on $KGd(WO_4)_2$ Raman laser

The spectra of the $KGd(WO_4)_2$ Raman laser with the E30 and E60 etalons in the fundamental cavity are shown in Figures 5.25 and 5.26 respectively. The corresponding power transfers is shown in Figure 5.27, while the plot of the Stokes FWHM is shown in Figure 5.28. Once again both etalons keep the main fundamental peak narrow (FWHM $<2\,\mathrm{cm}^{-1}$) across the entire range of pump powers, but the satellite peaks are much less prominent, appearing for only a few pump powers when using the E30 etalon. As shown in Section 5.4, SRS in $KGd(WO_4)_2$ induces less broadening of the fundamental than SRS in $BaWO_4$, thanks to the broader Raman line of $KGd(WO_4)_2$. This means that the satellite peaks are less likely to reach threshold in the $KGd(WO_4)_2$ system.

It can be seen from Figure 5.27 that both etalons reduce the output power of the Raman laser. Since the $KGd(WO_4)_2$ system is less prone to broadening, it may be that keeping the fundamental spectrum narrow via the use of an etalon does not provide sufficient benefit to outweigh any detrimental effects of the etalon, which were outlined previously. Once again, the output power was worse with the E60 etalon than with the E30, although only by a small margin.

Figure 5.28 shows that the Stokes spectrum becomes quite broad even when an etalon is used, in marked contrast to the $BaWO_4$ system (see Figure 5.24). This is because of the greater Raman linewidth of $KGd(WO_4)_2$. When a spectrally narrow fundamental field is Raman-shifted by the narrow Raman transition of $BaWO_4$, the resulting Stokes field is also spectrally narrow. However, when a similarly narrow fundamental field is Raman-shifted by the much broader Raman transition of $KGd(WO_4)_2$, the Stokes field will be broader also. If spectrally narrow Stokes output is desired from a Raman laser based on a material with a broad Raman line like $KGd(WO_4)_2$, it would be necessary to insert some form of spectral filter into the Stokes cavity also. This could be done in two ways – either a single etalon could be inserted into the shared arm of the coupled cavity to control the width of both fields or separate etalons could be used, one in the fundamental-only arm of the cavity and another in the Stokes-only arm. The former approach obviously involves fewer components, but it would be essential to find an orientation of the etalon such that transmission peaks were aligned with both a fundamental axial mode and a Stokes axial mode, separated by exactly the Raman shift, if maximum power were to be obtained. If such an alignment turned out to be impossible (due to the precise spacing of the cavity modes and the etalon modes)

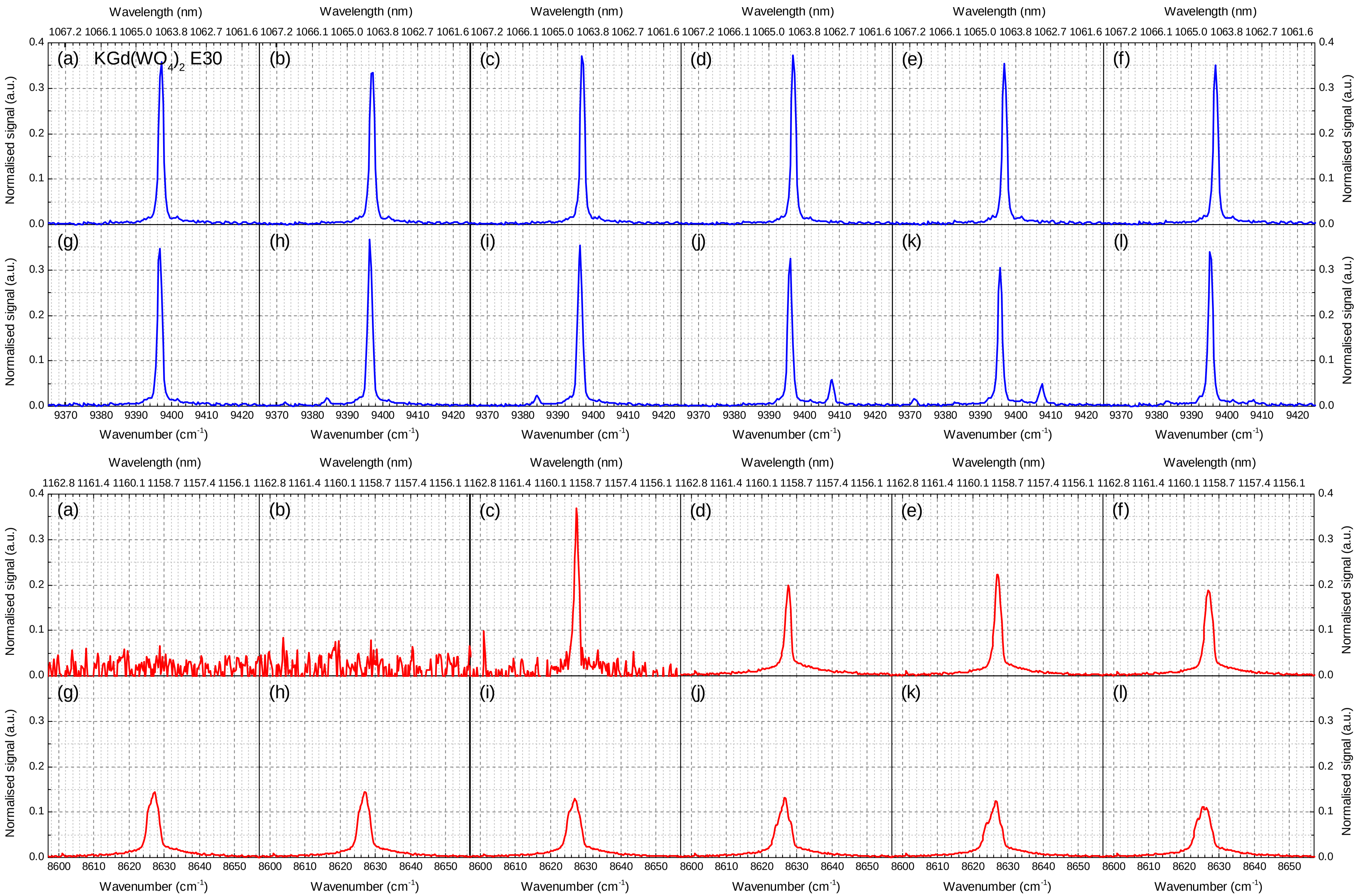

**Figure 5.25:** Spectra of KGd(WO$_4$)$_2$ Raman laser with the E30 etalon in the fundamental cavity. $P_{\text{abs}}$ = (a) 0.90 W (below Raman threshold), (b) 1.86 W (below Raman threshold), (c) 2.85 W, (d) 3.98 W, (e) 4.99 W, (f) 6.06 W, (g) 8.17 W, (h) 10.52 W, (i) 12.94 W, (j) 17.57 W, (k) 22.39 W, (l) 27.33 W.

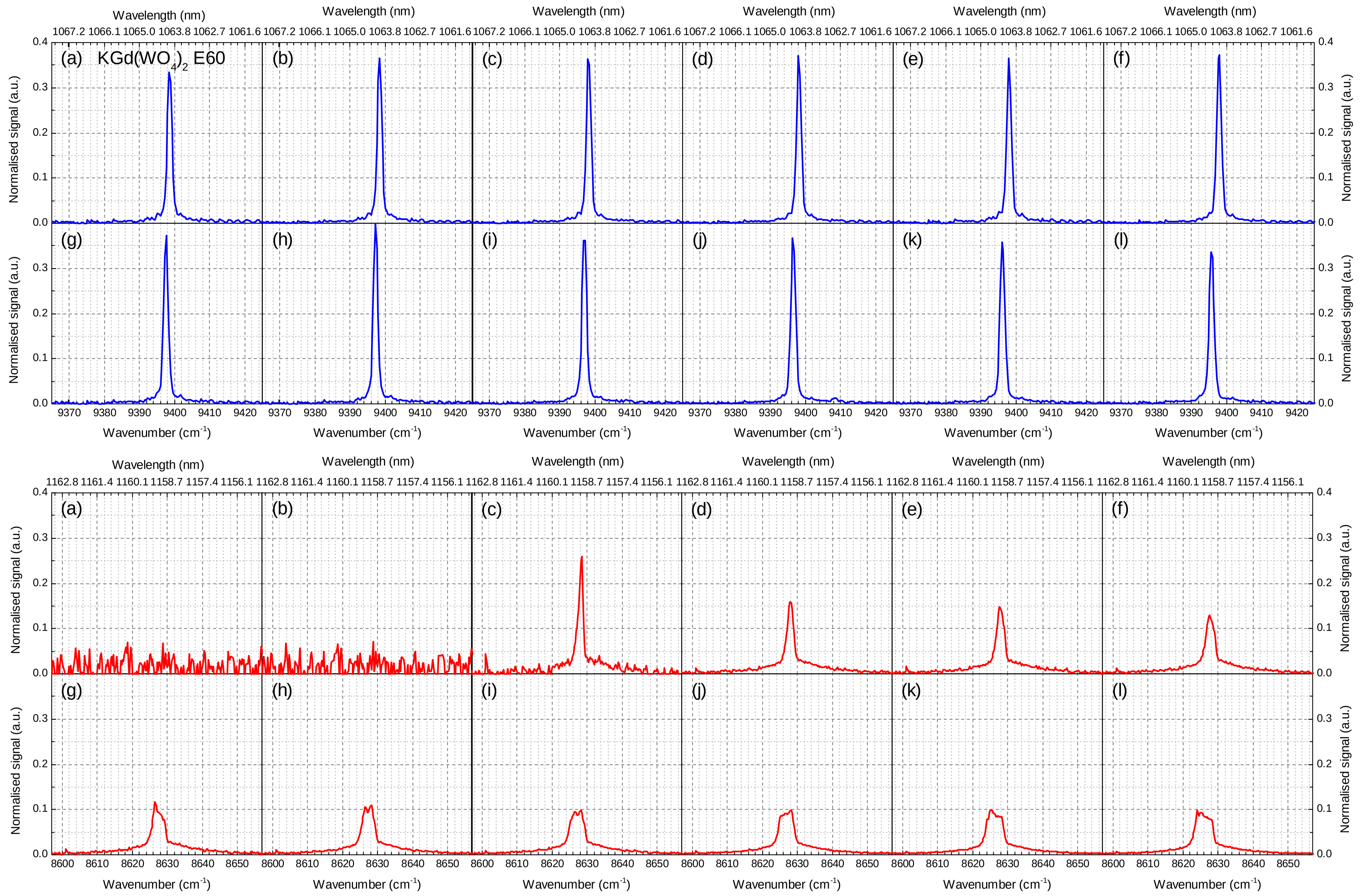

**Figure 5.26:** Spectra of KGd(WO$_4$)$_2$ Raman laser with the E60 etalon in the fundamental cavity. $P_{\text{abs}}$ = (a) 0.90 W (below Raman threshold), (b) 1.86 W (below Raman threshold), (c) 2.85 W, (d) 3.98 W, (e) 4.99 W, (f) 6.06 W, (g) 8.17 W, (h) 10.52 W, (i) 12.94 W, (j) 17.57 W, (k) 22.39 W, (l) 27.33 W.

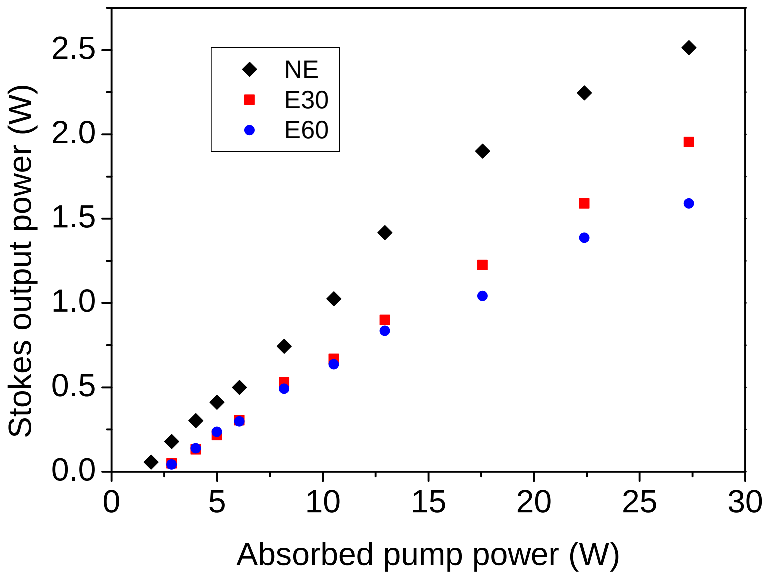

**Figure 5.27:** Power transfers for $KGd(WO_4)_2$ Raman laser with and without etalons.

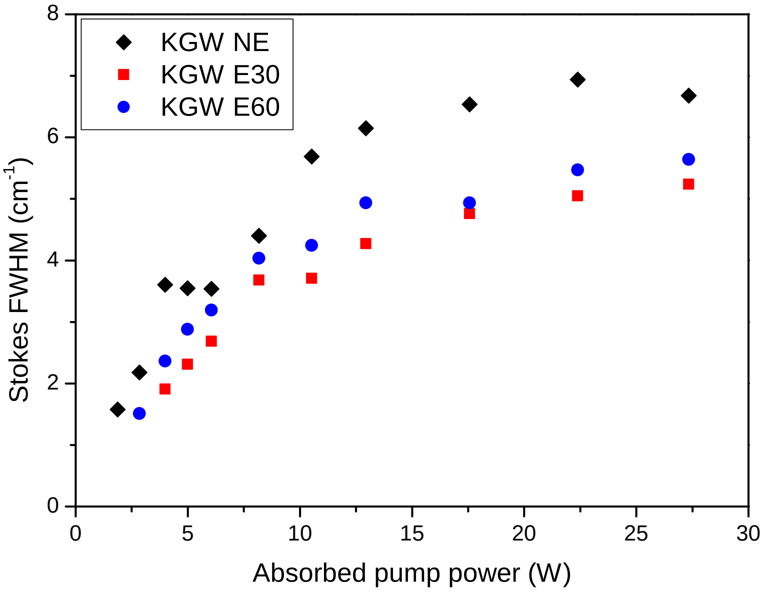

**Figure 5.28:** FWHM of the Stokes output spectrum as a function of pump power for the $KGd(WO_4)_2$ Raman laser with no etalon in the cavity and with the E30 and E60 etalons in the fundamental cavity (E30 and E60 respectively).

then either one of the fields would experience less than 100 % transmission through the etalon, or the Raman gain would be reduced since the fundamental and Stokes modes oscillating would not be separated by exactly the resonance frequency of the Raman transition. Using separate etalons in the fundamental- and Stokes-only arms of the cavity would provide more flexibility, but at the cost of more components requiring careful alignment.

### 5.5.3 Use of second etalon to eliminate satellite peaks in fundamental spectrum

The appearance of satellite peaks in the fundamental spectrum when the E30 or the E60 etalon is used could be detrimental to the performance of the laser since that energy is wasted. The satellite peaks oscillate at frequencies corresponding to the neighbouring transmission peaks of the etalon and therefore an etalon with a larger free spectral range (ie an optically thinner etalon) would be needed to suppress these modes. To this end, the uncoated, 50 µm thick YAG etalon was used in addition to the E30 etalon. While it would be preferable to use a single etalon, it was not possible to easily obtain an etalon that was both suitably thin and coated to provide a sufficiently high finesse. Therefore the low finesse, but very thin YAG etalon was used to suppress modes far from the centre of the gain bandwidth while the thicker, higher finesse glass etalon was used to keep the central fundamental peak narrow. Both etalons were placed in the fundamental cavity only. The spectra are shown in Figures 5.29 and 5.30 for the no etalon case and for the two etalon case respectively.

Note that due to fracture of the crystals used in the previous experiments, these experiments were performed using a 0.5 at.% Nd:$YVO_4$ disk (as opposed to 1 at.%) and a shorter $BaWO_4$ crystal (16.35 mm as opposed to 25 mm). The cavity length was adjusted to account for the shorter $BaWO_4$ crystal and very similar performance was obtained.

The presence of a double peak in the fundamental even below Raman threshold for the no etalon case (see Figure 5.29 (a), (b) and (c)) suggests that the bond between the heatspreader and the Nd:$YVO_4$ disk was imperfect and was causing an etalon effect itself. Otherwise, the spectral behaviour of the laser is very similar. It can be seen from Figure 5.30 that by using the two etalons together it is possible to obtain a single, narrow fundamental peak at all pump powers. The Stokes peak is also narrow. The FWHM of the fundamental and Stokes peaks for both cases are plotted as functions of pump power in Figure 5.31. When both etalons are used, the fundamental and Stokes peaks are both less than 2 $\text{cm}^{-1}$ wide across the entire range of pump powers.

The power transfers for the two cases are shown in Figure 5.32. The maximum power obtained with no etalons in the cavity was 2.86 W, while with both etalons in the cavity the maximum power was 2.52 W, a reduction of 12 %. However, the laser performance did tend to drift slightly over the time taken to collect the power transfer

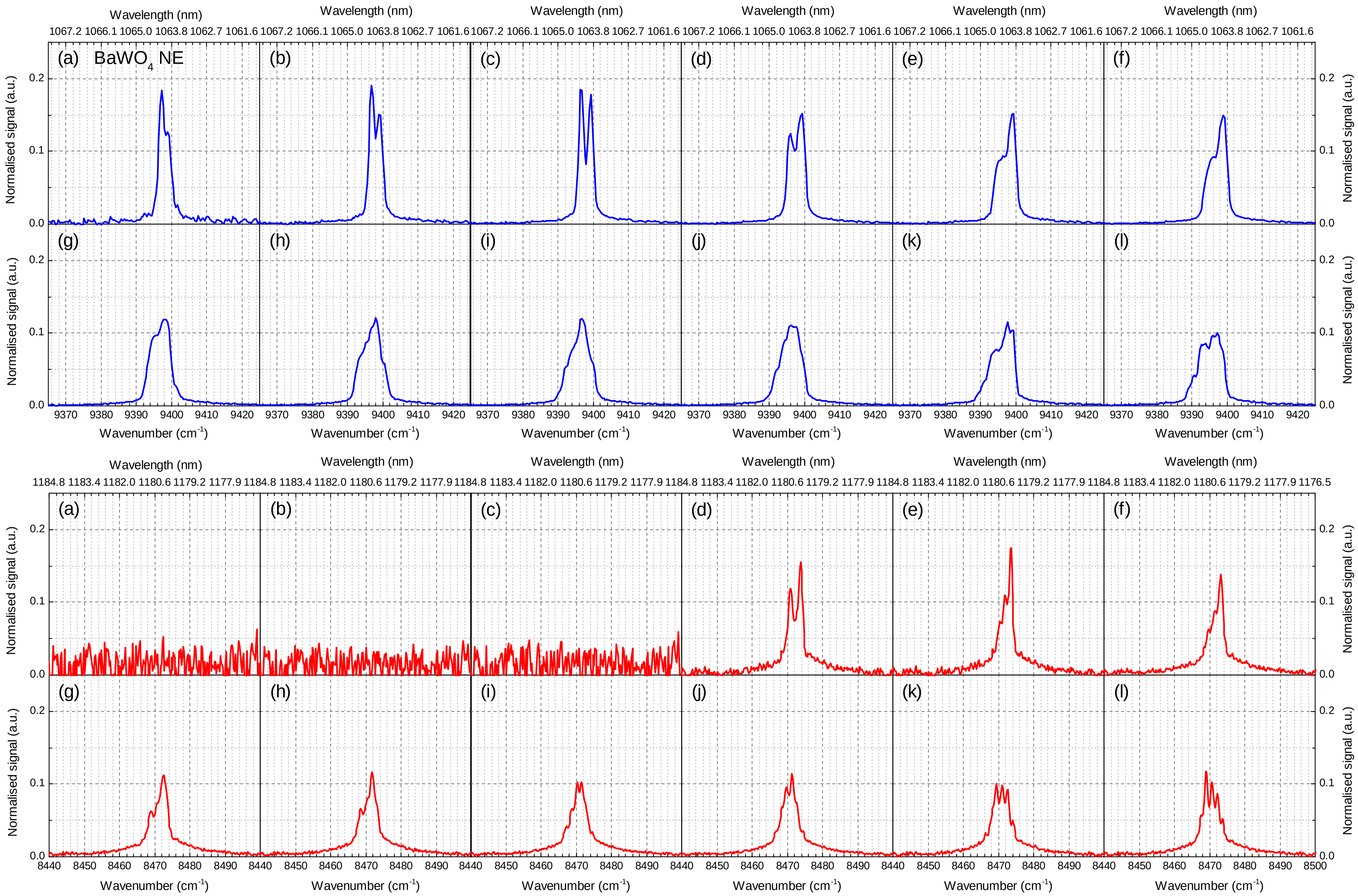

**Figure 5.29:** Spectra of $BaWO_4$ Raman laser with no etalon in the fundamental cavity, using a 0.5 % doped Nd:$YVO_4$ disk and a 16.35 mm long $BaWO_4$ crystal. $P_{\text{abs}}$ = (a) 0.72 W (below Raman threshold), (b) 1.57 W (below Raman threshold), (c) 3.16 W (below Raman threshold), (d) 6.49 W, (e) 10.18 W, (f) 14.23 W, (g) 18.48 W, (h) 22.46 W, (i) 27.04 W, (j) 29.37 W, (k) 31.54 W, (l) 33.87 W.

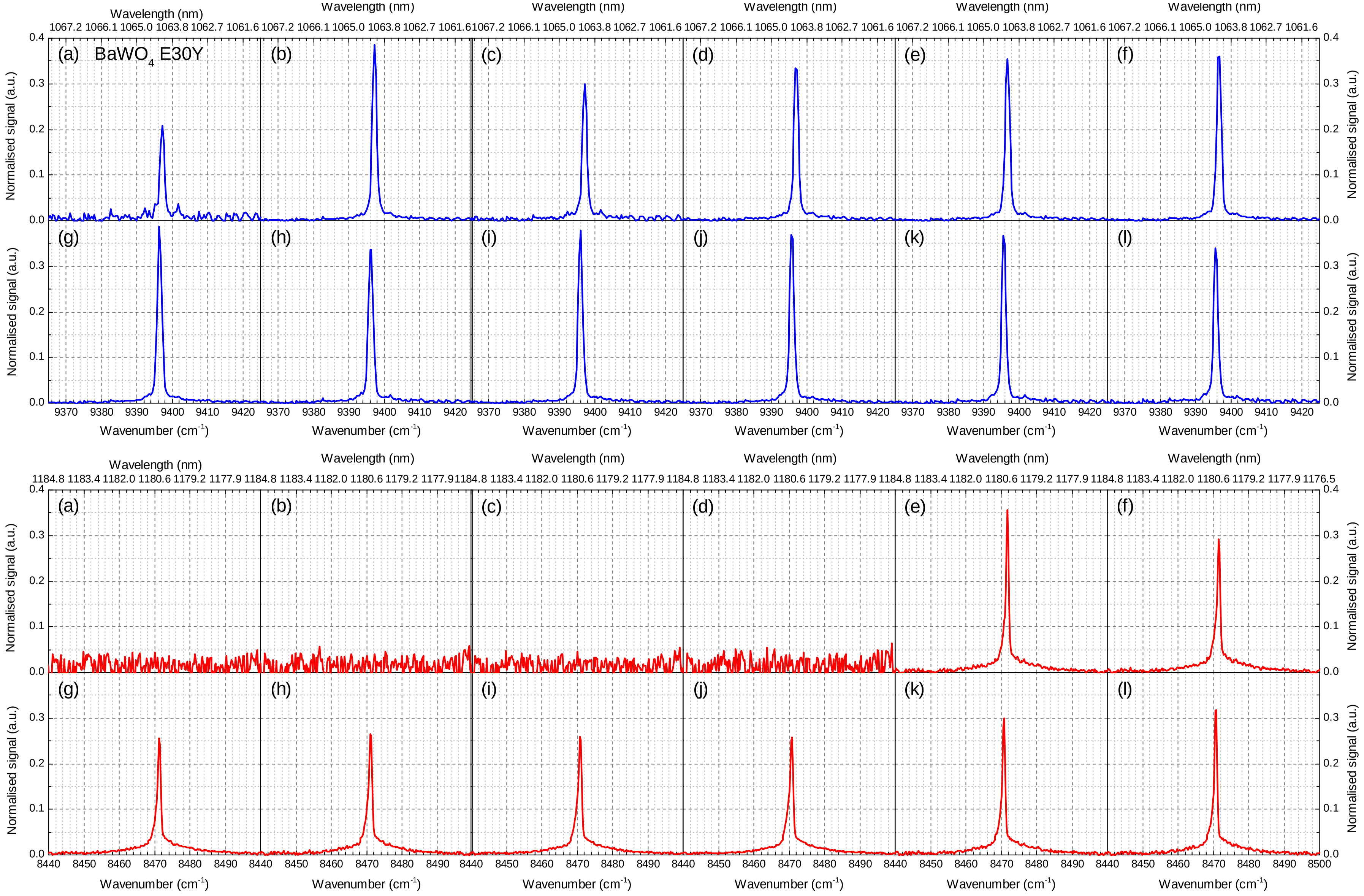

**Figure 5.30:** Spectra of BaWO$_4$ Raman laser with the E30 etalon and the YAG etalon in the fundamental cavity. $P_{\text{abs}}$ = (a) 0.72 W (below Raman threshold), (b) 1.57 W (below Raman threshold), (c) 3.16 W (below Raman threshold), (d) 6.49 W (below Raman threshold), (e) 10.18 W, (f) 14.23 W, (g) 18.48 W, (h) 22.46 W, (i) 27.04 W, (j) 29.37 W, (k) 31.54 W, (l) 33.87 W.

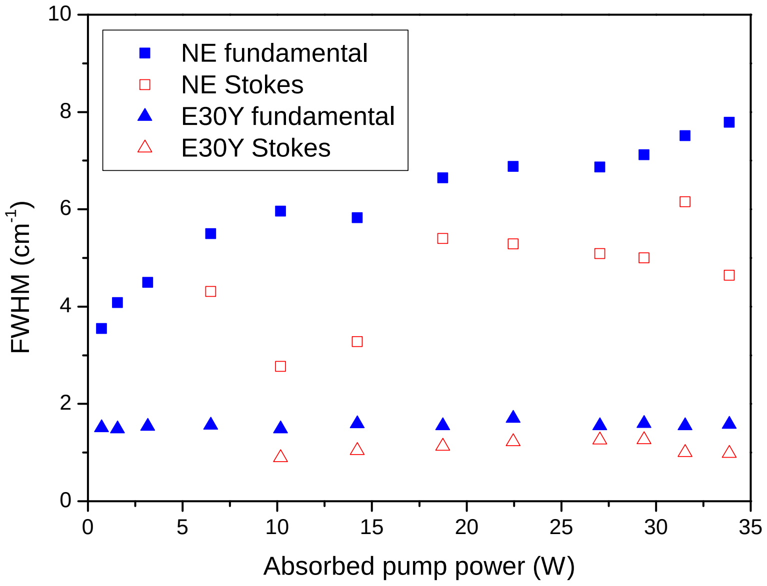

**Figure 5.31:** FWHM of the spectral peaks with no etalon (NE, squares) and with both the E30 and the YAG etalons (E30Y, triangles). FWHM of fundamental peaks are shown as filled blue symbols, FWHM of Stokes peaks as open red symbols.

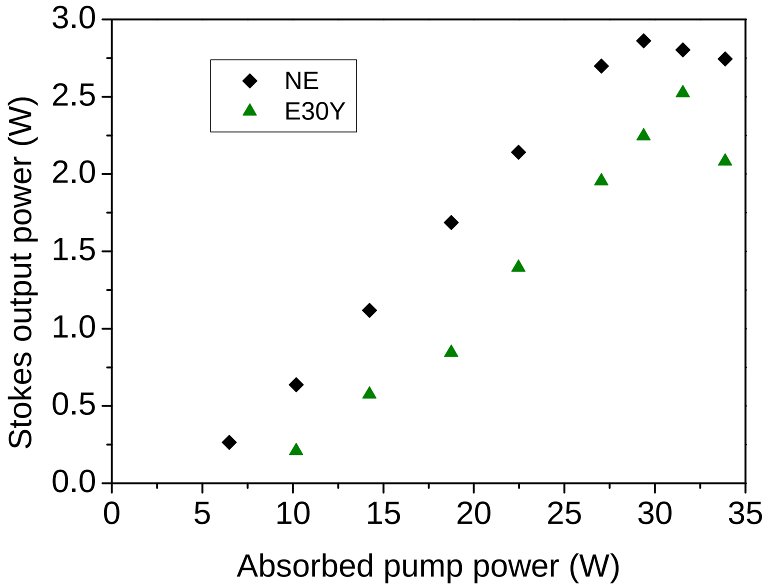

**Figure 5.32:** Power transfers for $BaWO_4$ Raman laser with no etalon in the cavity (NE) and with both the E30 etalon and the YAG etalon in the fundamental cavity (E30Y).

data. Immediately after optimisation for each case the maximum powers were 2.99 W and 2.87 W, representing a reduction of only 4 %. As was the case when the glass etalon was used on its own, it was possible to obtain a narrow fundamental spectrum with comparable Stokes output powers, but at the time of writing this thesis, no improvement in the output power was observed.

## 5.6 Numerical analysis of effect of broadening on effective Raman gain

In order to better understand the behaviour of the lasers with and without etalons, the effective Raman gain factor, $\varepsilon$ was calculated for each dataset using Equation 5.10. The Raman lines of $BaWO_4$ and $KGd(WO_4)_2$ were modelled as Lorentzian peaks with FWHM of $1.6\,\text{cm}^{-1}$ and $6.4\,\text{cm}^{-1}$, and centre frequencies of $925\,\text{cm}^{-1}$ and $768\,\text{cm}^{-1}$ respectively, while the actual measurements of the fundamental and Stokes spectra were used. These spectra were normalised to area as described in Sections 5.3.2 and 5.4 above. The HR4000 spectrometer exported data in wavelength steps that varied over the entire spectral range. This wavelength axis was converted to a wavenumber axis (also non-linear since $\tilde{\nu} = \lambda^{-1}$) and the spectra were then interpolated onto a regular wavenumber axis of step size $0.1\,\text{cm}^{-1}$ (the minimum step size in the spectrometer data was $0.21\,\text{cm}^{-1}$), which enabled a straightforward implementation of the convolution and overlap integral, yielding a value of $\varepsilon$ for each dataset. These values are plotted in Figures 5.33 and 5.34 for $BaWO_4$ and $KGd(WO_4)_2$ respectively. The MATLAB script for the calculation is reproduced in Appendix B.

There are several important things to note in this analysis. The values of epsilon for the $BaWO_4$ Raman laser, NE case are just above 0.1, implying that the effective Raman gain is reduced by almost 90 %. For the $KGd(WO_4)_2$ Raman laser, the reduction in the effective gain is not so severe, around 70 %. Equation 5.11, which gives the effective gain factor for the simple case of all Lorentzian peaks, illustrates why this difference exists - the much broader Raman transition of KGW means that it is less susceptible to reductions in the gain due to spectral broadening - only when the fundamental and Stokes spectra begin to approach the width of the Raman line is there a severe reduction in the effective gain. In the case of $BaWO_4$ the fundamental spectrum is already broader than the Raman transition even just above Raman threshold.

The values of $\varepsilon$ are also low for the E30 and E60 cases, showing little improvement over the NE case. This is mainly because of the satellite peaks in the fundamental, which generate no useful gain for the Stokes field. When two etalons were used in the $BaWO_4$ Raman laser (E30Y), a single narrow peak was obtained in both the fundamental and the Stokes fields, but it can be seen in Figure 5.33 that while there is some increase in $\varepsilon$ (from around 0.11 to 0.18), the improvement is not as much as might have been expected.

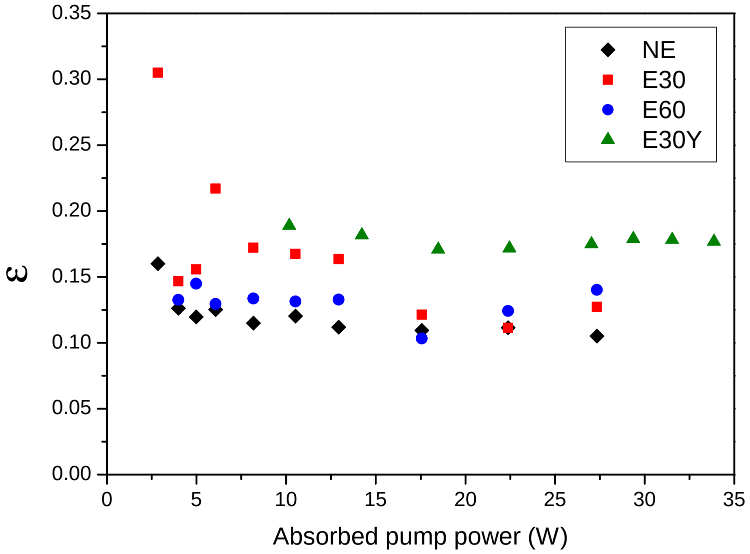

**Figure 5.33:** Effective Raman gain factor for $BaWO_4$ Raman laser with no etalon in the cavity (black diamond), with the E30 etalon (red squares), with the E60 etalon (blue circles) and with both the E30 etalon and the YAG etalon in the fundamental cavity (green triangles, E30Y).

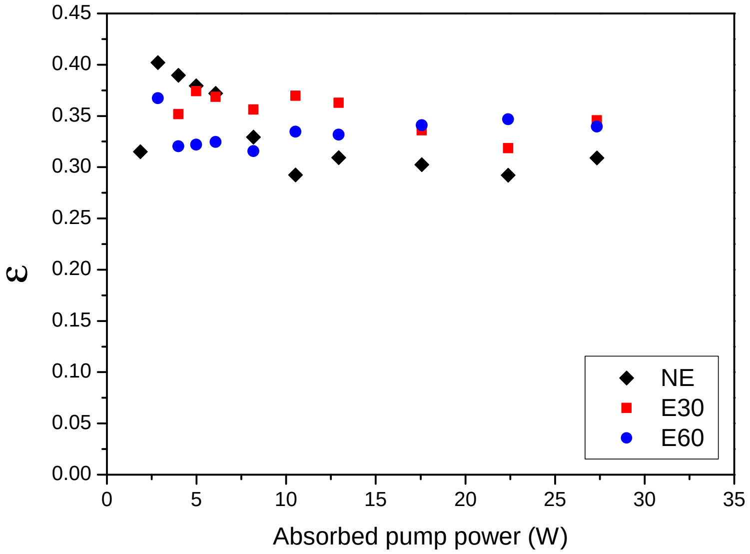

**Figure 5.34:** Effective Raman gain factor for $KGd(WO_4)_2$ Raman laser with no etalon in the cavity (black diamonds, NE), with the E30 etalon (red squares) and with the E60 etalon (blue circles).

Careful inspection of the spectra (see Figure 5.30) reveals that there is a substantial pedestal under the Stokes peak, which is in fact present in many of the spectra for the various cases although it is most obvious when the Stokes peak is narrow. This will reduce the value of $\varepsilon$ because it means that a significant fraction of the Stokes power is in the wings of the spectrum, where it experiences very little gain. To check the origin of this pedestal, the Stokes spectrum was measured with an optical spectrum analyser also (Agilent 86142B, resolution bandwidth 0.06 nm). It was found that the pedestal is an artefact of the HR4000 spectrometer but this discovery was made some time after the experiments were completed and there was no time available to take new data. This is unfortunate as it reduces the usefulness of the effective gain calculations outlined here. The HR4000 spectrometer had originally been used in preference to an optical spectrum analyser, since the sweep time of the latter instrument would result in the widely separated fundamental and Stokes spectra being measured at different times. In principle the measurements could be repeated using an optical spectrum analyser, but some consideration would have to be given as to whether this time delay would itself cause problems.

Nonetheless, the effective gain calculations do provide some useful insight into the effect of spectral changes on the effective Raman gain, and the more accurate the spectral data collected, the more useful the calculations would be. In the case of the present E30Y data for $BaWO_4$, the pedestal in the data makes it preferable to apply Equation 5.11, since the simple shape of the single fundamental and Stokes peaks should make this a reasonable approximation for $\varepsilon$. This leads to values of $\varepsilon$ between 0.35 and 0.4, three to four times the values calculated for the NE case using the full calculation. This suggests that using the two etalons to maintain a single, narrow peak in the fundamental spectrum should lead to a significant increase in the effective Raman gain. This brings up the question once again as to why no improvement in output power was observed when controlling the spectral behaviour successfully with the two etalons. Some of the potential reasons for this were discussed in Sections 5.5.1 and 5.5.2, and these will be summarised in the concluding section of this chapter.

## 5.7 Conclusions

The spectral behaviour of CW intracavity Raman lasers was investigated. Significant broadening of the fundamental spectrum was observed when using $BaWO_4$ as the Raman crystal. The fundamental peak had a FWHM of less than $3\,\mathrm{cm}^{-1}$ below Raman threshold, but broadened to more than $9\,\mathrm{cm}^{-1}$ at high powers. When SRS was suppressed by blocking the Stokes cavity, the fundamental FWHM remained below $5\,\mathrm{cm}^{-1}$. This non-SRS-induced broadening was attributed to spatial hole burning.

It was found that the broadening of the fundamental spectrum due to SRS is less severe when using a crystal with a broader Raman linewidth ($KGd(WO_4)_2$). In this case the fundamental FWHM reached a maximum of $5.5\,\mathrm{cm}^{-1}$. However, a small distinct peak appeared 21 cm$^{-1}$ from the main peak. The broad KGd(WO$_4$)$_2$ Raman line presented a broad loss to the centre of the fundamental gain bandwidth preventing broadening of the main peak, but modes in the extreme wings of the fundamental gain bandwidth could still reach threshold above certain pump powers. This behaviour is consistent with the theoretical picture of the broadening presented in Section 5.2. In the future it would be useful to make similar measurements using a Raman material with a Raman transition broader than the gain bandwidth of the laser gain material to verify that no SRS-induced broadening occurs. LiNbO$_3$ would be one candidate; the weak transitions around 300 cm$^{-1}$ to 400 cm$^{-1}$ in BaWO$_4$ and Nd:GdVO$_4$ [28] might be other possibilities if SRS on the stronger, narrower transitions could be suppressed.

Etalons were used to control the broadening of the fundamental field. The coupled cavity configuration made it possible to place the etalons in the fundamental cavity only so that the Stokes field was unaffected. When a 290 µm thick glass etalon (coated to have reflectivity of either 30 % or 60 %, denoted as the E30 and E60 etalons respectively) was used in the BaWO$_4$ Raman laser, both the fundamental and Stokes peaks were narrow (FWHM around 2 cm$^{-1}$ or less) but satellite peaks appeared in the fundamental spectrum at frequencies corresponding to the transmission peaks of the etalon. When either of these etalons was used in the KGd(WO$_4$)$_2$ Raman laser, the fundamental peak was similarly narrow but the Stokes peak was broader, as would be expected given the broader Raman linewidth of KGd(WO$_4$)$_2$. The satellite peaks were much less prominent in the KGd(WO$_4$)$_2$ system. When the E30 etalon was used in the BaWO$_4$ system, output powers comparable to those of the spectrally unconstrained laser were obtained. However the E60 etalon reduced the output power. Both etalons reduced the performance of the KGd(WO$_4$)$_2$ Raman laser. It was possible to eliminate the satellite peaks in the BaWO$_4$ system by using an uncoated, 50 µm thick YAG etalon in addition to the E30 etalon. A moderate decrease (12 %) in the maximum output power was observed compared to the spectrally unconstrained laser.

Calculations were performed to determine the impact of the spectral broadening on the effective Raman gain. These predicted an increase in the effective Raman gain for the BaWO$_4$ Raman laser when using the two etalons together to get a single, narrow fundamental peak. However, the accuracy of these calculations was limited by a pedestal under the Stokes peaks introduced by the spectrometer. This work should be repeated in the future, using data from a more accurate spectrometer or optical spectrum analyser.

Given the decrease in effective Raman gain for spectrally broad fundamental fields, it is surprising that constraining the width of the fundamental spectrum did not lead to an improvement in the performance of the Raman laser. It could be that imperfections in the etalons (for example poor flatness or parallelism) are introducing small losses, to which Raman lasers are extremely sensitive. Alternatively it may be that limiting the fundamental bandwidth has other detrimental impacts on the flow of energy between the population inversion and the fundamental and Stokes fields, which counterbalance the increase in the effective Raman gain. If possible, it would useful in the future to obtain a single, narrow fundamental peak using just one etalon rather than the combination of the YAG and glass etalons used here, since this would disturb the laser cavity less. A 50 µm thick etalon coated to 30 % reflectivity would likely be suitable.

As noted above, when etalons were used to control the spectral width of the fundamental field in the $BaWO_4$ Raman laser, the Stokes output was also spectrally narrow thanks to the narrow Raman linewidth of $BaWO_4$. In the case of $KGd(WO_4)_2$, the broader Raman line led to a broad Stokes spectrum even when the fundamental spectrum was kept narrow. The main focus of this chapter has been on controlling the spectral width of the fundamental in order to improve the effective Raman gain – the spectral width of the output Stokes beam has been a secondary consideration. However, the work presented here does lead to several points that should be taken into account when spectrally narrow output is required from an intracavity Raman laser. Firstly, it is beneficial to keep the fundamental spectrum narrow and to use a Raman crystal with a narrow Raman linewidth. However, as has been shown in the present work, SRS-induced broadening is more problematic when the Raman linewidth is narrow compared to the fundamental gain bandwidth. Taking into account other broadening effects such as spatial hole burning, it is therefore likely that some form of spectral control of the fundamental field will be required. If a Raman material with a broad Raman linewidth is used, then it may be necessary to directly control the Stokes spectral width also, either with a single etalon that interacts with both the fundamental and Stokes fields, or with a separate etalon for each field. It should be noted that the laser cavities presented here may lead to narrow Stokes output in some circumstances ($\sim 2\,\mathrm{cm}^{-1}$ or 0.2 nm), but given the short free spectral range of the cavities ($\sim 2\,\mathrm{pm}$) there may still be many axial modes oscillating. It would be difficult to get such a long cavity to run on a single-longitudinal mode (SLM), and if SLM operation was desired a much shorter cavity and/or much stronger spectral filtering would be advisable.

In summary, the SRS process can induce broadening of the fundamental spectrum in intracavity Raman lasers. The details of this effect depend on the relative widths of the Raman transition and the fundamental gain. A broad fundamental spectrum leads to a reduction in the effective Raman gain in CW crystalline Raman lasers. It is possible to obtain spectrally narrower fundamental and Stokes fields via the use of etalons, at output power levels comparable to those of Raman lasers without any etalons, yielding a higher spectral brightness. However, at the time of writing this thesis, no improvement in output power was observed.

# Bibliography

[1] P. Dekker, H. M. Pask, D. J. Spence, and J. A. Piper, "Continuous-wave, intracavity doubled, self-Raman laser operation in Nd:Gd$VO_4$ at 586.5 nm," *Optics Express*, vol. 15, no. 11, pp. 7038–7046, 2007.

[2] P. Dekker, H. M. Pask, and J. A. Piper, "All-solid state 704 mW continuous-wave yellow source based on an intracavity frequency-doubled crystalline Raman laser," *Optics Letters*, vol. 32, no. 9, pp. 1114–1116, 2007.

[3] L. Fan, Y. X. Fan, Y. H. Duan, Q. Wang, H. T. Wang, G. H. Jia, and C. Y. Tu, "Continuous-wave intracavity Raman laser at 1179.5 nm with Sr$WO_4$ Raman crystal in diode-end-pumped Nd:Y$VO_4$ laser," *Applied Physics B*, vol. 94, no. 4, pp. 553–557, 2009.

[4] L. Fan, Y. X. Fan, and H. T. Wang, "A compact efficient continuous-wave self-frequency Raman laser with a composite Y$VO_4$/Nd:Y$VO_4$/Y$VO_4$ crystal," *Applied Physics B*, vol. 101, no. 3, pp. 493–496, 2010.

[5] L. Fan, Y.-X. Fan, Y.-Q. Li, H. Zhang, Q. Wang, J. Wang, and H.-T. Wang, "High-efficiency continuous-wave Raman conversion with a Ba$WO_4$ Raman crystal," *Optics Letters*, vol. 34, no. 11, pp. 1687–1689, 2009.

[6] V. A. Lisinetskii, A. S. Grabtchikov, A. A. Demidovich, V. N. Burakevich, V. A. Orlovich, and A. N. Titov, "Nd:KGW/KGW crystal: efficient medium for continuous-wave intracavity Raman generation," *Applied Physics B*, vol. 88, no. 4, pp. 499–501, 2007.

[7] V. A. Orlovich, V. N. Burakevich, A. S. Grabtchikov, V. A. Lisinetskii, A. A. Demidovich, H. J. Eichler, and P. Turpin, "Continuous-wave intracavity Raman generation in Pb$WO_4$ crystal in the Nd:Y$VO_4$ laser," *Laser Physics Letters*, vol. 3, no. 2, pp. 71–74, 2006.

[8] D. C. Parrotta, A. J. Kemp, M. D. Dawson, and J. E. Hastie, "Tunable continuous-wave diamond Raman laser," *Optics Express*, vol. 19, no. 24, pp. 24165–24170, 2011.

[9] J. Lin, H. M. Pask, D. J. Spence, C. J. Hamilton, and G. P. A. Malcolm, "Continuous-wave VECSEL Raman laser with tunable lime-yellow-orange output," *Optics Express*, vol. 20, pp. 5219–5224, Feb 2012.

[10] V. N. Burakevich, V. A. Lisinetskii, A. S. Grabtchikov, A. A. Demidovich, V. A. Orlovich, and V. N. Matrosov, "Diode-pumped continuous-wave Nd:YVO$_4$ laser with self-frequency Raman conversion," *Applied Physics B*, vol. 86, no. 3, pp. 511–514, 2007.

[11] D. J. Spence - Private communication.

[12] Y. Sato and T. Taira, "Spectroscopic Properties of Neodymium-Doped Yttrium Orthovanadate Single Crystals with High-Resolution Measurement," *Japanese Journal of Applied Physics*, vol. 41, no. Part 1, No. 10, pp. 5999–6002, 2002.

[13] Y. Sato and T. Taira, "Comparative study on the spectroscopic properties of Nd:GdVO$_4$ and Nd:YVO$_4$ with hybrid process," *IEEE Journal of Selected Topics in Quantum Electronics*, vol. 11, no. 3, pp. 613–620, 2005.

[14] Y. Sato and T. Taira, "Temperature dependencies of stimulated emission cross section for Nd-doped solid-state laser materials," *Optical Materials Express*, vol. 2, pp. 1076–1087, Aug 2012.

[15] U. Keller and T. Chiu, "Resonant passive mode-locked Nd:YLF laser," *Quantum Electronics, IEEE Journal of*, vol. 28, no. 7, pp. 1710–1721, 1992.

[16] T. Basiev, A. Sobol, Y. Voronko, and P. Zverev, "Spontaneous Raman spectroscopy of tungstate and molybdate crystals for Raman lasers," *Optical Materials*, vol. 15, no. 3, pp. 205 – 216, 2000.

[17] T. T. Basiev, A. A. Sobol, P. G. Zverev, V. Osiko, Vyacheslav, and R. C. Powell, "Comparative spontaneous Raman spectroscopy of crystals for Raman lasers," *Applied Optics*, vol. 38, no. 3, pp. 594–598, 1999.

[18] A. Penzkofer, A. Laubereau, and W. Kaiser, "High Intensity Raman Interactions," *Progress in Quantum Electronics*, vol. 6, no. 2, pp. 56–140, 1979.

[19] E. A. Stappaerts, J. W. H. Long, and H. Komine, "Gain enhancement in Raman amplifiers with broadband pumping," *Optics Letters*, vol. 5, pp. 4–6, Jan 1980.

[20] J. Eggleston and R. Byer, "Steady-state stimulated Raman scattering by a multimode laser," *IEEE Journal of Quantum Electronics*, vol. 16, pp. 850 – 853, Aug 1980.

[21] A. T. Georges, "Statistical theory of Raman amplification and spontaneous generation in dispersive media pumped with a broadband laser," *Physical Review A*, vol. 39, pp. 1876–1886, Feb 1989.

[22] G. Turri, H. P. Jenssen, F. Cornacchia, M. Tonelli, and M. Bass, "Temperature-dependent stimulated emission cross section in $Nd^{3+}$:$YVO_4$ crystals," *Journal of the Optical Society of America B*, vol. 26, no. 11, pp. 2084–2088, 2009.

[23] X. Délen, F. Balembois, and P. Georges, "Temperature dependence of the emission cross section of Nd:$YVO_4$ around 1064 nm and consequences on laser operation," *Journal of the Optical Society of America B*, vol. 28, no. 5, pp. 972–976, 2011.

[24] S. M. Hooker and C. E. Webb, *Laser Physics.* Oxford University Press, 2010.

[25] J. J. Zayhowski, "The effects of spatial hole burning and energy diffusion on the single-mode operation of standing-wave lasers," *IEEE Journal of Quantum Electronics*, vol. 26, pp. 2052 –2057, Dec 1990.

[26] I. V. Mochalov, "Laser and nonlinear properties of the potassium gadolinium tungstate laser crystal $KGd(WO_4)_2$:$Nd^{3+}$-(KGW:Nd)," *Optical Engineering*, vol. 36, no. 6, pp. 1660–1669, 1997.

[27] W. Koechner, *Solid-State Laser Engineering.* Springer, 6th ed., 2006.

[28] J. Lin and H. M. Pask, "Cascaded self-Raman lasers based on 382 $cm^{-1}$ shift in Nd:$GdVO_4$," *Optics Express*, vol. 20, pp. 15180–15185, Jul 2012.

# Chapter 6

# Conclusions and outlook

Complex thermal and spectral effects occur in crystalline CW intracavity Raman lasers and approaches to managing these phenomena have been investigated, with a view to improving the performance of these devices. Thermal problems often limit the performance of CW intracavity Raman lasers, and these effects are more complex than in conventional lasers because two thermal lenses arise in the cavity, one in the laser gain crystal and one in the Raman crystal. These lenses behave differently, since the former is proportional to the pump power and the latter is proportional to the Stokes power, and this makes it difficult to compensate for their effects. Meanwhile, since the SRS process is occurring inside the cavity of the fundamental laser, it influences the behaviour of the fundamental laser leading to broadening of the fundamental spectrum which in turn can lead to a reduction in the effective Raman gain, as well as a spectrally broad Stokes output. The work presented in this thesis on managing these effects will now be summarised. This chapter includes a summary of the work presented in this thesis, followed by suggestions for future work. Finally, the main achievements of this PhD project will be highlighted.

## 6.1 Summary

### 6.1.1 Measurement of optical losses in synthetic diamond

In Chapter 2, intracavity measurements of the optical losses in CVD-grown single crystal diamonds were presented. Maintaining low optical losses is of critical importance for CW intracavity Raman lasers, in which the optimum output coupling is typically below 1 %. The extreme material properties of diamond [1], especially its high thermal conductivity, make it a promising Raman crystal; however, it will be possible to take advantage of these only if low birefringence, low loss synthetic diamond can be reliably sourced. Intracavity measurements of the optical loss at 1064 nm in three synthetic diamonds were made, using the Caird and Findlay-Clay techniques and the results of these experiments were compared to calorimetric measurements made by a colleague of the author. The Caird analysis and the calorimetric measurements were found to be in reasonable agreement about the relative losses of the different samples, although accurate absolute values are harder to obtain. The lowest loss sample out of the three studied had an attenuation coefficient of $0.010\,\mathrm{cm}^{-1}$ and by communicating this information to the diamond supplier (Element Six Ltd.) it was possible to identify and obtain diamond with even lower losses ($0.006\,\mathrm{cm}^{-1}$, measured via calorimetry by a colleague of the author). This identification of low loss diamonds led to the demonstration of multi-Watt diamond Raman lasers by colleagues of the author [2–4]. Other diamonds were purchased for use by the author but these had higher losses ($0.013\,\mathrm{cm}^{-1}$ and $0.017\,\mathrm{cm}^{-1}$) than specified and were unsuitable for use in CW Raman lasers. It is clear that diamond has potential as a Raman crystal, a fact that is demonstrated both by the loss measurements presented in this thesis and by the demonstration of a number of Raman lasers by various researchers [2–5]. However, the supply of suitably low loss diamond is not yet reliable and this must be resolved if diamond is to fulfil its potential as a useful Raman gain medium.

### 6.1.2 Thermal management in intracavity Raman lasers

Diamond's thermal conductivity is two to three orders of magnitude greater than that of most conventional Raman crystals. However, even if low loss diamond could be reliably sourced these other materials would remain of interest in order to maintain a choice of output wavelengths from Raman lasers, since the Raman shift is specific to the material used. Therefore, methods to mitigate and manage thermal lensing in Raman lasers based on more conventional materials remain of great interest and attention was turned to investigating such methods in a $\mathrm{BaWO_4}$ Raman laser.

A disk geometry was used to reduce the thermal lens in the laser gain crystal, specifically a 0.5 mm thick $\mathrm{Nd{:}YVO_4}$ disk bonded to a diamond heatspreader. An unconventional polarisation-rotating double-pass geometry was used for the pump beam, to obtain significant pump absorption with a relatively simple geometry. Finite element analysis was used to model the thermal lens in the disk and it was calculated that the focal length of the $\mathrm{d}n/\mathrm{d}T$ component of the lens and the radius of curvature of the deformed end mirror were both on the order of hundreds of millimetres for practical pump spot radii and powers. This is significantly weaker than the thermal lens focal lengths of tens of millimetres estimated for some rod-based systems [6]. The use of the disk geometry, with its weak thermal lens, facilitated the construction of longer and more complex cavities, which made it easier to probe the thermal behaviour of the laser (Chapter 3), provided greater flexibility to design an efficient Raman laser (Chapter 4), and facilitated the investigation of spectral broadening (Chapter 5).

The strength of the thermal lens in $\mathrm{BaWO_4}$ was measured using lateral shearing interferometry and it was found that the lens had a negative focal length and was highly astigmatic. These measurements are presented in Chapter 3 and they are, to the best of the author's knowledge, the first direct measurements of the thermal lens in a CW intracavity Raman laser built around separate laser and Raman crystals. Comparison of these results to the finite element modelling of the thermal lens in the Nd:YVO$_4$ disk showed that the negative thermal lens in the BaWO$_4$ crystal was comparable to or stronger than the positive thermal lens in the Nd:YVO$_4$ disk for several practical pump spot radii (180 µm, 300 µm and 400 µm), such that both lenses must be accounted for when designing the Raman laser. This information was then used to refine the cavity design and hence improve the performance of the laser.

A coupled cavity configuration was used in which the separate cavities for the fundamental and Stokes fields overlapped in the Raman crystal. This design had several benefits. Firstly, the Stokes field did not interact with the Nd:YVO$_4$/diamond disk unit and therefore experienced lower losses than would have been the case in a single cavity configuration. Secondly, the fundamental and Stokes cavities could, within limits, be optimised independently of each other and in particular, an optical element could be placed in only one of the cavities without affecting the other. In this way it was possible to modulate the Stokes field (and the SRS process) by placing a chopper in the Stokes-only arm of the cavity. This reduced the strength of the thermal lens in the Raman crystal while leaving the thermal lens in the Nd:YVO$_4$ crystal unaffected, thereby providing information that helped to partially disentangle the effects of the two thermal lenses, in addition to the information that could be obtained by chopping the pump beam (thereby reducing the strength of both lenses simultaneously). The thermal lens strengths determined in Chapter 3 were also fed into ABCD matrix models of the cavities, in order to predict how the overlap of the fundamental and Stokes modes in the BaWO$_4$ crystal and the $g_1$-$g_2$ stability parameters of the cavities varied with pump power. Together, these experiments and calculations provided information on the effect of the two thermal lenses on the behaviour of the cavity and it was found that the negative lens in the BaWO$_4$ crystal helped to stabilise the cavity against the effect of the positive lens in the Nd:YVO$_4$ disk.

By refining the cavity design based on this information, high performance was obtained from a 300 µm pump spot radius system, which produced a maximum Stokes output power of 3.15 W for an absorbed pump power of 33.9 W, representing a diode-to-Stokes conversion efficiency of 9.3 %. The Raman threshold was 4.7 W and the slope efficiency was 11.5 %. This is comparable to many multi-Watt, single-end-pumped CW crystalline intracavity Raman lasers, for example [7], but is somewhat less than the 4.1 W obtained by Lin *et al* from a double-end-pumped Nd:GdVO$_4$ self-Raman laser [8] or the 6.1 W obtained by Savitski *et al*, from a KGd(WO$_4$)$_2$ Raman laser in which the laser gain medium was a side-pumped Nd:YLF rod [4]. It should be noted, however, that the conversion efficiency in the latter system was only 4 % with respect to incident pump power in the commercial side-pumped Nd:YLF module.

When a larger pump spot radius was used (400 µm), in order to reduce the strength of the thermal lens in the Nd:YVO$_4$ disk even further, poorer performance was observed. It is not fully clear why this system performed poorly. It is challenging to design a cavity that has a large mode in the Nd:$YVO_4$ disk, to match the pump mode, and a small mode in the Raman crystal, to keep the Raman threshold low, and in such cavities, the mode sizes are often sensitive to the thermal lens strengths and vary significantly with pump power. There was insufficient time to fully optimise the design of this cavity and it is possible that further work on this system in the future might lead to improvements in performance.

### 6.1.3 Investigation of spectral broadening in intracavity Raman lasers

A comprehensive investigation of spectral broadening in intracavity Raman lasers was undertaken. Significant broadening of the fundamental spectrum was observed in a Nd:$YVO_4$ /$BaWO_4$ Raman laser. These measurements are consistent with previous observations by other researchers and groups [6, 7, 9–12], but while the effect has been noted by a number of groups, to the best of the author's knowledge no detailed investigation has been undertaken until now. The fundamental spectrum had a FWHM of less than $3\,\text{cm}^{-1}$ below Raman threshold, but broadened to more than $9\,\text{cm}^{-1}$ at high powers. It was demonstrated that a significant part of this broadening was due to the SRS process presenting a frequency-dependent loss to the fundamental field, while another contribution to the broadening was attributed to spatial hole burning. The dependence of the SRS-induced broadening effect on the linewidth of the Raman transition was investigated by comparing the spectra of a $BaWO_4$ Raman laser and a $KGd(WO_4)_2$ Raman laser. It was found that SRS in $KGd(WO_4)_2$, which has a broader Raman line than $BaWO_4$, induced less broadening of the fundamental spectrum, which is consistent with the proposed mechanism for the broadening process.

Etalons were used successfully to limit the broadening of the fundamental field. The coupled cavity configuration made it possible to place the etalon in the fundamental-only arm of the cavity, so that the Stokes field was unaffected. A 290 µm thick, $R = 30\,\%$ coated glass etalon kept the main fundamental peak narrow (FWHM around $2\,\text{cm}^{-1}$ or less) in both the $BaWO_4$ and the $KGd(WO_4)_2$ lasers, but satellite peaks appeared corresponding to neighbouring etalon transmission peaks. These were more prominent in the $BaWO_4$ Raman laser than in the $KGd(WO_4)_2$ Raman laser, which again is consistent with the theoretical picture of the broadening mechanism, which predicts that the narrower Raman line of $BaWO_4$ will cause more severe broadening of the fundamental spectrum. The output power of the $BaWO_4$ Raman laser was similar with and without the etalon, but the etalon reduced the output power of the $KGd(WO_4)_2$ laser. These satellite peaks may be detrimental to the performance of the laser as energy is "leaking" into these modes, which are not Raman-shifted. The addition of a 50 µm thick, uncoated YAG etalon to the $BaWO_4$ Raman laser, in addition to the 290 µm thick, $R = 30\,\%$ coated glass etalon, eliminated the satellite peaks. However, no increase in output power was observed. Again, time constraints were such that a wider selection of etalons could not be investigated.

The impact of the spectral broadening on the effective Raman gain was calculated and it was predicted that in the $BaWO_4$ Raman laser, the gain coefficient would be reduced by as much of a factor of 10 when no etalon was used to control the broadening. The effective gain in the $KGd(WO_4)_2$ Raman laser was predicted to be less sensitive to broadening of the fundamental field due to the broader Raman line of $KGd(WO_4)_2$. When both the glass etalon and the YAG etalon were used in the $BaWO_4$ Raman laser, the calculations predicted that the effective Raman gain should have increased by almost a factor of 2, and perhaps more since the calculations were negatively influenced by a broad pedestal introduced into the spectra by the spectrometer. This raises questions as to why the output power of the laser did not improve when the etalons were used. It is possible that imperfections in the etalons led to a small increase in loss, which balanced out the benefits of keeping the fundamental spectrum narrow.

Even though the output power did not improve, using the etalons in the $BaWO_4$ Raman laser did keep the fundamental spectrum narrow and hence the Stokes output also had a narrow spectrum ($\sim 1\,\mathrm{cm}^{-1}$) and so the spectral brightness of the laser was improved. In the $KGd(WO_4)_2$ laser, the Stokes spectrum was fairly broad ($\sim 5\,\mathrm{cm}^{-1}$) even when the fundamental spectrum was kept narrow by an etalon, due to the broad Raman transition in $KGd(WO_4)_2$.

## 6.2 Future work

### 6.2.1 Thermal effects

The work presented here has demonstrated the potential of the disk geometry for the laser gain crystal in intracavity Raman lasers to provide comparable performance to rod-based systems but with more flexible cavities. However, higher output powers were not achieved. The cavity analyses presented in Chapter 4 point towards several improvements that could be made in the future. It would be useful to make the cavity less reliant on the negative $BaWO_4$ lens for stability at high powers. One way to do this would be to further reduce the thermal lens in the Nd:$YVO_4$ disk by increasing the pump spot size. A 400 µm pump spot radius was tried, as reported in Section 4.5, but there was insufficient time to fully optimise the cavity to meet the fairly challenging mode-matching requirements of a large resonator mode in the Nd:$YVO_4$ disk and a small mode in the $BaWO_4$ crystal.

Another option would be to design the cavity to be less sensitive to the lens in the Nd:$YVO_4$ disk. A convex end mirror was used for this purpose in Section 4.4.1 and this yielded some improvement. However, the astigmatism of the thermal lens in the $BaWO_4$ poses some challenges - it would be better to use a cylindrical rather than a spherical end mirror since the cavity could then be properly compensated in both the tangential and the sagittal planes.

If the cavity could be made suitably insensitive to the relatively weak thermal lens in the Nd:YVO$_4$ disk (pumped with a 300 µm or 400 µm radius pump spot) then the next key thermal challenge would be the thermal lens in the Raman crystal. At this point, diamond might prove to be very advantageous if suitably low loss samples could be reliably sourced. A Raman laser based on a disk laser, pumped with a large pump mode, and a diamond rod would have only very weak thermal lenses in the cavity and should only encounter thermal problems at very high pump powers.

### 6.2.2 Spectral effects

Further work is also merited on controlling the spectral broadening in intracavity Raman lasers. The use of LiNbO$_3$ as a Raman crystal would provide further confirmation of the proposed mechanism for the SRS-induced broadening – LiNbO$_3$ has a Raman line that is much broader than the laser gain bandwidth of most Nd-doped laser crystals and therefore SRS-induced broadening should not occur in, for example, a Nd:YVO$_4$/LiNbO$_3$ intracavity Raman laser. The verification of this prediction would, in combination with the work presented in this thesis, provide very convincing evidence for the proposed broadening mechanism.

It remains unclear why the performance did not improve when the fundamental spectrum was constrained using etalons, despite the predicted increase in the effective Raman gain. This could be due to imperfections in the etalons reducing the peak transmission from 100 % and introducing losses to the cavity and so it would be useful to try to use a single, very high quality etalon with a sufficiently large free spectral range and high finesse that it could replace the two etalons that were used simultaneously in Section 5.5.3. A 50 µm thick YAG etalon coated to 30 % reflectivity would likely be suitable.

If narrowband (eg $\sim 1\,\mathrm{cm}^{-1}$) Stokes output is desired from a laser using a Raman crystal with a broad Raman transition, such as KGd(WO$_4$)$_2$, then it may be necessary to place an etalon in the Stokes cavity also. Some investigation would be required to determine whether it would be better to place a single etalon in the shared section of the cavity, or to place one etalon in the fundamental-only arm and another in the Stokes-only arm.

## 6.3 Achievements and outlook

It has been shown throughout this thesis that the disk laser geometry provides a useful test-bed for probing thermal and spectral effects in intracavity Raman lasers, thanks to the more flexible cavity design permitted by the weak thermal lensing that occurs in the laser gain disk. It has also been shown that CW intracavity Raman lasers based on a disk geometry can have comparable performance to rod-based systems. The flexibility of the disk-based cavities, especially the ability to build longer cavities and engineer a wider variety of mode sizes at various points in the cavity, may prove useful for Raman lasers that include additional elements such as $\chi^{(2)}$ nonlinear crystals for frequency conversion to the visible, or even saturable absorbers for modelocking, if ultrashort pulsed operation was desired.

The information obtained in this work by probing thermal and spectral effects in the disk-based system can be fed back into refining the design of the disk-based Raman laser itself, as described here, or to gain general insights applicable to other CW intracavity Raman laser designs also. It is clear from the work presented here that careful consideration must be given to both thermal and spectral effects when designing such systems. The choice of laser gain crystal and Raman crystal may be influenced by their thermal and mechanical properties, and also by the relative widths of the fundamental laser gain profile and the Raman transition. When possible, it is useful to have detailed information about the thermal lenses that arise in the chosen crystals, since these can have surprising properties such as the large astigmatism of the negative thermal lens in $BaWO_4$. Such information is required if accurate predictions are to be made of the behaviour of the cavity at various pump powers.

The existence of the two thermal lenses in intracavity Raman lasers, with their two different origins and scaling laws, makes it particularly complex to predict the thermal behaviour of these systems. A purely empirical approach of testing one cavity after another to find the optimal design would be one way to tackle this problem; however, the combination of numerical modelling of the cavity mode sizes and stability parameters with coupled cavity experiments, as described in Chapter 4, provides a more analytical approach, which makes it easier to identify the main limiting factors in a given cavity design and the changes that will most likely lead to improvements in performance. This method made it possible to improve the performance of the disk-based Raman laser described in this thesis, and further work along these lines may lead to further improvements in the future.

The work presented in Chapter 5 represents, to the best of the author's knowledge, the first detailed experimental investigation of SRS-induced spectral broadening in CW intracavity Raman lasers. The effect has been investigated using Raman crystals with different Raman linewidths. Furthermore it has been shown that it is possible to limit the broadening by using etalons in the fundamental cavity. This information will aid the design of future intracavity Raman lasers in cases where the spectral effects significantly influence the performance of the system. It was shown that most combinations of common laser gain and Raman crystals create the potential for spectral broadening of the fundamental field and therefore it is necessary to decide how, or indeed whether, to attempt to control this in a given Raman laser system. This decision will be influenced by whether or not the spectral width of the output Stokes beam is important for the target application and by whether or not the reduction in the effective Raman gain due to the spectral broadening is a limiting factor in the performance of the laser.

In summary, while intracavity Raman lasers are in principle simple devices, which extend the spectral coverage of solid state laser sources and require only small modifications to existing solid state laser technology, their behaviour is in practice highly complex. The work described in this thesis contributes significantly to our understanding of the physics that underlies the performance of CW intracavity Raman lasers. Both the specific results obtained in this work and the general methods developed may lead to further improvements in the performance of such lasers and increased uptake and deployment of these devices in the future.

# Bibliography

[1] I. Friel, S. L. Geoghegan, D. J. Twitchen, and G. A. Scarsbrook, "Development of high quality single crystal diamond for novel laser applications," in *Optics and Photonics for Counterterrorism and Crime Fighting VI and Optical Materials in Defence Systems Technology VII* (C. Lewis, D. Burgess, R. Zamboni, F. Kajzar, and E. M. Heckman, eds.), vol. 7838, p. 783819, SPIE, 2010.

[2] W. Lubeigt, V. G. Savitski, G. M. Bonner, S. L. Geoghegan, I. Friel, J. E. Hastie, M. D. Dawson, D. Burns, and A. J. Kemp, "1.6 W continuous-wave Raman laser using low-loss synthetic diamond," *Optics Express*, vol. 19, no. 7, pp. 6938–6944, 2011.

[3] D. C. Parrotta, A. J. Kemp, M. D. Dawson, and J. E. Hastie, "Tunable continuous-wave diamond Raman laser," *Optics Express*, vol. 19, no. 24, pp. 24165–24170, 2011.

[4] V. G. Savitski, I. Friel, J. E. Hastie, M. D. Dawson, D. Burns, and A. J. Kemp, "Characterization of Single-Crystal Synthetic Diamond for Multi-Watt Continuous-Wave Raman Lasers," *IEEE Journal of Quantum Electronics*, vol. 48, no. 3, pp. 328 –337, 2012.

[5] O. Kitzler, A. McKay, and R. P. Mildren, "Continuous-wave wavelength conversion for high-power applications using an external cavity diamond Raman laser," *Optics Letters*, vol. 37, pp. 2790–2792, Jul 2012.

[6] P. Dekker, H. M. Pask, D. J. Spence, and J. A. Piper, "Continuous-wave, intracavity doubled, self-Raman laser operation in Nd:GdVO$_4$ at 586.5 nm," *Optics Express*, vol. 15, no. 11, pp. 7038–7046, 2007.

[7] L. Fan, Y.-X. Fan, Y.-Q. Li, H. Zhang, Q. Wang, J. Wang, and H.-T. Wang, "High-efficiency continuous-wave Raman conversion with a BaWO$_4$ Raman crystal," *Optics Letters*, vol. 34, no. 11, pp. 1687–1689, 2009.

[8] J. Lin and H. Pask, "Nd:GdVO$_4$ self-Raman laser using double-end polarised pumping at 880 nm for high power infrared and visible output," *Applied Physics B: Lasers and Optics*, vol. 108, no. 1, pp. 17–24, 2012.

[9] P. Dekker, H. M. Pask, and J. A. Piper, “All-solid state 704 mW continuous-wave yellow source based on an intracavity frequency-doubled crystalline Raman laser,” *Optics Letters*, vol. 32, no. 9, pp. 1114–1116, 2007.

[10] L. Fan, Y. X. Fan, Y. H. Duan, Q. Wang, H. T. Wang, G. H. Jia, and C. Y. Tu, “Continuous-wave intracavity Raman laser at 1179.5 nm with $SrWO_4$ Raman crystal in diode-end-pumped Nd:$YVO_4$ laser,” *Applied Physics B*, vol. 94, no. 4, pp. 553–557, 2009.

[11] L. Fan, Y. X. Fan, and H. T. Wang, “A compact efficient continuous-wave self-frequency Raman laser with a composite $YVO_4$/Nd:$YVO_4$/$YVO_4$ crystal,” *Applied Physics B*, vol. 101, no. 3, pp. 493–496, 2010.

[12] V. A. Lisinetskii, A. S. Grabtchikov, A. A. Demidovich, V. N. Burakevich, V. A. Orlovich, and A. N. Titov, “Nd:KGW/KGW crystal: efficient medium for continuous-wave intracavity Raman generation,” *Applied Physics B*, vol. 88, no. 4, pp. 499–501, 2007.

# Appendices

# Appendix A

# Etalon specifications and mirror/crystal coatings

## Etalon specifications from manufacturers' websites

| E30 and E60 coated glass etalons (290 µm thick) CVI Melles Griot | |
|---|---|
| Adhesion and Durability | Per MIL-C-675C. Insoluble in lab solvents. |
| Clear Aperture | $\geq 21.5\,\mathrm{mm}$ |
| Coating Technology | Electron-beam multilayer dielectric |
| Diameter | 25.4 mm |
| Optical Material | UV-grade fused silica |
| Surface Quality | 10-5 scratch and dig |
| Transmitted Wavefront Error | $\lambda/10$ at 633 nm |
| Wedge | $\leq 1$ arc sec |
| CW Damage Threshold | $1\,\mathrm{MW\,cm^{-2}}$ @ 1064 nm |

| Uncoated YAG etalon (50 µm thick) Light Machinery | |
|---|---|
| Material | Undoped YAG |
| Wavelength range | 250 nm to 4 µm |
| Wedge | Less than 1 arc second typical |
| Clear aperture | 85 % of outside dimension |
| Surface quality | 10/5 or better |
| Matched surface figure | $\lambda/50$ |
| Diameter | 5.0 mm |

## Nd:YVO$_4$ disk used up to Section 4.4.5

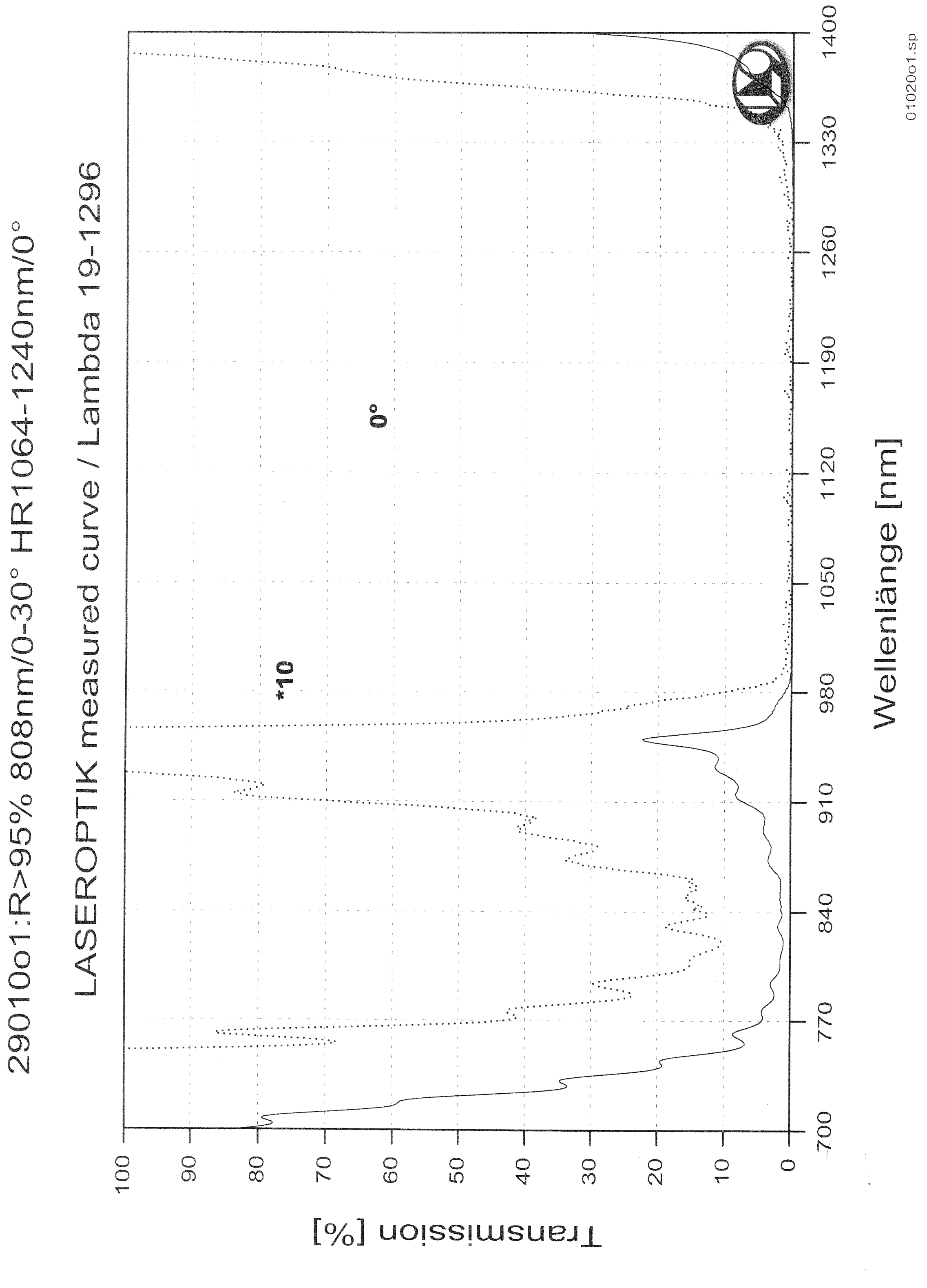

# Nd:$YVO_4$ disks used from Section 4.4.5 onwards

DL1, DL2, DL3

**Advanced Thin Films**

**PE900A** Spectrophotometer Data Time: 7:57:05 AM Date: 6/29/2011

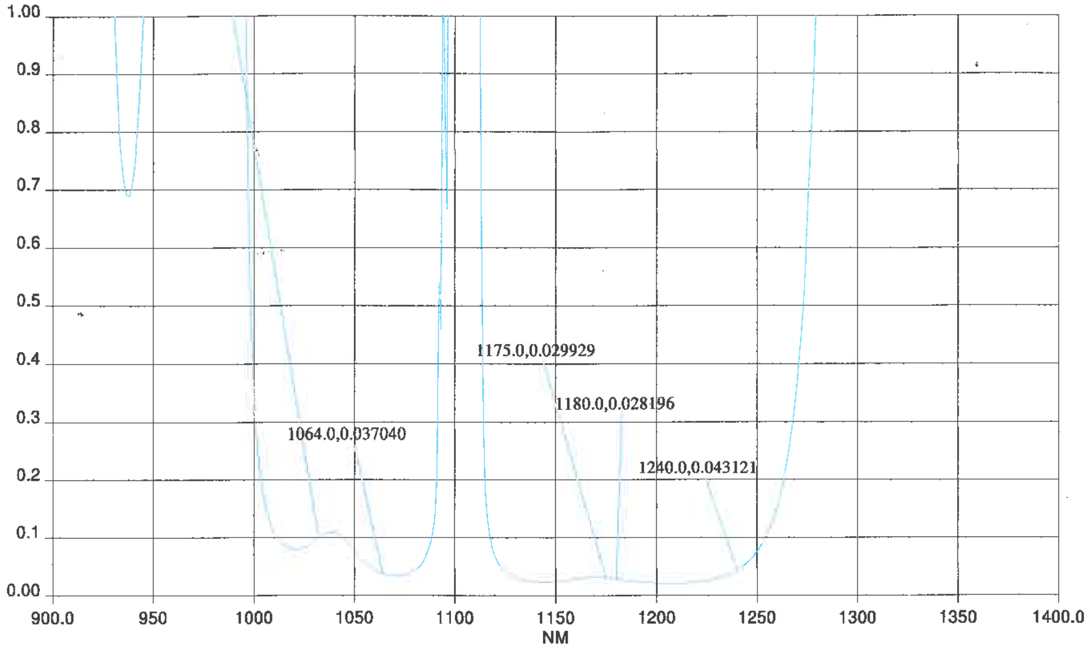

XXR606.SP - 6/29/2011 - V6-521, LiNbO3 Wit, BB, 0° AOI, F=0.01

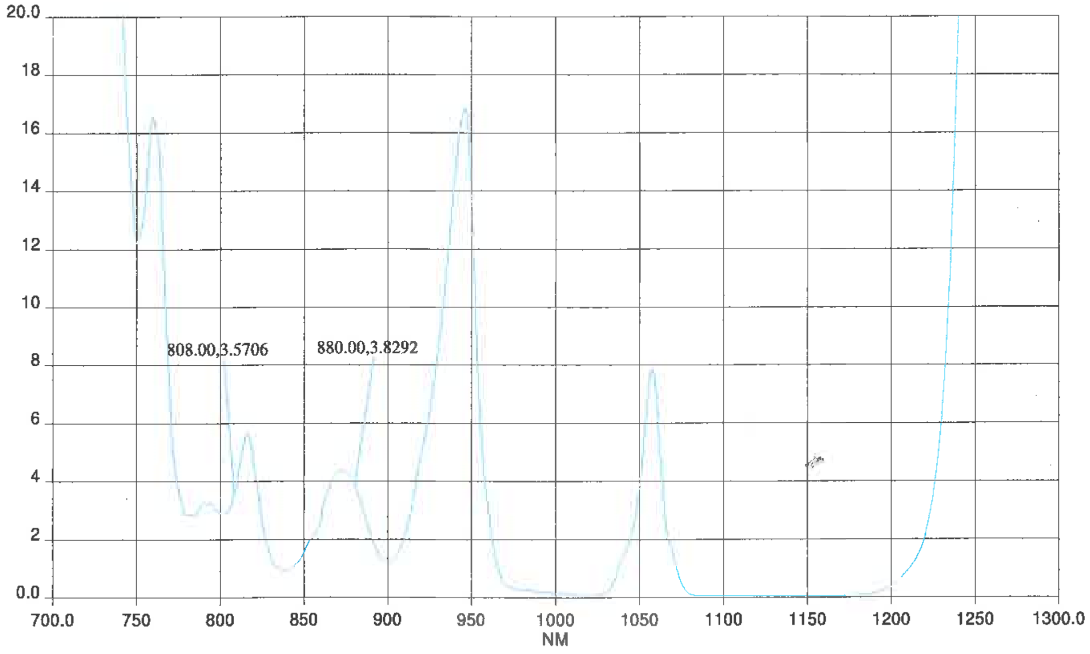

XXR607.SP - 6/29/2011 - V6-521, LiNbO3 Wit, BB,30°M-Pol, F=0.01

# Diamond heatspreader used up to Section 4.4.5

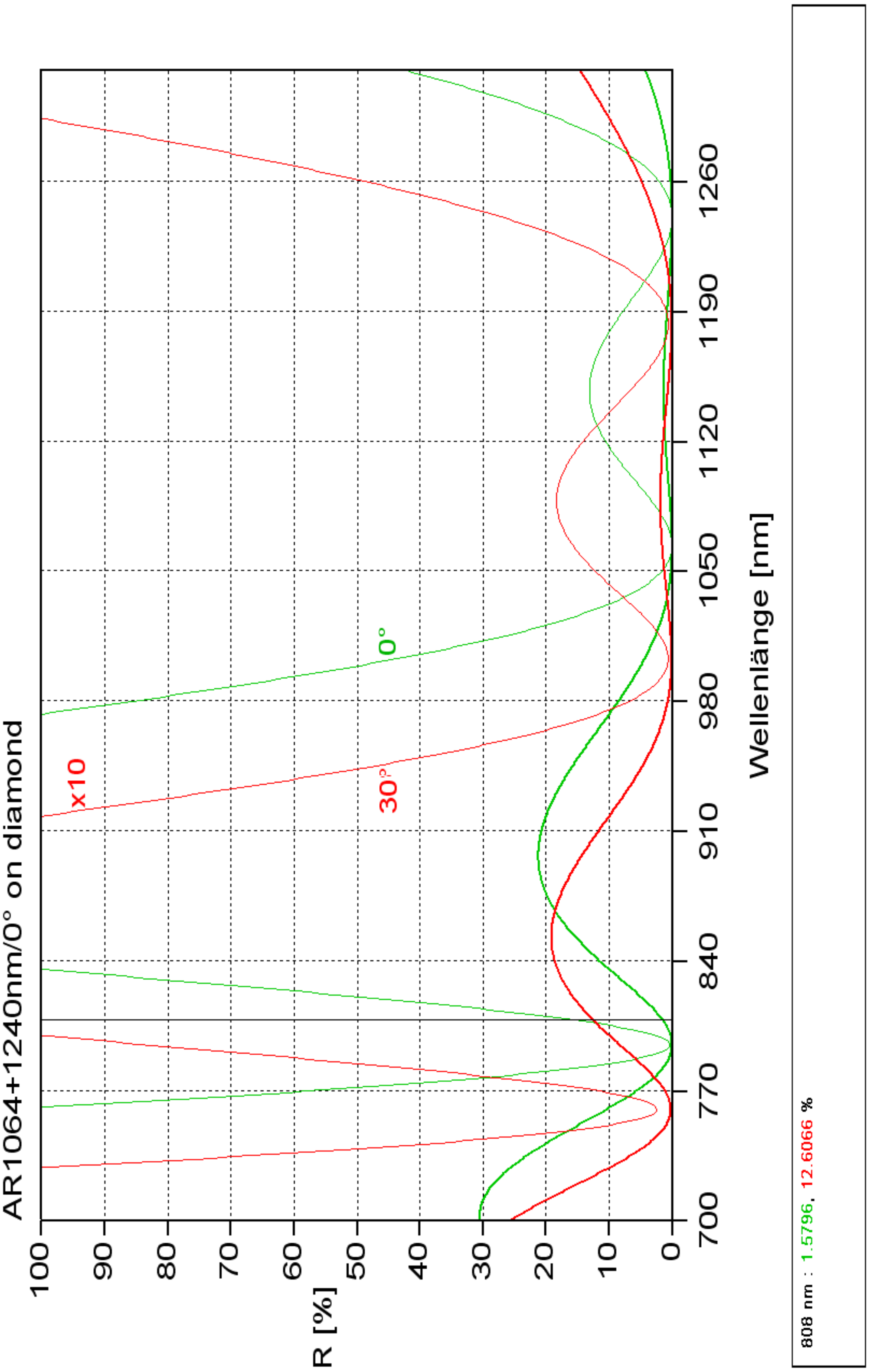

# Diamond heatspreaders used from Section 4.4.5 onwards

Coating runs were deposited on LiNbO3 witnesses, and models of spectral scans were plotted on diamond substrates below:

V4-1790-1 on LiNbO$_3$

model of V4-1790-1: Reflectance on LiNbO3 witness

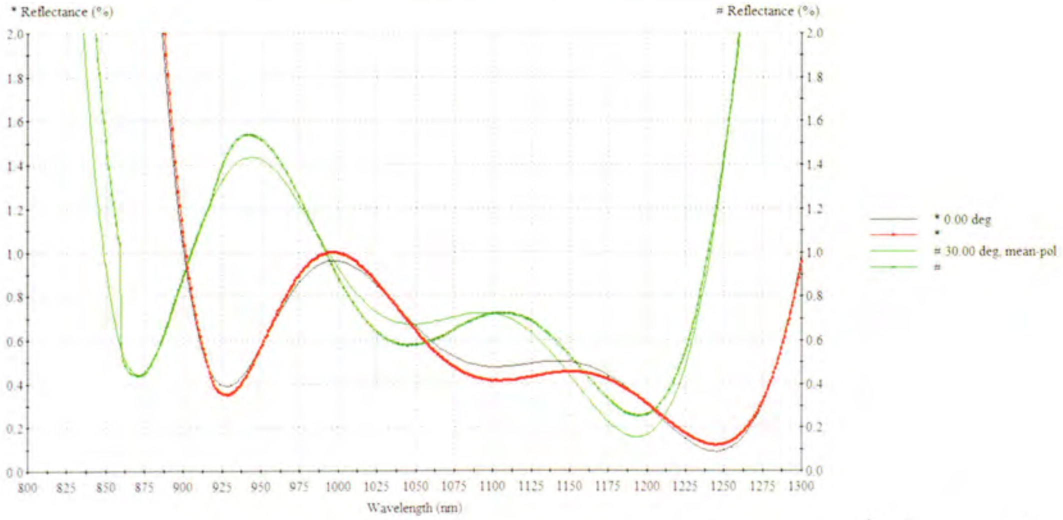

model of V4-1790-1 on Diamond

model of V4-1790-1 Reflectance on diamond

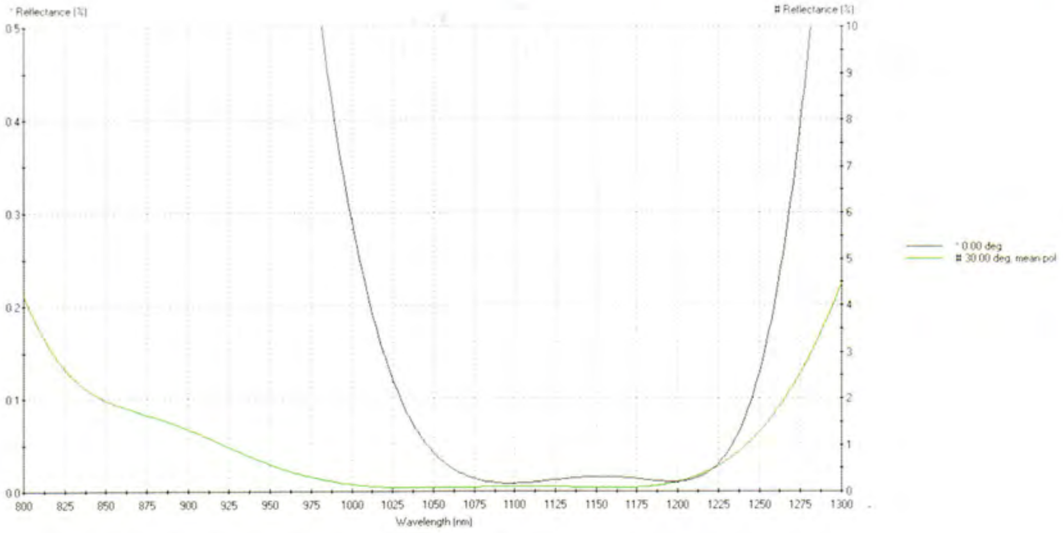

## 25 mm long BaWO$_4$ crystal

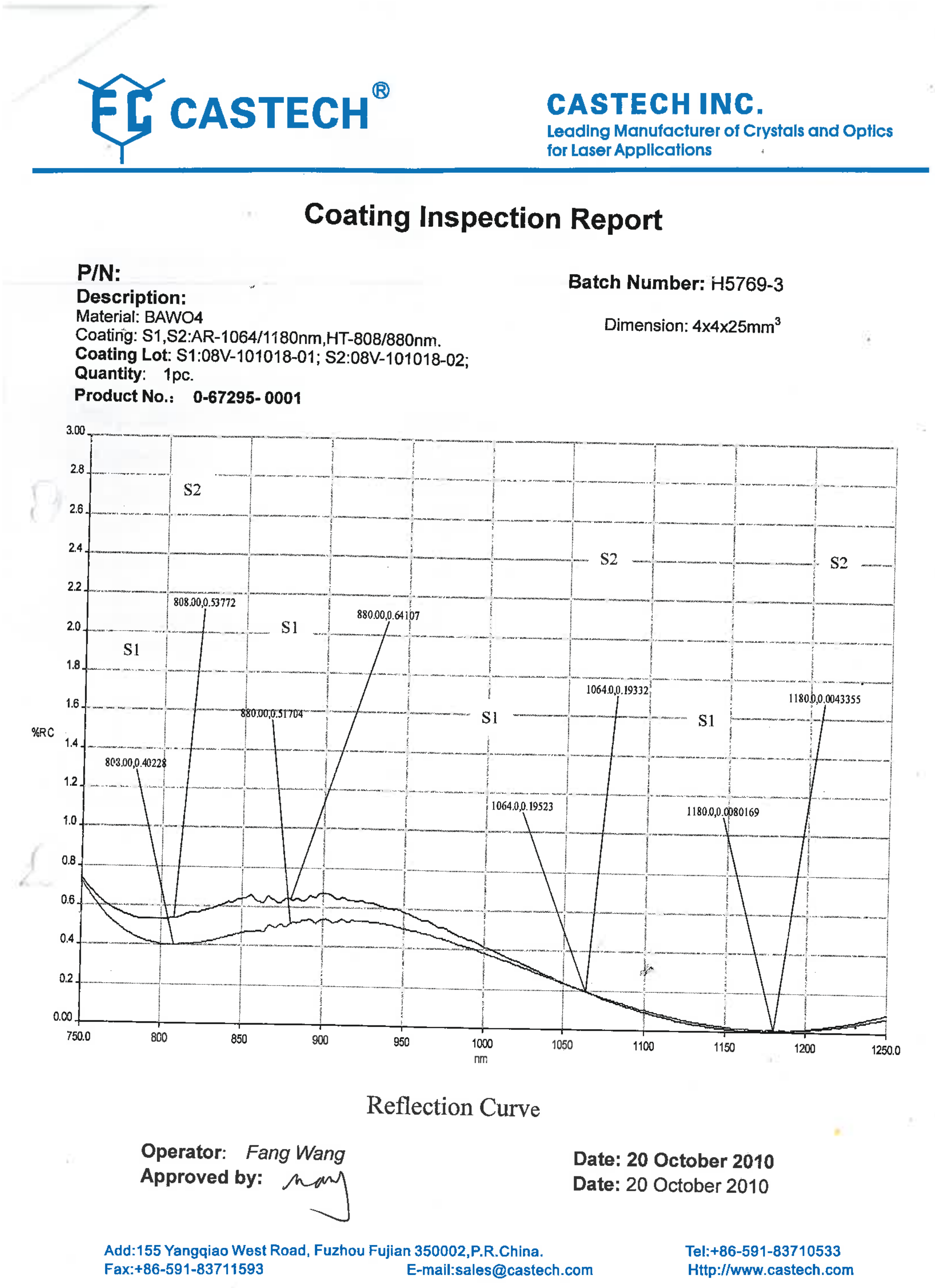

CASTECH®

**CASTECH INC.**
Leading Manufacturer of Crystals and Optics for Laser Applications

### Coating Inspection Report

**P/N:**

**Batch Number:** H5769-3

**Description:**
Material: BAWO4
Coating: S1,S2:AR-1064/1180nm,HT-808/880nm.
**Coating Lot:** S1:08V-101018-01; S2:08V-101018-02;
**Quantity:** 1pc.
**Product No.:** **0-67295- 0001**

Dimension: 4x4x25mm$^3$

Reflection Curve

**Operator:** *Fang Wang*
**Approved by:**

**Date: 20 October 2010**
**Date:** 20 October 2010

Add:155 Yangqiao West Road, Fuzhou Fujian 350002,P.R.China.
Tel:+86-591-83710533
Fax:+86-591-83711593
E-mail:sales@castech.com
Http://www.castech.com

## 16.4 mm long $BaWO_4$ crystal

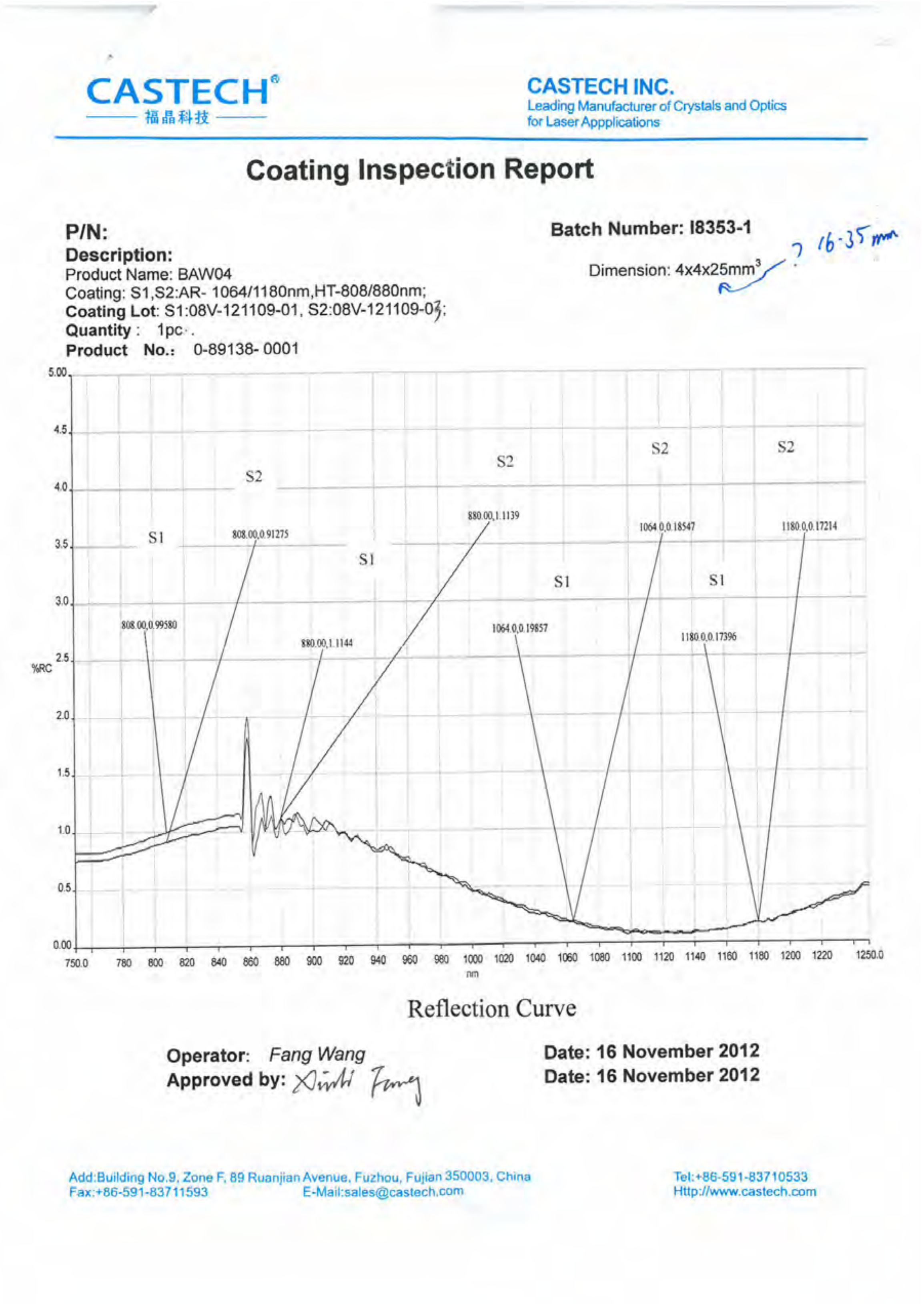

CASTECH®
福晶科技

CASTECH INC.
Leading Manufacturer of Crystals and Optics
for Laser Appplications

# Coating Inspection Report

**Batch Number: I8353-1**

Dimension: 4x4x25mm³ ? 16·35 mm

**P/N:**
**Description:**
Product Name: BAW04
Coating: S1,S2:AR- 1064/1180nm,HT-808/880nm;
**Coating Lot**: S1:08V-121109-01, S2:08V-121109-03;
**Quantity** : 1pc .
**Product No.:** 0-89138- 0001

Reflection Curve

**Operator:** *Fang Wang*
**Approved by:**

**Date: 16 November 2012**
**Date: 16 November 2012**

Add:Building No.9, Zone F, 89 Ruanjian Avenue, Fuzhou, Fujian 350003, China
Fax:+86-591-83711593
E-Mail:sales@castech.com
Tel:+86-591-83710533
Http://www.castech.com

## HR concave fold mirror

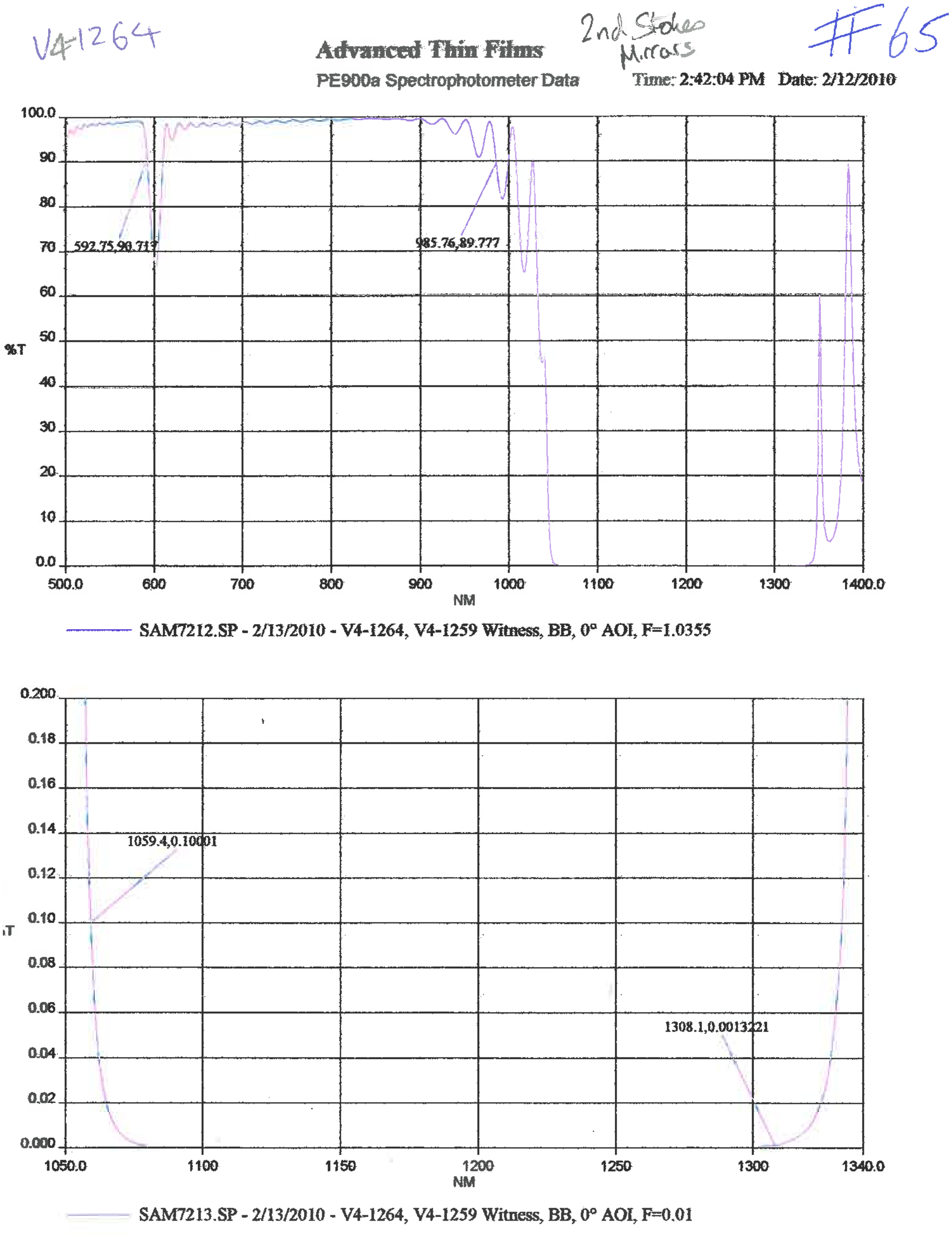

V4-1264

**Advanced Thin Films**

PE900a Spectrophotometer Data

2nd Stokes Mirrors

Time: 2:42:04 PM Date: 2/12/2010

#65

SAM7212.SP - 2/13/2010 - V4-1264, V4-1259 Witness, BB, 0° AOI, F=1.0355

SAM7213.SP - 2/13/2010 - V4-1264, V4-1259 Witness, BB, 0° AOI, F=0.01

## HR concave and convex end mirrors

ectra for
#60 – 72

**Advanced Thin Films** #60

**PE900** Spectrophotometer Data Time: 3:51:08 PM Date: 8/16/2006

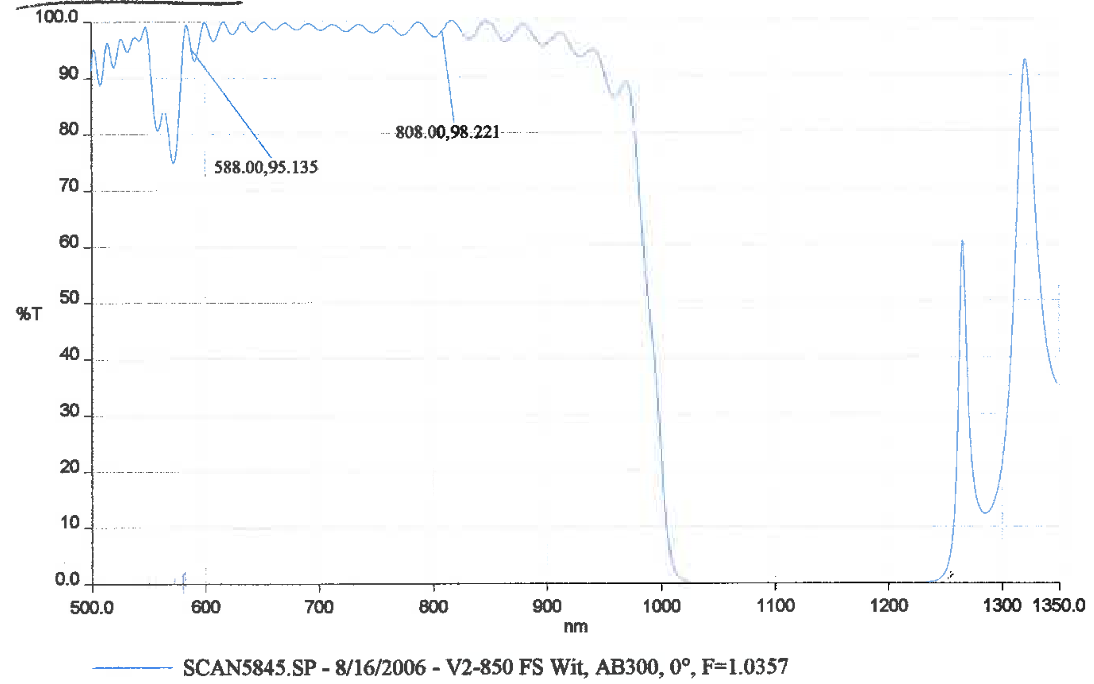

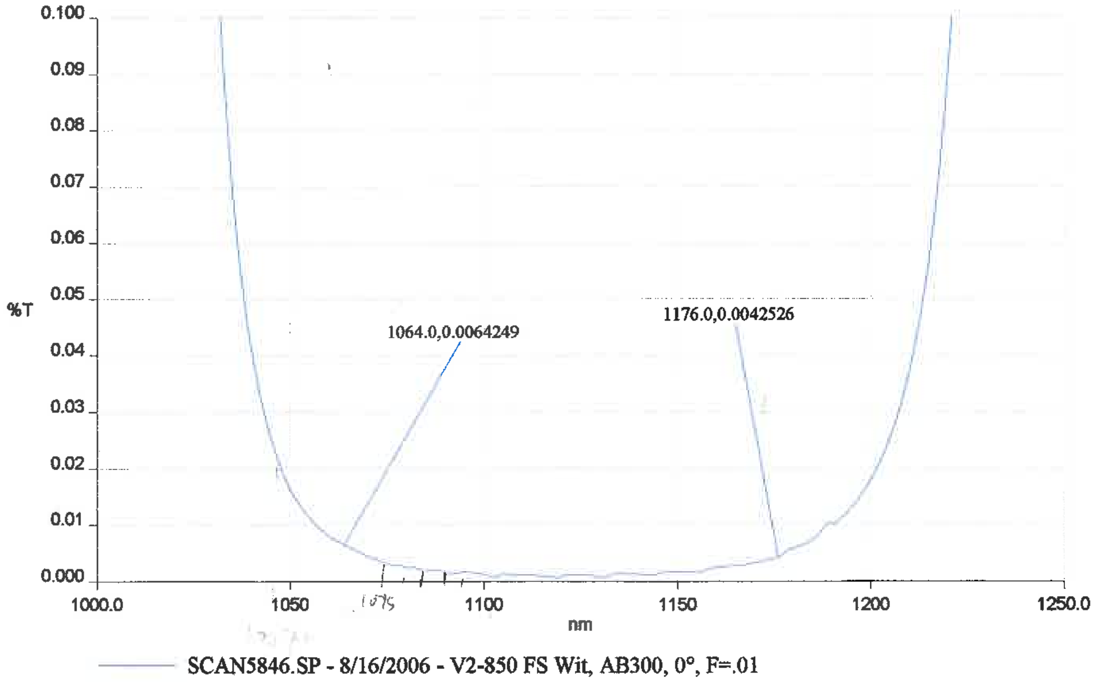

## Stokes output coupler

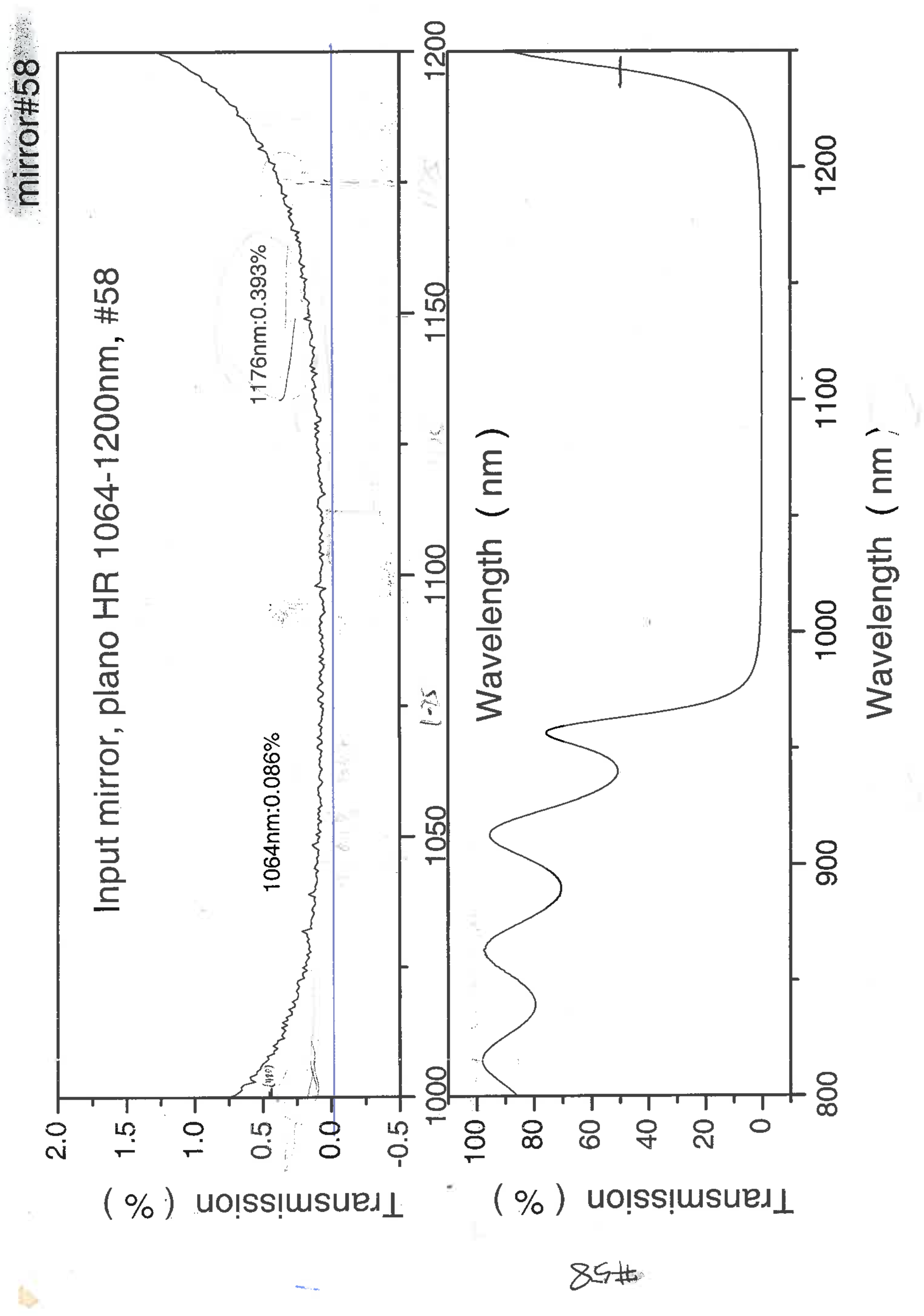

## IR dichroic mirror

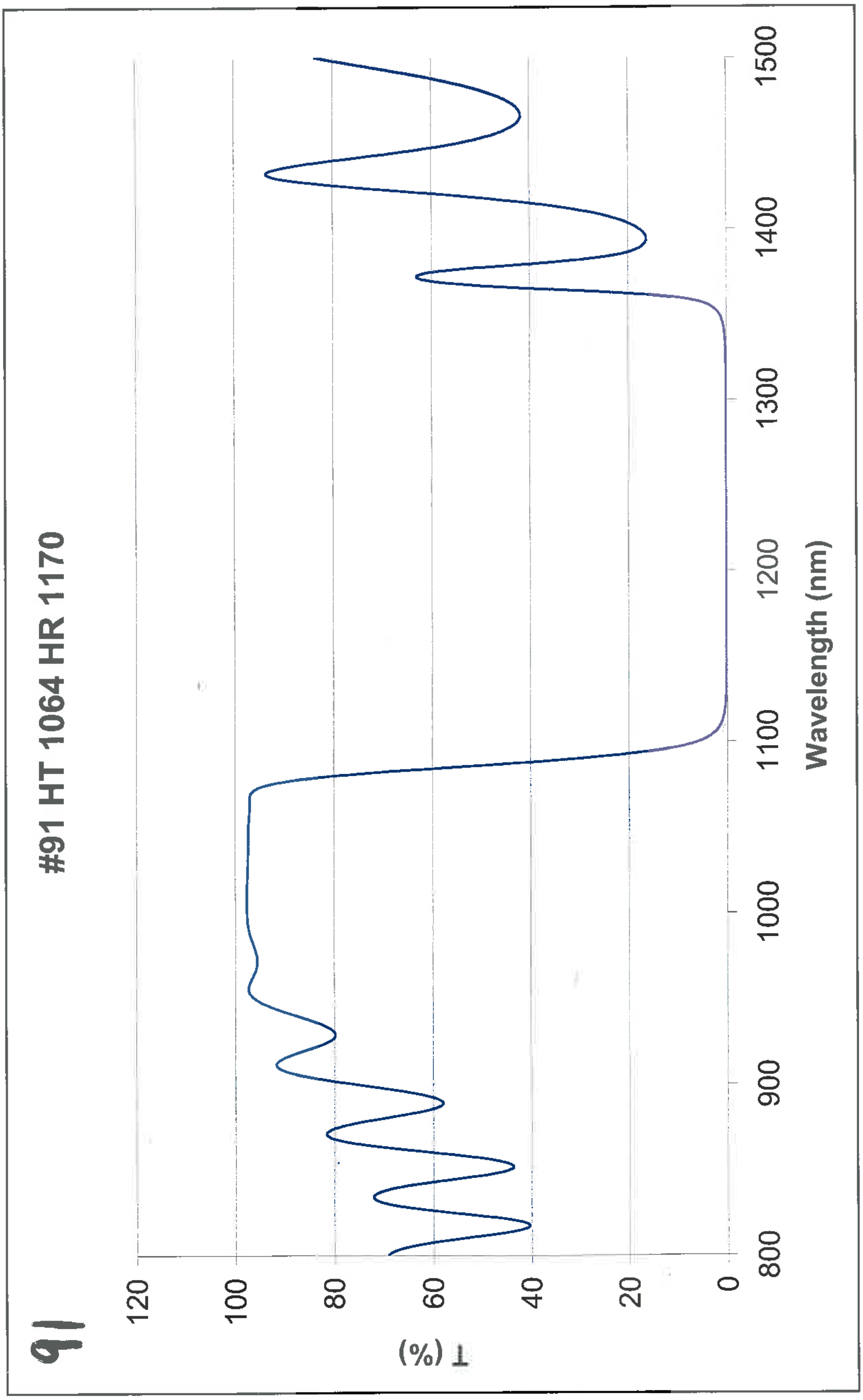

# Probe mirror for LSI experiment (IR/visible dichroic)

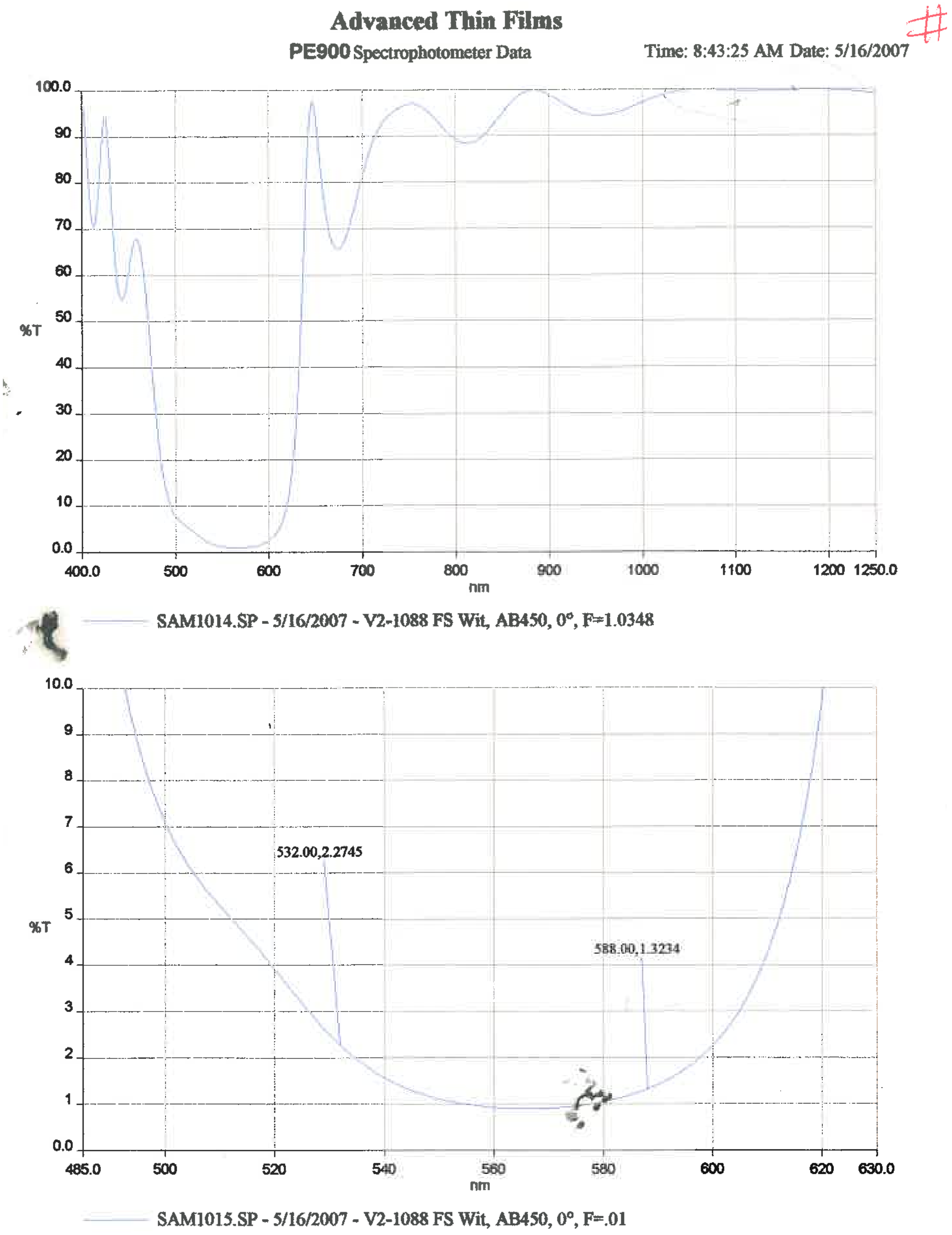

**Advanced Thin Films**

**PE900** Spectrophotometer Data

Time: 8:43:25 AM Date: 5/16/2007

#

SAM1014.SP - 5/16/2007 - V2-1088 FS Wit, AB450, 0°, F=1.0348

SAM1015.SP - 5/16/2007 - V2-1088 FS Wit, AB450, 0°, F=.01

# Probe mirror for LSI experiment (IR/visible dichroic)

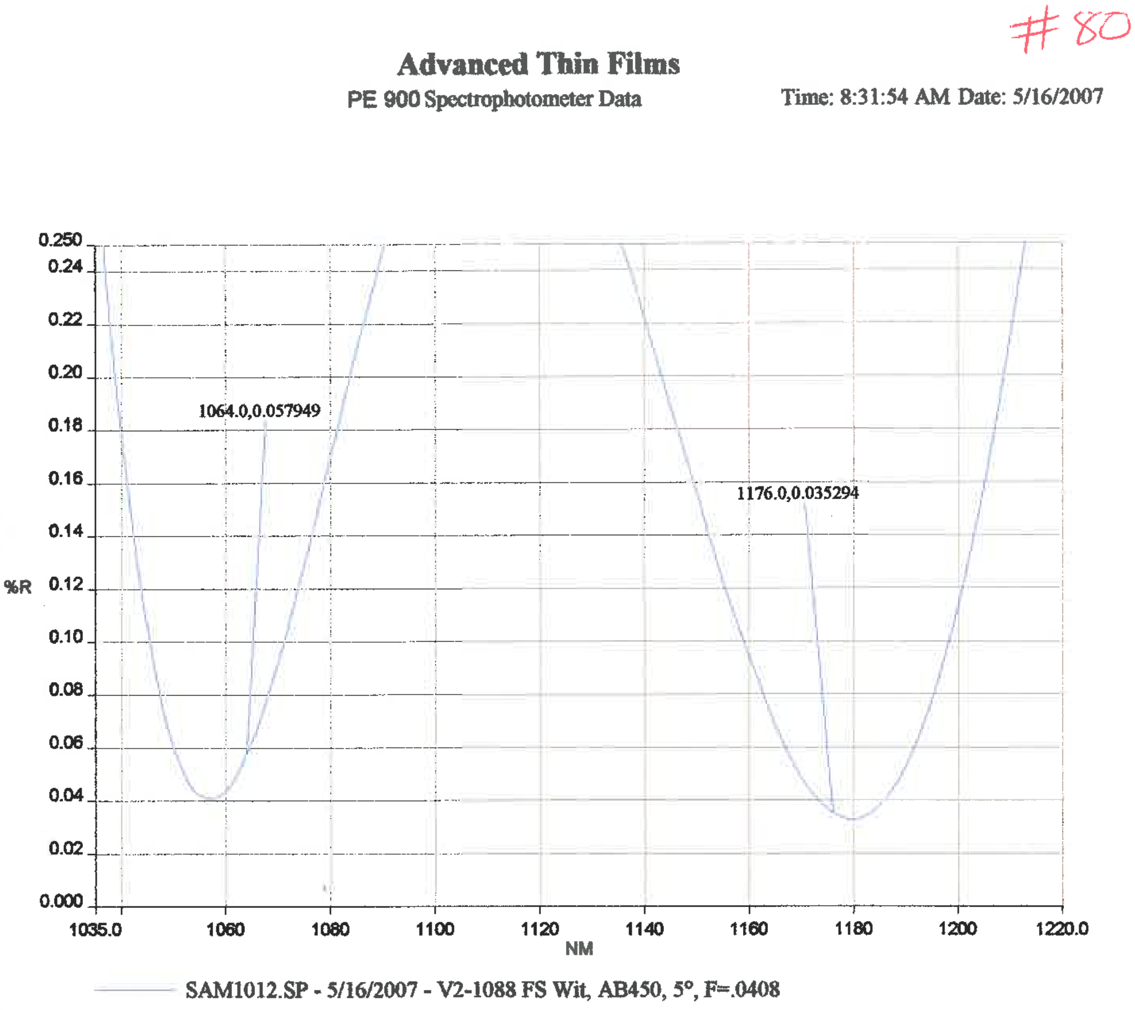

#80

**Advanced Thin Films**

PE 900 Spectrophotometer Data

Time: 8:31:54 AM Date: 5/16/2007

SAM1012.SP - 5/16/2007 - V2-1088 FS Wit, AB450, 5°, F=.0408

# Appendix B

# MATLAB scripts

## Stability parameters as a function of pump power

The following MATLAB script calculates the cavity stability parameters ($g_1$, $g_2$) for a range of pump powers, given the values of the thermal lens strengths for those pump powers in a file supplied by the user. The sample code shown is for the horizontal (tangential) plane of the fundamental cavity in Figure 4.15 – the ABCD matrices must be modified for different cavity designs and the radius of curvature of the fold mirror must be modified for the vertical (sagittal) plane.

```
%Load thermal lens data into matrix TLdatavmvabw (col 1 vanadate mirror,
%col 2 vanadate dn/dT lens, col 3 BW lens)
lensdatafile = uigetfile('.csv', 'Select␣data␣file');
TLdatavmvabw = csvread(lensdatafile, 1, 0);

%Pre-allocate g matrix (2 columns, same number of rows as thermal lens
%matrix ie one row for each pump power)
g=zeros(size(TLdatavmvabw,1),2);
%Pre-allocate L vector (effective cavity length)
L=zeros(size(TLdatavmvabw,1),1);

%Set cavity parameters

%Refractive indices
nbw=1.8;
ndc=1.5;
ndi=2.4;
nva=2.2;

%Lengths of transmissive components
Lbw1=0.008175;
Lbw2=0.008175;
Ldc=0.003;
Ldi=0.00075;
Lv1=0.00025;
```

```
Lv2=0.00025;

%Spacings between elements
L1=0.001;
L2=0.04365;
L3=0.0665;
L4=0.0965;

%Create matrices for changeable mirrors
Mem=[1,0;10,1];
Mfm=[1,0;-20.249,1];

%Create other matrices (except thermal lenses)
P1=[1,L1;0,1];
Pbw1=[1,Lbw1/nbw;0,1];
Pbw2=[1,Lbw2/nbw;0,1];
P2=[1,L2;0,1];
P3=[1,L3;0,1];
Pdc=[1,Ldc/ndc;0,1];
P4=[1,L4;0,1];
Pdi=[1,Ldi/ndi;0,1];
Pv1=[1,Lv1/nva;0,1];
Pv2=[1,Lv2/nva;0,1];

%Loop through all pump power data points
for i=1:size(TLdatavmvabw,1)
    %Create thermal lens matrices
    TLvm=[1,0;-TLdatavmvabw(i,1),1];
    TLva=[1,0;-TLdatavmvabw(i,2),1];
    TLbw=[1,0;-TLdatavmvabw(i,3),1];
    %Calculate total cavity matrix (1 pass)
    MT=TLvm*Pv2*TLva*Pv1*Pdi*P4*Pdc*P3*Mfm*P2*Pbw1*TLbw*Pbw2*P1*Mem;
    %Extract effective g parameters and length from total matrix
    g(i,1)=MT(1,1);
    g(i,2)=MT(2,2);
    L(i)=MT(1,2);
end

%Write out g for inspection
 g
 g(:,1)
 g(:,2)
 checkdet=det(MT)

%Define stability limit hyberbola for plot
g1ref=-3:0.1:3;
g2ref=1./g1ref;

%Plot stability diagram
stability_diagram(g(:,1),g(:,2),g1ref,g2ref)
```

## Normalisation of spectra

The following MATLAB script loads the output file from the Ocean Optics HR4000 spectrometer and separately normalises the fundamental and Stokes spectra with respect to area, writing each normalised spectrum to a file with both wavelength and wavenumber axes. The sample code shown is for $BaWO_4$. A different section of the data would need to be selected for the Stokes peak when other Raman crystals are used.

```
%This program selects designated sections for fundamental and Stokes peaks
%from HR4000 data files and normalises fundamental and Stokes separately.
%It then writes out the normalised spectra to another file for plotting in
%Origin.

%Get user to select data file and save filename to ”name” and spectral
    data
%to ”spectrum_all”
clear
file=uigetfile('.txt', 'Select␣data␣file');
[path,name,ext]=fileparts(file);
spectrum_all = importdata(file, '\t', 17);

%Pre-allocate variables
fundamental=zeros(216,3);
stokes=zeros(314,3);
fund_norm=zeros(216,3);
stokes_norm=zeros(314,3);

%Extract appropriate sections of spectra
for i=1:216
    fundamental(i,1)=spectrum_all.data(i+194,1);
    fundamental(i,3)=spectrum_all.data(i+194,2);
end

for j=1:314
    stokes(j,1)=spectrum_all.data(j+3109,1);
    stokes(j,3)=spectrum_all.data(j+3109,2);
end

%Convert wavelength to wavenumber
for i=1:216
    fundamental(i,2)=1/(fundamental(i,1)*10^(-7));
end

for j=1:314
    stokes(j,2)=1/(stokes(j,1)*10^(-7));
end

%Plot spectra to check
% figure
```

```
% subplot(2,2,1)
% plot(fundamental(:,1), fundamental(:,3))%
% subplot(2,2,2)
% plot(fundamental(:,2), fundamental(:,3))%
% subplot(2,2,3)
% plot(stokes(:,1), stokes(:,3))%
% subplot(2,2,4)
% plot(stokes(:,2), stokes(:,3))

%Normalise spectra with respect to area

for i=1:216
    fund_norm(i,1)=fundamental(i,1);
    fund_norm(i,2)=fundamental(i,2);
    fund_norm(i,3)=fundamental(i,3)/(trapz(flipud(fundamental(:,2)),flipud(fundamental(:,3))));
end

for j=1:314
    stokes_norm(j,1)=stokes(j,1);
    stokes_norm(j,2)=stokes(j,2);
    stokes_norm(j,3)=stokes(j,3)/(trapz(flipud(stokes(:,2)),flipud(stokes(:,3))));
end

trapz(flipud(fundamental(:,2)),flipud(fundamental(:,3)))
trapz(flipud(stokes(:,2)),flipud(stokes(:,3)))
trapz(fundamental(:,1),fundamental(:,3))
trapz(stokes(:,1),stokes(:,3))
trapz(flipud(fund_norm(:,2)),flipud(fund_norm(:,3)))
trapz(flipud(stokes_norm(:,2)),flipud(stokes_norm(:,3)))
trapz(fund_norm(:,1),fund_norm(:,3))
trapz(stokes_norm(:,1),stokes_norm(:,3))

%Plot normalised spectra to check
% figure
% subplot(2,2,1)
% plot(fund_norm(:,1), fund_norm(:,3))
% subplot(2,2,2)
% plot(fund_norm(:,2), fund_norm(:,3))
% subplot(2,2,3)
% plot(stokes_norm(:,1), stokes_norm(:,3))
% subplot(2,2,4)
% plot(stokes_norm(:,2), stokes_norm(:,3))

%create filenames and write normalised specra to files (one file for
%fundamental, another for Stokes.
fundstring='f_area_';
stokesstring='s_area_';
fund_fullname=strcat(fundstring,name,'.csv');
```

```
stokes_fullname=strcat(stokesstring,name,'.csv');
dlmwrite(fund_fullname, fund_norm, 'delimiter', ',', 'precision', 6);
dlmwrite(stokes_fullname, stokes_norm, 'delimiter', ',', 'precision', 6);
```

## Effective Raman gain

The following MATLAB script calculates the effective Raman gain for given fundamental and Stokes spectra, assuming a Lorentzian profile for the Raman transition. The example shown is for BaWO$_4$. The parameters of the Raman transition and the section of the spectrum corresponding to the Stokes peak need to be changed when other Raman crystals are used.

```
%This program selects designated sections for fundamental and Stokes peaks
%from HR4000 data files and normalises fundamental and Stokes separately.
%It then convolves the fundamental spectrum with a Lorentzian
%representation of the BW Raman peak to get the spectral gain, and takes
%the overlap of the spectral gain with the Stokes peak to determine the
%effective Raman gain.

%Get user to select data file and save filename to "name" and spectral
    data
%to "spectrum_all"

%-----------------------------------------------------------------------
clear
file=uigetfile('.txt', 'Select␣data␣file');
[path,name,ext]=fileparts(file);
spectrum_all = importdata(file, '\t', 17);

%-----------------------------------------------------------------------
%Pre-allocate variables
fundamental=zeros(216,3);
stokes=zeros(314,3);
fund_norm=zeros(216,3);
stokes_norm=zeros(314,3);

%-----------------------------------------------------------------------
%Extract appropriate sections of spectra
for i=1:216
    fundamental(i,1)=spectrum_all.data(i+194,1);
    fundamental(i,3)=spectrum_all.data(i+194,2);
end

for j=1:314
    stokes(j,1)=spectrum_all.data(j+3109,1);
    stokes(j,3)=spectrum_all.data(j+3109,2);
end
```

```
%-----------------------------------------------------------------------
%Convert wavelength to wavenumber
for i=1:216
    fundamental(i,2)=1/(fundamental(i,1)*10^(-7));
end

for j=1:314
    stokes(j,2)=1/(stokes(j,1)*10^(-7));
end

%-----------------------------------------------------------------------
%Normalise spectra to area of 1.
for i=1:216
    fund_norm(i,1)=fundamental(i,1);
    fund_norm(i,2)=fundamental(i,2);
    fund_norm(i,3)=fundamental(i,3)/(trapz(flipud(fundamental(:,2)),flipud
        (fundamental(:,3))));
end

for j=1:314
    stokes_norm(j,1)=stokes(j,1);
    stokes_norm(j,2)=stokes(j,2);
    stokes_norm(j,3)=stokes(j,3)/(trapz(flipud(stokes(:,2)),flipud(stokes
        (:,3))));
end

%-----------------------------------------------------------------------
%Flip spectra to give ascending wavenumner axis
fund_norm =flipud(fund_norm);
stokes_norm =flipud(stokes_norm);

%-----------------------------------------------------------------------
%Interpolate spectra on to regular grid.
nu_f=transpose(9355:0.1:9442);
F=zeros(871,1);
F=interp1(fund_norm(:,2),fund_norm(:,3),nu_f);

%-----------------------------------------------------------------------
%Plot original and interpolated spectra to check
%plot(fund_norm(:,2),fund_norm(:,3),nu_f,F)

%-----------------------------------------------------------------------
%Create Raman peak on grid of same spacing as nu_fPeak is Lorentzian,
%normalised to have a peak value of 1.
v=transpose(-968.5:0.1:-881.5);
R=zeros(871,1);
for i=1:871
    R(i)=(1/4)*((1.6)^2/((v(i)+925)^2+(0.5*1.6)^2));
end
```

```
%Delta functions for testing frequency axis calibration. Not to be used in
%real calculations.
% R(100)=1;
% R(750)=0.5;
%---------------------------------------------------------------------------
%Plot Raman peak to check
%plot(v,R)
%---------------------------------------------------------------------------
%Perform convulation to calculate spectral gain, G
G=zeros(1741,1);
for n=1:1741
    for m=1:871
        if ((n-m+1)<1||(n-m+1)>871)
           G(n)=G(n)+0;
        else
            G(n)=G(n)+R(m)*F(n-m+1)*0.1;
        end
    end
end

%---------------------------------------------------------------------------
%Define frequency axis for G
nu_g1=(8386.5:0.1:8560.5);

%---------------------------------------------------------------------------
%Interpolate G and stokes_norm onto grid
nu_g2=transpose(8439:0.1:8510);
S=interp1(stokes_norm(:,2),stokes_norm(:,3),nu_g2);
Gi=interp1(nu_g1,G,nu_g2);

%---------------------------------------------------------------------------
%Perform overlap integral. Note that g_eff is actually the epsilon factor
    I
%refer to in my thesis - multiply the measured Raman gain coeff by epsilon
%(g_eff here) to get effective gain.
g_eff=0;

for i=1:711
    %if (S(i)>=0)
        g_eff=g_eff+Gi(i)*S(i)*0.1;
    %else
    %end
end

%Print out g_eff to screen
g_eff
%---------------------------------------------------------------------------
%---------------------------------------------------------------------------
%test plots
h=figure;
```

```
subplot(2,2,1)
    plot(fund_norm(:,2),fund_norm(:,3),'b'); hold on;
    plot(nu_f, F, 'c'); hold off
    %Set x limits
    %xlim([0 429]);
    % Create xlabel
    xlabel('Wavenumber␣(cm^-1)');
    % Create ylabel
    ylabel('Normalised␣Signal␣(cm)');
    % Create legend
    legend('Normalised␣fundamental', 'Interpolated␣spec');
subplot(2,2,2)
    plot(nu_g1, G,'g'); hold on;
    plot(nu_g2, Gi, 'k'); hold off
    %xlim([881.3 968.6]);
    xlabel('Wavenumber␣(cm^-1)');
    ylabel({'Spectral␣gain␣(a.u.)'});
    legend('Spectral␣gain', 'Interpolated');
subplot(2,2,3)
    plot(stokes_norm(:,2), stokes_norm(:,3), 'r'); hold on;
    plot(nu_g2, S, 'm'); hold off
    %xlim([9350 9445]);
    xlabel('Wavenumber␣(cm^-1)');
    ylabel({'Normalised␣signal␣(cm)'});
    legend('Normalised␣Stokes', 'Interpolated␣spec');
subplot(2,2,4)
    plot(nu_g2, Gi, 'k'); hold on;
    plot(nu_g2, S, 'm'); hold off
    xlabel('Wavenumber␣(cm^-1)');
    ylabel({'Spectral␣gain␣(a.u.)␣or␣Normalised␣signal␣(cm)'});
    legend('Spectral␣gain␣(interp)', 'Stokes␣(interp)');
%--------------------------------------------------------------------------
%--------------------------------------------------------------------------

%--------------------------------------------------------------------------
%Save figure in MATLAB fig format
figurefilefig=strcat(name,'.fig');
hgsave(h,figurefilefig);

%Write interpolated spectral gain (Gi) and Stokes spectrum to csv file
data = [nu_g2 Gi S];
gainprefix = 'g_';
file_fullname=strcat(gainprefix,name,'.csv');
dlmwrite(file_fullname, data, 'delimiter', ',', 'precision', 6);
```

# Appendix C

# Publications

## Conference presentations (posters)

[1] **G. M. Bonner**, A. J. Lee, J. Wang, H. Zhang, H. M. Pask, and D. J. Spence, "Spectral Broadening in CW Intracavity Raman Lasers," in *Europhoton*, 2012.

[2] **G. M. Bonner**, T. Omatsu, A. J. Lee, A. J. Kemp, J. Wang, H. Zhang, and H. M. Pask, "Thermal Lensing in CW Intracavity Raman Lasers," in *Europhoton*, 2012.

[3] **G. M. Bonner**, H. Zhang, J. Wang, A. J. Kemp, and H. M. Pask, "Continuous-wave $SrMoO_4$ Intracavity Raman Laser Pumped Using a Disk Laser," in *CLEO Pacific Rim*, 2011.

Note that the results presented on the above poster related primarily to a $BaWO_4$ Raman laser due to damage to the $SrMoO_4$ crystal sustained after the conference paper was submitted.

[4] **G. M. Bonner**, W. Lubeigt, D. Burns, and A. J. Kemp, "Measurements of loss and birefringence in optical quality synthetic diamond and the implications for diamond Raman lasers," in *Photon10*, 2010.

## Journal papers

[1] **G. M. Bonner**, H. M. Pask, A. J. Lee, A. J. Kemp, J. Wang, H. Zhang, and T. Omatsu, "Measurement of thermal lensing in a CW $BaWO_4$ intracavity Raman laser," *Optics Express*, vol. 20, no. 9, pp. 9810–9818, Apr 2012.

In the above publication, the author designed and characterised the Raman laser. The lateral shearing interferometry experiments were carried out by the author working together with Prof. Takashige Omatsu, who analysed the resulting interferograms to obtain the thermal lens strength. The thermal lens data was interpreted by the author with reference to the material properties of $BaWO_4$.

[2] W. Lubeigt, V. G. Savitski, **G. M. Bonne**r, S. L. Geoghegan, I. Friel, J. E. Hastie, M. D. Dawson, D. Burns, and A. J. Kemp, "1.6 W continuous-wave Raman laser using low-loss synthetic diamond," *Optics Express*, vol. 19, no. 7, pp. 6938–6944, 2011.

[3] W. Lubeigt, **G. M. Bonner**, J. E. Hastie, M. D. Dawson, D. Burns, and A. J. Kemp, "Continuous-wave diamond Raman laser," *Optics Letters*, vol. 35, no. 17, pp. 2994–2996, 2010.

[4] W. Lubeigt, **G. M. Bonner**, J. E. Hastie, M. D. Dawson, D. Burns, and A. J. Kemp, "An Intra-cavity Raman Laser using Synthetic Single-crystal Diamond," *Optics Express*, vol. 18, no. 16, pp. 16765–16770, 2010.

In the above publications, the author measured the optical losses in various diamond samples, which aided in understanding the performance of the reported lasers and in identifying low loss diamond suitable for use in CW intracavity Raman lasers.